PLACE IN RETURN BOX to remove this checkout from your record.
TO AVOID FINES return on or before date due.

DATE DUE	DATE DUE	DATE DUE
SP 25 FEC 0 5		

MSU Is An Affirmative Action/Equal Opportunity Institution
c:\circ\datedue.pm3-p.1

AN INVESTIGATION OF FLUID FLOW DURING INDUCTION STROKE OF A
WATER ANALOG MODEL OF AN IC ENGINE USING AN INNOVATIVE
OPTICAL VELOCIMETRY CONCEPT -- LIPA

By

Bernd Stier

A DISSERTATION

Submitted to
Michigan State University
in partial fulfillment of the requirements
for the degree of

DOCTOR OF PHILOSOPHY

Department of Mechanical Engineering

1994

ABSTRACT

AN INVESTIGATION OF FLUID FLOW DURING INDUCTION STROKE OF A
WATER ANALOG MODEL OF AN IC ENGINE USING AN INNOVATIVE
OPTICAL VELOCIMETRY CONCEPT -- LIPA

By

Bernd Stier

Optical measurements on an axisymmetrical quartz component engine research model were made to evaluate the flow field encountered during induction. The measurement technique is LIPA (*L*aser *I*nduced *P*hotochemical *A*nemometry), a non-intrusive velocimetry concept that provides an investigator of fluid flow with a tool to attain planar information about three-dimensional velocity and vorticity vectors in a single measurement step. The goal of this investigation is to further develop this measurement technique and apply it to study the induction stroke of a water analog model of a four-stroke internal combustion engine.

The research conducted in the water analog model is a fundamental scientific inquiry into the flow fields that develop in the induction stroke of an engine at idling engine speeds. As this is the first investigation of its kind using LIPA technique, our goal has been to quantify, in a preliminary manner, the flow field features that develop during the intake stroke. In the process a more comprehensive understanding of the flow field features was developed, and tied to the quantifications. The study evaluated the flow field of the intake stroke by estimating fields of velocity and vorticity. On the basis of these data, information about fluid dynamics during induction at engine speeds of 10, 20, and 30 RPM (corresponding to 170, 340, and 510 RPM respectively, when air is the flowing medium) for three different valve lifts was obtained. The overall development of the flow field, its energy content (kinetic, fluctuation) for the different settings of the engine parameters, vorticity information, and cyclic variations have been quantified. These have been discussed in terms of mixing performance.

ACKNOWLEDGMENTS

I would like to take this opportunity to thank the many people whose help and assistance were invaluable for the realization of this work. The first 'thank you' goes to my advisor, Prof. Robert E. Falco, for providing me with the initial impulse and the guidance for this doctoral program. I thank the members of my committee, Profs. Daniel Nocera, Manoochehr M. Koochesfahani, and Harold Schock, for their fruitful scientific comments and procurement of insight throughout the project. Thomas Stuecken, Michael Hetherington, John Brandon, and Colin McKinnon assisted me in many questions of mechanical, electronical, and computational problems; I am intensely grateful for their efforts and input.

I thank Michael for his stimulating visits and my fiancée Amy for her warm encouragement via telephone as support during my solitude in a 'human-deserted' laboratory.

Finally I would like to express my gratitude for the financial support endowed by the Ford Motor Company in Dearborn, MI, by NASA Langley Research Center, and by the Center of Fundamental Material Research (CFMR) at the Michigan State University without whose financial aid this project would not have been possible.

TABLE of CONTENTS

LIST of TABLES

LIST of FIGURES

LIST of ABBREVIATIONS and NOMENCLATURE

BDC   bottom dead center
BrNp   Bromonaphthalene
CA   crank-angle
CCD   charge coupled device
CD   Glucosyl-β-cyclodextrin
CFD   computational fluid dynamics
CtC   cycle-to-cycle (variability)
DHN   Decahydronaphthalene
EA   abbreviation referring to data in the context of ensemble averaged results
EC   engine cycle
HIS   Highest Intensity Spot; algorithm for deduction of positions of illuminated particles
IA   intersection area
IAR   Reconstruction of IA; algorithm for deduction of positions of illuminated particles
IC   internal combustion
IIL   image intensifier lens
IP   intersection point
KSCN   Potassium Thiocyanate
LDA   laser Doppler anemometry
LIPA   Laser Induced Photochemical Anemometry
M   mol per liter
RMS   root mean square
RPM   revolutions per minute
t-BuOH   *tert*-butyl alcohol
TDC   top dead center
TRP   toroidal recirculation pattern
UV   ultra violet
VL   valve lift
2D   two-dimensional
3D   three-dimensional

buffer zone   An area on top of the piston head in which no consistent flow pattern exists.
induction angle   Angle under which the intake jet enters the engine cylinder.
interface zone   A region in which the intake jet and the main recirculation pattern interact.
recirculativity   A measure to evaluate how much structure a flow pattern contains and by how much fluid flow is recirculated within this flow pattern.

LIST of SYMBOLS

AM	angular momentum over certain area
b	width of nozzle
CV	measure for velocity fluctuation in connection with cyclic variations
D	diffusion coefficient
d	spatial distance between two circumferential components of the vorticity vector
dA	infinitesimal area
$d\bar{s}$	infinitesimal line segment
FE	specific energy in conjunction with velocity fluctuations
i, j, k	running indices
J	momentum flux
KE	specific kinetic energy
L	characteristic length
$\hat{\ell}_{dist}$	characteristic length of the order of laser line distortion
ℓ_J	length of intake jet axis between valve and cylinder wall
N	symbol for number of events
n	index of refraction
$\bar{n}$	normal (perpendicular) vector to area
Q	quality factor
r	radius
Re	Reynolds number
S	anhydrous solute weight per cent
Sc	Schmidt number
Sl	average of slope encountered in vorticity distribution
SG	sign changes in first derivative applied to vorticity distribution
ΔT_{Delay}	time between the acquisition of a distorted grid and the application of the laser grid
ΔT_{Exp}	time for which scene of investigation is exposed to camera
TU	measure for velocity fluctuation in connection with turbulence
$\bar{u}$	local velocity vector
u_z	velocity component in z - direction
u, w	x - and z - component of a velocity vector
U	characteristic velocity
U_c	velocity at centerline of a freestream jet
U_i	velocity of inner jet in coaxial jet
U_o	velocity of outer jet in coaxial jet
$\bar{v}$	velocity vector
$\overline{v}$	mean velocity
v'	velocity fluctuation
v_c	velocity at annular intake jet centerline
VE	specific vortical energy

w_{CF}	mean velocity within an engine cycle evaluated by curve fit
x, y, z	reference coordinate system of engine cylinder
∇	derivative operator
α	induction angle; angle under which the annulus intake jet enters the engine cylinder
Γ	circulation
η	self-preservation parameter for free jets
η^*	normalized parameter of distance ζ divided by the width of the free jet
ν	kinematic viscosity
μ	angle
ρ	density
ξ, ζ	coordinates in streamwise and lateral directions of the intake jet
θ	circumferential direction of engine reference frame
$\bar{\omega}$	vorticity vector
ω_c	vorticity component in circumferential direction

Chapter I

INTRODUCTION

The underlying scientific objective of this work is essentially two-fold. The two 'projects' consist of the application of *Laser Induced Photochemical Anemometry* (LIPA) -- an innovative optical velocimetry concept -- to a relevant and important fluid dynamics problem (induction fluid flow within an engine cylinder) in order to demonstrate the technique's potential and usefulness in the field of fluid dynamics in general, and the attempt of advances in engine research -- especially for four-stroke internal combustion (IC) engines -- by describing phenomenons of engine performance on fluid dynamical grounds based on the data acquired by LIPA in particular. The four-stroke IC engine will be represented by a motored axisymmetric water analog model. Water is the required medium for the employment of LIPA in this application.

I.1 History of Research performed in IC Engines and pertinent free Jet Experiments, and of Applications of LIPA

The engine research community is constantly seeking further optimization of an engine's performance. The latest round of discussions about improvements in engine performance on the verge of the completion of the millennium was partly encouraged by the US Vice president's ecological imperatives to produce 21st century automotive vehicles that achieve higher engine efficiency accompanied by a lower level of pollution than their ancestors. To accomplish this honorable goal by pushing for advances in engine performance the engine itself cannot be regarded a black box with respect to fluid flow generated within an engine

cycle anymore; instead, the physics of fluid flow within the engine cylinder have to be investigated.

An approach favored by the engine research community presently in the investigation of fluid dynamics experienced in an engine is to apply a hybrid experiment/calculation scheme where computational fluid dynamics (CFD) are employed to the compression process -- where the flow is relatively less complex and CFD can yield higher accuracy -- to evaluate fluid dynamical quantities (Trigui et.al. 1994a), and seek initial conditions for the compression stroke from experimental applications -- such as PTV/PIV (Trigui et.al. 1994b) or LDA -- to the induction stroke which is computationally more difficult to grasp.

The current study introduces a useful new optical velocimetry tool (LIPA) which is based on the phosphorescence of the flowing medium to examine the flow field in an engine -- particularly the induction stroke -- and to derive important parameters to describe, e.g., mixing of air/fuel phases during induction. The knowledge about these parameters enables engine designers to furnish improvements of engine performance.

There exist investigations that examined fluid flow in axisymmetrical assemblies -- the most simplified and abstract realization of an engine -- of four-stroke engines. They performed flow visualization (Ekchian and Hoult 1979, Namazian et.al. 1980, Regan et.al. 1987, Eaton and Reynolds 1989, and Stier and Falco 1993) as well as quantitative studies using Hot-wire and laser Doppler anemometry (LDA) techniques. From these works it becomes clear that the setup of the flow field consists essentially of the incoming annulus jet and two toroidal recirculation patterns one of which occupies most of the engine cylinder volume; the second rotates in the upper corner of the engine cylinder between cylinder wall and chamber head. At the Imperial College of Sciences and Technology in London an axisymmetrical engine configuration -- which is also a water analog model as in this study -- has been the object of thorough and intense study. Arcoumanis et.al. (1982a), Arcoumanis et.al. (1982b), Bicen et.al. (1985), Vafidis and Whitelaw (1986),

Arcoumanis et.al. (1987), and Arcoumanis and Whitelaw (1987) evaluated fluid flow in the model cylinder employing LDA at different locations in the engine chamber, and flow visualization, determining velocity and turbulence intensity distributions in selected planes as well as streamline plots.

Hot-wire and LDA technologies have been widely and exclusively employed in engine science up to recently for the quantification of flow fields (Lancaster 1976, Witze 1977, Rask 1979, Lee et.al. 1993, and Yoo 1994). These technologies are single probe measurement concepts, thus, their application provides velocity information at only one location in the flow field at a time. In order to extract planar information of the flow field, such as vorticity vectors and length scales, from velocity information one has to assume homogeneity and isotropy of the flow field. This assumption has been shown not to be true. Several investigators proved that the intake stroke and the beginning of the compression stroke are clearly inhomogeneous and anisotropic (Semenov 1963, Winsor and Patterson 1973, and Witze 1977). Recently, velocimetry approaches have become multi-point in nature with the implementation of techniques such as PIV and PTV (particle imaging and tracking ideas). LIPA, also a planar velocimetry approach, promises to be a very useful and important tool to investigate the physics of flowing fluid, as, for instance, in the case of this study during the intake stroke of a reciprocating engine.

Since water is the flowing medium in this application and water is incompressible, fluid dynamical issues can be explored only during the induction stroke. Nonetheless, previous results show that the induction stroke is an important part during an engine's cycle. The induction stroke sets up the flow field for the subsequent compression stroke which in turn provides the initial flow situation for the combustion process of the cycle. The induction stroke has, concerning mixing of air and fuel for example, a very direct influence on combustion performance since most of the mixing process takes place during intake. Furthermore, there has been evidence for a profound correlation between the

establishment of fluid dynamic quantities during intake and compression, and combustion performance. In particular, Witze et.al. (1984) showed that an increased level of turbulence intensity exhibited by the flow field is favorable for the quality of combustion. Optimization of the combustion process is the ultimate goal and crucial step in the attempt for improvement of engine performance.

The complexity of the flow field experienced during induction requires the flow field to be dissected into fluid dynamically meaningful elements, e.g. vortex structures and intake jet, which have to be identified and then analyzed separately. Investigations of singled out flow structures and their effect on engine performance have been conducted in numerous investigations examining flow structures like swirl -- a rotational flow about the cylinder axis -- and tumble -- rotational motion about an axis perpendicular to the cylinder axis -- which are generated during induction by specially designed boundary conditions. Both experimental as well as computational studies have been performed. As it turns out, existence of these flow patterns improved engine combustion. The effects of swirl have been investigated by Kent et.al. (1989), Henriot et.al. (1989), Shack and Reynolds (1991), Moriyoshi et.al. (1991), and Aïta et.al. (1991). The effects of tumble on engine performance have been studied by Kent et.al. (1989), Henriot et.al. (1989), Omori et.al. (1991), and Hadded and Denbratt (1991).

Complex flow structures such as swirl and tumble, whose characteristic lengths scale with the radius of the engine cylinder, provide high stratification of the flow field and store and preserve (angular) momentum. Also, transport is mostly done through these large scales. By stratifying the flow, swirl and tumble inhibit mixing mechanisms that would intermingle the different phases inherent in the flow field -- fuel/air -- thoroughly. In breaking up, these structures provide the flow field with high turbulence intensities which are preferable for enhanced mixing and subsequently for improved combustion performance. A compromise must be found in connection with the timing of the break-up

of these large scale structures because the sooner break-up occurs the more homogeneously the flow field will be mixed at the time of combustion. The later swirl or tumble breaks up, the higher will be the degree of turbulent intensity by the time of combustion; then again, the later they break up the larger are the length scales of flow structures prior to combustion.

When employing Reynolds' decomposition method to an instantaneous velocity vector (see Tennekes and Lumley 1972 for a modern account) to take into consideration the turbulent character of the flow field encountered during engine performance the mean velocity in the decomposition is usually evaluated by an ensemble averaging technique. The velocity fluctuation part of the decomposition cannot, for engines, be attributed directly to turbulence inherent in the flow field. The engine process being periodic, more precisely reciprocating, introduces velocity fluctuations that are due to variations in bulk flow velocity from engine cycle to engine cycle which is termed in engine science terminology 'cycle-to-cycle variability'. Separation of velocity fluctuations due to cycle-to-cycle variability from those due to turbulent flow within an engine cycle has been attempted in many studies. A review on the most important techniques has been provided by Catania and Mittica (1989). A summary of the review is furnished in section V.3.2.2 of this work. A simplistic model to separate the two sources responsible for velocity fluctuations was assumed in this investigation and its implementation as well as results on the basis of the procedure are presented in section V.3.2.3.

In the age of exploding computer power it becomes very attractive to attempt the prediction of flow fields in the field of fluid dynamics using computational abilities (computational fluid dynamics, CFD). Naturally, CFD has been employed in engine research. Some interesting papers on numerically simulated flows in engine science have been published. Henriot et.al. (1989), Moriyoshi et.al. (1991), and Aïta et.al. (1991), for instance, undertook an effort to model swirling motion in an engine. Gosman et.al. (1984)

and Aïta et.al. (1990) calculated three-dimensional air motion and port-valve-cylinder flow, respectively. Recall from the first paragraph in section I.1 that Trigui et.al. (1994a) most recently applied CFD to the combustion stroke of an engine.

Unreliable and inaccurate initial as well as boundary conditions are partially responsible for differences between calculated and experimental results. Furthermore, calculated results diverge from experimental ones with time or crank-angle as the in-cylinder flow develops. An attempt has to be made to provide accurate initial and boundary conditions. This investigation will yield some for an axisymmetrical engine.

The understanding of fluid dynamics of the annulus jet that enters the engine cylinder through the valve is crucial for the comprehension of the fluid dynamics exhibited by the entire flow field in an engine cylinder during induction. After studying the flow field development during the intake phase of the water analog model at three different valve lifts and constant engine speed on the basis of fields of velocity vectors provided by LIPA the importance of the intake jet became obvious.

A free jet in general, after leaving the geometrical constraint and entering the ambient fluid, incorporates basically two regions which can be described as 'transitional flow' and 'turbulent flow' (Yule 1978, see Figure V.2.5). At the beginning of the transitional flow, first order instabilities lead to waviness of the jet flow immediately after it leaves the geometrical constraint (this is not valid for very low Reynolds numbers, however, valid for the range of Reynolds numbers covered in this study). These first order instabilities are followed spatially by a roll-up of the shear layer of the jet forming a coherent vortex ring with simultaneous occurrence of entrainment of ambient fluid. At the end of the transitional flow the coherent vortex ring breaks up into small scale vortices which are embedded in large scale eddies. The core of the jet which exhibits potential flow in the transitional jet region breaks up as well. From then on the flow is turbulent.

Yule (1978) examined an axisymmetric jet. He found that the length of the transitional

flow is Reynolds number dependent and that for a Reynolds number of about 5000 --

based on the diameter of the nozzle and the velocity of the flow in the nozzle -- the break-

up of vortex rings occurs after four diameters of the nozzle. Dahm et.al. (1992) performed

flow visualization on coaxial flows. For one parameter set examined, the velocity of the

outer jet was significantly higher than the velocity of the inner jet and the velocity jump

across the inner mixing layer (between inner and outer jet) was of roughly the same

magnitude as the jump across the outer layer (between outer jet and quiescent ambient

fluid). This is similar to what is encountered in the case of the incoming jet of an engine

and, indeed, the street of vortex rings created in the transitional phase, as visible in the

visualization results by Dahm et.al., exhibit strong similarity to vortex streets visualized by

experiments within this work. Dahm et.al. found that the potential core of the transitional

flow ends abruptly (for the parameter setting given above) at about 7 widths of the annular

orifice -- $(d_o-d_i)/2$ -- downstream. The variation of the length of transitional flow with

annular orifice turns out to be an important feature in the overall development of the flow

field encountered in engine research during induction (section V.2.3). Champagne and

Wygnanski (1971) also investigated coaxial jets employing Hot-wire technology; they

found the length of the external (outer) potential core of the jet to be approximately 8

times the width of the annular orifice and assert that the length appears to be independent

of the velocity ratio between external and internal jet.

Ko and Chan (1978) analyzed an annular flow, i.e. the velocity of the internal jet of a

coaxial jet is zero, using Hot-wire probes. They named the transitional jet region 'initial

merging zone'. In their study the position at which the annular potential core ends was

found at about 6 widths of the annular orifice downstream and the investigators infer from

their data that the length is independent of the conditions in the center of the annular jet.

Furthermore, they cite several earlier works in which annular and two-dimensional dual jet

flows had been studied. Ko and Chan extract from information given in these publications the positions at which reattachment of the outer jets occur, i.e. the merging of two maxima in the velocity profile to only one maximum, and plot the results in a diagram of 'Distance to Reattachment' vs. 'Diameter Ratio' of orifice. A conclusion from this plot can be drawn stating that reattachment length -- and thus the length of the potential core which is arguably proportional to the reattachment length -- scales with the width of the annular orifice. In another study by Chan and Ko (1978) on annular jets the investigators observed that the annular-jet results agree in connection with overall pressure intensity very well with the results for a single jet and coaxial jets within the first four-and-a-half widths of the annular nozzle downstream from the orifice. They suggest that the jet vortices are not so easily affected during their formation and during their initial propagation downstream.

Rockwell and Niccolls (1972) examined planar, two-dimensional jets by applying flow visualization. Although Rockwell and Niccolls do not explicitly state the length for which a potential core exists in the jet flow in their application, their pictures depicting the planar jet indicate that the length of the potential core -- and thus the length of the transitional flow -- is longer than 6 widths of the annular orifice. They outline, however, that any study of the 'breaking length' is relatively meaningless without careful specification of the upstream spectral history of the confined flow. Furthermore, they found that the region where vortices are defined moves downstream with decreasing values of the Reynolds number. Also for two-dimensional jets, Miller and Comings (1957) distinguished a 'transition flow region' from the 'fully turbulent region' where the transition flow region extends from the nozzle to a location 7 times the width of the nozzle downstream.

Experimental information on free jets (White 1991) suggests that the mean-velocity profile for the velocity component in axial direction is self-preserving beyond about twenty jet diameters (x/d>20). The mean-velocity U of the profile in a cross-sectional plane can

be, after establishment of self-preservation, evaluated at any point by $U=U_sf(\eta)$ where U_s is the velocity at the centerline and f is a function of η according to $f=sech^2(\eta)$ with $\eta=7.67y/x$. It should be noted that the beginning of self-preservation of the mean-velocity profile coincides with the disappearance of the core of irrotational flow, and that it can be observed from experimental results (flow visualization) that the existence of the potential core is terminated by the break-up of vortex structures. The observation of the termination of the potential core establishes a bridge between analytical and flow visualization results.

The fact that the transitional length scales with the width of the orifice for fixed Reynolds numbers leads to the assumption that the transitional length of the incoming jet in the model engine of this study differs with valve lift. In section V.2.3 an attempt is made to link fluid dynamical behaviour exhibited by the flow field during induction to the length of the transitional flow experienced by the intake jet.

The optical velocimetry technique employed in this investigation (LIPA) was introduced and developed at the 'Turbulence Structure Laboratory' at Michigan State University by Professor R.E. Falco. Development of the method and implementation of LIPA to study a model of a four-stroke engine will be discussed in detail in chapter II. So far, LIPA has been applied in several research projects at the 'Turbulence Structure Laboratory'. Studies involving LIPA as a measurement technique to evaluate flow fields in terms of fields of velocity vectors were performed for measurements in a Stokes' layer and of the circulation of a vortex ring (Falco and Chu 1987), evaluations of vortex structures in connection with an airfoil (Falco et.al. 1988), determination of the skin friction on a compliant surface (Falco and Chu 1988), a nozzle flow at supersonic velocities (Falco et.al. 1989), quantification of the flow field of a two-stroke engine (Hilbert 1991, Hilbert and Falco 1991), examinations of a subsonic jet (Gieselmann 1991), studies of flow properties of wet solids (Falco and Nocera 1991), and evaluation of the flow of a two-phase fluid in a vertical pipe (Buchner 1992). For all these investigations, maps of

velocity and vorticity information were derived from the flow field of the flowing medium. Experiments were conducted using three different media as basis for the working fluid which served as vehicle for the phosphorescent dye: Kerosene, Nitrogen, and water. LIPA was extensively used as photochromic visualization technique by Chu (1987).

I.2 Outline of Investigations performed for this Work

One purpose of this work was to apply LIPA to the model of a four-stroke IC engine in order to gain new qualitative and quantitative understanding of the fluid dynamics of the engine's intake flow. This application of LIPA was to provide fields of velocity and vorticity vectors which will, among other goals, answer questions about mixing performance. We also hoped to establish an alternative to conventional processes of examination of an induction flow, e.g. LDA, PIV techniques. Preliminary LIPA results have been published by Stier and Falco (1994).

Investigations were performed in an effort to study in single measurement steps the flow field of the induction stroke in the entire engine cylinder as well as the annular free intake jet. For the former project, the influence of the variation of valve lift are examined in the water analog model at three different engine speeds in a range of 10 to 30 RPM which correspond to 170 to 510 RPM, respectively, for air. For the second project, results will be presented for two valve lifts (3 and 9 mm) at two engine speeds (20 and 30 RPM; corresponding to 340 and 510 RPM, respectively, in air). Fields of instantaneous as well as ensemble averaged velocity vectors will illustrate the development of the flow field during induction. Vorticity distributions are generated from the velocity fields which will be used to examine mixing performances. Several parameters are defined in this work which attempt to analyze flow fields stemming from different settings of the engine's parameters valve lift and engine speed.

As mentioned in section I.1 a simple approach offers a separation of velocity fluctuations due to cycle-to-cycle variations and turbulent motion inherent in the flow field. RMS fluctuations as well as turbulent intensities are presented.

To grasp the fluid dynamics in a qualitative approach flow visualization experiments were performed. Results of the unfolding of the flow field during intake will be given for 1.5 and 20 RPM engine speed at 3 mm valve lift.

As for the velocimetry technique LIPA itself, several requirements for this technique had to be established prior to its employment. These included finding optimal quantities for the constituents of the phosphorescent dye, writing a grid of laser lines into the flow field, and implementing algorithms to reduce data automatically. Only vague sketch-book ideas existed on the latter issue prior to this application of LIPA.

The strategy for the generation of fluid dynamical results on engine flow within this work was to, within the available timeframe, collect as much information as possible on the flow field encountered during intake of the axisymmetric model, to draw conclusions on the basis of this information, and to participate in the overall attempt of painting a picture that exposes fluid dynamics encountered during induction.

The study will, however, barely go into depth at any point with respect to aspects of fluid dynamics. In general, the author had to be satisfied with scientifically scratching the surface of topics relevant within engine science (e.g. mixing and cycle resolved analysis). However, going into depth was not the prime goal of this work. The goal was to establish the general mode showing the viability and promise of engine research using LIPA. With this work in hand as basis, a researcher can concentrate on special issues in the study of the induction stroke of this water analog or any geometrically more challenging model and apply suitable LIPA configurations for designed tasks.

Chapter II
DESCRIPTION OF LIPA AND LIPA'S IMPLEMENTATION
IN EXPERIMENTAL ENVIRONMENT

Velocimetry techniques based on the photoluminescence of the working fluid have been experimented with more intensively after laser power has been made available as a strong source of energy. Popovich and Hummel (1967) first suggested the idea of photoluminescent flow visualization and quantification. At the 'Turbulence Structure Laboratory' of Michigan State University various studies have been released employing LIPA (Laser Induced Photochemical Anemometry), a velocimetry concept based on a phosphorescent working fluid. These studies investigated, for example, vortices in connection with an airfoil (Falco et.al. 1988), the flow field of a two-stroke engine (Hilbert 1991, Hilbert and Falco 1991), and the flow of a two-phase fluid in a vertical pipe (Buchner 1992), to repeat three of the projects that were outlined in the '*Introduction*' of chapter I. Just recently, several investigations involving LIPA and LIPA - related velocimetry approaches at other universities (Chu et.al. 1991, Yurechko and Ryazantsev 1991, Lempert et.al. 1993) have documented the usefulness of this measurement concept in laboratories around the world. The techniques taking advantage of the photoluminescence of the convecting fluid provide planar -- and it is possible to extent the technique to the third dimension -- instantaneous velocity and vorticity information about a flow field.

In this work LIPA has been applied to the induction stroke of a water analog model of a four-stroke internal combustion engine in order to yield two-dimensional flow fields in terms of maps of velocity vectors. From these, vorticity distributions will be inferred immediately. The purpose of this research in the field of engine science employing LIPA is

-- as outlined in the introduction -- to demonstrate the potential of and promote LIPA in a practical application of LIPA in a discipline of fluid dynamics, and to, among other issues, illustrate cycle-to-cycle variability of the engine's reciprocating process and to undertake an attempt to attain information on mixing performance during induction in order to achieve advances in engine research.

II.1 LIPA as Velocimetry Technique

II.1.1 LIPA's concept

LIPA is a fairly new velocimetry concept which takes advantage of phosphorescent properties of the working fluid. It is optical, and thus non-intrusive, in that it is based on the excitation of molecules -- which exhibit photoluminescence, or photochromism (color change) upon stimulation by an energy input -- in the fluid whose flow field is to be examined. LIPA's underlying idea for the evaluation of a velocity vector is to simply place an energy input at any location of the flow field, thus illuminating a fluid 'particle', and visually following the illuminated and radiating fluid particle as it convects with the flow field. There is no slip between the traced fluid particle and the flow field as can be encountered in most common measurement techniques such as LDA or PIV. In fact, not even temperature gradients (if neglecting an insignificant increase of temperature in the flow field due to the energy input) or concentration gradients (since the phosphorescent additive dissolves thoroughly within the working fluid) exist which could signify a source of error. Furthermore, after an energy input to the fluid has been released, the fluid exhibits only negligible changes in its properties (e.g. bleaching of phosphorescent matter) and can therefore readily be used for next excitation. The fluid dynamical approach in connection with LIPA is Lagrangian as opposed to LDA and Hot-wire anemometry.

II.1.1.1 Demand towards chemistry as godfather of LIPA

Chemistry has to provide the dye that enables the marking of fluid particles in the flow field. The dye has to incorporate photoluminescent properties, has to dissolve thoroughly in the flowing medium, and ought to be safe to use and reasonably priced.

The phosphorescent dye used for LIPA which serves as an additive to append photoluminescence to the list of properties of the working fluid was designed and produced by the Department of Chemistry at Michigan State University under the direction of Professor D. Nocera. The 'LIPA dye' consists of three constituents; the vehicle for the phosphorescent compound is water (H_2O). The actual phosphorescent matter (providing excitable molecules) is Bromonaphthalene (BrNp). BrNp would, if exposed directly to water molecules, experience a quenching effect (lose its phosphorescent property) necessitating a protection (coat) for the BrNp molecules. This coat is facilitated by the other two components in the compound of the LIPA dye, namely a sugar, Glucosyl-β-cyclodextrin (Gβ-CD or for short CD), and an alcohol, *tert*-butyl alcohol (*t*-BuOH). These two components represent, in terms of a model, a cup and a lid for this cup, respectively, in which the BrNp molecules are embedded. Water as flowing medium together with the composition of the three constituents being dissolved in water is referred to as 'LIPA - chemical'. An optimum for the ratio of amount of alcohol, *t*-BuOH, necessary for a given amount of sugar, CD, had been evaluated by Buchner (1992). A recipe for the manual engendering of the LIPA chemical is given in section II.2.1.2. More information about the LIPA dye can be obtained from Ponce et.al. (1993).

II.1.1.2 Principle of evaluation of array of velocity and vorticity vectors

LIPA's purpose is to deduce from a three-dimensional flow field planar two-dimensional (2D) velocity vectors which are projections on the imaging plane. Intrinsically

LIPA provides 2D velocity vectors because data are inferred from 2D images captured by an imager that contain two-dimensional convection information of the illuminated particles. Since it is very difficult, if not impossible, to provide *point* energy inputs at different locations in the flow field at the same time to achieve planar velocity information, the excitation and illumination of fluid particles is accomplished in this work by imposing a grid of laser lines onto the flow field where the laser is the source of energy. Now, intersections of lines define the fluid particles which ought to be traced.

In this work, planar fields of velocity vectors are evaluated by recording the imposed laser grid when the working fluid is quiescent (here, engine is not running) to obtain the initial origin locations from where fluid particles convect (A', B', C', and D' in Figure II.1.1b), and capturing LIPA grids during engine performance a certain time interval after a laser pulse illuminated fluid particles to obtain the locations where fluid particles convect to (A", B", C", and D" in Figure II.1.1b). Velocity vectors can then be evaluated in the flow field by determining in the recorded images the distances fluid particles convected during the chosen time interval (also referred to as time delay). The evaluation is a simple division of traveled distance by the time interval. The time delay should not be too long since LIPA's intrinsic assumption of linearity of the fluid particle's path between its initial and convected position should not be violated. A scheme of evaluations of velocity vectors at the four points of a quadrolateral can be seen in Figure II.1.1b. Note that the origin of the evaluated velocity vector is located half-way between A' and A".

Vorticity vectors can easily be deduced from the distribution of velocity vectors. If one considers a quadrolateral spanned by the origins of four velocity vectors (Figure II.1.1c) one can consider the area of this quadrolateral a fluid particle associated with a characteristic length scale of the order of the resolution of the laser grid. Under consideration of distortion and rotation of this fluid particle set forth by the convection mechanisms at the four corners one is able by applying fluid dynamic identities which

incorporate information on the velocity vectors at the corners to infer a vorticity vector for this fluid particle where the origin of the vector is situated at the center of the area of the quadrolateral.

In general, vorticity is calculated from a velocity field by

$$\bar{\omega} = \nabla \times \bar{v} \qquad\qquad (\text{II.1.a})$$

which can be reduced for two dimensions (x, z - plane) to

$$\omega = \frac{\partial u}{\partial z} - \frac{\partial w}{\partial x} \qquad\qquad (\text{II.1.b})$$

where for this notation ω is a 'point' quantity.

An alternative approach for vorticity evaluation incorporates the determination of circulation. Along the contours of an assigned area, e.g. the quadrolateral in Figure II.1.1c, the circulation about that area can be evaluated by the following line integral,

$$\Gamma = \oint \bar{v} \cdot d\bar{s} \qquad\qquad (\text{II.1.c})$$

the line being a closed curve in the velocity field. The circulation for the abovementioned quadrolateral can be determined by a piecewise summation of averaged velocity projections onto the considered quadrolateral (Figure II.1.1c) multiplied by the distances between the corresponding velocity origins. The following equation then links vorticity and circulation:

$$\Gamma = \int (\bar{\omega} \cdot \bar{n}) dA \qquad \text{or} \qquad\qquad (\text{II.1.d})$$

$$\bar{\omega} = \frac{\int \omega \, dA}{A} \qquad\qquad (\text{II.1.e})$$

In this form an 'area averaged' vorticity is evaluated.

The evaluation scheme for 'area averaged' vorticity vectors presented by equations II.1.c and II.1.e is more suited for the form in which velocity information is available in this investigation (namely discrete values within the flow field) and thus adopted for this study.

A thorough analysis of error inflicted by the employment of LIPA on the basis of double differencing the LIPA grid -- which is the actual practical procedure to obtain vorticity -- can be found in Falco and Nocera (1993).

II.1.2 Phosphorescent characteristics of employed LIPA - chemical

From empirical experience it can be asserted that the five-component mixture [water as the convecting medium, KSCN to refractive index match water to quartz -- see section II.2.1.1 -- and three components from the LIPA dye] used as working fluid, possesses, with respect to the ability of phosphorescence, hardly any shelf-life. An attempt to reactivate a four week old compound by adding alcohol -- which is the component that goes out of solution at the highest rate through evaporation during the LIPA experiments -- was unsuccessful. Even within 24 hours it could be evidenced that the fluid lost a considerable amount of its phosphorescent potential.

To quantify the above stated observations, an investigation was carried out to determine the comportment of the phosphorescence of the LIPA - chemical with time when not being in use -- shelf-life -- as well as its behaviour through the conduction of sets of experiments -- problems with evaporation of alcohol component, exposure to laser energy, etc. The objective was to find out (a) the effect of intermolecular action on the phosphorescent material while the LIPA - chemical is in storage and (b) for what time frame it will be scientifically meaningful to employ the phosphorescent chemical in LIPA

experiments before the quality of the laser grid in terms of level of illumination decreases to a non-acceptable level. A third chemically interesting issue is whether the phosphorescent matter can be reactivated after depletion of phosphorescent activity -- as suggested by the designer of the LIPA dye -- by supplements of the alcohol component.

In order to obtain information on the time-dependence of the LIPA - chemical -- being in storage and in use -- a scheme of experiments had been devised. Eight point data series that determine the time interval of detectability of the phosphorescence after excitation by an energy input were to be performed. These data series were taken before and after a body of actual LIPA experiments as well as shortly before the chemical is put into storage and immediately after it is filled into the model engine. For every point in the data series a grid of laser lines was recorded with the fluid quiescent for a fixed exposure time and f-stop of the imager for eight different time delays (2, 4, 6, 8, 10, 13, 16, and 20 ms) -- a time delay being the time between the pulsing of the laser and the recording of the illuminated scene. In order to establish a curve where the degree of light intensity of the radiation emitted by laser grids is plotted versus time delay, the mean pixel intensity in the area covered by the laser grid was evaluated.

The results from the above outlined experimental operations are summarized in Figures II.1.2 and II.1.3. In Figure II.1.2 curves of pixel intensity versus time delay were evaluated on ...

> CL III: ... the day after engendering of LIPA - chemical; *before* body of
>   experimental procedure (LIPA)
>
> CL IV: ... the same day; *after* body of experimental procedure
>
> CL V: ... day 2 after engendering of LIPA - chemical; no LIPA experiments
>
> CL VI: ... day 4 after engendering of LIPA - chemical; no LIPA experiments

Note that no LIPA experiments were performed between the evaluations of curves IV and VI.

It would have been very interesting to observe, qualitatively, the phosphorescence of the LIPA - chemical before & after a set of experiments on the very same day it was generated and the degradation of it between day zero and day one of its engendering. Unfortunately, the decrease of laser power during the experimental phase on day zero of the generation of the LIPA - chemical and the recharging of the laser prior to the experiments on day 1 (CL III and IV) turned the two data series, CL I and II, into ambiguous information. For curves III through X laser power was constant.

Curves III and IV illustrate the degradation of the LIPA - chemical because it was in use. Apart from some waviness in curve III at the lower time delays -- which are presumably due to limitations in accuracy of the applied detectability evaluation procedure -- curve IV experiences a substantial shift down to a lower intensity level. This decrease in intensity level is due to bleaching of the phosphorescent dye.

The shift down in intensity from curve IV to V -- which is conceivably smaller than the shift from curve III to curve IV -- is caused by intermolecular activity within the LIPA - chemical while the chemical is not in use (shelf-life). The same argument applies for the decrease in intensity from curve V to VI. The decrease from the intensity level as encountered 2 days after the LIPA - chemical had been mixed (curve V) to the level as encountered 4 days after the LIPA - chemical had been generated (curve VI) is smaller than the decrease in intensity level from curve IV to curve V although only one day passed between the evaluations of the phosphorescence-detectability curves in the latter case. This suggests a non-linear behaviour of the degradation of the phosphorescent properties of the LIPA - chemical when in storage.

In Figure II.1.3 the effect of adding successively four complements of t-BuOH, 5 ml each, to the LIPA - chemical after the evaluation of the data series leading to curve VI, is demonstrated. It can be asserted that adding amounts of the alcohol component to the LIPA - chemical does not yield the desired refinement. For the most part of the range of

time delays examined the addition of alcohol does not change the level of light intensity radiated from the grid of laser lines. At small time delays a decrease of intensity is even encountered.

II.2 Experimental Apparatus and Method of Data Acquisition

II.2.1 Water analog model of four-stroke IC engine

The experiments for which LIPA was employed were performed in a motored water analog model of a four-stroke IC engine with flat cylinder and piston heads using an axisymmetrically seated, stationary valve. This most basic and simplified configuration as apparatus for investigation in engine research was chosen to enable the investigator to concentrate on the extraction of fluid dynamic quantities and their influence on mixing of air and fuel with residual fluid in the engine cylinder -- stemming from the previous cycle -- during induction, without being compelled to include considerations about the influence of complex boundary conditions. And also to demonstrate the applicability of LIPA without casting expensive engine environments.

Since LIPA is an optical measurement technique and the energy source used for this study is a UV laser (see section II.2.2.1) all components of the engine model in the vicinity of the area of investigation (piston head, engine cylinder wall, valve, and bottom of fluid reservoir or cylinder head) are made of quartz -- for a complete depiction of the apparatus of the engine model in form of a drawing as well as of an anatomization of its elements see Figure II.2.1 -- to ultimately accomplish thorough optical and visual access. Ultimately, because the difference between the refractive indices of quartz and water, and also between quartz and ambient air which causes electro-magnetic waves to bend at water/quartz/air interfaces, requires an effort to refractive index match the three phases. If the index of refraction of, for instance, the working fluid was different from that of the

quartz cylinder the curved cylinder wall would function as a lens and the mapping of intersection points onto the plane of the imager would not reflect their real locations in the physical space.

Refractive index matching of the entire system was attained by embedding the engine model in an aqueous medium that was refractive index matched with respect to quartz and by using index matched water as the working fluid in the cylinder. A Plexiglas tank holds the aqueous index matched fluid (see Figure II.2.1a). The tank has a quartz window to allow the UV light energy source to enter the test facility. A more detailed description of refractive index matching procedures can be found in section II.2.1.1 *'Refractive index matching of experimental environment'*.

Figure II.2.1b which displays the dissected components of the model engine shows a Rulon O-ring. Rulon was found to be a material (plastic) that could be used as O-ring for a water/quartz environment (for more information on the O-ring see Appendix A).

The experimental rig has been provided by the Ford Motor Company, Dearborn, MI.

An advantage associated with the use of water as the base for the working fluid is that the kinematic viscosity of water is 17 times lower with respect to the kinematic viscosity of air -- the standard flowing medium for engines. Thus, if equating Reynolds numbers,

$$Re = \frac{LU}{v}, \qquad \qquad (II.2.a)$$

where L is a characteristic length, U is a characteristic velocity, and v is the kinematic viscosity, piston speeds can be 17 times lower in the water analog model in order to produce equivalent flow field dynamics. Typical Reynolds numbers -- based on the width of the annulus (orifice) and the velocity of the flow in the orifice -- range in this application between low Re and Re=6300. For this engine configuration, the Reynolds number is -- to within a negligibly small margin -- independent of the valve lift; it is

however, dependent on the crank-angle. The main influence of the Reynolds number on the fluid flow in an engine is manifested by the dependency of the creation and destruction of toroidal vortex structures -- in the shear layer of the intake jet -- with Re.

A disadvantage associated with water as the base for the LIPA - chemical is its property of incompressibility. Hence, an effort had to be made to avoid the compression as well as the expansion stroke during engine performance (for the layout of the cam-shaft employed to omit compression & expansion see Appendix A).

II.2.1.1 Refractive index matching of experimental environment

Considerations of refractive index matching is always worthwhile contemplation when phases of different refractive indices are involved in an optical system. Every medium has its specific index of refraction n. The index of refraction of a medium can be manipulated by changing the composition of the medium's chemical synthesis. The most convenient medium to be manipulated is a liquid phase. The index of refraction of water (H_2O), for instance, which is smaller than that of quartz (see Table II.2.2), can simply be matched to that of quartz by adding an agent with an index of refraction that is greater than that of quartz and that dissolves in water thoroughly.

The point in a parameter space where a medium, a liquid for instance, is refractive index matched -- e.g. with respect to the quartz used for the model engine n_{quartz} -- is a function of the wavelength of the light for which index matching is to be achieved as well as of the ambient temperature (see Table II.2.2). For the experiments performed for this study the index matching agent for water was Potassium Thiocyanate (KSCN). KSCN has an index of refraction greater than quartz, dissolves in water, and is transparent with respect to energy from a UV laser beam. Analytically, the quantity of KSCN needed to refractive index match its solution with water to quartz can be calculated by the following

formulation derived by Buchner (1992) whose derivation was based on equations in a review about refractive index matching considerations by Mohr and Ertel (1986):

$$S[\%] = \frac{n_{total} - n_1}{n_2 - n_1}$$ (II.2.b)

where n_{total} has to be equal to n_{quartz} in order to index match for quartz, n_1 is the index of refraction for water and n_2 the one for KSCN. S represents the anhydrous solute weight per cent.

Apart from the theoretical prescription of the quantity needed for KSCN to index match water to quartz, scientific research incorporating trial and error led to the following 'rule of thump' recipe from empirical observation: 2000 ml H_2O + 2000 g KSCN + 270 ml H_2O index matches quartz at about 15° C for 308 nm wavelength. When the temperature of the solution increases more KSCN has to be added in order to refractive index match. The mixing of water and Potassium Thiocyanate is strongly endothermic (i.e. the solution becomes very cold).

Table II.2.2: Indices of refraction for diverse materials

Conditions for Temperature and Wavelength	Indeces of Refraction				
	Water	KSCN	Quartz	DHN	Hexane
20 degree C, 308 nm			1.485		
20 degree C, 589.3 nm	1.333	1.532	1.458		
25 degree C, 589.3 nm				1.474	1.372

For flow visualization experiments involving a photochromic chemical by Kodak -- procedure and results will be described in section IV.1 -- a chemical that belongs to the family of oils is preferable for being the basis of the working fluid. Decahydronaphthalene ($C_{10}H_{18}$) turned out to work very well in connection with the Kodak chemical.

Decahydronaphthalene (DHN) absorbs almost no energy at 308 nm wavelength and has an index of refraction of 1.474 -- at 25° C and 589.3 nm wavelength, Table II.2.2 -- which is fairly close to the one of quartz. To completely match the index of refraction of DHN to that of the quartz engine another organic component with a low index of refraction had to be found that furthermore exhibits high transparency in the UV range of the spectrum of electro-magnetic waves. During the phase in which this suited partner for DHN was sought it was experienced that the higher the ratio n/m in the formula C_mH_n for organic chemicals, the higher was the transparency of the chemical at 308 nm. At the end of the testing phase, Hexane (C_6H_{14}) was chosen as the index matching agent for DHN whose index of refraction is 1.372 -- also at 25° C and 589.3 nm wavelength, Table II.2.2. Contributions of 74.44 Vol-% Decahydronaphthalene and 25.56 Vol-% Hexane constitute a working fluid that is refractive index matched to the quartz used for the model engine at operating conditions. Note that the evaporation rate for Hexane is considerably high when the DHN/Hexane solution is exposed to air.

Due to the fact that oils are not aggressive towards the metal components in the engine apparatus -- in the contrary, they rather serve as lubrication -- the DHN/Hexane mixture was used as the index matched fluid in the outer tank embedding the quartz cylinder. This constitutes a rather prophylactic measure for the possibility of leaking.

For further empirical observations on refractive index matching refer to Appendix B.

II.2.1.2 Recipe for engendering of LIPA - chemical

After the flowing medium for the LIPA experiments (water/KSCN solution) was properly index matched for quartz the fluid had to be 'loaded' with the phosphorescent compound (BrNp molecules protected by sugar/alcohol shield; see section II.1.1.1). The loading process was accomplished by the following steps:

1. Add necessary amount of CD (for 4.5E-03 M CD in 800 ml H$_2$O/KSCN, an amount of 4.62 g CD is needed); stir vigorously.

2. Add necessary amount of t-BuOH (for 4.5E-03 M CD in 800 ml H$_2$O/KSCN, an amount of 42.3 ml t-BuOH is needed; this is 5.78E-01 M); stir.

3. The current mixture is, with respect to the desired matching of refractive indices to quartz, low on KSCN; add about 14 g KSCN to index match again.

4. Filter fluid through regular coffee filter.

5. Add one drop of BrNp as phosphorescent material; stir vigorously.

II.2.2 Aspects of data acquisition and its facilitation

II.2.2.1 Generation of laser grid -- optical assemblage

The optical accessories necessary for the generation of the LIPA grid of laser lines

which is superimposed onto the flow field and their configuration are exhibited in

Figure II.2.2. The energy source used (providing monochromatic, coherent light) is the

excimer laser LPX2 from Lambda Physik Lasertechnik. It was operated at 308 nm

(UV waves in electro-magnetic spectrum) by using a Xenon Chloride (XeCl) gas mixture,

the buffer gas being Helium (He). The exiting laser beam is of rectangular shape with

dimensions 20 by 65 mm; the frequency range of laser pulses comprises 1 to 200 Hz with

a pulse length of 17 ns; the maximum output attainable is 250 mJ per pulse; the laser can

be triggered externally.

The implementation of the grid of laser lines as employed for the majority of LIPA

experiments -- examination of fluid dynamics in a plane at one circumferential position θ

that covers most of the engine cylinder -- is accomplished as follows (for a sketch of the

setup refer to Figure II.2.2a): The exiting laser beam -- after diverting the beam by two

mirrors -- is splitted by a half-transmitting mirror into two sub-beams -- under 45° the

half-transmitting mirror splits the beam into two sublets of equal intensity. For each sub-

beam a convex quartz lens (500 mm focal length) focuses the beam at the measurement site. The long focal length assures the thinness of the laser grid lines at the region of interest. After passing through the lenses each sub-beam is divided into several parallel lines by means of a grating which is incorporated by an array of aluminum coated, parallel slim mirrors glued onto a base body. For a scrutinizing view of the beam divider see Figure II.2.2a. The laser lines from the two coplanar sets of parallel lines intersect at the area of investigation under a certain angle. This angle constitutes a compromise: On the one hand, the angle was to be as close to 90° as possible for reasons that will become clear in section III.3. However, since both sets of laser lines enter through the cylinder wall and since the Plexiglas reservoir as well as the metal piston are not transparent with respect to UV - light the two sets of parallel laser lines had to be adjusted in such a way to avoid blockage of energy by these mechanical parts. [A solution where one set of laser lines enters vertically through the quartz piston head in order to achieve intersection angles of 90° was considered and implemented, but had to be rejected, since from a certain crank-angle during the induction stroke on, the penetration of the laser lines was insufficient to sustain a grid in the upper part of the cylinder (attenuation, too much dye); information could only be obtained during early intake.] The plane spanned by the generated grid of laser lines intersects the cylinder axis of the engine. Local assignment of intersections of the laser grid, thus the definition of locations where the velocity vectors were to be evaluated, occurred rather randomly in the implementation phase of the grid. The reader is referred to Appendix B '*Optical issues*' for more information on the generation of the LIPA laser grid.

The laser grid implemented by the setup in Figure II.2.2a is depicted in Figure II.2.3a; it covers for quadrant I of the x, z - plane at the investigated circumferential position θ most of the cylinder. 74 locations were considered for the examination to be distinct enough and therefore qualified for data reduction. By these 74 locations a spacing between points of about 6 mm could be achieved. For one intersection of two laser lines the major axes of

the formed typical ridge-shaped core are, in the digitized image, about 11 x 30 pixel in length; thus, the area of the core is represented by 330 pixel (Figure II.2.3a). Laser lines intersect in general under an angle of about 50°. The longer major axis of an intersection coincides roughly with the x - axis of the reference frame.

In section V.5 a more thorough investigation of the annular intake jet is furnished by employment of an investigation grid offering a closer spatial spacing of laser line intersections than the one achieved by the optical setup in Figure II.2.2a. In order to attain the more dense spacing, 150 mm focal length lenses replacing the 500 mm lenses were placed behind the grating (the setup is shown in the photograph of Figure II.2.2b). At 15 locations velocity information could be obtained. The locations are depicted in Figure II.2.3b along with the geometry of a typical intersection of two laser lines. The number of pixel within the ridge-shaped core of a typical intersection is here significantly higher than for an intersection of two laser lines for the investigation grid in Figure II.2.3a.

Since the process under investigation is a reciprocating one where one boundary moves vertically, throughout parts of the intake stroke laser lines were blocked by the piston and only a certain number of intersection areas -- which increases with crank-angle -- could be evaluated for the first part of the induction stroke. Consequently, for the laser grid in Figure II.2.3a, not until shortly after midstroke could all 74 locations be studied. Thus, in the data reduction process, a map of locations had to be assigned to each crank-angle before midstroke to notify the data reduction process where information is available.

Optical systems generating the grids of laser lines were implemented using a mechanical support construction consisting of simple iron rods and aluminum elements connecting the rods where mirror and lens components were held in place by clamps that were screwed to the iron rods (Figure II.2.2b). Naturally, the degree of fine tuning of optical elements achievable with such an optical system is rather low; however, sufficient precision was

accomplished for the generation of laser grids employed for the experiments conducted within this study. A system based on an optical bench or table with micrometer adjustable enclosures for optical elements will enable the experimentalist to realize grids with close spacing of intersections of laser lines where laser lines are very thin.

II.2.2.2 On how to acquire grids of laser lines that constitute LIPA - data

Data acquisition was performed for the bulk of the experiments according to the scheme in Figure II.2.4a. Figure II.2.4c contains a more physical description of the abstract quotation of devices in Figure II.2.4a; Figure II.2.4b displays the engine apparatus and the imager in a photograph.

According to Figure II.2.4a, a motor puts out a constant angular torque that drives the cam-shaft. (The unique characteristics of the cam are described in Appendix A.) The cam-shaft generates for the induction stroke a sinusoidal movement of the piston -- the induction stroke being the mere subject of study in this work -- as input to the 'Volume of Investigation'. The measure for data acquisition of LIPA images is provided by the running engine model (for more detailed information on timing of the data acquisition process the reader be referred to Appendix C). An optical encoder which is mounted to the shaft between motor and cam and which serves as mechanical-electronic interface puts out a signal at every degree of rotation of the (cam-) shaft. This signal is transferred to an 'electronic signal valve' which serves as an 'AND' filter letting through information only when a signal fulfills two requisites: It is every 1st, or 2nd, ..., or 10th (choosable) signal AND it belongs to the crank-angle range of between 10° prior to the beginning of the intake stroke and 10° after the end of the intake stroke. (More on the 'electronic valve' can be obtained from Appendix C.) The output from the 'valve' is forwarded to the excimer laser and triggers it to pulse (to build up the grid of laser lines in the engine cylinder), contributing to the 'Volume of Investigation' as another input, Figure II.2.4a. The signal

from the 'valve' is also conveyed to a frequency generator that can manipulate incoming electronic information (e.g. delay transmission of incoming signal). This 'delay' generator schedules data acquisition for the imager. The imager receives input from the 'Volume of Investigation' in optical form. Because of the timing procedures enforced by synchronization requirements (Appendix C), for 10 RPM engine speed, data were obtained for every other degree crank-angle; for 20 RPM the flow field was examined at every 4th, and for 30 RPM at every 6th degree crank-angle.

To capture LIPA images an assembly of a regular Video camera by Canon and an image intensifier lens (IIL) mounted in front of the camera has been used (for more information about the imager see Appendix D). The optical axis of the imager system is perpendicular to the plane spanned by the grid of laser lines. Information on the timing procedure for the imager system can be gathered from Appendix C. The Video camera saves the received information onto tape (Figure II.2.4c). This information is digitized by an imaging processing facility [incorporated by MegaVision and working in conjunction with a Sun 3/260 Workstation; for a thorough description of the MegaVision system read Appendix D] and the images containing LIPA grids are then stored in the memory of a Sparc2 SunWorkstation. Implemented software, then, extracts coordinates of illuminated fluid particles from the LIPA images with subsequent calculation of fluid dynamic quantities such as velocity, vorticity, and fluctuation intensities. Implemented algorithms will be discussed in chapter III *On the Methodology of Data Reduction*.

II.2.2.3 Results from preliminary preparation-activities for series of LIPA experiments

After an extensive experimental phase preceding the actual LIPA experimental series where the LIPA method and chemical were tested thoroughly and results were recorded using the 35mm-4ML movie camera (series 2000) by Photo-Sonics, Inc., onto T-max 3200 black&white film from Kodak, the acquisition of an image intensifying system

enabled the application of the above mentioned Video camcorder from Canon to capture LIPA - data on video tape. In the data acquisition setup using the movie camera implemented for the preliminary testing of the LIPA concept, the movie camera triggered the laser on a 60 fps (frames per second) basis to build up the laser grid in the flow; no synchronization with the running engine was accomplished. Some results from the ground setting quest with the movie camera are presented in Figures II.2.5 and II.2.6.

Figure II.2.5 shows a laser grid depicting the origin locations of intersection points prior to convection, and grids exhibiting distorted laser lines for 20 RPM engine speed and 6 mm valve lift in black&white for the beginning of an engine cycle. Note that one set of laser lines enters through the piston head. The pictures in Figure II.2.5 hold valuable LIPA information.

In Figure II.2.6 color (ASA 1000, E6 processing) pictures taken with the movie camera of the early induction stroke of the model engine are shown where, again, one set of lines enters through the piston head. Figure II.2.6 also exhibits images of one laser grid showing origin locations as well as grids containing convected intersections of laser lines. In the background of the laser grid showing distortion and thus carrying the current LIPA information -- Figure II.2.6b through e -- one can perceive, nebuously, the highly distorted remains of the laser grid that was generated 16.67 ms before the grid that represents the current LIPA information. A detectability of the LIPA - chemical well beyond 17 ms enabled the acquisition of this picture. The recording of this image constitutes a genuine success for performing quantification and qualification of the flow field in one step.

II.2.2.4 Matrix of conducted LIPA experiments

Experiments involving the application of LIPA to quantify the flow field of the induction stroke of a model of an IC engine comprise a variation of two engine parameters, namely engine speed and valve lift (VL; the valve lift is defined as the vertical

length of the orifice between valve and head of engine chamber). For the experiments in the investigation of the whole engine cylinder (74 locations, Figure II.2.3a) the matrix in Table II.2.3a depicts the settings of engine parameters examined. (A double-'x' indicates that there is flow visualization information available for that particular setting to which the LIPA results can be compared.) Table II.2.3b denotes the experimental series that have been conducted in order to investigate the intake jet with the close-up look at the valve (15 locations, Figure II.2.3b). Note that by conversion of the engine speed as encountered for the water analog model in this work to an equivalent speed for an engine using air as working fluid -- by equating Reynolds numbers -- investigated engine speeds are 170, 340, and 510 RPM.

It should be noted at this point that due to memory limitations of the SunWorkstations fluid dynamical quantities could be averaged only over a confined number of engine cycles. For 10 RPM engine speed (data available at 90 crank-angle events within one realization of an intake stroke, see section II.2.2.2) the number of engine cycles over which averaging was performed is 21; for 20 RPM (45 crank-angle events) the number is 42, and for 30 RPM (30 crank-angle events) it is 63 ECs. The higher the resolution in crank-angle the lesser is the number of engine cycles due to constant memory of computer; however, on the other hand, the smaller the engine speed the lower are the cyclic variations (see section V.2.2) and the less important is thus the need for sample size.

Table II.2.3: Matrix of experiments performed for the investigation of (a) whole engine cylinder and (b) intake jet.

Engine Speed	Valve Lift [in mm]		
[in RPM]	3	6	9
10	x	x	x
20	xx	x	x
30	x	x	x

(a)

32

Engine Speed [in RPM]	Valve Lift [in mm]		
	3	6	9
10			
20	xx		x
30	x		

(b)

II.2.3 Estimates for parameters relevant for description of quality of LIPA - data

II.2.3.1 Delay time

In general, a map of velocity vectors is evaluated by taking two images of the grid of laser lines during convection of the flow field and determining the distances that corresponding intersection points traveled during the time interval between the acquisition of the two images.

For this work, the LIPA - data representing the 'first' image are, as mentioned above, taken with the working fluid quiescent (i.e. the piston is not moving). These images contain grids which depict the origins of intersection locations of laser lines prior to convection -- they will be referred to as 'undistorted' or 'reference' grids (Figures II.2.5a & II.2.6a) -- and were recorded always right before a set of data incorporating one setting of the engine parameters was acquired. Uncertainties about accurate inference of the origins from the reference grids will be discussed in section III.3.

In order to resolve the range of velocity magnitudes encountered in the investigated model engine (0 - 3.5 m/s), and with the prerequisite of linearity of particle paths in mind, time delays for acquisition of the LIPA information consisting of laser grids that present illuminated particles after their convection with the flow, were in the range between 0.3 and 1.1 ms. No imager device was available to take images at a rate of 1000 Hz or faster which would enable the experimentalist to record successively the reference image and its

distorted relative. This lack of equipment forced the investigator of this study to record the undistorted grids with the working fluid quiescent. Undistorted grids were acquired a certain time delay after the laser pulses (in fact the same time delay as was used for the corresponding data set was chosen) in order to avoid fluorescent background noise in the images.

The images containing the convection information were taken during engine performance a certain time delay (between 0.3 & 1.1 ms) after the laser pulsed and the energy input illuminated the fluid particles. These images hold data that are referred to as 'distorted' grids (Figures II.2.5b-e & II.2.6b-e). Now, a field of velocity vectors can be inferred by calculating the quotient of the distance each fluid particle convected to the time delay between the application of the laser grid and the acquisition of the distorted grid. This time delay is a crucial parameter for the conduction of LIPA experiments. It ought to be estimated by considering the highest occurring velocity magnitude in the flow field that the investigator is interested in to evaluate. LIPA is, for the current study, based on the assumption of linearity between a fluid particle's original location and the location it convected to, as mentioned earlier. Linearity means that only the first term in an expansion is used and that higher order terms are negligible. Under this assumption velocities are deemed to be constant and locally uniform between the acquisition of the two images which contain the reference and the distorted investigation grid. Nonlinearity of a particle's path is usually associated with the region of the highest velocities and the highest spatial velocity gradients, it is the region where one generally finds highest strain. In this application of LIPA to the water analog model of an IC engine the highest velocities and, thus, the highest nonlinearities occur in the region governed by the incoming annulus jet. Hence, it is meaningful to estimate a reasonable delay time by the reciprocal value of the quotient of the velocity at the jet centerline v_c and a characteristic length $\hat{\ell}_{dist}$ which is of the order of distortion allowed under the requirement of linearity.

$$\Delta T_{Delay} = \dfrac{1}{\dfrac{|\bar{v}_C|}{\hat{L}_{dist}}} \qquad\qquad\qquad \text{(II.2.c)}$$

For 20 RPM engine speed and 6 mm valve lift a typical velocity magnitude in the seat area of the valve is calculated to be about 2 m/s. Linearity is assured, according to visual observations during the distortion of laser grids, at convection distances smaller than 1.3 mm (corresponding to 10 pixel in a LIPA image). Plugging these numbers into equation II.2.c yields a delay time of 0.65 ms. This first estimate was used in a preliminary test phase. Eventually, the delay time for 20 RPM and 6 mm VL was corrected to 0.7 ms.

II.2.3.2 Exposure time

The exposure time expresses the time interval for which the CCD array of the camcorder is exposed to the illuminated scene in the model engine. The exposure time ought to be as small as possible to avoid blurring in the image. Variation of illumination intensity within the investigation grid that is spanned by the laser lines in the measurement area -- in x - and z - direction of the reference frame -- inflicts a manual adjustment of the exposure time.

Variation of intensity within the laser grid occurs in the x - direction because the laser line entering the cylinder through the wall experiences attenuation so that the intersection points further in towards the cylinder axis have lower maximum intensity. Then, the level of energy intensity inherent in each laser line differs from line to line before the lines' entrance into the cylinder -- basically for two reasons: the initial laser beam that leaves the laser is inhomogeneous over its rectangular extent, and, due to the fact that the two splitted laser beams go through the focusing lens before they are divided by the grating so that the mirrors situated on the beam divider further away from the lens reflect higher intensity light (Appendix B). Furthermore, there are two laser lines that pass through the

quartz bottom of the reservoir which are for this reason weaker than the other lines involved in the generation of the grid.

The exposure time was adjusted so that the intersections of laser lines close to the lower cylinder wall exhibiting highest light intensity would not saturate the phosphor in the image intensifier [saturation of the phosphor is equivalent to assuming pixel values of 255 after digitization into the 8-bit grey scale scheme provided by the MegaVision system]. The exposure time was thus found empirically by trial and error. For the main body of experiments it was between 1 and 10% of the delay time.

By leveling out the differences in intensity distribution exhibited by the laser lines the determination of exposure times can be made easier.

II.2.3.3 Quality of LIPA - data

In order to create a quantitative and objective measure to compare the grade of a particular realization of a laser grid within the flow field, a quality factor is defined. This quality factor will also enable the investigator to decide what kind of data reduction process can be employed (section III.1). The suggested quality factor Q incorporates information about intensity of illumination (which depends on laser power, concentration of LIPA dye and age of chemical, and so forth), the sharpness and thinness of the laser lines, the grade of index matching, the distance of penetration of laser lines into the flow, and the degree of image intensification (photon magnification) and resolution provided by the imager. Q is proportional to these parameters. Q is reciprocal to the intensity level of the background, the exposure time (fuzziness of lines), and the time delay between the application of the laser grid to the flow and the recording of the LIPA image (diffusion of energy in lines). In a very simple, just-plug-in formulation of the above mentioned influences on the quality of LIPA grids a mathematical proportionality relation reads:

$$Q \cong \frac{INT * SHARP * THIN * INDMATCH * PENE * MAGN * RES}{(BACK + 1)* \Delta T_{Exp} * \Delta T_{Delay}} \qquad \text{(II.2.d)}$$

where $INT/(BACK+1)$ can be replaced by information about contrast of the laser lines in the test facility achieved in the image. $BACK$ is given as pixel intensity. This is why $BACK$ is incremented to avoid a Q of infinity when $BACK$ is zero. Since no data are available to compare an evaluation of this quality factor to, no quantification of Q will be furnished in this work.

To get a qualitative impression of the grade of LIPA - data that were acquired for this work three images bearing information on one undistorted -- (a) -- and two distorted grids -- (b) and (c) -- recorded for 20 RPM engine speed and 3 mm valve lift as data for the investigation of the whole engine cylinder are displayed in Figure II.2.7. The images were recorded with the image-intensifier/Video combo. As mentioned in Appendix C, the camcorder was turned by 90° in order to make most use of the CCD array of the Video camcorder, thus, the valve is on the right side of the picture, the cylinder wall at the bottom, and the piston head on the left side. In Figure II.2.7b and c one can hardly perceive distortion of laser lines. Highest distortion is, during engine performance, encountered at the axis of the intake jet. This axis is in the lower right corner of the pictures. With a scrutinizing look one can discern slight waviness of the laser lines. Low distortion assures the assumed linearity of particle paths. Furthermore, the pictures demonstrate that fairly deep penetration -- beyond the axis of the cylinder -- could be accomplished in the experiments.

In Appendix D it is noted that for calibration purposes a fixed reference point was added to the LIPA images. This reference point can be seen in the pictures of Figure II.2.7 in the upper left corner. It is situated within a crescent-shaped area formed by the mirror that reflects the light from an LED onto the CCD array of the camera.

Chapter III
ON METHODOLOGY AND ACCURACY OF DATA REDUCTION

LIPA can be efficient and survive profound criticism from the velocimetry community only if the data reduction process of raw data provided by the acquisition of LIPA information (distorted grids of laser lines) from LIPA's application to a flow field, provides a high level of accuracy along with quickness in the deduction of results. Consequently, the data reduction process ought to be thoroughly automated. Quickness of the data reduction process, then, in terms of automation, is ultimately limited by the speed and communication abilities of computer systems; quickness is, thus, basically a matter of hardware and only to a limited extent a matter of software. Accuracy is, as far as data reduction is concerned, considerably affected by the method and architecture of the software that infers fluid dynamical information from the raw data. The focus of research in the field of computer science, as far as LIPA is concerned, has to be on the implementation of software that is suited to reduce LIPA - data with the highest degree of accuracy attainable, while keeping a squinting eye on the progress of computer hardware.

For this work, all essential hardware/software requisites for data reduction of LIPA information were available with the exception of an algorithm that extracts coordinates of illuminated fluid particles from an image, and algorithms for the calculation of fluid dynamical quantities as well as their statistics. On the administrative side, a demand towards the data reduction process incorporates the process being able to manage the vast amount of data necessary for statistical independence of flow quantities that describe turbulence inherent in an encountered flow field. Data administration utilities and routines designed for this purpose were implemented on a UNIX platform. Limitations in computer memory forced the process of data reduction to seek a compromise between

administrative necessities and sample size for the generation of fluid dynamic quantities. These limitations confine, in this work, the total of frames over which ensemble averaged results can be obtained to a certain number.

The generation of algorithms that calculate the actual fluid dynamical quantities associated with a flow field was performed on a FORTRAN platform; the algorithms do not bear any significant or fundamental scientific innovations and will, thus, not be deliberated in this work. The same holds true for the utilities which are written in a UNIX environment and serve to administer the LIPA - data. Therefore, only the software that detects illuminated fluid particles in the LIPA images will be discussed.

In order to implement the software inferring coordinates of illuminated fluid particles from LIPA images, the illuminated particle itself as it is represented in an image has to be examined thoroughly. The particular realization of a grid of laser lines as it was achieved in this study, in connection with the resolution provided by the imager system and digitizing facility, yielded at intersections of laser lines illuminated *areas* that consist -- in the digitized images -- of about three hundred pixel (Figure II.2.3a); hence a fluid particle is represented in an image by an area of illumination. Within these areas which are surrounded by a background of constant intensity, the distribution of pixel intensities (on a range of 256 grey scale levels) resembles -- speaking in metaphorical terms -- that of a bell or an igloo sitting on flat ground; see Figure III.1.4b. The intensity values within the intersection area (IA) are significantly greater than those of the background. In order to calculate a velocity by considering the spatial distance between two temporally separated occurrences of the same fluid particle, this intersection area -- spanned by the crossing laser lines -- ought to be represented by one intersection point (IP) which comprises the center of a pixel. It is an imperative to any algorithm that determines intersection points from LIPA images to find the representative IP within this area consistently. As long as

this representation *is* chosen consistently the intersection point can be any characteristic point within the IA, e.g. the spot with the highest pixel intensity.

Motivation for the generation of software that was to automatically infer the coordinates of intersection points (illuminated fluid particles) from LIPA images was derived from the fact that deduction by hand is enormously time consuming and greatly imprecise. In fact, a sufficient amount of data necessary for statistical independence of velocity fluctuation information would not have been assured if data reduction had been performed manually.

Figure III.1 gives an idea of the uncertainty about hand-sampled coordinates of illuminated particles. For this plot three different persons deduced intersection points from a distorted laser grid in a LIPA image independently, each intersection point five times. -- The dotted lines are results from the application of an algorithm that reduces extensive laser lines to one-pixel, skeleton representations of a laser line; crossings of these skeleton lines denote intersection points of the laser grid. -- Not only is there considerable fluctuation within one cluster of the five points for one intersection and one person, but the centers of the three clusters neither coincide with each other for one intersection nor do they coincide with the intersection point suggested by automatic data reduction.

III.1 Illustration of two Approaches to deduce Coordinates of Intersection Points from LIPA Images, and Pre-Conditioning of these Images

For the inference of the coordinates of illuminated particles from LIPA images -- namely the coordinates of their intersection point representations -- two basic approaches had been considered. One approach incorporates the reconstruction of two laser lines in an intersection area that lose the information about their edges within the IA due to their crossing. After the recovery of the lost information the laser lines can be shrunk to

'skeleton' lines or 'centerlines' (with a width of one pixel) whose crossing denotes the intersection point for the particular intersection area. The other approach constitutes a more simplistic model where the algorithm looks essentially for the area of highest occurring pixel intensities within an intersection area and chooses its peak as intersection point. For both algorithms FORTRAN is the computer language they are composed in and FORTRAN77 the utilized compiler.

As has been experienced during data reduction, the point of highest intensity in an intersection area moves with respect to the intersection of the skeleton representations of the two intersecting laser lines. The problems in connection with these occurrences will be discussed later in this chapter.

III.1.1 Reconstruction of Intersection Area (RIA)

This approach is the more complex and precarious one. In order to apply it to LIPA images to infer intersection points from the grid of laser lines, a considerable contrast between laser lines and background is a necessary prerequisite. The process of IP deduction, which involves the recovery of information about the edges of the two intersecting lines which make up an intersection area and thus the reconstruction of the IA (RIA), consists in its most general form of the following computational procedure (for nomenclature refer to Figure III.1.1):

☐ First, an edge detection routine extracts within the intersection areas those dots from the two laser lines involved in an intersection that depict edges of the lines. Edge detection was based on a threshold criterion: An edge is defined at a location within a LIPA image with the property that a transition occurs of pixel intensity from intensities lower (higher) than a certain threshold to higher (lower) than this threshold. The applied threshold is determined based on information of local pixel intensity distribution by employing a

statistical analysis on a set of pixel values that consists of randomly chosen pixel intensities drawn from an IA and its vicinity.

☐ Next, each single edge element in the detected cloud of dots is assigned to its respective line it lies on by clustering the elements according to the *nearest-neighbor rule* (Jain and Dubes 1988). Thus two crossing lines are portrayed by the 'chaining' of edge elements. During the chaining procedure four significant points -- 'crucial points' -- are marked: these points are localized where the edges of the two laser lines cross. They are detected when during the chaining procedure a significant change in direction of the congregating chain is experienced.

☐ The next step is to consider two of these crucial points (any pair except a pair of two opposing points). The goal is to interpolate the edge of an interrupted laser line between these two considered points. In order to do so the ten closest edge elements of the two corresponding edges (which are chained away from the IA) at each of the two crucial points are considered. With these twenty data points one can perform any interpolation procedure thinkable. For this study a first order least square fit had been applied. Now, the recovery of information about laser line edges which was lost in the intersection area due to the crossing of the laser lines has been accomplished.

☐ The ultimate objective of the RIA algorithm is, however, to deduce the representative intersection point from the intersection area. For this, the recovered laser lines are shrunk to skeleton lines using the edges of the laser lines found by interpolation and the pixel intensity distribution within the intersection area. By intersecting these skeleton centerline representations of the laser lines it is possible to find the IP representation of the fluid particle for this approach.

The results achieved with the RIA approach were satisfactory when, in a preliminary test phase, applied to a set of undistorted LIPA grids originating from a different LIPA project.

The outlined procedure is established to find the IP for any IA; no a priori knowledge about shape, size, intersection angle, or orientation of the examined IA is necessary. Concern about deformed intersection areas after distortion of the laser grid which would cause problems when applying versions of RIA that require specific information about an IA was motivation to seek an algorithm of generalized form.

Preliminary procedures incorporating the shrinking of grid lines to a width of one pixel with subsequent intersection of the shrunk lines in order to find a one-pixel representation of the IA by using components of an existing software package provided by MegaVision (refer to Appendix D for more information on MegaVision) constituted the first step of and were the basis for the RIA approach. It turned out that the accuracy obtained by the MegaVision software was not sufficient so that software had to be implemented that was better suited for the task.

Edge detection software from the computer science literature such as 'Sobel' and 'LoG' (see Ballard and Brown 1982) had been implemented to serve as step 1 in the computational procedure outlined above. This software has been applied to LIPA images with minor success. All edge detection algorithms employed require by definition an abrupt change in pixel intensity as one examines a cross-section in an image in order to acknowledge an edge. The distribution of pixel intensity within a laser line is, however, of rather Gaussian nature condemning the edge detection algorithms to fail.

III.1.2 Search for Highest Intensity Spot in IA (HIS)

The second approach was originally implemented to support the first approach outlined in the preceding section. It was meant to serve as a 'second opinion' corroborating the result of the application of the RIA approach to a LIPA image. For the approach discussed in this section, the area of highest pixel intensity is found within an intersection area and its

center or peak -- the highest intensity spot (HIS) -- is defined as the intersection point of an IA. The off-set between the IPs detected by the RIA option and the HIS option and its variation for one IA with several LIPA images of information was to be used as a measure for accuracy. The HIS approach represents a more simplistic model; its mere presumption is that the laser lines intersect properly enough in order to generate a bell-shaped intensity distribution within an IA.

The computational procedure for HIS comprises a scanning routine which scrutinizes an intersection area to determine its subregion of highest pixel intensity and to appoint its center as the representative intersection point for an intersection of two laser lines.

The process of finding the highest intensity spot begins with a coarse assignment of a starting point in the vicinity of the area of highest intensity within an IA. Information about starting points is readily obtained from the locations of the IPs in the reference grids. Around this starting point an area of 10 x 10 pixel is examined. In order to find the highest intensity spot in the square area consisting of these hundred pixel around the reference IP the computer algorithm integrates subsequently for every one of the hundred pixel the intensity distribution over a square matrix of 7 x 7 pixel where the pixel under investigation is the center of this applied matrix. The algorithm, thus, takes into account information that is contained in the vicinity of each examined pixel in the 10 x 10 pixel array. There is a preassigned weight for each of the 49 members of this matrix. The weights in the matrix were chosen on the basis of an optimization procedure that incorporated empirical observations; the three-dimensional distribution of the weights resembles that of a 2D Gaussian distribution and is depicted in Figure III.1.2. The center pixel of that matrix that exhibits the highest integrated intensity within the 10 x 10 pixel array when the moving average is applied to an IA is selected the IP for an intersection area. With this method the coordinates of an IP can be evaluated to within a half pixel.

This is one contributing issue in connection with spatial resolution achievable with LIPA. The program implementing the HIS approach is listed in Appendix E.

III.1.3 Issues concerning the two IP detection approaches and the decision for one over the other

The advantage of the HIS over the RIA approach is that it is more stable and less sensitive to the 'landscape' of pixel distribution in a LIPA image. The disadvantage associated with HIS is that HIS's detection algorithm is confined to the digital pixel pattern (resolution) established during the digitization of the images. Furthermore, HIS is more sensitive to noise in the measurement procedure (for the occurrence of noise and its impact on accuracy read section III.3); a consequence of this sensitivity is that the moving of the highest intensity spot within the intersection area during convection of the IA as a whole is detected. A necessary criterion for RIA is the presence of a certain contrast in the images to discriminate between background and IA. In terms of the quality factor defined in section II.2.3.3 by equation II.2.d, RIA requires a higher value of this factor than HIS. RIA also requires a certain extension of the intersection area. An advantage in conjunction with RIA is that it overcomes the limitation prescribed by the chessboard-like pixel pattern by shrinking laser lines to their skeleton representations. All things considered, the RIA approach yields more accurate results.

As a matter of fact -- as experienced during manual data reduction -- the human cognition system (i.e. eye and brain) uses both forms of information: it looks for the highest intensity occurring within an IA and at the same time incorporates information about the shape and orientation of the laser line edges that form the IA. A phase II algorithm should try to simulate and adopt human nature behaviour.

Only in an ideal case do the two intersection points as deduced by RIA and HIS fall together. That is when the two crossing laser lines exhibit the theoretically exponential

cross-sectional distribution of intensity and the phosphorescent chemical is distributed homogeneously within the intersection area. The application of RIA and HIS to a LIPA image generated within a previous project that employed LIPA as velocimetry technique yielded coordinates for IPs that did not coincide, however, lay very closely together (see Figure III.1.3). It is not necessary that RIA and HIS find their respective IP at the same coordinate pair as long as the axis connecting the two detected IPs assumes a consistent length and position in 2D space for one IA for the frames containing the undistorted and the distorted LIPA information. As soon as this assumption is violated, however, models have to account for the variation of this axis.

In the grid of laser lines employed in the experiments conducted for this study the intersection point evaluated by HIS was generally off in x - direction (longer major axis of IA) when compared to the IP detected by RIA. It was off in the direction towards the cylinder wall, i.e. towards the origin of the laser lines.

The quality of the LIPA images that contain the distorted and undistorted grids which were acquired within this study was insufficient to apply the RIA approach, i.e. Q was too low. In particular, the condition that the contrast between the illuminated areas and the background being sufficient was violated. This was because of high background noise in the regions between the laser lines caused primarily by lower order laser light that is diffracted at the grating (read Appendix B *Optical issues* on influence of diffraction). Thus, for the data reduction of all LIPA information, HIS was employed. This implies that one has to be concerned and conscious about relocation of the highest intensity spot within the IA. It was possible to perceive this relocation for some intersection points by eye, essentially for the close-up grids in the investigation of the intake jet; the IP as deduced by HIS moved considerably within the intersection area when observed over several reference grids. The question emerges of what specifically are the causes for the movement of the intersection point within an intersection area. Two sources for the

movement are thinkable as most prevailing: Vibration of the experimental rig and small scale convection mechanisms in the flow field where only vibration in the apparatus yields uncertainties in connection with reference grids. The effects of convection mechanisms forcing IPs to roam within intersection areas for distorted LIPA grids will be discussed next.

In order to resolve the fluid motion associated with a certain length scale the intersection area of two laser lines has to be much smaller than this length scale. Fluid dynamics on length scales that are of the order of the major axes of an IA distort the intersection area. This causes IAs to not only translate but to also rotate and twist, thus deform. In this context, incorporating convection of the highest intensity spot within the intersection area into the translation of the IA as a whole by an application of the HIS approach, assures LIPA's strict assumption to merely consider translation of a fluid particle. The movement of the highest intensity spot within the borders of IAs during convection contains also valid convection information which through HIS is used in the data reduction process. Deformation of the IA was encountered mainly in the experiments in connection with the study of the intake jet -- as mentioned above -- and there particularly at the edges of the jet. This data should be analyzed in the awareness of the problem of relocation of the highest intensity spot within the IA. As soon as it is possible to quantify the mechanisms within the flow field that cause the highest intensity spot to move within the IAs more precisely, it is legitimate to utilize this data unrestrictedly.

To accommodate partly for the disadvantage in connection with HIS, namely the restriction to the resolution-imposed pixel pattern, was one reason why coordinates of intersection points in the reference grid were averaged over several reference grids yielding a non-integer number for the origin of a fluid particle before convection. Through the application of the averaging procedure considerable fluctuation of IP coordinates for one IA over several 'undistorted' grids was encountered. This 'phenomenon' is due to the

movement of the IP within an intersection area; it will be dealt with in more detail in section III.3. By averaging pixel intensity over a bell shaped area of 7 x 7 pixel in order to infer the highest intensity spot in an intersection area (as described above) a further increase in certainty about the actually evaluated location of the IP, and thus accuracy, is achieved. The application of the HIS algorithm enables the investigator to reduce data so ambiguous -- for which intersection areas exhibit rather flat regions of highest intensity -- that it cannot be reduced properly by hand.

III.1.4 Computational manipulation of LIPA images

The LIPA images as they are offered at the output of the video camera, stored on tape, and then digitized by MegaVision are, as they present themselves in digitized form, of minor quality concerning pixel intensity distribution. The images require comprehensive conditioning.

First of all, every other horizontal line contains no intensity information because there was information available for only every other line due to the manner of data acquisition (sampling in RS170 mode) as discussed in Appendix C. This problem was taking care of by just filling in every line that is without information with the content of the neighboring line. It is likely that better results are obtained by interpolating between preceding and proceeding lines instead of just copying the neighboring line.

Next, as can be seen in Figure III.1.4a the distribution of pixel intensities is very rough. High frequency fluctuation of pixel intensity with moderately high magnitudes is encountered in the intensity distribution within a LIPA image. The tribute had to be paid for using a non-scientific video camera purchased from the commercial video market. Scientific cameras would offer an additional electronic feature that intelligently prepares the image for scientific use. The problem was being taken care of by applying a simple 3 x 3 averaging procedure on the image which yields an astonishingly smooth surface of

48

the intensity distribution in the 3D plot; see Figure III.1.4b. By this averaging process the lines in a LIPA image which carried no information and were replaced by a simple copying process (as discussed in the preceding paragraph) are, as a positive side effect of the averaging process, adjusted to their neighboring lines so that one arrives now at a smoothed image with 512 x 512 pixel. The disadvantage with averaging procedures is, on the other hand, that since averaging is of an integrating nature there is a loss of contrast experienced in the images. Transitions are diminished or at least weakened. This loss of contrast contributes to the inhibition of the application of the RIA approach for the deduction of intersection points from LIPA images.

In order to increase the dynamic range and thus the accuracy of the data reduction process every pixel unit was cut into four sub-pixels named 'quarts'. After the liberation of the quarts from their constraint to assume the value of the pixel 'host' a 3 x 3 averaging procedure is applied on the 1024 x 1024 quarts (stemming from the 512 x 512 original array of pixel) in which, as initial condition prior to the averaging process, the quarts keep the values of their pixel hosts. The coordinates of IPs can be evaluated now to within a quarter of a pixel of the original image.

All three elements that condition the LIPA image are incorporated in the FORTRAN program that implements the HIS approach as a prestage preparation prior to the application of HIS itself. For a listing of the software see Appendix E.

III.2 Mathematical Formulation of Fluid Dynamical Quantities

III.2.1 Reynolds' decomposition as basis for a model to separate sources of velocity fluctuations

According to Reynolds' decomposition theorem for turbulent flow (Tennekes and Lumley 1972, Fox and McDonald 1973, Potter and Foss 1982) an instantaneous local velocity vector can be decomposed into an invariable mean part and a part constituting velocity fluctuations. The mean velocity can be obtained by different methods, for example ensemble averaging procedures. Reynolds' decomposition reads:

$$v = \bar{v} + v' \tag{III.2.a}$$

There are three components responsible for velocity fluctuations v' as encountered in the reduced data of this work, two of which are due to fluid dynamics of the flow field — cycle-to-cycle variability and turbulent motion of the flow field — whereas the third component is related to 'noise' in the velocimetry system. Noise is defined to consist of all errors that are encountered in the data reduction process (e.g. vibration of experimental apparatus). Thus v' can be decomposed as follows:

$$v' = v'_{CtC} + v'_{turb} + v'_{Noise} \tag{III.2.b}$$

In this study the mean velocity is calculated using ensemble averaging (EA) techniques. Considering this and plugging III.2.b into III.2.a, III.2.a yields for an instantaneous local velocity vector as encountered in sections V.3 and V.5.2

$$v = v_{EA} + v'_{CtC} + v'_{turb} + v'_{Noise} \tag{III.2.c}$$

An effort has been undertaken in section III.3 to eliminate the 'noise' component from equation III.2.c. In section V.3.2 an attempt is made to quantify the individual fluctuation sources v'_{CtC} and v'_{turb} which are in this work functions of crank-angle, location within flow

field, and engine cycle. Summation of $v_{EA} + v'_{CrC}$ gives a local mean velocity for a particular crank-angle and engine cycle.

III.2.1.1 Formulations employed for ensemble averaging

Figure III.2.1 helps to explain the procedure of ensemble averaging which was performed to obtain $\bar{v}$ in equation III.2.a as mentioned in the preceding section. Sketches of LIPA images are exhibited for one engine cycle (EC; #5) at different crank-angles -- horizontal mode -- and at one crank-angle (28°) for eight different engine cycles -- vertical mode. The averaging software ensemble averages at one crank-angle and one location within the flow field over all investigated engine cycles. This yields the local ensemble averaged velocity vector at that particular crank-angle. EA velocity vectors are functions of location within the examined flow field and of crank-angle $v_{EAloc, CA}$. In mathematical terms this reads:

$$\bar{V}_{loc,CA} = V_{EA_{loc,CA}} = \frac{1}{N} \sum_{j=1}^{N} V_{loc,CA,EC_j} \qquad (III.2.d)$$

Velocity fluctuations are expressed in terms of a 'Root Mean Square' (RMS) value evaluated over all v' encountered during the application of an ensemble averaging procedure. v_{RMS} is calculated according to the following formula:

$$V_{RMS_{loc,EA}} = \sqrt{\frac{1}{N} \sum_{j=1}^{N} V'^2_{loc,CA,EC_j}}$$

$$= \sqrt{\frac{1}{N} \sum_{j=1}^{N} \left(V_{loc,CA,EC_j} - \bar{V}_{loc,CA} \right)^2} \qquad (III.2.e)$$

N in equations III.2.d and III.2.e is the number of engine cycles available for the averaging procedure. As mentioned in section II.2.2.4 this number had to be limited due to confined workspace of the employed computer system.

To find out about the legitimacy of the ensemble averaged numbers the convergence of the ensemble averaging procedure was checked during the calculations performed by the software, by monitoring the change of the RMS value of the velocity fluctuations as data were being added by the ensemble averaging process. From this, satisfactory convergence was observed during the ensemble averaging procedure where towards the end of the incorporation of all data available for a certain set, the change of the RMS value describing the fluctuation of events about the mean was only between 2 and 3% between the incorporation of two succeeding events.

III.3 Critical Assessment of Accuracy Issues for LIPA

At the end of the two chapters that introduced LIPA as a velocimetry technique and that described the general data acquisition and reduction procedure, a section discussing critical issues in connection with the application of LIPA in general, and for this study in particular, is mandatory to follow. Some topics concerning accuracy have already been discussed in depth elsewhere in this work so that in this chapter, for reasons of completeness, a mere repetition has been furnished of these matters. -- In fact, throughout the entire text of this work one can find issues concerning the accuracy of LIPA that are being assessed critically. --

LIPA is based on the underlying assumption that the influence by convection processes on the development of the flow field is much larger than the influence by diffusion processes. The parameter that describes the relationship between the flux of momentum and the rate of mass transport between flow structures is Schmidts number which is defined by

$$Sc = \frac{\nu}{D} \qquad\qquad (III.3.a)$$

where ν is the kinematic viscosity and D the mass diffusion coefficient. Schmidts number for water assumes a value of about 600. This number indicates that the influence on fluid flow associated with convection processes with water as the base for the working fluid is three orders of magnitude higher than that associated with diffusion mechanisms which is sufficient to consider diffusion processes as negligible in this work. For air, Sc is about 1. Thus, in air LIPA has to be careful about the effects enforced on the flow field by diffusion.

III.3.1 Overview of encountered sources of error in connection with the LIPA technique

III.3.1.1 Movement of intersection point within intersection area as main source of error

Artificial or virtual velocity fluctuation enforced by the method of evaluation of an instantaneous local velocity is intrinsic -- to various degrees -- to almost all anemometry techniques; for every technique one has to seek a minimization of this effect. The primary source of error as it presents itself in this work is established by the fact that the intersection area (IA) -- marking of fluid particle -- does not consist of just one pixel which would be considered the representative intersection point for the IA, but has extension and thus a certain intensity distribution within the area. As mentioned earlier a relocation of the spot representing highest intensity -- which is detected by HIS -- within the intensity distribution of an intersection area can be observed for one IA and several reference grids. This relocation of the IP is undesirable and constitute the main error source. The relocation due to convection as deliberated upon in section III.1.3 is captured by the HIS approach and included in the calculation of velocities. In order to separate the relocation mechanism due to noise in the system from that due to convection and study these issues individually, undistorted reference grids of laser lines where only influences by, e.g., vibration in the apparatus are encountered since the images are recorded with the engine quiescent, should be considered for the study of the influences of noise on the relocation of the highest intensity spot. This has been done in the proceeding paragraphs.

It has been observed during the interrogation of reference grids that the intensity distribution within an intersection area varies from laser pulse to laser pulse with respect to highest intensity regions due to a non-homogeneous, vacillating distribution of the LIPA - chemical in the Water/KSCN solution. The alteration of the non-homogeneous distribution in between laser pulses, specifically within the intersection areas, is caused by 'noise' where supposedly vibration of the experimental rig constitutes the main influence.

The redistribution of the LIPA - chemical on the molecular level enables the highest intensity spot to move within the IA. Since the HIS approach employed in this study finds the spot representing the highest intensity within an IA, the algorithm finds a different intersection point with every laser pulse. A quantitative measure for the movement can be found in Table III.3.1.

The uncertainty in connection with the relocation of the highest intensity region within an intersection area accounts for the strongest contribution to the third component of the threefold velocity fluctuation model, the third component being the contribution of system "noise" v'_{Noise} to velocity fluctuations in connection with the application of the velocimetry technique; see section III.2.1, equation III.2.b.

Statistical law implies that the uncertainty in conjunction with the undesired moving of the highest intensity region within an intersection area due to 'noise' cancels out for the reference grids when an average is taken over an infinite number of instantaneous velocities. Hence, the effect comprising the relocation of the IP within an IA vanishes hypothetically in the EA domain. The mean becomes unaffected by the movement of the highest intensity region within an intersection area, not the fluctuations. One has to, thus, pay enhanced and more careful attention to the plots that contain instantaneous velocity data. The uncertainty in connection with noise-related movement of the IP is removed as well in the evaluation of mean velocity profiles in cycle resolved analyses when curve fit routines are employed to instantaneous velocity profiles as will be done in section V.3.2.

In this study reference grids are taken prior to a set of experiments with the working fluid quiescent. This approach offers some advantages as outlined in chapter II. What the acquisition of reference data with the engine standing still also signifies, however, is that one does not really follow one specific fluid particle during data acquisition of distorted LIPA grids in the experimental phase, as is the idea of the Lagrangian approach assumed by LIPA, since acquisition of initial origin location of fluid particle and location particle

convected to are decoupled. This constitutes a source of error because due to 'noise', that relocates an intersection point within an intersection area, the location of an IP within an IA for a particular intersection of laser lines in an undistorted grid recorded with the working fluid quiescent is statistically different from the one in the reference grid that contains the initial positions for an acquired distorted grid and that cannot be captured because the sampling rate of the imager is not high enough; section II.2.3.1. In this work sets of initial fluid particle locations from undistorted grids are therefore generated by statistically averaging over twenty reference grids.

The fact that the acquisition of reference information is decoupled from the acquisition of the distorted grids together with the fact that averaging is performed over 20 reference grid realizations to deduce the initial positions of fluid particles implies, with respect to the Lagrangian approach employed by LIPA, that one follows a fluid particle that presumably leaves from a location where one assumes it to be based on statistical probability. Since one cannot average over an infinite number of LIPA grids in the ensemble averaging process, i.e. remove uncertainty due to 'noise' in the system completely, the uncertainty in connection with the movement of the highest intensity area within an IA because of 'noise' remains in the data discussed in this work. This uncertainty is a function of the degree of fluctuation of the intensity distribution, and therefore movement of the intersection point, within the IA as well as of the extent of the intersection area.

There are ways to avoid the above discussed problems: 1) The extension of the intersection area should be only a fraction of the distance the average fluid particle travels. (An enhanced effort on the optical side of the LIPA technique should be undertaken.)
2) For every distorted grid its own original reference laser grid at the moment when it is imposed onto the flow field should be recorded during engine performance so that one considers the intrinsic origin of the convected fluid particle. (A camera offering an appropriate sampling rate has to be available for this.)

III.3.1.2 Intersection angle, resolution of LIPA image, and dynamic range as issues in the discussion of accuracy

The fact that for the investigation grids employed in this study two crossing laser lines do not intersect under an angle of 90° poses another unfortunate condition upon the data reduction process. Due to the thus established inequality in length of the two major axes in each intersection area, unequal uncertainty in conjunction with the relocation of an intersection point within an IA is forced upon the detection of the intersection point coordinates for the x - and z - direction. As mentioned in section II.2.2.1 the laser lines of the grid that covers most of the engine cylinder exhibit intersection angles of about 50° yielding a ratio of the major axes of about 3. Thus, because of the ridge-shaped pattern of the IA with the longer extension being in x - direction the uncertainty in the deduction of an IP in connection with the x - direction is potentially three times higher. In the x - direction there is a higher sensitivity to a change in the intensity distribution due to system noise within the IA.

An interesting issue to be discussed can be formulated by the question of how the number of pixel in LIPA images (not necessarily resolution) effects the accuracy of the data reduction process in conjunction with the uncertainty impelled by the movement of highest intensity regions within an intersection area. The influence of the number of pixel in a LIPA image on the extraction of accurate positions of intersection points has been investigated in the following by detecting IPs in ten undistorted grids employing the HIS approach, evaluating the fluctuation in the detection of these IP locations for a particular intersection area, and comparing these results for different LIPA images having different numbers of pixel displaying the grid information. The values representing a measure for the fluctuation of the detected IP locations that will be compared for different LIPA images with different numbers of pixel in the images, are obtained according to the

following scheme: For one IA, the variation of the coordinates of detected intersection points over several (10) reference grids is evaluated in an RMS approach. This variation is determined for each intersection area in the set of the ten images with the same number of pixel with subsequent evaluation of the mean of these variations over all intersection areas. Two representative numbers for the x - and z - direction are obtained as measure for the fluctuation encountered. The results for four sets of LIPA images where undistorted grids are represented by a different number of pixel for each set are presented in Figure III.3.1.

First of all, there *is* fluctuation, indicating the existence of error due to system noise (ideally the fluctuation for the reference grids should be zero, of course). Secondly, the eminently higher uncertainty for proper evaluation of IPs in the x - direction for cases I, II, and III is due to the abovementioned fact that the extension of the intersection area of laser line crossings is greater in the x - direction than in the z - direction (non-perpendicular intersection of laser lines).

In Figure III.3.1 the four cases I - IV represent the following stages of manipulation (conditioning) of the reference grids: Number I depicts the uncertainties about accurate detection of initial positions in the images containing undistorted grids after all conditioning steps as outlined in section III.1.4, namely the filling in of missing information with subsequent application of an averaging procedure and quartering of pixel units, have been conducted (1024 x 1024 pixel in image). Number II denotes the uncertainty after filling in lines of information and averaging over the image; no quartering of pixel units is performed (512 x 512). For number III only the missing information has been added to the image (256 x 512). Number IV reflects the uncertainty about the detection of IPs in a reference grid after those horizontal lines that do not contain any information have been taken out in the images (256 x 512). This move corresponds to a virtual 50% compression of the -- real physical world -- engine cylinder in x - direction by the mapping of the cylinder into an image. Along with this compression in the x - direction

the extension of the longer axis in the intersection areas is cut in half and, thus, reduced to be fairly close to the width of the IA in z - direction.

A very obvious feature in the plot of Figure III.3.1 is the dramatic decrease of the RMS fluctuation in connection with the detection of intersection points in x - direction for case IV to almost the level of uncertainty experienced in the z - direction. This can be attributed to the fact that for case IV the length of the intersection areas is only slightly longer than the width of the IAs and that therefore the accuracy is of the same order for the two directions. The remaining difference is arguably not due to the difference in the number of pixel used to display the grid information for the x - and z - direction but is due to the fact that the axis of the IA in x - direction is still longer than the one in z - direction; thus indicating the minor influence of the number of pixel in an image on accuracy in connection with the movement of an IP in an IA, since the number of pixel for the z - direction is twice as high when compared to the one for the x - direction. The increase of the variations about detected IP locations in x - direction as encountered in a transition from case IV to case III illustrates the disadvantage in conjunction with the elongation of one major axis of the IA and thus the demand for laser lines to intersect perpendicularly in order to avoid non-isotropy in the data reduction process. The fluctuation in the unmanipulated z - direction when comparing III and IV is considerably smaller for case IV — although for III and IV the same number of pixel is used to display undistorted grids (256 x 512) — since the effect of the modifications performed on the LIPA images in the x - direction for case IV enters the calculations of the fluctuation of IP coordinates for the z - direction through the use of the 'Gaussian' shaped bell that was utilized to deduce IPs (section III.1.2). The bell couples results obtained for quantities in x and z.

The RMS fluctuations in connection with the detection of IPs in intersection areas as presented in Figure III.3.1 appears to be effected only marginally by the increase in the number of pixel within a LIPA image (see sequence III to I in Figure III.3.1). However, there is a weak but perceivable trend for the fluctuations that suggests that with increasing

number of pixel in a LIPA image the variations about the detection of coordinates of intersection points inherent in a sequence of images containing reference grids are decreasing. -- For validity considerations of the numbers in Figure III.3.1 bear in mind that a sample size of ten is not exceedingly representative. -- With an increase in the number of pixel in a LIPA image two effects concerning the sought after decrease in fluctuation intensity and thus increase in certainty are working against each other: Since the centers of neighboring categories (pixel units) into which highest intensity spots can fall are closer together in the case where a larger number of pixel are used in an image, fluctuation decreases with an increase of pixel units. However, on the other hand when using a smaller number of pixel in an image, the probability that events fall into the same pixel unit is more likely. A more detailed study including considerations from this phenomenon would be beyond the scope of this study.

In summarizing the above analysis one can say that an increasing number of pixel in a LIPA image does not effectively improve the accuracy in the detection process of reference data in conjunction with the attempt of elimination of errors due to system noise that forces the region of highest intensity to move within an intersection area. Of course, an increase of the number of pixel representing distorted and undistorted grids improves the accuracy of the data acquisition process as a whole (e.g. dynamic range) and that is desired.

The accuracy of LIPA in general is strongly dependent on the resolution that can be achieved during digitization of the flow field. For the 'whole cylinder' approach 7 pixel represent about one millimeter in a digitized LIPA image. A maximum distortion of 1.3 mm in real space was allowed in one direction in order to ascertain linearity between two points. This 1.3 mm is approximately represented by 10 pixel after digitization. The accuracy in connection with the detection of intersection points in the digitized images is -- with respect to the pixel scheme in the images -- a quarter of a pixel after quartering

pixel units (as was outlined in section III.1.4). This leads to a hypothetical dynamic range of 1:40 -- based on velocity magnitudes -- if one considers 10 pixel of maximum convection for a fluid particle in each direction. The actual effective dynamic range is smaller as will be delineated in section III.3.3 when uncertainties due to the movement of the highest intensity spot within the IA are included.

Certainty about the inference of IPs from IAs is enhanced due to the facts that 1) averaging was performed over several reference grids in order to find the initial locations of the fluid particles which frees the HIS approach from its restriction to assign coordinates of illuminated particles within the pixel pattern, and 2) the IP detection algorithm (HIS) examined arrays of 7 x 7 pixel to find highest intensity spots, thus, including information of each pixel's environment yielding a higher accuracy than the nominal one of a quarter of a pixel.

III.3.1.3 Miscellaneous sources of error

In any data acquisition and reduction system unavoidable sources of error are encountered of whose extent the investigator should be aware. Some of these sources of error which enter v'_{Noise} in equation III.2.b are addressed in this section.

When data are to be ensemble averaged, corresponding data blocks have to, in the EA procedure, exhibit identical engine speeds and have to be drawn from equal crank-angle positions of the piston. There are uncertainties encountered in this context for this study due to instabilities in engine speed in the experimental phase and due to difficulties in proper assignment of LIPA images to crank-angles during the data reduction process (more on these difficulties can be found in Appendix C). Also, problems arise when two maps of instantaneous velocity vectors from different engine cycles or different sets of data are to be compared. The results in the maps are off marginally by engine speed and crank-angle.

Uncertainties about the absolute values of the velocity vectors arise due to reading errors in the calibration process using a white square in the determination procedure of appropriate scaling factors (pixel/mm; Appendix D). This error is unimportant in the comparison of the results which stem from an application of one particular investigation grid, e.g. laser grid for the study of the whole engine cylinder (fixed focus length of the imager).

Further elements influencing the accuracy of LIPA include the size and the shape of the 'Gaussian' bell used to detect IPs in the HIS approach, depth of field, change in index of refraction of liquids due to change in ambient temperature and evaporation of constituents, perturbation of the intake flow due to vibration of the experimental rig, etc.

The contribution of all these error sources can be considered negligible in the face of those delineated in the preceding two sections, but are summarized here for the purpose of completeness.

III.3.2 Actual quality of LIPA - data

The HIS software itself has demonstrated to deliver sufficient accuracy, that is to say the algorithm itself is exact, i.e. it finds the region with the highest occurring intensity within the assigned area (10 x 10 pixel). The decision and confirmation for HIS as being the IP detection *approach* of choice in this study, however, has to be made on grounds of an analysis incorporating the issue of how well the detected highest intensity spot serves as a representation for an intersection area. Or rather what is the degree of the variation of detected IPs for a particular IA in consideration of several reference grids. That leads immediately to the question: What is the degree of quality of the raw data -- LIPA images -- necessary so that the HIS approach yields results that are of acceptable accuracy? What actually is 'acceptable accuracy'?

For reference grids the intersection points deduced by HIS should be for one IA consistently at the same pair of coordinates, thus the detection of IPs in images of undistorted grids should essentially be fluctuation-free. That was not the case in this work as could be seen in section III.3.1.2 (otherwise the discussion of issues describing the accuracy of LIPA would be a brief one).

With LIPA, a quantification of the (in)accuracy encountered in the data reduction process due to relocations of an intersection point within an intersection area can be conducted based on the images that contain the undistorted grids. The fluctuation in the detection of IP locations for these grids should be zero so that any value different from zero encountered in the following analysis of reference grids can be considered inaccuracy induced by the measurement technique. The quantification of the inaccuracy of reference data -- used for the generation of fields of velocity vectors in chapter V -- as it is reduced by employing HIS, was based on the approach used to obtain fluctuation measures to demonstrate the effect of the number of pixel in a LIPA image on data reduction in section III.3.1.2. The presented numbers in Figure III.3.2a and b are, thus, for each set of engine parameters and direction (x and z) an average of RMS fluctuations over all fluctuations encountered at the individual intersection areas in the reference images. In fact, the evaluation of the RMS fluctuations was a by-product stemming from the calculation that determined the mean coordinates for initial positions of fluid particles in a LIPA grid conducted over 20 reference grids. Figure III.3.2a holds a comparison of RMS fluctuation values for the uncertainty in connection with the relocation of an IP within an IA for the laser grid with which the whole engine cylinder has been examined. In Figure III.3.2b the fluctuation numbers are exhibited for the laser grid with which the intake jet has been examined (close-up grid).

From Figure III.3.2a which contains the fluctuations encountered in the reference grids for the investigation of the entire engine cylinder one can see that the fluctuations in

connection with the x - direction are about four times higher compared to those in the z - direction. (The sequence shown is for the three valve lift cases examined at 30 RPM engine speed; Table II.2.3.) This is an immediate reflection of the difference in length of the major axes within intersection areas for the x - and z - direction even if the encountered value of four does not match exactly the one of three found for the ratio of the major axes of an IA earlier in this chapter. In the z - direction the inaccuracy is marginally higher than the resolution with which HIS detects intersection points, namely a quarter of a pixel (see section III.1.4). In the x - direction the uncertainty is in the average one pixel and a half, a considerable vagueness in the determination of a velocity vector. The values describing the RMS fluctuation for the x - and z - direction are, to within the accuracy obtainable in conjunction with a sample size of 20 reference grids, essentially congruent when considering all nine sets of data stemming from the nine engine parameter settings (Table II.2.3).

The values for the RMS fluctuations associated with the close-up grid of laser lines in the investigation of the intake jet in Figure III.3.2b are twice as high for the z - direction and about 1.5 times as high for the x - direction when compared to the corresponding values for the investigation grid applied to the entire engine cylinder. The difference in the proportionality factors for the x - and z - direction is due to the fact that the major axes of the IAs encountered in the laser grid that is employed for the investigation of the intake jet do not coincide with the x - and z - direction of the reference frame of the engine cylinder (see Figure II.2.3b), thus decreasing the ratio of major axis in x - direction to the one in z - direction. The overall increase in uncertainty for the close-up laser grid is experienced because an intersection area consists of about twice as many pixel in connection with this close-up grid when compared to the 'whole cylinder' investigation grid. There is a clear correlation -- almost linear -- between the size of an intersection area and the degree of accuracy, as should be anticipated. Uncertainties of around 2.6 pixel as stated in Figure III.3.2b for the x - direction is considerably high. A fluctuation of 2.6 pixel means

that the flow direction of fluid particles that convected a distance of less than 2.6 pixel -- which corresponds to 0.34 m/s for 20 RPM engine speed and 9 mm valve lift -- in the digitized image cannot be resolved, i.e. 2.6 is the threshold for direction ambiguity. The values for the three cases examined in connection with the close-up grid are for the x - and z - direction congruent again to within the certainty achievable by a sample size of 20.

Overall, the accuracy in the z - direction, particularly for the 'whole shot' laser grid, is satisfactory which is why velocity fluctuation data are being furnished only for the z - component.

The reader should bear in mind that the numbers for the fluctuation in the determination of IPs in reference grids in the previous paragraph are averages over the entire area of investigation. If one breaks these average values up and discusses the distribution of uncertainties in connection with individual intersection areas over the area covered by a laser grid one notices quickly that the distribution of the inaccuracy is dependent on several parameters. For instance, the uncertainty about the detection of the accurate IP in an IA increases with the penetration of the laser lines. For 20 RPM engine speed and 3 mm valve lift the distributions of the RMS fluctuation -- representing the variation in conjunction with the detection of intersection points in reference information -- are for the close-up laser grid exhibited in Figure III.3.3 for x - and z - direction. In the plots the laser lines enter from right. The gridlines in the x, z - plane of the 3D needle plot depict the orientation for one set of parallel laser lines. The line-up of the needles in the plot under 45° denote the other set of laser lines. It can be seen that the uncertainty increases -- in the average -- with penetration of the laser line, however, does not increase with penetration, speaking in mathematical terms, in a monotone way. The ups and downs in the measure for the fluctuation for one laser line can be explained by the fact that not all laser lines within one set of parallel lines exhibit equal intensity, as outlined in section II.2.3.2 and

Appendix B. This generates IAs of different intensity distribution along one laser line and thus different values of fluctuation.

The characteristics of the fluctuation profiles for the laser lines with penetration are, as one should expect, essentially the same for the x - and z - direction (Figure III.3.3a & b). The average value of 'four' found previously describing by how much the uncertainty is higher in conjunction with the x - direction compared to the one in the z - direction is reflected by Figure III.3.3. When considering the individual uncertainties associated with the individual intersection areas it turns out that there are proportionality factors between the uncertainty in z and x in the range of about 2 to 5.

Some security check mechanisms have been implemented to avoid the most crude mislocations of intersection points within intersection areas.

☐During the IP detection process a detected highest intensity spot that lies outside the assigned area of 10 x 10 pixel is discarded. Recall that a convection of 10 pixel was assumed to be the limit within which the convection can be considered linear. This limit was set empirically by watching laser lines distort on a TV monitor.

☐At the final computational level, a filtering procedure is applied in order to eliminate stray velocity vectors. If the velocity fluctuation of a local instantaneous velocity vector is higher than 3 times the RMS fluctuation encountered at this location during the ensemble averaging process, this vector will be removed. The value of 3 was determined empirically.

III.3.3 Estimation of errors in plots of velocity vectors

Following will be given a rough quantification of the order of errors encountered in the diverse presentations of fields of velocity vectors within this work.

For velocity plots containing instantaneous velocity vectors one has to add the uncertainty associated with the fluctuation of the detection of the intersection point due to

the movement of the highest intensity region within an intersection area -- as introduced in section III.3.2 -- to that associated with image resolution. Two globally averaged -- over all examined intersection areas -- numbers for the uncertainty in the detection of the IP due to relocation of an intersection point within an IA for the x - and z - direction are determined from an analysis of reference grids for each of the two laser grid realizations ('whole cylinder' and close-up) independent of engine parameter setting. These numbers do not, naturally, reflect the exact fluctuations in connection with each individual intersection area. However, they can be considered good approximations for each IA. For the 'whole cylinder' and the close-up investigation grids the measures for the uncertainty in the detection of the IP due to system noise are depicted in Table III.3.1. The summation of the uncertainties for the two sources of fluctuation mentioned in the first sentence of this paragraph is performed in this table. The numbers in row three are the actual measures for the uncertainties of the velocity vectors in pixel which will be denoted along with a reference velocity vector in the maps depicting velocity vector distributions in chapter V. From this row it can be inferred that the best accuracy attained in this application of LIPA has a dynamic range of about 17. Numbers in row four of Table III.3.1 show errors in percent when referring to the maximum convection allowed for fluid particles for each direction of 10 pixel.

Table III.3.1: Uncertainties in the maps of velocity vectors

| Field of ... | Uncertainty due to ... | RMS Uncertainty in pixel | | | |
| | | 'whole cylinder' grid | | close-up grid | |
		x	z	x	z
instantaneous ...	mov. of IP in IA	1.53	0.38	2.61	0.92
	image resolution	0.25	0.25	0.25	0.25
	Σ	1.78	0.63	2.86	1.17
	error in percent	17.8	6.3	28.6	11.7
ensemble averaged...	25% of row 3	0.45	0.16	0.72	0.29

- - - Velocity Vectors

In the EA domain both uncertainties, the one by limited image resolution and the one due to movement of the highest intensity spot within the IA, are mainly filtered out during the ensemble averaging procedure, however, certainly, not completely. As a first, conservative approximation one can assign an upper limit for the error for ensemble averaged velocity vectors -- to be on the safe side -- to about 25% of the original uncertainty. This is a rather arbitrary, yet reasonable pick. The accuracy for an ensemble averaged velocity vector results from the values in the third row of Table III.3.1 and is written down in the fifth row of the same table.

Although, e.g., vibration characteristics within the engine apparatus and thus relocation issues of IPs in IAs are different -- to say the least -- when the piston of the engine is moving as opposed to when the engine is quiescent, the values of the quantification of RMS fluctuation encountered during IP detection at individual IAs in reference grids as delivered in section III.3.2 were used as a first approximation for v'_{Noise} in an attempt to cleanse EA velocity fluctuations defined by equation III.2.b by subtracting the values found in Figure III.3.3 (row 3). For a more accurate quantification of this uncertainty one will have to implement a model for relocation processes of an IP within an intersection area due to, among others, vibration in the apparatus on a length scale comparable to that of the major axes of an intersection area to find the exact correlation between relocation mechanisms and the associated uncertainty about the intersection point, which then can lead to an accurate removal of this contribution of system noise. In this study, however, a first approximation must suffice.

The primary difference between the uncertainty in connection with image resolution and the one with the motion of the highest intensity point within an IA is the fact that the former is homogeneously distributed over the area of investigation (at intersections of laser lines) and that the latter is dependent on the length of penetration of a laser line together with the light intensity exhibited by an individual laser line (keyword: size and

pixel intensity of intersection area). Whereas the influence of image resolution on the uncertainty in velocity vectors increases the level of velocity fluctuation due to system noise evenly by adding the same constant at each location within the area of investigation, the influence of variation in the evaluation of IP coordinates for one IA and several LIPA grids on the uncertainty will lead to a 'distortion' of velocity fluctuation information throughout the field of investigation. In this work (section V.5.3) only the uncertainty in conjunction with relocation processes of the IP within an IA is removed from EA velocity fluctuation information in order to undo this 'distortion'. Since no precise measures for particular uncertainties with respect to system noise are available for this investigation, no effort has been undertaken to adjust for the exact level of EA velocity fluctuation magnitudes.

Chapter IV
THE INTAKE FLOW FIELD IN THE AXISYMMETRIC
ENGINE EXAMINED BY FLOW VISUALIZATION

The fluid dynamical process which is examined in this study namely the intake stroke of a four-stroke internal combustion engine is a reciprocating, i.e. periodic, hence unsteady one. The intake stroke features very complex timing and geometry of fluid flow. It therefore results in a fluid dynamically complicated flow field, which incorporates several different flow structures and instabilities of flow patterns which quantitatively -- and sometimes to a certain extent even qualitatively -- differ from intake stroke realization to intake stroke realization. The application of LIPA results in velocity vector information in two-dimensional maps of finite resolution. Thus, the turbulent motion on scales smaller than the resolution of the mesh size of the laser grid (i.e. fine scale eddies) cannot be detected in the flow fields of induction strokes when employing LIPA. However, the large and intermediate scales generated (as we shall see) are resolved directly from the two-dimensional information. Therefore, instantaneous velocity vectors obtained do not contain the small scale information, but as we hope to show using flow visualization, do contain the essential information embodied in the important large scale structures that develop.

The need to determine the dominant scales of the flow structures to gain an understanding to the resolution required in the LIPA grids was the primary motivation to perform visualization. A secondary motivation was to use the visual data to help interpret the quantitative velocity and vorticity data that LIPA would give. By considering velocity maps as quantification of flow visualization, one is more likely to arrive at the correct

interpretation and understanding of the flow field. In general, it is always desirable to have a visual image as analog information of a flow field.

Two visualization techniques have been used which are alike with respect to the visualization concept they are based upon, and different with respect to the assignment of the position of an observer who views the flow. The analogy is derived from the fact that both techniques are based on visualization by excitation of photoluminescent molecules dissolved in the working fluid. The difference is mainly manifested by the distinction in the frames of reference when describing the flow field: For one technique the approach is Eulerian (reference frame rests relative to the flow), a fluorescent dye was used here; for the other it was Lagrangian (reference frame moves with flow), a photochromic dye was the marker for the fluid particles in this case. For the Eulerian approach -- where a fluorescent dye is employed that emits radiation only during the time of excitation by an energy source -- the instantaneous situation of the flow field is recorded; with this technique one freezes the flow at a certain time by taking a snapshot of it. When using photochromic dye -- which emits energy for a certain time after the molecules have been excited -- as for the Lagrangian visualization approach it is possible to trace particular fluid particles in the flow field as the flow field evolves (which is actually LIPA's intrinsic idea). The latter approach naturally yields a better understanding of the development and restructuring of flow patterns inherent in the flow field.

The experiments involving the photochromic dye were performed at 1.5 RPM engine speed (25.5 RPM in air) and 3 mm VL. The experiments involving the fluorescent dye were conducted at 20 RPM engine speed (340 RPM in air) and also 3 mm valve lift.

IV.1 Results from Application of Photochromic Dye

IV.1.1 Experimental procedure

The chemical used was a photochromic dye, namely 1',3',3'-Trimethylspiro-8-nitro(2H-1-benzopyran-2',2'-indoline) from Kodak (reference-# 52590). This dye changes from being transparent to emitting upon excitation, radiating visible, blue light for a lifetime of several seconds. It requires an alcohol or an oil as its carrier for which several candidates had been considered and tested. There were various demands towards the carrier of the dye, one being that the index of refraction was to be close to that of the quartz engine. Furthermore, the fluid had to be transparent in the UV range of the spectrum of electro-magnetic waves, the dye had to dissolve thoroughly in it, and an applied excitation to the flowing medium had to yield both high intensity radiation and high penetration. The chemical complying with basically all cited requirements is Decahydronaphthalene ($C_{10}H_{18}$). The index matching agent was Hexane (C_6H_{14}) as had been outlined in section II.2.1.1. The concept of visualization in connection with the 'photochromic' dye — which is a chemical that consists of complex molecules -- is to excite the dye molecules dissolved in the working fluid with an energy input which is, for instance, implemented by a laser. The molecules are twisted by the applied energy; in this state the chemical changes color which can be made visible by exposing it to regular white light. As soon as an excited molecule releases its energy by assuming its original shape it loses its ability to 'reflect' the blue in the incident white light.

For the experimental series, excitation of molecules was mainly achieved at the throat of the fluid reservoir (quartz chamber head, Figure II.2.1a) by a focused laser beam (excimer laser, 308 nm) which produced coloration in the dye by pulsing at a rate of 100 Hz. Since the valve is made of quartz the applied laser beam excites fluid particles in two planes on either side of the valve which are 180° apart in circumferential direction.

With respect to the pictures in Figure IV.1.1, the laser beam enters from the right side and is partially absorbed by the dye, generating a higher level of intensity on the respective side of the cylinder. Prior to its application to the engine throat, part of the laser beam's energy was split off, focused, and passed vertically through the piston head at the cylinder axis of the engine. An incandescent light bulb provided the white light that visualizes the excited molecules. Between light bulb and engine cylinder a rectangular piece of white glass was installed in order to diffuse this white light more evenly over the test area. The photochromic lifetime of the chemical is of the same order as the time necessary for one realization of an induction stroke, so that all phosphorescence generated during the induction stroke fades before the beginning of the next engine cycle, allowing data to be taken in a reciprocating manner.

Results of the flow visualization experiments were recorded by the Hi-8 Canon L1A camcorder. There was no controlled timing between the camera and the engine rig. The camera took pictures of the flow field at its standard 30 Hz sampling rate. From the video, the start and the end of the induction stroke can be determined by observing piston motion, and with the knowledge of the data sample rate the engine speed can be evaluated and the individual images can be assigned to crank-angles. Due to the low intensity level of the reflected blue light from the 'indirect' (direct laser light prepares the molecules for excitation) white lighting, the exposure time had to be set at 33.33 ms (i.e. shutter of camera was open) to compensate for the low intensity level, thus valuable results could only be obtained at very low engine speeds (1.5 RPM) -- for low engine speeds the fluid dynamics of the flow field are associated with large time scales. At higher engine speeds these long exposure times yield fuzzy images.

Although the engine speed of 1.5 RPM which corresponds to 25.5 RPM in air is too low to be considered relevant to practical engine research, the results at this speed have, nonetheless, shown some relevance. In particular, even at this low speed the overall flow structure, incorporating vortex rings and toroidal recirculation patterns, was found to be

the same as at higher engine speeds (see results from employment of fluorescent dye at 20 RPM engine speed in section IV.2 and of LIPA in chapter V). One major reason why the results of the experiments with the photochromic dye at this low engine speed will be discussed is that in the experiments employing the photochromic dye information of the flow will be available throughout the entire induction stroke and within the whole engine cylinder which is not the case in connection with the application of the fluorescent dye. The photochromic experiments were conducted using a line of laser light above the valve to mark fluid particles, whereas the fluorescent dye experiments were conducted using a sheet of laser light (see section IV.2). This leads, in connection with the photochromic experiments, on the one hand to illuminated flow within the entire engine cylinder, and on the other hand to higher contrast between illuminated and non-illuminated phases of the flow field.

IV.1.2 Flow visualization results

The experiments with the photochromic dye unveil flow structures of the flow field during induction at 1.5 RPM engine speed that are similar to those discovered by other investigators at a diverse range of engine speeds. All investigators found the global structure of the flow field during intake to consist essentially of two toroidal recirculation patterns. One recirculation pattern occupies most of the cylinder volume (main toroidal recirculation pattern [TRP]), the other rotates in the corner between cylinder wall and cylinder head (upper corner toroidal recirculation pattern). The latter is smaller and rotates in the opposite direction when compared to the main pattern. The results of the flow visualization experiments with the photochromic dye, an example of which is shown in the pictures of Figure IV.1.1, document the genesis of these features, as well as their role and significance in the development of the flow field as a whole.

However, beyond the results of all investigations on flow visualization in axisymmetric engines known to the author and mentioned in the introduction, this technique can obtain a coherent picture of the flow field incorporating diverse flow structures on much finer scales than has been previously available. **For instance**, the roll-up of the vortex rings of the incoming jet as encountered in annular jet flows and described in section I.1 of the *'Introduction'* has, to the knowledge of the author, never been visualized before in engine research and can be seen in Figure IV.1.1. The toroidal vortex rings start to shed from the axisymmetric intake jet at about 30° crank-angle (Figure IV.1.1d, Re=158). **Furthermore**, Regan et.al. (1987) mention in passing that the angle under which the intake jet enters the cylinder (induction angle) oscillates between 10° and 70°. In the experiments using the photochromic dye a variation of the induction angle is clearly perceivable: At first the angle inclines towards the cylinder axis due to the accelerating piston (Figure IV.1.1a-e); the jet is then pushed back towards the cylinder head when the main recirculation pattern visibly gains strength (a quantification of the fluctuation of the induction angle will be given in section V.1.2). **Moreover**, it can be observed, especially for the 3 mm valve lift case shown in Figure IV.1.1, that what is referred to as toroidal recirculation pattern in the upper corner between cylinder head and cylinder wall can only be called a recirculation pattern after midstroke. Before midstroke the flow does not recirculate in the upper corner. A confirmation for this circumstance is attained in section V.5 when the intake jet is examined in more detail. **Also**, a distinguishable lump of dye could be followed visually in one recorded engine cycle as it enters with the intake jet, then rotates with the upper corner TRP, subsequently joins the main recirculation pattern and finally ends up in a 'buffer' area (for more detail on the 'buffer' area refer to section V.1.1) above the piston head indicating that a fluid particle is not constrained to one particular flow structure, and hence confined to the region of that structure's evolution, in the flow field.

For a detailed description of the initiation of flow patterns and continuance of their development for the entire engine stroke, the reader is referred to section V.1.1 where for 20 RPM engine speed and 3 mm valve lift the flow structures encountered during intake are presented in terms of maps of velocity vectors. The description includes the evolution of the main recirculation pattern.

During the examination of the flow, an interesting vortex structure was observed: A slim vertical vortex located at the cylinder axis and with its 'foot' or 'base' on top of the piston head. Due to its visual appearance it was named a *tornado* vortex. The tornado can be seen in Figure IV.1.1f through i. The vertical laser beam through the piston head was implemented so as to visualize this tornado. According to observations, the rotating tornado appears to be generated by a slight asymmetry of the annulus intake jet flow due either to a non-perfect axisymmetry of the geometry of the model configuration (for example, slight misalignment between the axes of valve and cylinder causes asymmetry), or, possibly, an asymmetry in the growth rates of the instabilities forming at different azimuthal positions. The tornado starts spinning as soon as the perimeter of the non-axisymmetric main recirculation system reaches the cylinder axis at any circumferential position θ; in the case of the pictures in Figure IV.1.1 this occurs at a crank-angle of about 53° (IV.1.1f). The spinning continues throughout the intake stroke indicating that the vortex is stable for the entire intake stroke. To quantify the tornado, its number of rotations was counted for different engine speeds and valve lifts. Interestingly, it turns out that the number of rotations stays constant for all cases at about 6 per induction stroke realization; a definite rotational direction could, however, not be assigned for the tornado. The constant number of spins performed by the tornado during induction means that the vorticity of the tornado increases proportionally with increasing engine speed. The evaluation of the number of rotations of the tornado, however, was a very crude determination of spins by eye and the result has to be treated with caution. LIPA studies

of the horizontal plane should depict and quantify the tornado. Eaton and Reynolds (1989) observed a similar ('spiral') vortex in their flow visualization experiments in an axisymmetric configuration at 1000 RPM in air between crank-angles 72° and 87°.

With these flow visualization results (Figure IV.1.1) it is possible to study axisymmetrical aspects of the toroidal intake jet for the two-dimensional plane considered. It can be asserted from this study that at an engine speed of 1.5 RPM the two parts of the intake jet which are 180° apart in the circumferential direction and visualized by experiments, exhibit axisymmetry with respect to the overall behaviour of the incoming annular jet (for example shedding of secondary vortices, induction angle, etc.), however, show considerable differences in size of flow structures and timing of fluid dynamical events. The reasons for these asymmetries are mentioned above. They can never exist in results stemming from the application of numerical or analytic models to (potentially) axisymmetrical flow fields.

In general, fine scale structure can be distinguished easily for the 1.5 RPM engine speed, especially during the early intake phase and in the region of the intake jet, throughout the whole induction stroke. A vortex ring created by the annulus jet flow on the side of the jet facing the main recirculation pattern, for example, can be pursued by eye from its genesis to its collapse (this can be done because the photochromic dye has such a long excitation time, and allows Lagrangian information to be obtained). Vortex rings roll up at the interface of the intake jet with the surrounding fluid, grow, mix with the main TRP, deform, and eventually are embedded and merged with the TRP where entrainment is indicated by the fact that the dye depicting the vortex structure dissolves entirely. This process essentially represents the large scale mixing that takes place during the intake stroke.

The entrainment of an expanding vortex ring into the main recirculation pattern can be seen in some particular cases as a source of an *imm*ediate supplement of angular

momentum to the main TRP -- as opposed to the overall source emanating from the inbound turning of the inducted flow along the cylinder wall (see section V.1.1). In order to investigate how an immediate supply of angular momentum (that is stored in a vortex ring) to the angular momentum of a TRP can be achieved, the video sequence visualizing the intake jet for a valve lift of 6 mm (not shown in this work) was thoroughly analyzed and the following fluid dynamical mechanism could be observed: Qualitatively, the vortex rings formed by the intake jet for 6 mm VL sustain their angular momentum -- acquired as the intake jet convects downstream -- after the impact of the jet on the cylinder wall and distribute their rotating motion in the TRP by expansion of their volumes in radial direction.

After thorough analysis of the flow visualization results for all valve lifts examined it turns out that the contribution to the angular momentum of the TRP stemming from the integration of the angular momentum of vortex rings seems -- at this low speed -- to be strongest for the 6 mm valve lift case. For 3 mm VL this effect is observable as well; however, the majority of vortex rings get destroyed before they can contribute their angular rotation to the main TRP.

At 9 mm valve lift the vortex rings are not fully developed before the intake jet turns at the cylinder wall and thus, the observer does not see the effect of the coupling of the vortex rings with the recirculation pattern as clearly. It can be observed in the flow visualization pictures that the expansion of the vortex rings created in the case of a 9 mm valve lift is suppressed by the rotating motion of the two recirculation patterns to either side of the intake jet. For 9 mm VL the intake jet has its momentum most widely distributed of the three cases examined due to the lowest centerline intake jet velocity at the orifice, thus transferring the least amount of momentum onto its shedding vortex rings. Therefore, the vortex rings associated with a 9 mm VL are more susceptible to effects of the boundary conditions.

It would be very interesting to achieve the same visualization quality -- that enables the experimentalist to trace vortex rings -- at higher engine speeds in order to document the history of vortex rings and evaluate their behaviour as they develop with the incoming annular jet in regard to their contribution to the main recirculation pattern. A study at higher RPM is presented in the next section.

IV.2 Results from Application of Fluorescent Dye

Experiments with fluorescent dye were conducted at 20 RPM engine speed, corresponding to 340 RPM in air, and a valve lift of 3 mm. The dye used was 'fluorescein', and the fluid was water mixed with KSCN, to refractive index match water to the quartz apparatus. Fluorescein dye emits, upon excitation by a source of energy, electro-magnetic waves in the green range of the electro-magnetic spectrum of waves. The lifetime of green emission -- fluorescein being a fluorescent dye -- is of the order of the time interval during which the energy source is applied. The source of energy was for this series of flow visualization experiments a sheet of laser light. The laser employed was the excimer laser at 308 nm wavelength (UV, XeCl); recall that the time for one laser pulse -- and thus approximately the time of fluorescence -- is 17 ns. The sheet of laser light is spanned by focusing the rectangular laser beam with a cylindrical lens to the site of investigation; it intersects the axis of the engine cylinder. The sheet enters through the right wall (when considering Figure IV.2.1), explaining areas of local overexposure of the film in the near-wall region to the right of the cylinder axis. The fact that the fluorescent molecules emit the electro-magnetic waves of the applied laser energy source results in a higher level of illumination when compared to the case of the photochromic dye in section IV.1. The lifetime of the chemical (or the temporal window for the application of the laser sheet) is here equal to the effective exposure time of the imager system, independent of the time the shutter of the camera is in an open state. Flow visualization experiments could therefore

be conducted at higher speeds since short exposure times in connection with a high level of photoluminescence guaranteed that fine flow structures could be resolved.

Flow visualization results were captured by a Photo-Sonics 4ML 35 mm movie camera (series 2000). The rate at which frames were recorded was 60 Hz achieving a resolution of 2° crank-angle for 20 RPM engine speed. The camera triggered the laser externally in order to ensure that the entire illumination radiated from the scene was sensed by the film. The medium used for storage of the visualization information was an ASA 1000 color slide film (E6 process). The actual time the film was exposed to the scene of the evolving flow field was 1.89 ms per frame.

Following are the revelations of flow structures as visualized by two different realizations of flow visualization experiments employing fluorescent dye, each of which consisting of a different mode according to which flow marker were supplied to the site of investigation.

IV.2.1 Flow visualization Mode I

Data acquisition was performed as follows: The engine cylinder was filled with a pure index matched water/KSCN solution prior to the start of piston motion, and the reservoir above the (closed) valve was filled with an index matched water/KSCN solution in which fluorescein was dissolved thoroughly. At the beginning of piston motion marking the initiation of the intake stroke the valve was opened and fluid from the reservoir was able to enter the cylinder. In chemical terms there is a two-phase flow where only one phase is optically sensitive to an energy input so that upon excitation the incoming jet flow can be distinguished from the non-sensitive fluid in the cylinder. Fluid dynamically, on the other hand, the fluid consists of only one phase since the concentration of the dye is negligibly low (10 drops from a pipette into 800 ml aqueous KSCN), hence fluid dynamical mixing

of the two chemical phases is neither inhibited nor encouraged by concentration differences.

The disadvantage with the visualization technique involving the fluorescent dye in an application according to the concept described above is that after a certain crank-angle the concentration of the dye in the cylinder becomes so high that the contrast between the fresh incoming fluid and its surroundings, especially in the region where the toroidal recirculation pattern rotates, becomes too low to resolve flow structures comfortably.

Since the approach with the fluorescent dye is Eulerian the images recorded can be regarded individual 'snapshots' of the flow field, i.e. it is not possible to follow one particular fluid particle as it convects in the flow. These snapshots are exhibited in Figure IV.2.1. In Figure IV.2.1a a sheet of light can be discerned that spreads on top of the piston head. Leakage of dye through the closed valve prior to piston motion settles on top of the piston (quartz on quartz does not provide superior sealing). This fluorescent chemical illuminates upon excitation by the laser and results in the sheet of light above the piston head.

For early intake the images in Figure IV.2.1 confirm the revelations of flow field structures attained from the experiments with the photochromic dye discussed in section IV.1.2. The images exhibited by this higher engine speed (20 RPM) -- featuring the creation of coherent vortex rings by means of a roll-up of fluid at the boundary between incoming jet and ambient fluid, the fluctuation of the angle under which the incoming jet enters the engine cylinder, the impingement of the intake jet on the piston head, the formation of the main toroidal recirculation pattern, and so forth -- support the statement made in section IV.1.1 that the basic overall characteristics of the flow fields at 1.5 and 20 RPM are fundamentally identical. Differences can be found however, in the time scales for the onset of the waviness of the incoming annular jet, and the time at which vortex rings begin to shed from the edge of the jet.

The abovementioned sheet of light spread on top of the piston head can naturally serve as flow marker as well. One can observe this illuminated sheet as it gets compressed to a lump of fluid located at the cylinder axis by the generation of the main toroidal recirculation pattern which is supplied with momentum by the incoming jet. Interestingly, through crank-angles 16° to 32° for which the sheet of light can be discerned as it gets compressed (Figure IV.2.1b-e), there is at the cylinder axis no motion in negative z - direction (towards the valve) relative to the piston head. The accelerating downward motion of the piston seems to, for early intake, balance at every moment the upward motion forced upon by the rotating recirculation pattern.

The vortex streets encountered in the experiments at 20 RPM engine speed have strong resemblance to the vortex streets visualized by Dahm et.al. (1992; case U_o/U_i=4.16 and Re=1133) and Rockwell and Niccolls (1972; for Re=5220) if one filters out -- for the incoming jet as encountered with the engine examined in this study -- low frequency instabilities, i.e. waviness, of the jet about the jet axis which are assumably due to geometrical constraints, and thus pressure gradients imposed by the engine model.

IV.2.2 Flow visualization Mode II

For the pictures in Figure IV.2.2 the same experimental procedure as described in the preceding section had been employed with the exception that the aqueous KSCN solution containing the fluorescent dye was in the engine cylinder and the pure water/KSCN solution was in the fluid reservoir. This method yields lower local concentration peaks of the dye at the beginning of the intake stroke -- thus, the intake jet is not overexposed by the laser sheet as it was the case for 'Mode I' after a few degrees of crank-angle -- and, therefore, results in higher contrast images for a greater range of crank-angles. Consequently, the flow structures (e.g. the vortex street of the jet) can be visualized in

greater detail, and information of the flow field is available until about midstroke
(90° crank-angle).

In addition to the results obtained from 'Mode I', one can get, by employing 'Mode II',
an improved qualitative perception of the order of axisymmetry exhibited by the flow field
of the induction stroke by comparing size and orientation of individual toroidal vortex
rings -- that are created by instabilities experienced by the intake jet -- in different planes
(see sequence of the pictures in Figure IV.2.2). As definition for a measure of the level of
axisymmetry of an annular intake jet one can thus use the degree of similarity between
'two' corresponding vortex rings separated circumferentially by 180° (to the left and to the
right of the valve in the examined plane). According to this measure, axisymmetry is
established quite well at some crank-angle positions of the piston as can be substantiated
from the images in Figure IV.2.2; namely at CAs 24°, 28°, and 32°.

When comparing Figure IV.2.2f and g at crank-angles 28° and 32° one perceives very
congruent flow patterns for the intake jet to the right side of the cylinder axis. The
difference in CA is 4° which corresponds to a time interval of 33.33 ms. A typical velocity
for a fluid particle moving along with the intake jet is 2 m/s for this particular setting of
engine parameters, as will be shown in chapter V. This means that for a time interval of
33.33 ms the jet convected about 70 mm. If, in a mental experiment, the two images for
28° and 32° CA in Figure IV.2.2f and g are thought of being superimposed, the evaluated
distance of 70 mm matches roughly the distance between the center of the vortex ring at
28° CA that is just developing on the side of the jet that faces the corner between cylinder
head and wall, and the center of the second (geometrically with respect to the valve)
vortex structure at 32° CA facing the corner as well. The fact that the calculated distance
matches the one found in the images implies that the latter vortex structure (at 32° CA) is
the vortex structure that matured from the one that can be perceived as just being
developing at 28° CA. Intermediate information available at 30° crank-angle (but not

included in Figure IV.2.2) strongly suggests the aboveoutlined assertion. Very similar statements can be made for the development of the flow field between crank-angles 32° and 36°. Note, however, that whereas there is a certain degree of congruity for the vortex structures in the annulus intake jet at 28° and 32° CA to the left side of the cylinder axis there is hardly any affinity for those at 32° and 36° crank-angle. It can be concluded from the above discussion that it is possible to use the time interval of 33.33 ms as a typical time scale for the development of vortex structures in the crank-angle range between 25° and 40°.

As far as size, and in this context a typical length scale, of the vortex structures is concerned one has to be careful in an attempt to just measure the extent of dye representing vortex rings and to use this measure as characteristic length scale. As mentioned in the beginning of section III.3 diffusion processes in conjunction with mass -- $\delta_D \sim (Dt)^{1/2}$ -- are of much lower order of magnitude than diffusion processes in conjunction with vorticity -- $\delta_v \sim (vt)^{1/2}$. Thus, the area of fluid dynamical influence by a vortex structure that is shed from the intake jet extents further in ζ - direction than is indicated by the dye (for a definition of ζ refer to Figure V.2.4). Nevertheless, the size of vortex ring structures have been evaluated for crank-angle 36° from the image in Figure IV.2.2h since it can be shown that the spread of vorticity is proportional to the spread of mass, namely $\delta_v \sim (Sc)^{1/2} * \delta_D$ where Sc is the Schmidt number of the problem. In Figure IV.2.2h the flow field at 36° CA (Re=2476) exhibits (on the 'left' side with respect to the cylinder axis) a singular flow structure, incorporating two counter-rotating vortex rings, that appears separated as a coherent flow pattern. From this pattern typical dimensions of secondary vortices have been inferred. The diameter of the smaller vortex is 2.4 mm, the diameter of the larger vortex (this vortex was generated earlier in time than the smaller vortex which then got knitted together into this particular, coherent flow pattern) is 3.6 mm. The distance between the axes of the two vortex rings is also 3.6 mm.

An interesting flow visualization technique had been unintentionally applied in addition to the one based on fluorescence: Because the cylinder axis of the water analog model was not exactly parallel to the direction of gravitation, an air bubble was formed at the cylinder head when the cylinder was filled with the $H_2O/KSCN$/fluorescein solution (this bubble disappears of course during engine performance in LIPA experiments). The air bubble gets entrained into the jet at some crank-angle during the intake stroke and disperses into smaller bubbles. These small bubbles serve as flow marker in the flow field. Due to the buoyancy of the air bubbles it can be expected that they are forced to the low pressure center of the main toroidal recirculation pattern. Figure IV.2.2k verifies this prediction; it shows the air bubbles accumulated where the center of the main TRP is located (for a qualitative evaluation of the location of the center the reader be referred to section V.1.1).

IV.3 Comparison of Flow Visualization Results at two different Engine Speeds

Flow fields of the induction stroke of a water analog model were evaluated in the two preceding sections from visual information at two different engine speeds, 1.5 RPM and 20 RPM. Although the overall fluid dynamical behaviour of the induction flow is alike for the two engine speeds, there *are* significant differences in the presentations of the flow fields during intake as displayed in Figures IV.1.1 and IV.2.2.

At 16° crank-angle, for instance, the annular intake flow at the higher engine speed exhibits advanced waviness and vortex shedding, Figure IV.2.2c, whereas the intake flow at the low speed can be seen to consist of a straight propagating free jet, Figure IV.1.1a. The incoming flow is much more unstable and complex during early intake at 20 RPM engine speed. Single flow structures at the head of the jet separate which is not the case in conjunction with the low engine speed where the head of the jet forms a whole complex and coherent structure (like a classical 'starting jet').

For 20 RPM engine speed the angle under which the intake jet enters the cylinder (induction angle) inclines closer towards the cylinder axis than the induction angle at 1.5 RPM. The reason for this is that the higher piston speed in the case of the 20 RPM engine speed induces a higher pressure gradient between the piston head and the cylinder head. At the 1.5 RPM engine speed the recirculation pattern that builds up between the intake jet and the cylinder wall (Figure IV.1.1c and d) is much more developed, and contains much more energy during early induction than the main recirculation pattern.

The more rapid rate of spread of flow structures in connection with the intake jet for the 20 RPM case results in the flow field developing much earlier than for 1.5 RPM. For instance, for 20 RPM engine speed the main toroidal recirculation pattern is taking shape already at 32° CA (Figure IV.2.2g; see also Figure IV.2.1e) and its extension almost reaches the cylinder axis implying that the tornado will start spinning shortly after 32° CA. At this crank-angle the main TRP for 1.5 RPM is not yet developed. Recall that for 1.5 RPM the generation of the tornado occurs at about 53° CA.

The size of the vortex ring structures enforced by the two engine speeds is essentially equal as can be expected for identical nozzle width and constant diffusion coefficient D.

Since an engine speed of 1.5 RPM is a very unrealistic case in the field of engine research, the results of employing photochromic dye will not be discussed further. However, it should be emphasized that overall fluid dynamical behaviour and establishment of flow structures as encountered at this low speed was similarly observed in the experiments where a fluorescent dye has been employed (20 RPM engine speed; as discussed in section IV.2) and will be similarly encountered in the maps of velocity vectors describing flow fields evaluated by LIPA (chapter V; 10, 20 and 30 RPM engine speed) establishing the relevance and legitimacy of the discussion of fluid dynamical results at the low engine speed.

On the basis of results on vortex ring dynamics described in section IV.1.2 one could speculate that the essential difference between flow fields at small and large valve lifts as well as at low and high engine speed is based on a mechanism set forth by the instability of the annular jet flow, i.e. the roll-up and successive break-down of the vortex rings. Partial prove for support of this hypothesis will be provided by quantitative fluid dynamical parameters given in section V.2.3.

Chapter V
SCIENTIFIC FINDINGS IN RESEARCH OF ENGINES
OBTAINED FROM LIPA - DATA

The following sections contain results on fluid dynamics during induction of a water analog model that were obtained from the reduction of data acquired with LIPA.

Firstly, the induction stroke as a whole will be discussed with the employment of the 'whole cylinder' investigation grid. This study comprises sections V.1 through V.4. In sections V.1 to V.3, the development and characteristic features of the flow field in the induction stroke of an axisymmetric water analog engine will be outlined based on the projections of the three-dimensional field of velocity vectors onto the two-dimensional imaging plane of the camera. Several fluid dynamical parameters will be defined in the text which will serve to differentiate between flow fields induced by different settings of engine parameters (engine speed and valve lift). A new hypothesis will be disclosed which will help to examine the flow field of the induction stroke in a more focused way. In section V.3 an attempt is undertaken to separate the influences of cycle-to-cycle variability and of turbulence inherent in the flow field as sources for velocity fluctuations. Section V.4 deals with vorticity distributions which are regarded a useful tool for the evaluation of mixing performance.

Finally, in section V.5, by employing a 'denser spacing' version of a grid of laser lines to the area between chamber and piston head when piston is at TDC, the intake jet will be investigated more closely. Superposition of plots of velocity vectors onto corresponding pictures provided by flow visualization confirm two things: there is strong congruity between the fields of velocity vectors depicting structures of the intake flow with results from flow visualization. And secondly, superposition of LIPA - data with flow

visualization results helps to understand the quantitative data: bridging the gap between the very high resolution of dye flow visualization, which does not allow quantification of the fields, and the lower spatial spacing of information provided by the employed laser grid, which could lead to misinterpretation of the features of the flow field.

The main tool to display the flow field of the induction stroke in this chapter will be two-dimensional maps of velocity vectors; velocity vectors being the most immediate results from an application of LIPA. Intrinsically, the plots denote distances and directions that particular fluid particles convected during a certain time interval. To compare plots of convection distances one has to make certain that the underlying time intervals are identical. We will assume that the data imaging system acquired all of the images in the field instantaneously, and thus we will speak of velocities instead of convection distances.

Within a plot the velocity vectors are distributed according to the locations of intersection points generated by the laser grid. In the figures displaying fields of velocity vectors the setting of the plots comprises geometrical elements such as a valve, the cylinder wall, and the piston head for orientation purposes. These plots will be referred to as 'maps of velocity vectors'. Maps of velocity vectors will be utilized in sections 1, 3, and 5 of this chapter. Each figure containing maps of velocity vectors shows a reference vector denoting the magnitude of a vector of 1 m/s, and estimations for errors in each direction (x and z) according to Table III.3.1. The errors are depicted with respect to a magnified velocity vector of 1 m/s.

A less common tool for data representation is a surface or contour distribution of vorticity in a three-dimensional plot. These plots are used to portray mixing performance during the induction process.

V.1 Description of Induction Stroke Flow Field in Terms of Maps of Ensemble Averaged Velocity Vectors

The flow field patterns during induction as represented by maps of velocity vectors at selected crank-angles will be discussed in the following section for an engine speed of 20 RPM (340 in air) and a valve lift of 3 mm (highest Reynolds number at midstroke is equal to 4213). This set of parameters was chosen so that the following results can be compared directly to the flow fields revealed by the visualization technique discussed in section IV.2. The maps of velocity vectors can be regarded a quantification of the qualitative flow visualization results. The velocity vectors in the maps displayed in Figure V.1.1 are ensemble averaged (EA) over 42 engine cycles (EC); I will be referring to these ensemble averaged results when I am speaking of the 'EA domain'. Recall from section II.2.2.4 that memory limitations of the SunWorkstation used for data reduction was the reason for being restricted to 42 ECs. However, it turned out that a data base of 42 engine cycles seemed sufficient since considerable convergence of the fluctuation intensity of the velocity components could be observed (section III.2.1.1).

V.1.1 Genesis and fluid dynamical behaviour of features of the flow field in water analog model

Following is a fairly comprehensive account of the flow characteristics of the induction stroke as can be interpreted from the velocity vector maps in Figure V.1.1.

Prior to piston motion the fluid in the engine is, in the average, quiescent (very low magnitude of velocity vectors, Figure V.1.1a; in fact, from the maps of velocity vectors of individual cycles in section V.3 it will be apparent that there is initial motion in the flow fields prior to piston motion). After the piston moved downwards a certain distance, velocity vectors obtain magnitude and direction and depict motion of the intake jet and its

surrounding. The angle under which the intake jet enters the engine cylinder (induction angle) is, in the beginning of the intake stroke, prescribed by the geometrical shape of the valve. The intake jet impacts onto the piston head and separates into a flow towards (and then up) the cylinder wall, and into a flow towards the cylinder axis (Figure V.1.1d&e; for more information refer also to Figure IV.2.2). The flow towards the axis will, in three dimensions, create the main toroidal recirculation pattern (TRP) mentioned in chapter IV which occupies most of the cylinder volume; the flow up the cylinder wall develops into a toroidal recirculation pattern in the upper corner between cylinder wall and head. (The two toroidal recirculation patterns present themselves as vortices in two dimensions, thus encouraging the author to refer to the main TRP as the *main* vortex as opposed to *upper corner* vortex, alias the upper corner TRP.) Since the intake jet -- carrying linear momentum -- is forced to turn at the piston head and recirculate (main vortex), the linear momentum of the intake jet becomes angular momentum with respect to the examined x, z - plane of the engine cylinder.

One can infer from the sequence of velocity maps in Figure V.1.1 that as crank-angle evolves and thus piston speed increases, the axis of the intake jet inclines towards the cylinder axis until a crank-angle of about 44° is reached and the incoming jet enters the engine almost parallel to the cylinder axis, Figure V.1.1f. (Note that the figure does not clearly show this; one has to envision the intake jet by visually interpolating between velocity vectors #7, 12, and 18, which presumably depict fluid dynamical behaviour of parts of the intake jet; for assignment of velocity vectors refer to Figure II.2.3a.) The reason for the inclination of the jet axis towards the cylinder axis is possibly an increasing pressure gradient between piston and chamber head which is induced by the accelerating piston. (Note that throughout the whole stroke the flow of fluid is governed by the pressure distribution within the engine.) As the momentum of the intake jet increases with increasing piston speed, the supply of angular momentum to the main vortex becomes enhanced. The main vortex grows in extent, degree of structure, and energetic content; at

72° CA (Figure V.1.1j) it assumes a roughly circular shape. As is denoted by the velocity fields in Figure V.1.1g through k, the main vortex which becomes stronger by the continual supplement of momentum starts to push the intake jet back up towards the cylinder head until the induction angle assumes, from 92° CA on, a constant value. The convergence towards this final angle is faster for smaller valve lifts as will be illustrated in section V.1.2 'Profiles of induction angle'.

From crank-angle 72° (Figure V.1.1j) on, a 'buffer' zone is created in the region just above the piston head. In this buffer zone no particular flow structure dominates, nor is there a consistent directional flow when taking 42 individual engine cycles into consideration. Thus, the summation of velocity vectors over these 42 cycles yields in the buffer zone for the EA domain a low magnitude flow field with a random flow pattern. Note, however, that discussed flow patterns are those perpendicular to the piston -- there could be significant swirl velocities. The investigation of the horizontal plane on top of the piston head will yield conclusive data for this matter. The creation of the 'buffer' zone on top of the piston head could be caused by an establishment of a high pressure region above the piston head where the fluid flow along the cylinder wall does not possess the necessary momentum to overcome this pressure gradient as it approaches the piston. Also, curvature effects of the toroidal recirculation pattern are important in the discussion of the creation of the buffer zone. The same time scale encountered for the convergence of the induction angle can be established for the time of initiation of the buffer zone: The smaller the valve lift, the earlier the buffer zone can be observed in the velocity maps.

Based on the velocity maps in Figure V.1.1 a qualitative observation can be stated considering the center of rotation of the main vortex: This center moves with evolving crank-angle down and towards the cylinder wall (in positive z - and x - direction) until about midstroke (90° CA). This result gathered from the velocity maps is in accordance with visual observations made during the LIPA experiments in individual realizations of induction strokes.

After the incoming jet assumed a constant induction angle (about 100° CA,

Figure V.1.1m) the flow field demonstrates a very stable, structured flow in the region of

examination (region spanned by the laser grid). One can almost speak of a 'fully developed'

flow field or of self-preservation of the flow field in the region examined. 'Fully developed'

paraphrases the fact that the orientation of a velocity vector at a particular location in the

EA flow field stays essentially constant throughout the remainder of the stroke, including

the velocity vectors around the axis of the intake jet. It seems that each velocity vector in

the investigated area can be mapped for different crank-angles according to a universal

formula. This holds even true for the case where the velocity fluctuations are highest --

30 RPM (510 in air) and 3 mm VL, see section V.2.2. The center of rotation of the main

vortex stays at one location. It should be recalled at this point that ensemble averaged

results are the subject of analysis here; as will be demonstrated in section V.3 there is no

such thing as a stable flow field in individual engine cycles.

For this fully developed flow field the fresh incoming fluid through the valve flows

tangentially along the periphery of the main vortex and impinges on the cylinder wall. Only

a fraction of the fluid flows up along the wall (negative z), most of the fluid flows down

along the wall (positive z). At a certain point (z - location) the flow along the wall in

positive z - direction turns inward towards the cylinder axis. This 'separation' point is

determined by the assumed -- but meaningful -- existence of an increase in pressure as the

flow approaches the piston head (adverse pressure gradient). This inward turning fluid

flow supplies the main vortex with momentum (this addition of momentum to the main

vortex can be called 'mediate' or 'indirect' supplement as opposed to an 'immediate'

supplement of momentum whose mechanism is described in sections IV.1.2 and V.2.3).

The boundary layer flow along the cylinder wall is confined to a small depth with a small

momentum thickness. As the flow turns towards the cylinder axis the width of the flow

broadens and extends to even more volume as it enters into a region between the center of

rotation of the main vortex and the cylinder axis. (The pattern of the turning and expanding boundary layer flow resembles that of a radial diffuser.) Here, the flow is in negative z - direction (towards the valve). Here, the flow decides whether -- depending on valve lift and engine speed -- to primarily mix the fuel/gas constituents of the flow in a fine scale structured flow field and dissipate momentum, or to primarily conserve momentum, stratify the flow, and redistribute the momentum within the main recirculation pattern. It is this region -- besides the region around the axis of the intake jet -- in which the basic differences between the flow fields enforced by different settings of engine parameters, i.e. engine speed and valve lift, establish themselves through, e.g., characteristic length scales in the flow field and degree of velocity fluctuation. This region which is a sub-area of the main recirculation pattern will be subject to a more detailed investigation and is therefore called 'area of scrutiny' (see Figure V.1.1o for the location and description of this area). Motivation of an investigation of the area of scrutiny is derived also from the fact that it is desired to keep up air/fuel mixing in this region. Note that most of the mixing is established by the intake jet. In the area of scrutiny it is wishful to obtain most improvements.

By studying the intake stroke of an engine using information provided by maps of velocity vectors it was possible to distinguish different regions in the flow field characterized by different flow patterns such as intake jet flow, toroidal recirculation patterns, and boundary layer flow along cylinder wall. This dissection of the flow field will be very helpful for its analysis. Furthermore, the importance of the 'area of scrutiny' was pointed out. In section V.2 this region within the flow field will be examined more closely.

The flow field of the induction stroke of a water analog model as described above using EA velocity vectors for 20 RPM engine speed and 3 mm valve lift is representative for all nine flow fields as enforced by the nine different settings of the engine parameters (Table II.2.3): The flow features such as intake jet flow, toroidal recirculation patterns,

boundary layer flow along cylinder wall, and buffer zone above piston head were encountered as flow structures in all nine flow fields. Differences in the nine engine cases were manifested in the magnitudes of flow quantities, timing of initialization of flow patterns and location of flow structures within the engine cylinder. For crank-angle 132° the nine flow fields are exhibited for the EA domain in Figure V.1.2. These nine flow fields will be the basis for investigations made for the area of scrutiny in section V.2.

For crank-angles 16°, 20°, 32°, 36°, 44°, and 92° (Figure V.1.1b, c, d, e, f, and l) Figure IV.2.2c, d, g, h, i, and k exhibits the corresponding flow visualization results. One can denote profound conformity between the qualitative and quantitative representations of the flow field. The flow field in terms of velocity vectors quantifies the rate and direction of convection of flow structures that are visualized in the images of Figure IV.2.2. These results illustrate the usefulness and potential of a visualization-quantification hybrid technique.

V.1.2 Profiles of induction angle

A more detailed study of the angle under which the intake jet enters the engine cylinder, induction angle α, has been conducted where the induction angle has been evaluated as a function of crank-angle for each element in the matrix of experiments in Table II.2.3. With the help of the results from this study it will be possible to distinguish fluid dynamical behaviour during induction as it is experienced in connection with the different settings of the engine parameters. The basis for the evaluation of the induction angle were the maps containing the ensemble averaged velocity vectors. Although the extraction of the angles was performed by hand and although a considerable uncertainty exists about what velocity vectors do actually represent the intake jet in the maps -- thus, there is a substantial error evoked by this data reduction process -- it should be considered legitimate to infer some trends from the α-vs-CA plots. The results are exhibited in Figure V.1.3. To emphasize

the rather qualitative nature of this set of data a spline fit procedure has been applied to each curve in Figure V.1.3 and the single data events have been omitted.

In general, the incoming jet enters at first under an angle prescribed by geometrical design (45°; observable best for 10 RPM engine speed, Figure V.1.3a). It then inclines towards the cylinder axis, for some engine parameter settings up to 0°. After reaching a local minimum -- the definition of the induction angle α is given in Figure V.1.3 --, the induction angle increases towards a local maximum after which the angle decreases again and assumes a considerably constant plateau value. For 20 RPM engine speed and 3 mm valve lift flow visualization results have been presented in section IV.2.2. If one examines the sequence of flow visualization pictures for this setting of engine parameters in Figure IV.2.2 documenting the induction stroke from its start to midstroke one can observe that the smallest, i.e. steepest induction angle (local minimum) is encountered at about 44° CA (Figure IV.2.2i). This matches exactly the crank-angle found for the local minimum of the induction angle in the maps of the ensemble averaged velocity vectors in the case of 20 RPM engine speed and 3 mm VL (Figures V.1.1f and V.1.3b).

There are two obvious tendencies that can be deduced from the plots in Figure V.1.3. Firstly, the smaller the valve lift, the earlier (crank-angle-wise) does the induction angle reach the abovementioned plateau value. Secondly, the greater the valve lift, the lower is the plateau value. This can be attributed to the fact that the actual mean angle of the induction jet is slightly less as the valve lift increases because the axis of the intake jet is at higher z - coordinates for higher valve lift. However, to a certain extent one can assert that both tendencies mentioned in this paragraph also indicate that the main toroidal recirculation pattern contains more momentum (as will be, in fact, verified in section V.2.2) in the case of a smaller valve lift, thus being able for this configuration to push the intake jet back up faster and higher.

The overall observations for the induction angle in the preceding two paragraphs are independent of engine speed meaning that all the features exhibited by the induction angle profile can be perceived at 10, 20, as well as 30 RPM engine speed; Figure V.1.3a, b, and c, respectively. Tentatively, a distinguishing factor for the three sets of induction angle profiles corresponding to the three engine speeds can be established when a comparison is performed in each set of the difference between the lowest and the highest plateau values towards which the induction angle converges for each considered valve lift. This difference between the lowest and the highest plateau value seems to decreases with increasing engine speed. This can be explained by the fact that as the engine speed increases, the plateau becomes less dependent on the valve lift. One has to be careful in the interpretation of this data though, since the scatter in the data is too large to make definite conclusions.

It should be noted that many of the results outlined in the previous two sections (V.1.1 and V.1.2) have been observed in the flow visualization experiments with the photochromic dye at 1.5 RPM engine speed discussed in section IV.1.2. This illustrates that basic flow field components that are created at an engine speed of 1.5 RPM continue to persist, with quantitative differences, of course, in the investigation of flow fields at higher engine speeds.

V.2 Discrimination of Flow Fields as enforced by different Parameter Settings of the Engine

In order to distinguish flow fields which are enforced by different settings of engine speed and valve lift within the parameter space, three characteristic values were chosen to provide measures to differentiate between the flow fields at 132° crank-angle. These three characteristic parameters have been evaluated in the 'area of scrutiny' in order to establish an understanding of the influence of the parameters engine speed and valve lift. In the area of scrutiny 22 velocity vectors were examined to evaluate the three parameters. The area of scrutiny is circled in the velocity map of Figure V.1.1o.

V.2.1 Definition of parameters

First, the *kinetic energy content* in the area of scrutiny has been determined for each of the nine flow fields. In the EA domain the magnitudes of the velocity vectors do not properly reflect the content of kinetic energy contained in a specific region since positive and negative contributions of velocity components tend to cancel each other out. Thus, an average of the kinetic energy contained in the individual engine cycles in the area of scrutiny has been calculated, with subsequent summation of these averages over the number of engine cycles analyzed and division by the number of ECs. Kinetic energies are scalars, the information on orientation has been stripped from the velocity vectors. The kinetic energy content is evaluated as follows:

$$KE = \frac{1}{\#ECs} \sum_{j=1}^{\#ECs} \left(\frac{1}{N} \sum_{i=1}^{N} |\bar{u}_i|^2 \right)_j \qquad (V.2.a)$$

where #ECs is the number of engine cycles over which the average is taken, N is the number of velocity vectors in the area of scrutiny, namely 22, and u_i is the local velocity.

From the equation it is obvious that a specific energy is being evaluated since KE is normalized by mass.

Secondly, *energy associated with velocity fluctuations* of the z - component has been evaluated for the area of scrutiny (the z - component has been chosen because of the higher accuracy of velocity evaluation in this direction; see section III.3.3), in a similar manner as the kinetic energy, according to the following expression:

$$FE = \frac{1}{\#ECs} \sum_{j=1}^{\#ECs} \left(\frac{1}{N} \sum_{i=1}^{N} \left(u_{z_i} - u_{z_{i,EA}} \right)^2 \right)_j \qquad (V.2.b)$$

where $u_{z,i,EA}$ is the local ensemble averaged velocity in z - direction. Equation V.2.b defines a specific energy as well. Note that the fluctuation energy includes contributions from cycle-to-cycle variability as well as from velocity fluctuations due to turbulent motion of the flow.

Thirdly, a measure for *recirculativity* has been formulated in terms of normalized angular momentum. This measure indicates when applied to velocity vectors in the area of scrutiny to what degree the fluid reenters the main vortex from the area of scrutiny as well as the order of regularity in this area (stratification). The argument goes that if the velocity vectors in the flow field in the area of scrutiny are oriented such that they suggest that the flow stays in an overall circular motion the fluid from the area of scrutiny reenters the main recirculation pattern. Angular momentum was used as parameter to describe recirculativity because it is sensitive to whether or not the flow field is roughly circular about a center. The angular momentum is normalized by local quantities of radius to center of flow structure and velocity magnitude so that only the orientation of a velocity vector with respect to the center of the recirculation pattern would enter the angular momentum evaluation which is performed according to the following formulation:

$$AM = \frac{1}{\#ECs}\sum_{j=1}^{\#ECs}\left(\frac{1}{N}\sum_{i=1}^{N}\frac{r_i\cdot|\bar{u}_i|\cdot\cos\mu}{r_i\cdot|\bar{u}_i|}\right)_j \qquad\qquad\qquad\text{(V.2.c)}$$

where r is the radius from the center of the recirculation pattern to the local velocity and

μ is the angle that the local velocity vector forms with a line that is perpendicular to the

radius. Recirculativity equal to 'one' corresponds to a circle.

V.2.2 Information about different flow fields in terms of defined parameters

A compilation of nine maps of velocity vectors -- one for each engine parameter setting

-- each at a crank-angle of 132° can be seen in Figure V.1.2. The velocity vectors are

ensemble averaged. For 30 RPM engine speed the analysis was based on 63 engine cycles,

for 20 RPM engine speed 42 engine cycles were considered, and for 10 RPM 21 ECs as

mentioned in section II.2.2.4. At a first approximation by eye one can readily detect

differences between the nine flow fields in the area of scrutiny in orientation and

magnitudes of the velocity vectors. In order to achieve objective qualitative measures that

unambiguously classify the flow field the above defined parameters (equations V.2.a

to V.2.c) were applied to velocity information from the nine sets of data in the area of

scrutiny.

The results of the evaluation of the parameters are plotted in Figures V.2.1 to V.2.3.

From Figure V.2.1a where the specific kinetic energy contained in the area of scrutiny for

132° CA is shown in a single logarithmic plot in dependence of the valve lift for three

different engine speeds it is evident that the kinetic energy content in the area of scrutiny

decreases -- non-linearly -- with increasing valve lift for constant engine speed. It also

increases with increasing engine speed for constant valve lift as can be seen in

Figure V.2.1b where the same data as available for Figure V.2.1a are plotted as a function

of engine speed in an arithmetic coordinate system. These curves are as expected since one anticipates that the momentum carried by the incoming annulus jet flow and transported to the area of scrutiny increases with engine speed. This relation (engine speed ⇑ ⇒ momentum ⇑) established from Figure V.2.1 receives support from an analytical calculation by Miller and Comings (1957) as well as from Tennekes and Lumley (1972) who reduced the Reynolds equation in streamwise direction for two-dimensional jet flow -- two-dimensional jet flow is a very reasonable approximation for the annulus jet flow encountered in this research project. The formula the Reynolds equation was reduced to is, for momentum flux J in the direction of the flow, in the notation of Miller and Comings,

$$J = \rho b U_c^2 \qquad\qquad\qquad\qquad \text{(V.2.d)}$$

where b is the opening of the nozzle, and U_c is the velocity at the centerline.

Figure V.2.1a contains for each of the nine data points an indication (bars) of how much the specific kinetic energy fluctuates over the respective number of engine cycles analyzed. The bars denote RMS fluctuation. The bars include errors due to mis-calculation of velocity vectors from the area of scrutiny and can thus serve as a rough indicator for system error. It can be noted that Figure V.2.1a shows that there is no 'overlap' between the curves representing the kinetic energy for the three different engine speeds, i.e. the values for 9 mm VL for 30 and 20 RPM are higher than those for 3 mm VL and 20 and 10 RPM, respectively, even when considering the bars that denote error estimations. In Figure V.2.1b the non-linear behaviour for the kinetic energy with respect to engine speed becomes obvious. The increase of kinetic energy with engine speed is similar for the 6 and 9 mm valve lift cases. For 3 mm valve lift this increase is more emphasized.

The curves of the specific energy associated with velocity fluctuations in the z - direction for the area of scrutiny at 132° CA are exhibited in Figure V.2.2, also in a single logarithmic plot. The curves strongly resemble those of the kinetic energy discussed in the

previous paragraph and displayed in Figure V.2.1a, however, on this (different) logarithmic axis. As a rule of thumb one can establish that the energy associated with velocity fluctuations of the z - component is about one tenth of the kinetic energy. Keep in mind that the velocity fluctuations discussed here include cyclic variations of the bulk flow as well as velocity fluctuations due to turbulent flow within individual engine cycles. It can be speculated at this point that after separation of the cycle-to-cycle velocity fluctuations from those caused by turbulent motion of the flow, the trend suggested by Figure V.2.2 for velocity fluctuations in general, namely that velocity fluctuations increase with engine speed as well as with decreasing valve lift, holds true for the velocity fluctuations due to cycle-to-cycle variability. From Figure V.2.2 it can then be argued that the low velocity fluctuations at high valve lifts are an indication that due to less cycle-to-cycle variability the flow field in an engine is more predictable for large valve lifts. It can also be speculated using the information provided by the curves in Figure V.2.2 that the turbulent energy is higher in connection with the smaller valve lifts implying that enhanced mixing of fuel/air phases can be achieved at smaller VLs. However, a confirmation of these speculations has to be furnished on the basis of further analysis of the velocity fluctuations.

Figure V.2.2 also contains bars indicating the variation of the specific velocity fluctuation energy with engine cycle. With one exception these 'error' bars do not overlap for different engine speeds at the three valve lifts indicating that the tendencies suggested by the curves are considerably accurate.

In Figure V.2.3 the normalized angular momentum evaluated in the area of scrutiny as a measure for the recirculativity is plotted versus valve lift for 132° crank-angle. Each point symbolizes an average for the angular momentum over a crank-angle window of 10° and an average over a certain number of engine cycles. For the evaluation of the values in Figure V.2.3 a center of rotation had to be assigned. Interestingly, it turned out that considering the accuracy achievable with the given spatial spacing of intersection areas in

the investigation grid the center of rotation moves only marginally when the setting of engine parameters changes.

The curves in Figure V.2.3 illustrate for 10 and 30 RPM engine speed that the recirculativity increases with increasing valve lift and decreasing engine speed. The slope of increase with valve lift is steeper in conjunction with 30 RPM engine speed than with 10 RPM. For 20 RPM engine speed the available data points do not fall into a scheme suggested by the results for the other two engine speeds. After reading section V.2.3 the difference to the other two curves will become clear.

High recirculativity, if it is expressed in terms of normalized (by local quantities of radius and velocity magnitude) angular momentum, means high regularity and degree of order of the flow field (circular flow). Thus, it can be inferred from Figure V.2.3 that for 9 mm valve lift the flow field in an engine exhibits highest degree of regularity and the fluid in the area of scrutiny is most likely to reenter the main recirculation pattern. At 9 mm VL rotation information is preserved. Note that a high degree of order expressed by the flow field implies stratification of the flow field and thus inferior mixing performance. On the other hand high degree of order (structure) enforces higher cycle-to-cycle predictability which is why high recirculativity for large valve lifts will be a key to explain the lower velocity fluctuations for 9 mm VL found in Figure V.2.2. For 3 mm valve lift recirculativity suggests that the flow field in the area of scrutiny is least structured and the fluid is least likely to reenter the TRP. With decreasing engine speed the likeliness of recirculation increases.

These statements, arrived at by interpreting the plot denoting recirculativity for different engine parameter settings (Figure V.2.3), can be confirmed by closer examination of the maps of EA velocity vectors in Figure V.1.2.

A hypothesis will be presented in the following section which elucidates a relation between the physics of the annulus intake jet flow and the trends of the curves of

recirculativity as well as the curves denoting energy associated with velocity fluctuations -- which are representative measures for a flow field in the area of scrutiny.

V.2.3 Discussion of the correlation between intake jet flow and the fluid dynamics of the intake stroke with special reference to the area of scrutiny

In order to explain the low fluctuation energy and the high degree of recirculativity associated with large valve lift and the high fluctuation energy and the low degree of recirculativity associated with small valve lift the fluid dynamical process as a whole as well as bilateral associations between flow structures have to be considered and evaluated.

As has been pointed out in section IV.1.2 for low engine speed (flow visualization results with photochromic dye) the supply of angular momentum to the area where the main toroidal recirculation pattern 'dwells' is imparted *imm*ediately by convection into this volume of vortex rings that shed from the annulus intake jet on the side facing the main TRP and that have the same sense of rotation as the TRP. The mechanism that communicates the angular momentum of the vortex ring with that of the TRP can be regarded as a kind of superposition of the toroidal axis of the vortex ring with that of the main recirculation pattern (Figure V.2.4); it can be described as pairing of two vortical structures that have infinite extension in their axial direction. Presupposition for this ingestion of one vortical structure into another to take place is that the coherent vortex rings on the one hand contain a considerable amount of angular momentum, and on the other hand are not yet broken up and dispersed into small scale, incoherent turbulent motions, an occurrence that takes place after the incoming jet has convected a certain distance (see next section as well as the '*Introduction*'). To determine the characteristics of a toroidal vortex ring when the incoming annulus jet turns at the cylinder wall a study of annulus jet flow shall be undertaken.

V.2.3.1 Review of background of annulus free jet flow

Various investigations on two-dimensional, planar, or annulus free jet flows can be found in the literature of which some have been briefly reviewed in the *'Introduction'*. Following is a quick summary on the physics of annular jet flow: An annular jet entering ambient, quiescent fluid stays a stable jet with its core exhibiting potential flow for very low Reynolds numbers (Re). With increasing Re, instabilities of the jet flow arise. The jet first starts to propagate in a wave-like shape of long wave-length. With further increase in Re 'secondary' vortices start to roll up at the interface between the jet and its surrounding. These vortex rings entrain fluid from the jet's surrounding, gain strength and extent as the jet flow proceeds downstream and, eventually, break up. Over the distance between the entering of the jet into the ambient fluid until the burst of the vortex rings the flow is named 'transitional' (Yule 1978; see Figure V.2.5). After their break-up the vortex rings create small scale, incoherent eddies (small vortical structures) in a what is now called 'turbulent' flow. According to the investigations on free jets the length of the transitional flow -- the end of the transitional flow coincides essentially with the termination of the potential core flow of the annular jet -- varies with Reynolds number and width of the nozzle at which the jet enters. The length of transitional flow has been evaluated for annular jets to be approximately between 6 and 8 times the width of the nozzle (for Reynolds numbers in the range of 1000 to 2000). This implies for the case of an induction flow of an engine that the break-up of the coherent vortex rings which initiates turbulent flow motion within the intake jet occurs further downstream for larger valve lift at constant engine speed (the Reynolds number is approximately constant with constant engine speed and varying VL).

Another important issue is the size of the vortex rings that are created by the intake jet. Vortex ring structures initially scale with the width of the nozzle at which a free jet enters ambient fluid as can be confirmed by the flow visualization experiments from chapter IV.

In the context of vortex ring ingestion into the main TRP it seems intuitively appealing that the larger vortex ring structures are more favorable to merge with the main toroidal recirculation pattern by superposition of their axes -- in the cases where the vortex rings reach the cylinder wall -- since the length scale of their structures is closest to the length scale associated with the main recirculation pattern.

V.2.3.2 Application of knowledge about annular free jet flow to fluid dynamical aspects in engine

Let us consider the following case: If for a certain combination of engine speed (Reynolds number) and valve lift the vortex rings associated with an incoming jet just do not burst when the jet reaches the cylinder wall the contribution of angular momentum of the vortex rings to the main toroidal recirculation pattern will be maximum. This is the ideal case. All of the cases investigated in the preceding paragraphs deviated from this.

Interpretation of the curves in Figure V.2.3 based on fluid dynamical behaviour of the intake jet flow will be attempted in this paragraph. Considering the curve for 30 RPM engine speed (Reynolds number at midstroke is equal to 6319) in Figure V.2.3 the degree of regularity increases with increasing valve lift. This makes sense now after establishing the physics of intake jet flow. The coherent vortex ring structures for the 3 mm valve lift case get destroyed at the shortest ξ (for a definition of ξ refer to Figure V.2.4). The vortex ring structures live longest for 9 mm VL, however, presumably break up as well at this engine speed before reaching the cylinder wall since otherwise we would not expect the curve to exhibit a generally linear characteristic. Ingestion of the vortex rings into the main TRP does not take place for any of the examined valve lifts at 30 RPM. The increase in regularity with VL at this engine speed is due to the fact that the vortex rings break up later for larger VL, and that therefore the turbulent motion is less established when the flow supplies the toroidal recirculation pattern. Furthermore, the vortex rings are larger in

extent for the 9 mm VL case and provide thus eddy structures on larger length scales in the turbulent flow after the break-up of the vortex rings. Consequently, there is altogether more large scale 'structure' in the main TRP and thus higher recirculativity for 9 mm valve lift than for 6 and 3 mm. This is reflected by the curve in Figure V.2.3 for 30 RPM.

For 10 RPM engine speed the respective curve for recirculativity in Figure V.2.3 is linear as well. Since the Reynolds number is three times smaller at this engine speed than for 30 RPM, one can imagine that in this case vortex rings shedding from the annular intake jet survive for this particular model engine at all three examined valve lifts until the intake jet reaches the cylinder wall so that ingestion takes place for all vortex rings, supplying the TRP with (immediate) angular momentum at all three VLs. This means that the only difference for the three valve lift cases at 10 RPM engine speed is manifested through the size of the vortex rings when the jet flow reaches the cylinder wall which accounts for the increase in angular momentum with VL as found in Figure V.2.3, and accounts also for the fact that the slope of increase of recirculativity with valve lift is less steep for 10 RPM engine speed when compared to the slope for 30 RPM.

The case for 20 RPM engine speed represents an intermediate state between the two cases analyzed in the two preceding paragraphs which is supposedly why the three data points in Figure V.2.3 for 20 RPM engine speed do not follow the scheme proposed by the curves derived from experiments conducted at 10 & 30 RPM engine speed. Data available at this point are not sufficient to discuss the case of 20 RPM engine speed.

The above delivered hypothesis is a very simplistic one. One has to perform more visualization and LIPA experiments in order to verify the proposed mechanisms.

Altogether, it is possible to conclude from this section that high engine speed with small valve lift is favorable for fine scale flow structures in the flow field of an engine, low degree of stratification, and hence, best mixing performance during induction in the area of scrutiny. Large valve lift along with low engine speed establishes a structured flow field

which yields inferior mixing performance, however, on the other hand, also low cycle-to-cycle variability. Qualitative verification of results about correlations between annular intake jet and fluid dynamical behaviour in the area of scrutiny from flow visualization experiments is discussed next.

V.2.3.3 Flow visualization results revisited

The ingestion of toroidal vortex rings, created by the incoming jet, into the main recirculation pattern as hypothesized above was observed, as outlined in section IV.1.2, in the results of the flow visualization experiments with the photochromic dye. The observations on the ingestion of the vortices as observed in the photochromic dye experiments will be partially repeated here, now in the light of the findings about annulus intake jet flow. The experiments discussed in section IV.1.2 were performed at a low engine speed of 1.5 RPM (25.5 RPM in air). Due to the low Reynolds number the length of the transitional flow exceeds the distance between the orifice and the cylinder wall ℓ_J (see Figure V.2.4 for the definition of ℓ_J), in particular for the 6 and 9 mm valve lift cases. Thus the vortex rings associated with the intake jet can be traced in the video film from their creation up to the cylinder wall, and their behaviour at $\xi=\ell_J$ where the free jet turns into a constrained boundary layer flow can be studied. It was observed for the vortex rings that the region that contains their angular momentum expands -- entrainment of ambient fluid -- as the jet convects and that especially after the main flow of the jet turns to a flow along the wall, the rotation induced by a vortex ring on the side of the jet that faces the main recirculation pattern is merged into the rotation of the main recirculation system supplying it immediately with angular momentum. As mentioned in section IV.1.2 the entrainment of the angular momentum was most efficient for the vortex rings encountered with a 6 mm valve lift. Note that the ingestion mechanism can only take place for a certain crank-angle range which is symmetric about midstroke since at the beginning and towards

the end of the intake stroke the Reynolds number is too small to destabilize the jet flow and form toroidal vortex rings. It was learned in section IV.1.2 that for 1.5 RPM engine speed vortex shedding sets in at about 30° crank-angle (Figure IV.1.1d). Coherent vortex ring structures that can supply angular momentum to the main toroidal recirculation pattern by ingestion can be observed from about 50° CA (Figure IV.1.1f) on.

The generation, development, and break-up of vortex rings can be also observed in the images which were generated employing fluorescent dye (Figure IV.2.2) for 20 RPM engine speed and 3 mm valve lift (section IV.2.2). Since experiments were performed at a higher Reynolds number than for 1.5 RPM the distance where the flow can be referred to as transitional is shorter for constant valve lift, meaning that the break-up of the coherent vortex rings formed by the intake jet into small scale turbulent motion occurs at shorter ξ when compared to the results obtained from experiments at 1.5 RPM engine speed. Due to the higher engine speed and small VL the length of transitional flow can be determined from the images in Figure IV.2.2 to be less than $\ell_j/3$. From these images it is observable that the length of the transitional flow decreases as crank-angle evolves; the break-up of the coherent vortex structures for crank-angles around midstroke (Figure IV.2.2k) occurs shortly after the intake jet enters the cylinder. This implies that during the engine stroke the flow field experiences constantly changing initial conditions as far as the physics of the intake jet flow are concerned.

In the section on comparison of the flow visualization results for the two engine speeds (1.5 RPM and 20 RPM) in section IV.3 it was established that waviness and vortex shedding occur much earlier for an engine speed of 20 RPM, and that the flow field enforced by 20 RPM engine speed exhibits much faster spread of flow structures. This is due to the higher maximum Reynolds number in connection with the higher engine speed (maximum Re of 4213 for 20 RPM over 316 for 1.5 RPM) which lead to higher Re at any given crank-angle during intake. The threshold Reynolds number to cause instabilities in

the annulus free jet is thus encountered at a lesser crank-angle. Also, the length of the transitional flow decreases more rapidly with evolving crank-angle for an engine speed of 20 RPM than with one of 1.5 RPM. This implies that turbulent flow exhibited by the intake jet is encountered earlier in the intake stroke for the higher speed. Early generation of turbulent motion will spread out the flow structures faster.

Concluding from the above it seems fair to hypothesize that fluid dynamical behaviour in the area of scrutiny can be predicted largely by consideration of the intake jet and ultimately by the setting of engine parameters such as engine speed and valve lift. By varying, for instance, ℓ_J (moving valve or changing valve/bore ratio) and valve lift at constant engine speed (e.g. idling) the engine designer could manipulate the characteristics of the intake jet at ℓ_J in order to accomplish a variety of objectives. One being the search for a compromise at idling conditions between low cyclic variations in order to obtain steadiness of engine performance at low engine speed, and high turbulent motion within an engine cycle to achieve enhanced mixing; two ambitions that do not necessarily go hand in hand.

The results from these studies of an axisymmetrical assembly of a four-stroke IC engine might be an explanation why off-center valves as well as an implementation of two valves in commercial IC engines exhibit better engine performance. Both configurations should yield better mixing during intake through earlier break-up of coherent vortex structures.

V.3 Data from Evaluations of Instantaneous Velocities

V.3.1 Maps of instantaneous velocity vectors

Considering velocity fields from maps containing instantaneous velocity vectors, it can be asserted a priori -- and will be shown later -- that the main toroidal recirculation pattern cannot be resolved distinctly at all crank-angles after midstroke. There is only a weak indication of the main recirculation pattern in the form the TRP was encountered in the EA domain (for the TRP in EA see section V.1.1). This result is comparable to visual observations of the induction flow field during the actual LIPA experiments when the human eye by integration with respect to time and space discerns a dominating rotational flow, i.e. the recirculation pattern, and a temporal analysis reveals that instantly there may be no measurable large scale rotation. This should be considered a warning to be cautious in an analysis where ensemble averaged data are interpreted. Furthermore, the degree of mixing, and the turbulent structures, as well as their length scales, cannot be deduced from EA data -- unless the prerequisite of negligibly low cycle-to-cycle variability is given. This situation served initially as motivation for the analysis of instantaneous velocity information, where cycle-to-cycle variability would not result in loss of information.

It is an exhaustive effort to analyze the entire scope of instantaneous velocity data available for the nine variations on the engine parameters (see Table II.2.3 in chapter II). Each of the nine sets of data comprises a number of engine cycles -- that contributed to the ensemble averaging procedure in sections V.1 and V.2 -- where each cycle covers a crank-angle range of 180 degrees. To stay within the framework set forth for this work, the author had to focus on topics in the discussion of instantaneous velocity information that promised interesting results.

V.3.1.1 Results from individual engine cycles for 20 RPM and 3 mm valve lift

In Figure V.3.1 the entire induction stroke is exhibited for 20 RPM engine speed and 3 mm valve lift as the flow field evolves *instantaneously* (engine cycle #27). Features of the flow field as recognized in section V.1.1 in the maps of EA velocity vectors can be identified in the maps that contain instantaneous velocity vectors as well -- intake jet, boundary layer flow along cylinder wall, recirculation pattern, variation of induction angle. Also, the development of the flow field is comparable to that found in the EA domain; this is emphasized by the fact that from about midstroke on the area of scrutiny is exclusively governed by the flow that turns inbound away from the cylinder wall. It is in the detail where the maps of instantaneous data and the maps from the EA domain differ. For instance, in the EA domain the velocity vectors in the area of scrutiny display, after midstroke, a clear and structured toroidal recirculation pattern as sole rotational motion; the instantaneous velocity vectors depict for the same area and crank-angle range smaller scale rotational flow where a TRP motion serves generally as a fluid dynamical embedding (Figure V.3.1m-x). The degree of difference between results from instantaneous and EA data is reflected in the value of velocity fluctuations as calculated by equation V.2.b in section V.2.

With respect to congruity between the flow patterns encountered in velocity maps stemming from instantaneous observation and ensemble averaging technique, it can be said that -- for this set of data -- there is profound similarity concerning the overall flow structure. This justifies the application of ensemble averaging techniques in the analysis of problems in fluid mechanics. In this context, the reader's attention should be focused on the flow situation at crank-angle 48°, for instance. Comparing the content of Figure V.3.1g with the content of Figure V.1.1g the overall correspondence between the two flow fields becomes obvious; what constitutes the differences between the two flow fields are the details of orientation and magnitude of the individual velocity vectors.

From Figure V.3.1, it can be found that for crank-angles after midstroke, when the maps of ensemble averaged velocity vectors exhibit rather stable flow fields, this stability does not exist in the case of the 'real' instantaneous flow within an individual engine cycle. In general, vortical structures with a length scale of the radius of the cylinder, i.e. the main toroidal recirculation pattern, can be only weakly perceived after midstroke -- to various degrees -- in the flow fields of Figure V.3.1; at times a rotational structure of this length scale can be barely observed (128° CA, Figure V.3.1p). A high amount of irregularity is encountered in conjunction with the vortical flow patterns, like cross-flows between the layers of the main TRP. Only at certain crank-angles (e.g. 112°, 156°; Figure V.3.1n&u) does the flow field comprise a distinct vortical structure with a length scale of the radius of the engine cylinder, namely the projection of the main toroidal recirculation pattern onto the examined x, z - plane. However, these are singular occurrences.

High variation with respect to the structure of the flow field within one engine cycle is experienced as crank-angle evolves illustrating that the mechanisms of turbulence are inherent in the flow fields.

Figure V.3.1 illustrates the actual complexity of the induction flow for an individual engine cycle. Complexity of the flow field cannot be perceived in the maps containing EA velocity vectors (section V.1.1) since it is essentially filtered out during the ensemble averaging procedure.

Following are some interesting issues in connection with instantaneous velocity information discovered during the analysis of the velocity maps in Figure V.3.1 highlighting the notion of flow field complexity encountered with instantaneous velocity data.

From Figure V.3.1a (CA 4°) it can be noticed that there is fluid motion prior to piston movement in an individual engine cycle that cannot be observed in EA velocity maps. The 'high' velocity magnitudes encountered at 4° crank-angle indicating preexisting motion

cannot stem from piston motion which just started to accelerate. Magnitude and orientation of this initial movement of the fluid prior to piston motion differs with engine cycle. Hence, the initial conditions are different for every engine cycle which is one of the main causes for cyclic variations of the fluid dynamic quantities encountered during induction.

It can be observed that, at times, the flow field around the axis of the engine cylinder is rather symmetrical in the examined plane where the fluid is essentially convecting parallel to the z - axis in negative direction (CA 148°, Figure V.3.1s). On the other hand, during intake it is also possible that this symmetry is broken up by fluid that convects across the cylinder axis, as seen at crank-angles 128° and 140° (Figure V.3.1p&r).

At 132° CA (Figure V.3.1q), a very strong circular vortical motion can be observed depicted by four velocity vectors that are marked in the corresponding map in Figure V.3.1. As will be seen in section V.4 this vortex accounts for a distinct peak in the distribution of the corresponding vorticity vector (Figure V.4.5).

It is interesting that by the end of the intake stroke (CA 180°, Figure V.3.1x), there are local areas of considerably high kinetic energy. Also, no predominating flow structure can be discerned. The end of the intake stroke marks the beginning of the compression stroke and is thus important with respect to providing initial conditions for compression.

It can be concluded that the flow field within an individual engine cycle is actually highly complex and evolves with significantly different motions from cycle to cycle. The EA based analysis washes out this pseudo random detail. A message should be conveyed to be cautious with results originating from applications of ensemble averaged analyses as well as from applications of its related computational technique CFD. The description of the flow field in the EA domain as consisting of discrete toroidal recirculation patterns is a model; for individual engine cycles *distinct* recirculation patterns vary a lot and rarely look like the ensemble averaged pattern. The precise recirculation pattern exhibited in the EA

domain never actually exists in the individual realizations. The smaller the valve lift and the higher the engine speed, i.e. the higher the cycle-to-cycle fluctuations (see Figure V.2.2 in section V.2), the higher is the degree of variability from the EA.

V.3.1.2 Variation of flow field with engine cycle and change in engine parameters

In order to examine the difference in the instantaneous behaviour of flow fields for three consecutive engine cycles at a particular crank-angle, maps of instantaneous velocity vectors are shown in Figure V.3.2 for 20 RPM engine speed and 3 mm valve lift at 132° CA (ECs #27, 28, and 29).

The notion of cycle-to-cycle variability becomes clear when comparing the flow fields for the three engine cycles in Figure V.3.2. For EC #27 a strong vortical motion dominates the flow field. For engine cycles #28 and 29 no distinct rotational flow with a length scale of the radius of the engine cylinder can be perceived. In fact, the flow fields in connection with these latter two engine cycles exhibit considerable similarity to each other, especially in the upper left corner of the area of scrutiny where in Figure V.3.2b and c velocity vectors denote a flow towards the center of the valve. This is the crucial region where the flow has to decide whether to recirculate -- as it is roughly the case for EC #27 at 132° CA -- or to convect towards the valve -- as it is predominantly the case for EC #29 at 132° CA. The velocity maps in the EA domain yield, naturally, a compromise in this question of recirculation.

Furthermore, the flow in the lower right corner of the three fields in Figure V.3.2a - c depicted by velocity vectors #73 and 74 (for location of velocity vectors #73 and 74 within grid of laser lines see Figure II.2.3a) exhibit for EC #27 a vertical flow towards the piston head, for EC #28 a flow turned inbound towards the cylinder axis, and for EC #29 a flow towards the corner between piston head and cylinder wall. The variance in the flow behaviour in this lower right corner of the engine cylinder exhibited in these three engine

cycles is the underlying factor that results in the existence of a buffer zone above the piston head -- as it was described in section V.1.1 -- that is seen in the EA domain.

The degree of cycle-to-cycle variations as encountered in the previous paragraphs is dependent on the settings of the engine parameters (see section V.2.2, Figure V.2.2). This is demonstrated by an investigation of flow fields at one crank-angle for three consecutive engine cycles from two additional, different data sets. Examined are the flow fields for 10 RPM engine speed and 9 mm valve lift, as well as for 30 RPM engine speed and 3 mm VL. Recall from Figure V.2.2 (section V.2.2) that for these settings of the engine parameters velocity fluctuations are the lowest and the highest, respectively. Note that the sequence of Figures V.3.2 to V.3.4 shows velocity maps -- or rather distances and directions fluid particles traveled -- after employment of time delays of 0.32 ms for 30 RPM (Figure V.3.3), 0.64 ms for 20 RPM (Figure V.3.2), and 0.96 ms for 10 RPM engine speed (Figure V.3.4). The difference in underlying time delay implies that the magnitude of velocity vectors in Figure V.3.3 is generically two times and three times higher with respect to the magnitude of velocity vectors in Figures V.3.2 and V.3.4, respectively.

It is apparent by visual examination of the lengths of the arrows in the velocity maps in Figures V.3.2 and V.3.3 that these lengths are about as high for 30 RPM engine speed as they are for 20 RPM indicating a factor-of-two difference in the velocity magnitude -- due to the difference in the underlying time delay. This means that while the engine speed increases by a factor of 1.5 -- where the valve lift stays the same -- the velocity magnitudes are doubled in the flow field.

It is obvious from the flow fields of the three consecutive engine cycles in connection with 10 RPM engine speed and 9 mm valve lift (Figure V.3.4) that there are cyclic variations. However, the three flow fields have very similar characteristics, such as the tendency to recirculation. Cycle-to-cycle variability is rather small, leading to increased

predictability of cyclic motion in connection with low engine speed and large valve lift. The flow fields in conjunction with 30 RPM engine speed and 3 mm VL, on the other hand, exhibit at one crank-angle during induction profound cycle-to-cycle variability as can be seen in Figure V.3.3a - c. There is hardly any similarity between the three flow fields displayed in Figure V.3.3.

The essence from this section of an analysis of cycle-to-cycle variations during engine performance for three different data sets is that a visual verification of the results manifested by the curves in Figure V.2.2 (section V.2.2), which indicate increase of velocity fluctuations with decreasing valve lift and increasing engine speed, is established.

V.3.2 Time history of a velocity vector -- an approach towards cycle resolved data analysis

This section will explore profiles of instantaneous velocity vectors -- with respect to crank-angle of the piston movement -- at selected locations in the flow field. The recording of time histories of velocity vectors at a specific point within the engine cylinder on the basis of LIPA - data is legitimate because the marking of one particular fluid 'particle' in a flow field by the corresponding intersection in the grid of laser lines occurs consistently at the same location within the engine cylinder for each laser pulse throughout the intake stroke. (A more detailed analysis reveals that a slight fluctuation in the coordinates of a particular origin location of a velocity vector is encountered; this is due to the actual assignment of the vectors' origin by incorporating information about to where the fluid particle convected after excitation, section II.1.1.2; this 'mis'location is however of much smaller order than the size of coherent structures studied in the flow field and, thus, negligible.) In section V.3.2.1 several velocity profiles will be exhibited for the induction stroke and fluid dynamical conduct of the flow field will be inferred from them.

So far, we have been dealing with velocity fluctuations in general without really distinguishing the fluid dynamical nature of the fluctuations which is essentially twofold: Fluctuation in orientation and magnitude of velocity vectors is due to (1) cycle-to-cycle (CtC) variability and (2) to turbulent motion of the flow field within an individual realization of an engine cycle. In the preceding section (V.3.1) we obtained a notion about cycle-to-cycle variability by qualitatively comparing maps of velocity vectors for one setting of the engine parameters at one crank-angle for consecutive engine cycles. From the same maps one can also infer flow structures suggested by the orientation of velocity vectors in a certain neighborhood and thus attaining a feeling for turbulent motions in the flow field. However, it has not been possible in the study of engines thus far to achieve qualitative measures. In this section an attempt is made to separate the two sources of velocity fluctuations -- cycle-to-cycle variability and turbulent motion in the flow field -- by means of a *cycle resolved analysis* based on velocity profiles at selected locations in the flow field.

Cyclic variation during the performance of an engine is the result of different fluid mechanical behaviour of the flow field (e.g. strength and location of vortex structures) from engine cycle to engine cycle. This is caused by different initial conditions for each engine cycle prior to the movement of the piston, which are partly due to the dissimilarity of initial motion of fluid particles in the flow field at the beginning of the intake stroke. Turbulence inherent in the flow field is characterized by the strength and length scales of vortex structures in the flow field.

In a cycle resolved analysis, with the goal to differentiate between the influences of CtC-variations and turbulent motion as causes for velocity fluctuations, results have been obtained in this work for 10 RPM engine speed and 3 mm valve lift. (A cycle resolved analysis makes use of velocity profiles as will be outlined in section V.3.2.2.) An engine speed of 10 RPM was chosen because at this engine speed data acquisition achieved the

highest temporal resolution within the volume of experiments performed, namely 2° crank-angle. (Unfortunately, this still has to be considered a low resolution in the context of cycle resolved analyses.) The cycle resolved analysis has been conducted in the vicinity of the axis of the intake jet (location #07) and in the area of scrutiny (location #26); see Figure II.2.3a for position of locations within engine cylinder. In the cycle resolved analysis only the z - component of the two-dimensional velocity vector was subject to examination because this component is, in this study, affiliated with the highest accuracy; see section III.3.

V.3.2.1 Presentation of velocity profiles

Since in *EA* an average is given of all the fluid dynamical action taking place within the examined 21 individual engine cycles (for 10 RPM engine speed, ensemble averaging is performed over 21 ECs; section II.2.2.4) the task of velocity profiles from the EA domain is to suggest a trend or tendency that cannot be apprehended in the examination of individual engine cycles.

In the vicinity of the axis of the intake jet (location #07) the EA velocity profile for the *w*-component of the 2D velocity vector exhibits an ascending curve towards a local maximum that is at about 45° CA (Figure V.3.5). Then the velocity decreases almost symmetrically to the value which is encountered at the beginning of the stroke although the piston speed increases until crank-angle 90°. This property of the velocity profile at location #07 for 10 RPM engine speed and 3 mm valve lift is due to the deviation of the induction angle with crank-angle as outlined in section V.1.2. From the respective curve in Figure V.1.3 one can see that the intake jet first inclines towards the cylinder axis (until about 45° CA) and then backs up towards the cylinder head. Location #07 is fixed with respect to the x, z - coordinate system. Hence, the axis of the inclining intake jet approaches this location and for the furthest inclination, location #07 falls approximately --

for this setting of the engine parameters -- onto the jet axis generating the observed high magnitudes of velocity in the z - direction at location #07. When the incoming jet inclines back towards the cylinder head, location #07 moves, with respect to the jet axis, towards the outer region of the incoming jet (increasing ζ) and thus into regions with lower velocity magnitudes. After midstroke w increases slightly towards a second local maximum at about 120° CA which is much smaller and barely recognizable. Then, w decreases towards the end of the stroke.

For location #26 (Figure V.3.6) a sharply descending curve can be noted for the EA velocity in the z - direction between crank-angles 40° (when this location is being passed by the accelerating piston head) and about 68°. From then until the end of the stroke an essentially ascending curve is encountered. The orientation of the bulk flow at location #26 is such that it is directed towards the valve throughout the entire stroke -- thus in opposite direction to the piston movement. The velocity profile depicting the magnitude of the z - component of the velocity vector reflects in EA for location #26 the average strength of the main toroidal recirculation pattern. From Figure V.3.6 it can then be maintained that the energy content of the main TRP is highest for 10 RPM engine speed and 3 mm valve lift at a crank-angle of about 68°; the maximum occurs thus considerably before midstroke when the piston speed reaches maximum. This indicates that in addition to the momentum flux of the incoming jet flow, geometrical constraints, and thus boundary conditions, play an important role in the development and timing of the main recirculation pattern.

Velocity profiles from *instantaneous* velocity data can, for some engine cycles, demonstrate significant differences to the velocity profiles from ensemble averaged data discussed in the preceding paragraphs. The instantaneous velocity profile of the z - component shows at location #07 (Figure V.3.5) for engine cycle #23, for instance, a very distinct second maximum around 110° crank-angle. Within other engine cycles there is no

second maximum at all in the velocity profile at this location (see Figure V.3.7 where velocity profiles from eight engine cycles are shown for location #07). The behaviour of the velocity magnitude for crank-angles around the second maximum is summarized within the profiles in EA and displayed by a sketchy hill. The first maximum, however, is encountered in the profiles for all engine cycles investigated which is why this maximum can thus be found distinctly in the velocity profile from the EA domain. When considering the velocity profiles from EC #04 and 23 in Figure V.3.5 one can perceive profound differences between the profiles, signifying cyclic variations of fluid dynamical behaviour at location #07.

For location #26 the two individual velocity histories in Figure V.3.6 demonstrate very similar characteristics as the one stemming from the EA analysis. In fact, when qualitatively studying all velocity profiles from individual engine cycles at this location less fluctuation about the ensemble averaged curve when compared to the results at location #07 could be observed. Nevertheless, there are sufficient differences between the individual velocity profiles which make it possible to group them according to curve characteristics: for several engine cycles, the descending and ascending parts of the velocity profiles possess about the same slopes (#10, 11, 17, 24, and 26). This idea of grouping realizations of engine cycles according to similarities in the behaviour of fluid dynamic quantities is the basis for conditional sampling, an approach that clusters results and evaluates mean quantities from each cluster. Conditional sampling is another approach used in engine research -- besides cycle resolved analysis -- towards discrimination of velocity fluctuations.

V.3.2.2 Notes on cycle resolved analyses

The objective of numerous investigations in the field of reciprocating engines is the separation of velocity fluctuations due to cycle-to-cycle variability from those due to

turbulent motion within an engine cycle based primarily on velocity information. There have been different methods to extract turbulence intensities from the velocity fluctuations.

One method which is used sometimes in firing engines is a conditionally-sampling technique (Witze et.al. 1984, Foster and Witze 1988). In this case data are classified into sets according to the value of a specified parameter, e.g. flame arrival time. Witze et.al. (1984) employed a conditionally-sampling technique to avoid a smearing of the ensemble averaged mean velocity profile.

The method that has received most attention in the engine research community is based on the evaluation of a mean velocity profile within *one* engine cycle (cycle resolved analysis) from instantaneous velocity data. Since exclusively single probe measurement techniques offered the velocity information in previous investigations of the fluid dynamics in engines, data were -- for one engine cycle -- available only at one location in the flow field. This available velocity information is plotted as a function of crank-angle and takes a form of a velocity profile or history. The difference between the instantaneous and a mean velocity profile within one engine cycle signifies, in this approach, a measure for velocity fluctuations due to turbulent motion of the flow field. The difference between the curve from an ensemble averaging analysis and the mean velocity profile in one engine cycle is a measure for cyclic variations. For the method of cycle resolved analysis, approaches differ in how to determine the mean velocity profile.

In order to summarize work that has been done in an attempt to evaluate mean velocity profiles within one engine cycle on the basis of instantaneous velocity profiles, the author will lean on a review on cycle resolved analyses furnished by Catania and Mittica (1989) who discussed the most important techniques -- including one modeled by themselves -- in a paper and compared the performances of the different techniques to each other. There are, according to Catania and Mittica (1989), essentially five different schemes. Of these, Lancaster (1976), Rask (1981), Catania and Mittica (1985), and Daneshyar and Fuller

(1986) divided the velocity profile from instantaneous velocity data for the entire stroke into crank-angle segments or windows and determined mean velocity profiles by time-averaging (Lancaster 1976, Catania and Mittica 1985, and Daneshyr and Fuller 1986) and cubic spline fitting (Rask 1981) procedures. The fifth method by Liou and Santavicca (1985) constitutes the application of a Fourier transform to the complete instantaneous velocity profile. In the frequency domain, the argument goes that low frequencies are related to fluctuations in the bulk flow of an engine and thus, to cyclic variations; high frequencies are considered to be found in connection with velocity fluctuations due to turbulent motion. A cut-off frequency, which is according to Liou and Santavicca (1985) assumed to be related to a characteristic time of the engine combustion process, then separates the influences on velocity fluctuations due to turbulence and CtC-variability.

More recently, Hilton et.al. (1991) suggested a routine that -- according to them -- is closer to the physics of the flow. The method they outline in their publication incorporates discrimination on the basis of phase stability. Their 'unified method' allows the investigator to adopt an entirely parametric representation of the various flow components in the model where the parameters can be estimated by minimizing the difference between estimated and theoretical autocorrelation functions in a least-square sense.

The author of this work decided to employ a cycle resolved analysis because of the nature of the available velocity data. In order to establish the mean velocity profile within one engine cycle, curve fitting by a polynomial of 5th order, Fourier transform procedures, and data smoothing techniques have been experimented with and applied to the profiles of velocity vectors acquired in this study. None of the above yielded satisfactory results. Eventually, a simplified version of the approach suggested by Daneshyar and Fuller (1986) emerged and was adopted for the separation of the sources of velocity fluctuation. An adoption of one of the more sophisticated methods that were recapitulated above would have been beyond the scope of this work.

V.3.2.3 Procedure and results of cycle resolved analysis

The intention of the application of a cycle resolved analysis in this study is primarily to provide a blueprint of the concept and the demonstration of the possibility of cycle resolved analysis in conjunction with LIPA. Therefore, a simplistic approach was chosen for this study with respect to the cycle resolved analysis in that the representations for mean velocity profiles within one engine cycle consist of simple straight lines within assigned crank-angle segments or windows. A straight line was chosen to curve fit the instantaneous velocity profile also because a more sophisticated cycle resolved analysis would be unwarranted in the light of the rather mediocre accuracy of the present data sets (on accuracy of the data see section III.3). The straight lines are evaluated through a linear regression technique provided by a software package.

For the analysis at location #07 (area of intake jet) the set of 90 data points (resolution of 2° CA) was divided into three subsets of contiguous crank-angle for which within a subset the linear regression technique evaluates the curve fit constituting the representing mean velocity profile. The assignment of crank-angle ranges for the three subsets was done by hand through incorporation of information on flow behaviour (e.g. fluctuation of induction angle) inferred from the studied velocity profiles. The basic setup of profiles at location #07 exhibiting essentially two ascending characteristics and one slightly descending one as for example for EC #23 (Figure V.3.5), stimulated the investigator of this study to dissect the curve into three sections. In Figure V.3.7 results from the curve fitting process for the three segments in connection with eight velocity profiles from location #07 can be seen. The fluctuation of the instantaneous velocity information about the linear curve fits symbolizes velocity fluctuation due to turbulent motion in the flow field.

For the analysis at location #26 (area of scrutiny) the established 71 data points could be divided into essentially two subsets representing two phases of fluid dynamical conduct

(increasing and decreasing velocity magnitude, see section V.3.2.1). In Figure V.3.8 linear curve fits for velocity profiles at location #26 are exhibited.

At location #07 the curve fitting straight lines were evaluated for each of the three subsets of an engine cycle, successively for all 21 engine cycles (setting of engine parameters: 10 RPM engine speed, 3 mm valve lift). Then, for each of the 63 subsets, the fluctuation of the instantaneous velocity profile about the curve fit was calculated employing an RMS approach as a measure for the turbulent motion encountered in this crank-angle window. Note that the crank-angle windows are rather extensive [in the average 30 degree] so that no momentary information on the turbulence inherent in the flow field can be obtained; only a global value characterizing the overall turbulent motion for crank-angle ranges of about 30 degree is being furnished for the flow field of an intake jet. An arithmetic average for each subset (I through III) over the investigated 21 engine cycles is then evaluated and included in Table V.3.1. This number for the fluctuation due to turbulence is evaluated by the following overall formula:

$$TU_{I,II,III} = \frac{1}{\#ECs} \sum_{k=1}^{\#ECs} \left(\frac{1}{N_j} \sum_{i=1}^{N_j} \left(w_i - w_{CF_{j_i}} \right)^2 \right)_k^{1/2} \qquad \text{(V.3.a)}$$

where TU is the fluctuation due to turbulent motion in the examined flow field, #ECs is the number of engine cycles examined (21), N_j is the number of data points (crank-angle positions) in the respective subset I, II, or III; w_i is the instantaneous velocity in an individual EC, and $w_{CF_{j_i}}$ is the corresponding value of the linear curve fit.

In order to obtain a measure for the cycle-to-cycle variations (CV) an RMS value has been determined for the difference between the curve stemming from an ensemble averaging procedure over the instantaneous velocity profiles and the linear curve fit. The evaluation scheme for CV is identical to that in equation V.3.a for TU after replacing w_i by w_{EA_i} and reads

$$CV_{I,II,III} = \frac{1}{\#ECs} \sum_{k=1}^{\#ECs} \left(\frac{1}{N_j} \sum_{i=1}^{N_j} \left(w_{EA_i} - w_{CF_{J_i}} \right)^2 \right)_k^{1/2}$$

(V.3.b)

Naturally, the lower the intensity of the cyclic variations over several realizations of intake strokes (CV) the better is the representation of the mean velocity profile within one engine cycle by the ensemble averaged velocity profile.

Fluctuation intensities were evaluated as well by normalizing TU and CV within each subset I, II, and III. The normalization factors for the three sections are inferred from the ensemble averaged velocity profile in Figure V.3.5 by taking an arithmetic average of the EA values in the respective crank-angle sections I, II, and III. For instance, for section I the normalizing factor for the calculated velocity fluctuations is the arithmetic mean of the first 30 data points of the EA velocity profile.

For location #26 the same formulas, equations V.3.a and V.3.b, and evaluation mechanisms for the normalization factors are effective. The difference is that they are applied to only two subsets, I and II.

In Table V.3.1 the results of the application of the two equations V.3.a and V.3.b to the LIPA - data is exhibited for location #07; Table V.3.2 contains the results for location #26.

Table V.3.1: RMS fluctuation and intensities in connection with turbulent motion and cycle-to-cycle variability at a location in the vicinity of the axis of the intake jet.

	Location #07					
	Section I		Section II		Section III	
	RMS [in m/s]	Intensity	RMS [in m/s]	Intensity	RMS [in m/s]	Intensity
Turbulence	0.177	0.702	0.161	1.226	0.105	1.541
CtC - Variation	0.116	0.461	0.117	0.889	0.077	1.142

Table V.3.2: RMS fluctuation and intensities in connection with turbulent motion and cycle-to-cycle variability at a location in the area of scrutiny.

	Location #26

	Section I		Section II	
	RMS [in m/s]	Intensity	RMS [in m/s]	Intensity
Turbulence	0.078	0.466	0.079	0.788
CtC - Variation	0.065	0.387	0.052	0.515

Table V.3.1 demonstrates that for 10 RPM engine speed and 3 mm valve lift the RMS fluctuation as well as the fluctuation intensity of the z - component of the velocity vector evoked by turbulent motion of the flow field is, at a location in the region governed by the incoming jet (velocity vector #07), consistently -- throughout the induction stroke -- higher than the fluctuations and the intensities stemming from velocity fluctuations due to cycle-to-cycle variability; a factor of about 1.5 can be deduced for each section. For both sources of velocity fluctuation the 'decrease' (there are only three representing values for a crank-angle range of 180°, making it hard to speak of a real decrease) of absolute RMS fluctuation with crank-angle shows the same characteristic: For both, turbulence and cyclic variations, the RMS values for sections I and II are about the same; then, towards the end of the stroke, RMS fluctuation decreases. For the fluctuation intensity -- normalized by ensemble averaged velocity information -- a different picture is presented. Turbulence intensity as well as fluctuation intensity based on CtC-variations increase consistently with crank-angle.

The cycle resolved analysis reveals for the area of scrutiny (location #26, Table V.3.2) that RMS fluctuations of *w* in connection with turbulence as well as turbulence intensities are, for an axisymmetric engine configuration run at 10 RPM engine speed, 1.2 and 1.5

times, for sections I and II respectively, higher than RMS fluctuations and normalized intensities caused by CtC-variability. Considering the averaged values in Table V.3.2, there is no decrease of RMS fluctuation caused by turbulence as crank-angle evolves from CA 40° to the end of the stroke (180° CA). Table V.3.2 witnesses, however, a decrease of RMS fluctuation in conjunction with CtC-variability as crank-angle advances from section I to section II. Again, fluctuation intensities increase as crank-angle evolves for both sources of velocity fluctuation which is, particularly for the turbulence intensities, a very welcome fact since high turbulence intensities account for an enhanced mixing performance in the flow field of an engine. Moreover, studies have shown that an increased level of turbulence intensity improves combustion performance.

When comparing the results obtained in the vicinity of the axis of the intake jet (location #07) with those obtained in the area of scrutiny (location #26), it can be inferred that for the time scales considered (smallest time scale resolved is 33.33 ms) velocity fluctuations -- absolute as well as normalized -- of the z - component of the velocity vector due to turbulence as well as due to cyclic variations are higher in the region governed by the intake jet than in the area of scrutiny by a factor between 1.5 and 2.

For a regular production engine run at 1600 RPM engine speed Catania and Mittica (1989) performed cycle resolved analysis at a location 3.5 mm underneath the flat cylinder head between intake valve I and II. The result of their analysis is that velocity fluctuations due to turbulence are only a quarter of the fluctuations due to cycle-to-cycle variability. This is in strong contrast to results found in this study and demonstrates the profound influence of boundary conditions and engine speed on the fluid dynamics of the flow field.

It goes without saying that in order to understand fluid dynamical mechanisms that influence the flow field during induction of an engine -- particularly those of the turbulent motion within the flow field -- velocity fluctuations caused by turbulence have to be evaluated for concise crank-angle windows whose time-equivalent intervals are, in an

optimal case, smaller than the smallest characteristic time scale encountered in the flow field. This could not be accomplished in this study due to the quality (e.g. low temporal resolution) of the LIPA - data at hand so that averages for the velocity fluctuations due to turbulence had to be evaluated over ranges of between 30 and 100 degree (section II in the analysis of location #26) crank-angle. However, LIPA has the potential to provide the necessary velocity profiles for a thorough investigation of turbulent motion on any length and time scale and at any location within an individual engine cycle.

At this point only some qualitative observations concerning the dynamics of turbulent motion during intake can be deduced from the plots of velocity profiles in Figure V.3.7 and V.3.8. Firstly, within section I of location #07 (region of intake jet) there is -- as can be expected -- an increase of turbulent motion from crank-angle 0° on (increasing fluctuation of instantaneous velocity profile about cycle resolved mean velocity). It is of considerable importance to know the behaviour of velocity fluctuations in conjunction with turbulence as intake approaches the end of the stroke (section III for location #07 and section II for #26), in particular for the area of scrutiny, since this knowledge can be used as initial condition for the compression stroke. This leads to the second statement on dynamics of turbulent motion during intake, according to which, inferred from examining the plots in Figures V.3.7 and V.3.8, it can be stated that the velocity fluctuations caused by turbulent motion of the flow field cease only gradually towards the end of the induction stroke, and that there is considerable turbulent motion by the end of the stroke in the region around the axis of the intake jet, as well as in the area of scrutiny.

It is clear that this technique (LIPA) has the potential to cleanly separate the turbulence from the cycle-to-cycle variability. It is the author's opinion to not go into further depth with this investigation because it does not make sense to base a more thorough investigation of velocity fluctuations incorporating cycle resolved analysis on the basis of the present data base; especially at this low engine speed which is of merely academical

interest. It is suggested that experiments using higher temporal resolution of the acquisition scheme for LIPA - data and higher engine speeds, as well as longer ensemble averages be made to yield significant information about the turbulence and cycle-to-cycle variability in various engine designs.

V.4 Vorticity Contour Maps -- Indicator for Mixing Performance

In the evaluation process of a vorticity vector -- in conjunction with an application of LIPA -- a boundary is placed around a certain set of velocity vectors and the behaviour of these encircled velocity vectors with respect to magnitude and orientation is summarized in one vorticity vector. This yields two -- among others -- characteristics of vorticity distributions that have been taken advantage of in this work. (1) Distributions of vorticity vectors can serve as indicator for the degree of structure encountered in a flow field which, in turn, can be used to derive information about mixing performance. It is intuitively appealing that the higher the degree of structure of the flow field the worse is the resulting mixing performance due to the inhibition of molecular exchange between layers of flow. (2) When using vorticity distributions, convection mechanisms of flow structures can be observed qualitatively over ranges of crank-angle since flow structures stand out distinctly in these distributions, e.g. a region of vortical flow is denoted by high vorticity and a region of parallel flow by vorticity equal to zero. Also, axisymmetrical aspects of the flow field can be studied easier in the vorticity domain.

Concerning data reduction of vorticity data, the same as what has been said about the data available on instantaneous velocity vectors holds true for vorticity information: The vast amount of vorticity data -- characterizing the intake flow of an engine -- made accessible through LIPA cannot be analyzed within the frame of this work. However, a initial investigation -- which should serve as a starting point in the thorough study of the

vorticity information at hand at a later point -- featuring vorticity distributions for the whole engine cylinder at one crank-angle as they differ for the diverse settings of the engine parameters, will be performed.

For this investigation each vorticity vector is calculated from three neighboring velocity vectors. Thus, from the investigation grid in Figure II.2.3a 116 vorticity vectors can be inferred as can be seen in Figure V.4.1. Since the two-dimensional x, z - plane of the engine model at a particular location θ has been investigated in this study only the component of the vorticity vector perpendicular to the x, z - plane could be evaluated. This component lies in the circumferential direction of the cylinder.

In Figures V.4.2 to V.4.10 the vorticity distributions are represented as contour surfaces in two- and three-dimensional plots. In this investigation, there are nine sets of data corresponding to the nine settings of the engine parameters (see Table II.2.3 in chapter II) from which data will be presented. More specifically, data are available for the three engine speeds examined (10, 20, and 30 RPM) along with the three valve lifts investigated (3, 6, and 9 mm). Each Figure (V.4.2 through V.4.10; all in all nine, one for each data set) contains vorticity information at crank-angle 132° for one realization of an individual engine cycle. The presentation of vorticity data will be delivered in two- and three-dimensional contour plots where each plot confers a different perspective of the vorticity distribution to achieve a complimentary picture of the whole distribution. The 3D plots are exhibited for two different views with respect to the azimuth.

The 2D plots in Figures V.4.2 to V.4.10 depict the geometrical setting in which the circumferential component of the vorticity vector (ω_c) has been evaluated. In the 3D plots the magnitude of this component is denoted as a surface contour. For these plots, the valve has to be pictured to be in the corner at small x - and small z - values. It has to be noted that the perimeter locations of the array of locations where vorticity vectors are being evaluated do not form a rectangle (see Figure V.4.1). This induces difficulties for

the software used for the generation of these plots. The software can render only rectangular grids for the determination of contour plots. This means that at areas for which there is no vorticity data available the software extrapolates the existing data. These extrapolations account for the steep vorticity distributions in the corners of the plots for the two- as well as the three-dimensional vorticity contours.

Leafing vaguely through the contour plots in Figures V.4.2 - V.4.10 one perceives that the vorticity distributions which are derived from instantaneous velocity information exhibit surfaces in the two- as well as in the three-dimensional plots which can be described as landscapes that include features like hills and valleys. Hills correspond to areas of positive circumferential vorticity; positive vorticity encountered on the right hand side of the cylinder axis is defined for the direction of the vorticity as possessing the same orientation as the main toroidal recirculation pattern. Valleys, then, correspond to negative regions of the circumferential vorticity.

From intuitive principles it makes sense to associate mixing performance -- of the fresh entering fluid with the fluid already in the cylinder -- during induction with the landscape formed by the vorticity distribution. Vorticity distributions depicting high hill/valley fluctuation indicating small scale structure in the flow field suggest enhanced mixing mechanisms. Enhanced mixing mechanisms intermingle the new and old phases of fluid present in the cylinder on the molecular level in order to provide a homogeneously mixed fluid. These aspects of the vorticity distribution will be discussed in this section by using the presented vorticity data.

There is one hill/valley formation that can be found for all data sets at the same region within the examined x, z - plane. It is the hill/valley configuration characterizing the free intake jet encountered during induction. The hill is located on the starboard side of the intake jet, the valley on the port side. The existence of this configuration can be explained when studying the Reynolds-averaged velocity profile of the streamwise velocity

component of the free intake jet. This profile is characterized by a Gaussian-like distribution in the lateral direction where the maximum velocity of the profile coincides with the axis of the jet. For an observer who is situated in the flow field on the starboard side of the intake jet axis facing downstream, the high magnitude velocity vectors of the jet center are to his/her left side. On his/her right side is an area of lower magnitude velocity vectors. This setup yields vorticities of positive orientation on this side of the intake jet and thus a hill in the contour plot. A similar argument explains the negative orientation of the vorticity on the port side of the jet. This hill - valley combination can be observed in the contour plots of the vorticity distributions in this section, especially in the 2D plots.

V.4.1 First and second derivative of vorticity distribution in area of scrutiny

It is desirable to quantify the degree of hill/valley fluctuation along with the magnitude of this fluctuation to achieve a measure with which it is possible to obtain insight into mixing performance, and also to discriminate between landscapes of vorticity distribution, particularly in the area of scrutiny, stemming from the nine sets of data.

There are 27 locations in the area of scrutiny at which the circumferential component of the vorticity vector has been evaluated in this study. (In Figure V.4.1 these 27 locations are connected by lines denoting the shortest distance between two locations of vorticity evaluation; these lines form a hexagonal pattern.) This number of 27 does not suffice to perform accurate two-dimensional Fourier transform calculations which would yield the desired quantification of the hill/valley fluctuation. For this work other solutions had to be sought that are more fit for this particular problem. A solution was found in the form of the first and second derivative of the vorticity distribution. An evaluation of first derivatives (slopes in vorticity landscape) within a region of investigation together with information about the variation -- more precisely the sign changes -- of the second

derivative (number of hills and valleys) within this same region provide information on the magnitude and the frequency of the hill/valley fluctuations.

V.4.1.1 Introduction of measures for the first and second derivative

Measures describing the first and the variation of the second derivative of the vorticity distribution are evaluated for the area of scrutiny. Averaging procedures were employed on the basis of these evaluations yielding single measures for one particular crank-angle and one particular engine cycle and, subsequently, for one complete set of data (corresponding to one setting of the engine parameters). The evaluation of the measure in connection with the first derivative goes according to the scheme outlined in the proceeding paragraph.

With the vorticity data in the area of scrutiny being available in discrete form at 27 locations — in networking these 27 locations where locations are only connected to their nearest neighbors, a hexagonal pattern is generated (Figure V.4.1) — the first derivative is evaluated by calculating the slope between neighboring vorticity evaluations on the hexagonal scheme. To come up with a measure for the first derivative for one particular crank-angle within one engine cycle the arithmetic mean of the slopes evaluated for all vorticity pairs in the area of scrutiny is determined. This measure is then calculated consecutively for all engine cycles within one set of data with subsequent application of an averaging procedure over the results from the individual engine cycles. This calculation yields one point in the diagram in Figure V.4.11 representing the measure for the first derivative (degree of slope) within the area of scrutiny for this set of data. In a mathematical formulation the calculation reads for one particular CA:

$$Sl = \frac{1}{\#ECs} \sum_{j=1}^{\#ECs} \left(\frac{1}{N} \sum_{i=1}^{N} \frac{(\omega_{c1} - \omega_{c2})_i}{d_i} \right)_j \qquad (V.4.a)$$

where #ECs is the number of engine cycles over which averaging is performed, N is the number of vorticity pairs in the area of scrutiny (namely 33; from hexagonal pattern), and d is the spatial distance between the two locations of the two circumferential components ω_{c1} and ω_{c2} of the vorticity vector.

The evaluation of a measure for the variation -- sign changes -- of the second derivative is with respect to the averaging process the same as the one for the first derivative. First, the sign changes of the second derivative are determined in the area of scrutiny for individual engine cycles at a particular crank-angle and these numbers are averaged over all individual ECs for that data set. A sign change of the second derivative is determined by comparing the signs of two neighboring evaluations of slope in the vorticity distribution that is represented by the 27 vorticity evaluations. If there is a difference in sign between the two considered slopes either the top of a hill or the sole of a valley is detected and an index in the algorithm is incremented. Comparison of two slopes for the detection of sign changes includes three consecutive, 'chained' vorticities in the hexagonal pattern. Thus, 53 comparisons are performed in the area of scrutiny. The determination of SG being the average of all sign changes occurring within all engine cycles for one data set is performed for one crank-angle according to the following notation:

$$SG = \frac{1}{\#ECs} \sum_{i=1}^{\#ECS} \#sign\_changes_i \text{, where for one particular engine cycle}$$

$$\#sign\_changes = \#sign\_changes + 1, \quad if \quad sign\left(\frac{(\omega_{c1} - \omega_{c2})}{d_I}\right) \neq sign\left(\frac{(\omega_{c2} - \omega_{c3})}{d_{II}}\right) \quad \text{(V.4.b)}$$

The results in conjunction with the evaluation of the above defined parameters (SI and SG) can be seen in Figures V.4.11 and V.4.12.

V.4.1.2 Application of measures

Figures V.4.2 to V.4.10 illustrate that for each engine speed examined (10, 20, and 30 RPM) the sequence for the three valve lifts (3, 6, and 9 mm) exhibits -- for 132° crank-angle -- a decrease of magnitude in the vorticity distributions with increasing VL. The tendency suggested by this visual observation from the 2D and 3D contour plots is confirmed in Figure V.4.11 which contains at a crank-angle of 132° a measure for the steepness (Sl, equation V.4.a) between hills and valleys in the landscape of the vorticity distribution in the area of scrutiny. In this figure, where curves are plotted in a single logarithmic coordinate system, the three curves for the three engine speeds demonstrate clear trends with valve lift. It can be inferred that the larger the valve lift the less steep are hills in the vorticity distribution. Also, Sl decreases for one valve lift with decreasing engine speed. The curve for 30 RPM engine speed which suggests a linear behaviour in the logarithmic plot must be considered the most reliable because averaging has been performed over 64 engine cycles (20 RPM $\Rightarrow$ 42, 10 RPM $\Rightarrow$ 21).

Figure V.4.12 exhibits the measure for the frequency of the hill/valley fluctuation -- represented by SG -- in the landscape of the vorticity distribution in the area of scrutiny at 132° CA. To within the margin of accuracy the three curves corresponding to the three engine speeds not only align but are also constant with valve lift. This is an interesting fact implying that the frequency of the hill/valley fluctuation is, in conjunction with the length scale resolved by the applied LIPA laser grid, independent of engine speed and valve lift. To take it one step further, one might conclude on the basis of the results presented in Figure V.4.12 that, on the length scale investigated, mixing performance is considerably alike at all parameter settings of the engine. These results indicate how misleading an analysis of mixing based on length scale alone can be. Clearly, the shape and magnitude of

the kinetic energy and vorticity energy spectrum must be taken into account, as well as the range of the spectrum.

Although mixing is initiated on the scales the LIPA grids can resolve, ultimately mixing is associated with small length scales which could not be resolved in this study. Further investigation with denser spacing of laser lines in the investigation grid can yield insight on what happens on those scales. As far as the large scales are concerned, the differences in the nine investigated flow fields are within experimental error.

The constant values for SG along with increasing values of Sl (for engine speed ⇑ & VL ⇓) indicate that in the examined engine cylinder much stronger vortical motion exists in connection with high engine speeds and small valve lifts on identical length scales.

V.4.2 Energy contained in vortical motions

A third quantity is established in this section, namely the energy contained in the vorticity evaluated at the 27 locations in the area of scrutiny. This energy associated with vortical motion -- on the length scale examined -- in the area of scrutiny was evaluated for each of the nine settings of the engine parameters. The evaluation was performed at 132° CA in order to compare the results to the evaluations of the kinetic energy in section V.2. The nine values in Figure V.4.13a and b depicting measures for the vortical energy are averages of the energy associated with the circumferential component of the vorticity vector over the area of scrutiny and the number of engine cycles examined for each set of data. The calculation of the vortical energy (VE) is similar to that of the kinetic energy in equation V.2.a and reads:

$$VE = \frac{1}{\#ECs} \sum_{j=1}^{\#ECs} \left(\frac{1}{N} \sum_{i=1}^{N} |\omega_{ci}|^2 \right)_j \qquad (V.4.c)$$

where N is the number of vorticity evaluations in the area of scrutiny (27) and ω_c is the circumferential component of the vorticity vector.

Information on velocity magnitude *and* orientation from several velocity vectors are incorporated into the value of a local vorticity -- and thus into the vortical energy defined by equation V.4.c -- as mentioned earlier. The kinetic energy, on the other hand, is a scalar which denotes merely the order of the velocity magnitude. When comparing curves containing energy information in connection with vorticity with curves containing kinetic energy information in the same regions of interest, one can note -- based on the statements made in the preceding two sentences -- the following: If the structure (which is based on orientation information from the velocity vectors) of the examined flow fields was to be essentially the same for all nine flow fields resulting from the nine settings of engine parameters, orientation of velocity vectors becomes insignificant and it should be possible to superpose curves for kinetic and vortical energy -- as defined by equations V.2.a and V.4.c -- by appropriate scaling. In other words, if the orientation of velocity vectors with respect to each other was, in the average, identical in the flow fields of the nine data sets, the change of vorticity (energy) would be only dependent on the velocity magnitudes, and, thus, the kinetic energy.

Figure V.4.13 demonstrates that for 10 and 30 RPM engine speed the curves denoting KE and VE could be overlapped by appropriate scaling, however, not for 20 RPM engine speed. Employment of small data sample size and low resolution of the LIPA grid demand caution, though, in the discussion of the vortical energy data, particularly for the higher engine speeds and low valve lifts where small scale flow structure characterizes the flow field which cannot be resolved appropriately (higher error in vorticity energy).

In Figure V.4.13a the actual energy magnitudes are plotted for the vortical and kinetic energy in the area of scrutiny for the nine sets of data for 132° CA. In Figure V.4.13b these curves have been normalized for each engine speed by the energy values for 9 mm

valve lift. The idea behind normalization was to try to find for one engine speed, the differences between the two energy curves (KE and VE) with respect to valve lift. The question after assimilation of the two energy curves at 9 mm VL is whether vorticity energy increases proportionally with kinetic energy -- if the two curves collapse it will be seen as a verification of the fact that the flow structure is essentially the same for the three valve lifts at one engine speed. Or whether there are differences encountered at the other two VLs (3 and 6 mm) -- these differences must be due to differences in the structure of the flow field.

The result is intermittent. While the two curves for kinetic and vortical energy in Figure V.4.13 for 10 and 30 RPM engine speed coincide to within the margin of error, the two energy curves for 20 RPM engine speed exhibit conceivable differences. One notices that for this speed the values for the vortical energy at 3 and 6 mm valve lift decrease with respect to the corresponding values for the kinetic energy, particularly for the normalized curves in Figure V.4.13b. One could speculate on slightly slippery grounds [since the differences could be due to inaccuracy in the data reduction process; however, this uncertainty will be put aside at this point for argument's sake] that the essence from the preceding sentence implies that the structure of the flow field becomes different with decreasing valve lift on the length scale resolved. From the above observations, and taking into account what has been said in section V.2.3 about the break-up of vortex structures created by the intake jet, it is possible to conclude that for 20 RPM and 3 and 6 mm valve lift the vortex rings of the intake jet break up before the jet reaches the cylinder wall -- as opposed to the 9 mm VL case where the vortex structures presumably survive until the jet impinges on the wall -- and thus creating the lower degree of structure responsible for the non-unity ratio of kinetic and vortical energy for 3 and 6 mm VL.

Recall that the circumstance that the results for 20 RPM engine speed deviate from the results for 10 and 30 RPM engine speed was also found in the discussion of the

recirculativity in section V.2.2. For an axisymmetric assembly with a bore/stroke ratio of about '1' there must be some kind of transition in fluid dynamical behaviour at maximum Reynolds numbers of around 4000.

V.4.3 Miscellaneous topics involving vorticity distributions

V.4.3.1 Axisymmetry of the flow field

From the two-dimensional contour plots of the vorticity distributions in Figures V.4.2 to V.4.10 one can assert that the degree of axisymmetry about the cylinder axis exhibited by the flow field is generally rather low for instantaneous vorticity data (recall that the vorticity distributions in the upper and lower left corners are due to the extrapolation procedure set forth by the used software). However, there are occasional times when events exhibit some degree of axisymmetry, as for instance for 10 RPM engine speed and 3 mm valve lift (Figure V.4.2) where a hill to the left side of the cylinder axis has its counterpart in a valley to the right of the axis. The marginal shift of the hill/valley formation with respect to the cylinder axis might be due to slight asymmetries in the setup of the engine model as has been experienced in the investigation for and outlined in chapter IV.

For the highest engine speed (30 RPM), the author of this work perceived considerable asymmetries of the flow field about the cylinder axis during the actual LIPA experiments (taking advantage of the optical character of LIPA to provide a form of flow visualization). Particularly for a valve lift of 6 mm it could be observed that the setup of the intake flow structure exhibits very high variations from cycle to cycle. For some cycles the 'left' main recirculation pattern or 'vortex' (in the observed plane) dominates, at others the 'right' one. Then, during some cycles, considerable axisymmetry was encountered. Other engine cycles witnessed convection of the left vortex to the right and again others

saw the right vortex convecting to the left, crossing the cylinder axis. Less frequently, a stream of fluid crossing the cylinder axis diagonally towards the valve was noticed which stems from the flow at the outer perimeter of the main vortex (left or right). The fluid at the perimeter of the vortex cannot follow the high curvature flow and breaks off.

In general, it was observed qualitatively during the LIPA experiments that axisymmetry of the flow field essentially prevails until around midstroke and that the flow field then becomes highly three-dimensional. The flow field during induction is naturally a function of piston position. There is a steady build-up of the main toroidal recirculation pattern (as has been shown in section V.1.1). At midstroke the distance between piston and chamber head is about equal to the radius of the main toroidal recirculation pattern. Thus, the particular boundary conditions around 90° crank-angle are favorable for the main TRP where the adverse pressure gradient the intake jet experiences above the piston head turns the flow towards the cylinder axis and forces the fluid into a rotational flow (the cylinder axis can in this context and in fluid dynamical terms be considered a plane wall); Figure V.4.14b. Also, at midstroke the incoming jet flow has the highest momentum flux, resulting in the strongest rotational flow exhibited by the main TRP. After midstroke the momentum flux of the intake jet decreases and the distance between piston and chamber head increases with the consequence that the supply of momentum to the main TRP becomes smaller, and that the adverse pressure gradient that serves as a mechanism to turn the flow into the main TRP moves downwards and becomes less important; Figure V.4.14c. Consequently, after midstroke, the main toroidal recirculation pattern cannot sustain its momentum against dissipation. Its two-dimensional appearance in the laser grid plane diminishes, and out-of-plane motion can be perceived. This visual observation has yet to be verified by LIPA - data.

V.4.3.2 Vorticity distribution in the EA domain

LIPA offers the opportunity to acquire planar data that is based on instantaneous information of the flow field for both, maps of velocity vectors as well as for vorticity distributions. This is one tremendous advantage that LIPA possesses over single-point measurements performed by, e.g., Hot-wire and LDA techniques. Vorticity information in the ensemble averaged domain, as offered by Hot-wire and LDA, cannot reflect, naturally, the fluid dynamical mechanisms during individual engine cycles and therefore cannot truthfully account for mixing performance. This shortcoming in conjunction with single-probe measurement techniques is demonstrated in an impressive way by Figure V.4.15 where a vorticity distribution evaluated from an ensemble averaged velocity field for 20 RPM engine speed and 3 mm valve lift at 132° crank-angle (Figure V.4.15a and b) is displayed side-by-side with a typical vorticity distribution from an individual engine cycle with the same engine parameters (Figure V.4.15c and d). [Note, that for the 2D plots in this figure and for all 2D plots in the following figures, the 2D plots display vorticity information for the same region as for the one in Figures V.4.2 through V.4.10.] The 3D plots show that the actual magnitude of the circumferential component of the vorticity vector assumes much higher values within individual engine cycles than indicated by the landscape of the vorticity distribution from the EA domain, where the vorticity distribution presents itself as rather smooth. The hill/valley fluctuation appears to be higher in an individual engine cycle as well.

In the beginning of section V.3.1 the author raised concerns about the validity of conclusions based on results from the EA domain. Here, these concerns experience support. However, to be fair to results stemming from an analysis of EA data, information from the EA domain has its legitimacy in connection with evaluations of, for instance, the induction angle and the center of rotation of the main recirculation pattern.

V.4.3.3 Influences of crank-angle and engine cycle on vorticity distributions

Figure V.4.15 also contains a comparison of results at 132° CA (Figure V.4.15c and d) and at 180° CA (end of stroke, Figure V.4.15e and f), both taken from the same engine cycle (#27) at 20 RPM engine speed and 3 mm VL. It is very useful to obtain information about fluid dynamical quantities as they are encountered towards the end of the induction stroke since this knowledge can be used as initial conditions for computational evaluations of fluid dynamical quantities throughout the compression stroke.

For 180° CA one can see in the plots of Figure V.4.15e and f that the hill/valley configuration characterizing the intake jet nearly disappears as can be expected since the incoming flow through the valve ceases towards the end of the stroke. However, the vorticity magnitudes in the distribution for the flow field at 180° CA seem to be not much smaller when compared to those at 132° CA. The hill/valley fluctuation even appears to be about the same. In fact, calculations of SI, SG, and VE -- which are defined above in equations V.4.a to V.4.c and whose evaluations can be obtained from Table V.4.1 -- for 180° crank-angle in the area of scrutiny indicate that the values of SI, SG, and VE for this particular engine cycle are well in the range of the respective average-values encountered at 132° crank-angle also provided in Table V.4.1 (column 3). Within the engine cycle, SI decreases moderately as the flow evolves from 132° CA towards the end of the stroke, SG actually increases marginally, while the vortical energy decreases significantly. From these evaluations of SI, SG, and VE obtained for an individual engine cycle one can deduce that for 20 RPM engine speed and 3 mm VL the average vorticity magnitude in the area of scrutiny decreases strongly towards the end of the intake stroke, and that the spatial structure of the flow field remains appreciably constant.

Table V.4.1: Comparison of Sl, SG, and VE between two different crank-angle positions for individual engine cycle as well as averaged over 42 ECs.

		20 RPM, 3 mm VL, EC #27		Average at 132 deg from 42 ECs
		132 deg CA	180 deg CA	
Sl	(in 1/smm)	39.69	32.22	31.79
SG	(in %)	47.2	52.8	28.0
VE	(in 1/s^2)	32843	16097	18103

In Figure V.4.16 vorticity distributions for 20 RPM engine speed and 3 mm valve lift at crank-angle 132° have been plotted for three consecutive engine cycles (#27, 28, and 29). From Figure V.4.17, where the value of Sl within individual engine cycles prior to the application of the averaging procedure over the number of engine cycles for this set of engine parameters (20 RPM engine speed and 3 mm VL) is shown as a function of engine cycle, it can be seen that ECs #27, 28, and 29 exhibit considerably different levels of slopes between neighboring locations of vorticity evaluations. This is, to some extent, discernible qualitatively in the two- and three-dimensional plots in Figure V.4.16a through f. Slopes between hills and valleys in the distribution of the circumferential component of the vorticity vector appear to be higher in the area of scrutiny in Figure V.4.16a and b than in Figure V.4.16c and d, for example.

In an effort to point out differences and similarities between the vorticity distributions encountered for the three consecutive engine cycles it can be noticed that one substantial difference between the vorticity distributions for engine cycles #27 and 29 is established by a long-stretched area of vorticity located below the hill/valley configuration that is created by the intake jet. In engine cycle #27 this area contains negative vorticity, in EC #29 positive vorticity values are observed. In engine cycle #28 no such long-stretched region can be observed at all. The differences in the landscapes of the vorticity distribution

between engine cycles for one set of data and one crank-angle illustrate and symbolize the cycle-to-cycle variability that is so often the subject to research in the engine community.

It is, in the discussion of vorticity data, also interesting to study for one particular engine parameter setting the evolution of the vorticity distribution with crank-angle within one engine cycle. Using vorticity distributions, one can more directly answer questions about development and dissipation of flow structures than it is from a sequence of maps containing instantaneous velocity vectors. As mentioned earlier, one vorticity vector combines information on magnitude and orientation of several velocity vectors which makes it easier to depict flow structures in distributions of vorticity. The study of the evolution of flow structures with crank-angle on the basis of vorticity distributions has been done for 10 RPM engine speed and 9 mm valve lift. At 10 RPM engine speed, the highest temporal resolution could be achieved for this work (2° crank-angle). A valve lift of 9 mm was chosen because the structures in a flow field in connection with 10 RPM engine speed and 9 mm VL can be expected to exhibit, in terms of fluid dynamics, the most stable behaviour among the flow fields investigated due to the lowest momentum flux of the incoming jet. Therefore, it is for this case the most likely that flow structures, as denoted by vorticity distributions, can be identified in one plot and followed as crank-angle evolves.

The results are presented in Figure V.4.18 for a sequence of distributions of the circumferential vorticity component right around mid-stroke (88°, 90°, and 92° CA). Despite an overall similarity of the three plots it is not possible to distinguish unambiguously areas of vorticity that stem from an evolvement of one hill or valley as crank-angle advances; no unequivocal statement can be rendered according to which a particular hill (valley) in the vorticity distribution at one crank-angle can be identified in the distribution at the proceeding crank-angle position.

Another sequence of vorticity distributions for three consecutive crank-angles is exhibited in Figure V.4.19 at lower *piston* speed at crank-angles 150°, 152°, and 154°. Here again, the vorticity distributions appear similar and it is again not possible to point out specific vorticity structures and follow them through the sequence.

The time scale in connection with the rearrangement of the vorticity distribution between examined crank-angles is obviously smaller than the data sample rate of 33.33 ms – even for this setting of low engine speed and large valve lift; thus, not allowing for an unambiguous identification of a particular hill (valley) in vorticity distributions at two consecutive crank-angles. There is possibly one exception, however. In the lower left corner of the two-dimensional plot in Figure V.4.19e a very distinct and prominent hill/valley system can be discerned for 154° crank-angle. The early phase of development of this system can be perceived vaguely in Figure V.4.19c (152° CA). This system must be, for several degrees of crank-angle of piston motion, so stable that it does not get destroyed, or rotated so as not to be oriented normal to our data plane. In fact, it could be observed at 156° CA (map of vorticity distribution for this CA is not shown in figure) as well; between crank-angle 154° and 156° the system is however dissipating and thus becoming very weak.

V.5 Annulus Intake Jet

The LIPA grid of laser lines has been re-scaled to provide higher resolution data in a region around the valve in order to investigate the incoming free annulus jet. Velocity vectors could be determined at 15 locations from this application of LIPA. More detailed information on the applied grid (Figure II.2.3b), its resolution, and the accuracy of the measurements is available in chapters II and III. The intake jet is examined at three different settings of the engine parameters (engine speed and valve lift); two valve lifts -- 3 and 9 mm -- are considered at an engine speed of 20 RPM, and the 3 mm valve lift case is investigated at an engine speed of 30 RPM. Ensemble averaged results as well as maps of instantaneous velocity vectors will be discussed in the following sections.

The most interesting fluid dynamical issue in the study of the intake jet 'under the magnifying-glass' are the interactions between the annular intake jet and the two toroidal recirculation patterns bordering the jet, in particular that of the main TRP. The goal in this section on the scrutiny of the intake jet is then to achieve a physical description of these interactions and to measure the strength of the generated and manipulated flow structures of the intake jet as they evolve in space and time. The interactions between the jet and the periphery of the main TRP appear to be one of the major keys for the fluid dynamical processes in the entire engine as has been suggested in section V.2.

The maps of velocity vectors -- or better, the maps containing distances that fluid particles convected in the direction denoted by arrows -- presented in the following sections, depict the flow field as it is represented 0.17, 0.34, and 0.51 ms (for 30 RPM engine speed and 3 mm VL, for 20 RPM and 3 mm VL, and for 20 RPM and 9 mm VL, respectively) after the laser fired to build up the grid that illuminates the fluid particles. Note that the time intervals are in integer multiples of 0.17 to simplify the act of comparison of the plots for different engine speeds and valve lifts.

Except for a few issues that concern fluid dynamical descriptions of the global behaviour of the intake jet, it is not feasible to compare the results obtained from experiments with 3 mm valve lift to those obtained with 9 mm valve lift, e.g. to relate velocity vectors on a vector-to-vector basis. This is because the grid of laser lines marks fluid particles at different locations with respect to the axis of the intake jet for the two cases (the investigation grid was moved for the LIPA experiments examining the intake jet at 9 mm VL in order to have intersections of laser lines at fluid dynamically interesting spots in that flow field). Additional difficulties arise when trying to compare results because of the fluctuation of the induction angle, which causes the locally fixed velocity vectors to represent — as crank-angle evolves — different areas within the flow field. This, furthermore, makes it difficult to compare results for one engine parameter setting at different crank-angles.

V.5.1 EA domain

The ensemble averaged results are obtained from 40 engine cycles for the 20 RPM engine speed, and from 60 engine cycles for 30 RPM. Again, reasonable convergence was found. As in section V.1.1, the case of the 20 RPM engine speed with the 3 mm valve lift will be examined in greater detail since flow visualization results are available for this set of engine parameters, and the results are reasonably representative for those obtained with different engine speed and different valve lift.

V.5.1.1 20 RPM engine speed, 3 mm valve lift

In order to illustrate at what locations within the engine cylinder, especially with respect to the free annulus jet, the grid of laser lines enables a quantitative analysis of the flow field to be made, superpositions of maps of EA velocity vectors onto pictures (instantaneous realizations) generated by flow visualization have been constructed (this

also reduces the chances of misinterpretations of flow structures). The superpositions have the effect of filling in the space between individual vectors with information. The superpositions were done at crank-angles 32°, 52°, and 92°. The result is shown in Figure IV.2.2g, j, and k.

In studying the congruity of velocity vectors with the flow structures, it is obvious that the ensemble averaged velocity vectors do not and cannot describe in Figure IV.2.2g, j, and k exactly the particular instantaneous flow situation denoted by the flow visualization results, primarily within the region dominated by the intake jet [recall that EAs describe *preferred* directions of the flow field]. Both the fact that the jet is turbulent and because of cycle-to-cycle variability at the moment of data acquisition (whether via flow visualization or LIPA), the imager faces different details of the flow structure.

As a first result from the sequence of the three superposed images in Figure IV.2.2g, j, and k it is obvious that the length of the transitional flow decreases between 32° CA and midstroke because of the increasing Reynolds number. This observation is congruent with the results by Yule (1978).

Table V.5.1: Assignment of individual velocity vectors to flow structures

Velocity Vector #	Region of the flow field that is described by these velocity vectors
2 and 4	Edge of intake jet close to inlet valve
1, 3, and 5	Corner between cylinder wall and cylinder head
7, 10, 13, and 15	Periphery of main recirculation pattern
6 and 8	Edge of intake jet that interferes with motion from upper corner flow
9 and 12	Edge of intake jet that interferes with periphery of main TRP
14	Around axis of intake jet
11	indecisive

Based on the superposed data in Figure IV.2.2g, j, and k one can assign the 15 velocity vectors to certain flow regions and structures. (Figure II.2.3b contains the number assignment for each of the 15 velocity vectors examined in this chapter. For Figure IV.2.2g, j, and k the investigation grid was flipped.) Velocity vectors #7, 10, 13, and 15 are located in the periphery of the main recirculation pattern. This flow structure has a rotational bulk flow with turbulent motion associated with the smaller length scales within the TRP. One expects these length scales to be smaller than the spacing density of laser lines in the investigation grid indicating that these four velocity vectors must be statistically independent from each other. Velocity vectors #2 and 4 denote the upper edge of the incoming jet close to the valve when the jet commences to exhibit instabilities, i.e. waviness. Velocity vectors #1, 3, and 5 represent the fluid motion in the corner between the cylinder head and wall, including that of the toroidal recirculation pattern in this area. Velocity vector #11 cannot be assigned to any particular flow structure; to variable degrees and intermittently, depending on the crank-angle, it describes the upper corner TRP and the intake jet. The remaining five velocity vectors portray the intake jet after the jet matured downstream. In Figure IV.2.2g (32° CA) velocity vectors #6, 12, and 14 depict coherent flow structures; in Figure IV.2.2j and k (52° CA and 92° CA) velocity vectors #6, 8, 12, and 14 denote eddies in the turbulent jet after it experienced vortex ring break-up. A summary of the role of each velocity vector in the description of the flow field is given in Table V.5.1. From Figure IV.2.2g, j, and k one can conclude that the velocity vectors appear to be very reasonable representations of the motion of the flow structure that they quantify.

It is apparent that the coarse spacing of the grid of laser lines offers very low spatial resolution between velocity vectors. No fluid dynamic quantity defined by spatial integration or differentiation, e.g. length scales from integration, can be determined for particular flow structures with this setup since the procedure of integration or

differentiation over several velocity vectors in the present maps would include information from other flow structures which leaves the calculation invalid. Also, since some of the velocity vectors are statistically independent they cannot be the basis for the calculation for one specific integration quantity. Furthermore, the temporal resolution (4° crank-angle corresponding to 33.33 ms) is too low to determine turbulence intensities or length and time scales from velocity vector profiles at one location by employing, for instance, Taylor's hypothesis in an interpolation scheme. Hence, the way we will use the data will be analogous to having 15 individual probes in the flow that are non-intrusive and which give velocity information in any direction without bias.

There is a region in the flow field dominated by the incoming jet which can be called the 'interface zone'. In the interface zone the flow structures of the incoming free annulus jet and the main toroidal recirculation pattern meet, interact, and change each other. More specifically, in this area the azimuthal vortex ring structures created by the intake jet come into contact with the turbulent periphery of the main TRP. The evolution of fluid dynamics in this zone manifest the mechanism of direct transfer of momentum to the main TRP. In the velocity maps for 20 RPM and 3 mm valve lift acquired for this work this zone comprises basically, unfortunately, only two vectors, #9 and 12. From these, supported by flow visualization results, it can be observed that the contact of the main TRP with the intake jet is essentially tangential. Because of the low spatial resolution, however, it would be rather risky to infer further manifestations from an observation of the two single velocity vectors #9 and 12 for the purpose of a deduction of fundamental fluid dynamics from the interface zone. At this point it is worthwhile mentioning that the potential ultimate goal as outlined in the beginning of section V.5 -- namely, a thorough investigation of the interactions of the intake jet with the two TRPs -- cannot be met in this work due to the coarse spacing of lines in the investigation grid. One can see however, that an analysis of the interface zone involving higher spatial resolution of the

LIPA grid, though, will yield remarkable insight into the fluid dynamics of the interactions between the intake jet and the main recirculation pattern which in turn influences the main TRP and thus the induction stroke as a whole. This, of course, presupposed that both a high resolution LIPA grid and 'simultaneous' flow visualization results are obtained from one and the same engine cycle. What the author can do in this study, nevertheless, based on the data inferred from the applied coarse laser grid is deliver singular pieces of information of a mosaic, where the mosaic is the comprehensive description and modeling of the jet-TRP interactions, and possibly furnish speculations about fluid dynamics and suggestions for the improvement of the measurement technique on grounds of these pieces.

Hence, despite the coarse spacing, some interesting properties of the intake flow can be unveiled by the ensemble averaged velocity maps in Figure V.5.1 where velocity information is given for 20 RPM engine speed and 3 mm valve lift at selected crank-angle positions.

In general, the maps exhibit considerably stable flow fields after midstroke, which is a verification of results obtained in section V.1.1, although there are some velocity fluctuations observable as crank-angle evolves in the periphery of the main TRP as well as in the interface zone which can be expected due to highly turbulent motion and the limited number of images over which the EA procedure was performed.

As can be seen in the pictures of Figure IV.2.2g, j, and k the core of the intake jet is confined to such a small width compared to the spatial resolution of the grid of laser lines that it is difficult to capture the intake jet with intersections of laser lines in order to infer fluid dynamical quantities from the jet's core. The jet appears to be depicted, though, in the velocity maps of Figure V.5.1g at 84° CA by velocity vectors #2, 4, 8, and 11, however, it is not clear to what extent and where within the jet. Nevertheless, by considering orientations of velocity vectors it is possible to 'construct' the intake jet by eye

and thus geometrically classify fluid dynamical conduct of the flow field in an engine. For example, one can observe the inclination behaviour of the intake jet as it inclines first towards the cylinder axis and is being pushed back up again (Figure V.5.1a through g).

In studying the individual maps containing ensemble averaged velocity vectors in Figure V.5.1 one notices that until shortly before midstroke (about 80° CA) velocity vectors #7, 10, 13, and 15 which after midstroke depict the periphery of the main TRP, document the inclination of the intake jet towards the cylinder head. Another interesting observation is that from 80° CA on (after the intake jet has been pushed back up by the main TRP) it seems to be possible to discern the flow of vortex ring structures in the interface zone in the velocity maps (depicted mainly by velocity vector #12). The presumably observable flow of vortex structures in the velocity maps is denoted by the fact that the orientation of vector #12 prescribes a flow away from the axis of the intake jet. However, information provided by this one velocity vector is too ambiguous to arrive at qualitative conclusions about vortex structures generated by the intake jet.

It is an interesting occurrence that velocity vector #2 experiences a reorientation towards the end of the induction stroke by about 180°. From Figure V.5.1 one can see that velocity vector #2 assumes at crank-angles 172° and 180° a direction opposite from that of what the intake jet prescribes throughout the stroke. This reorientation process is encountered for an engine speed of 30 RPM (3 mm VL) as well; in this case it sets in earlier.

The upper corner toroidal recirculation pattern also has an influence on the development of the intake jet. A set of four velocity vectors (#1, 3, 5, and 11) essentially represent the upper corner TRP as mentioned at the beginning of this section. They evidence a very stable flow pattern in the upper corner after midstroke. The generation of the TRP takes place in the upper corner shortly before midstroke as discussed in section IV.1.2 and outlined in section V.5.1.3 in the discussion of the results for 20 RPM

and 9 mm valve lift. Unfortunately, the flow of the fluid transported by the upper corner TRP cannot be unambiguously characterized when it is approaching the jet (velocity vectors #6 and 8). This is because the actual intake jet cannot be discerned clearly from the maps, and one therefore cannot estimate the space available to the TRP to turn into the direction of the jet. It is evident again that the spatial spacing of IAs in the laser grid for the examination of the intake jet is far from satisfying. One is compelled to speculations about the fluid dynamics at the site where the upper corner recirculation pattern and the intake jet join, in particular about the meaning of velocity vectors #6 and 8 in the velocity maps. Two interpolation scenarios are possible. If the jet evolves close to the two vectors (#6 and 8) the flow in the upper corner will impinge onto the incoming jet and the contact of the upper corner flow with the intake jet will directly impart momentum to the flow in the upper corner through shear forces. The upper corner flow does not really recirculate (however, considering continuity aspects of the impinging flow, it seems fair to say that it turns into the direction of the intake jet flow), and it would seem that the flow in the upper corner forces, by impinging onto the incoming jet, a downward motion onto the jet. If the intake jet is further away from vectors #6 and 8 it would give the upper corner flow more room to turn into the direction of the jet and recirculate. However, it does not seem likely that there is enough room for the upper corner recirculation pattern to reorient to such a degree that it would touch the intake jet tangentially as does the main TRP on the other side of the jet. In this case, fluid carried by the upper corner TRP gets entrained into the intake jet by the toroidal vortex rings shedding from the jet.

The effect of the upper corner toroidal recirculation pattern on the intake jet is of a considerably different nature than the one of the main TRP. Although this is a qualitative result, it is not the type that can be inferred from the flow visualization pictures in chapter IV.

In the EA domain, when the field of velocity vectors indicate similar orientation in connection with equally high velocity magnitudes, we can assume that there is a very

structured flow. The velocity vectors in the upper corner (#1, 3, and 5) exhibit just that, suggesting that the recirculation pattern in the upper corner is much more structured than, for instance, the periphery of the main TRP depicted by velocity vectors #7, 10, 13, and 15. These indicate uncorrelated, low magnitude velocities. The turbulent flow field constituting the periphery of the main recirculation pattern consists of flow structures that convected a long way after their creation by the intake jet and, through that convection, have undergone diverse interactions with the different elements of the entire intake stroke, such as the boundary layer flow along the cylinder wall, explaining the fine scale structured flow field in the periphery of the main TRP. The eddy structures of the upper corner recirculation pattern have a shorter history. Velocity vectors #1, 3, and 5 depicting the upper corner TRP indicate that the TRP's bulk flow dominates over the motion of the eddies.

The accounts of fluid dynamical behaviour outlined in the preceding paragraphs are based on the results of 15 data points distributed throughout the region of investigation, and rely heavily on the previous quantifications and flow visualizations. Even with 15 data points in this region, it is very clear that the physics cannot be easily determined -- this speaks very loudly for the need to area information of the LIPA type. To verify the suggestions made above a study is required where a grid of laser lines with much denser spatial spacing is employed.

V.5.1.2 30 RPM engine speed, 3 mm valve lift

Velocity distributions look very much alike for 20 and 30 RPM engine speeds with 3 mm valve lift, which is why the 30 RPM case will not be discussed in depth; only a few notes are worthwhile mentioning.

First, momentum of the intake jet increases with engine speed as has been outlined in section V.2.2. The distances denoted in the maps in Figure V.5.2 for 30 RPM engine

speed are representative for the flow field after 0.17 ms, which means that the velocities would be twice as high in a time frame that is associated with the results for 20 RPM engine speed and 3 mm valve lift in Figure V.5.1 (0.34 ms). From Figure V.5.2 it is then possible to infer that the velocity at the valve is indeed significantly higher for 30 RPM (compare flow situations around midstroke, Figures V.5.1h and V.5.2c).

Then, the increased inclination of velocity vector #4 (which depicts the upper edge of the incoming jet for the 3 mm VL case) towards the cylinder axis throughout the intake stroke in the velocity maps for 30 RPM engine speed as compared to the inclination of the same vector for 20 RPM suggests that the induction angle for the intake jet associated with 30 RPM engine speed is smaller, thus the intake jet steeper. This is a verification of the corresponding curves in Figure V.1.3 from section V.1.2 (induction angle vs CA). This occurrence makes sense from first principles according to which the higher engine speed (30 RPM) imposes a higher pressure gradient which in turn leads to a steeper route of the intake jet when it enters the cylinder.

V.5.1.3 20 RPM engine speed, 9 mm valve lift

As mentioned in the beginning of this chapter, for 9 mm valve lift the investigation grid had been adjusted to have intersection points, and thus velocity information, at potentially interesting locations in the flow field. Unfortunately, no embedding of the velocity vectors in a picture of flow visualization results can be achieved here due to the lack of flow visualization results at this engine parameter setting. Hence, it is not possible to properly assign the individual velocity vectors to flow structures and the interpretation of the flow fields is, in conjunction with the low laser grid resolution, even more vague. However, some general issues can be discussed on the basis of the results with this engine parameter setting.

The flow patterns for the realization of 20 RPM engine speed and 9 mm valve lift as displayed in Figure V.5.3 in terms of maps of velocity vectors is very stable after midstroke until the very end of the stroke which is not, to this degree, the case for the smaller valve lifts. This must be an indication for the more structured flow patterns in connection with slower development of flow structures as typical for larger valve lifts which has been discussed in section V.2.

For this setup of the laser grid, one laser line passes through the cylinder very close to the evolving intake jet; see for example the flow situation at 96° crank-angle (Figure V.5.3c) when the induction angle reaches a local maximum (see Table V.5.2). Before CA 96° the strength of the main TRP increases with crank-angle and pushes the intake jet upward. This had been observed in section V.1.1. During this phase the flow pattern in the upper corner does not exhibit strong momentum. From 92° CA on it could be observed for 20 RPM engine speed and 9 mm VL that the upper corner flow of fluid seems to gain strength. As a matter of fact, the motion in the upper corner can be described a toroidal recirculation pattern only from this moment on, as has been confirmed by flow visualization results at low speeds (section IV.1.2). The created upper corner TRP forces the intake jet to move slightly back down towards the cylinder axis. From 108° CA on the induction angle stabilizes and fluctuates marginally about the plateau value (see Table V.5.2). The fluctuation is governed now by the interactions of the azimuthal vortex structures of the intake jet with the recirculation patterns to either side of the jet.

The grid of laser lines did not reach far down enough in these experiments with the 9 mm valve lift in order to display what has been called the interface zone in the previous sections. In fact, with the awareness of what the LIPA grid of laser lines did not accomplish one can go back to the experimental phase and improve the grid. The application of LIPA to a particular problem is a reiterative process.

V.5.1.4 Comparison between investigated cases

In general, very good conformity can be established between the maps of velocity vectors that present the intake jet, and the ones that present the overall fluid motion in the engine cylinder which had been discussed in section V.1.1. Furthermore, very good affinity can be found when comparing the intake flow at 20 RPM engine speed and 3 mm valve lift as represented by the velocity maps with the intake flow as represented in the flow visualization pictures. The agreement of the two sets of LIPA results for the two different views with each other and their agreement with the flow visualization results establishes an additional sense of the accuracy of the LIPA experiments which leads to confidence in the results.

A profile of induction angle versus crank-angle can be extracted qualitatively from the plots of velocity vectors in Figure V.5.1 as the induction angle decreases towards a local minimum, increases towards a local maximum, and then fluctuates about a fairly constant plateau value (compare to results in section V.1.2). A detailed quantitative measurement of the induction angle is not undertaken because the velocity vectors are considerably ambiguous about what the actual angle is under which the intake jet enters the engine cylinder since one does not know where in the velocity maps the axis of the intake jet is exactly. One is thus compelled to interpolate between velocity vectors which contain velocity components from the vortex rings shed from the jet in order to evaluate the induction angle. A partial quantitative verification of the results obtained in section V.1.2 is, however, accomplished if one determines the crank-angle at which the induction angle assumes its highest value (highest drift back up towards the cylinder head) as well as the crank-angle from which on the induction angle assumes its plateau value. The appropriate numbers for the three data sets investigated in section V.5 can be found in Table V.5.2. The accuracy of these numbers is believed to be higher than the ones in section V.1.2

because of the increased spatial spacing of laser lines in the LIPA grid with which the intake jet is being examined. The correspondence to the results in conjunction with induction angles as determined in section V.1.2 is safely within the uncertainty associated with the evaluation of the induction angle itself.

Table V.5.2: *Occurrence of specific events in profile of induction angle; the numbers indicate the degree of crank-angle.*

	induction angle assumes local maximum	angle at which plateau is started
20RPM 3mm	84	92
20RPM 9mm	96	108
30RPM 3mm	78	90

V.5.1.5 The intake flow in terms of non-linear chaotic system dynamics

Based on the results gathered in the preceding sections one can summarize and theorize the following: The azimuthal vortex ring structures created by the free annulus jet come into contact with the periphery of the main toroidal recirculation pattern in the interface zone. The fluid dynamical interactions of the vortex structures with the recirculation pattern determine the shape of the flow field downstream including that of the main TRP. The induction stroke, thus, appears to consist, in terms of a model, of a reiterating control system with one input -- namely the free jet -- where the main TRP challenges the intake jet and the manipulated intake jet in turn influences the physics of the main TRP. The system is governed by steadily changing boundary conditions, i.e. the vertically moving piston head. In the EA domain this control system reaches equilibrium some time after midstroke when the boundary condition becomes unimportant. At this time, according to

section V.5.1.3, the toroidal recirculation pattern in the upper corner is created. The upper corner TRP also effects the intake jet which in turn influences the development of the upper corner TRP. Hence, after midstroke, a second control system is set up. In this context, a literature research on dynamics of non-linear chaotic systems might be helpful. The consideration of the induction flow field in terms of models will be beneficial for computerized analysis of the induction flow, in particular of the fluid dynamical characteristics of the main toroidal recirculation pattern, e.g. in terms of mixing performance. For this, of course, the interactions of vortex rings with the main TRP in the interface zone have to be understood.

As a practical application of system philosophy according to which the intake jet flow can be regarded as consisting of two reiterating systems (see preceding paragraph), a 'flip-flopping' mechanism maintained by the two control systems is thinkable after midstroke that explains the fluctuation of the induction angle. Flip-flopping could take place according to the following scheme: As a result of the intake jet's inclination away from the cylinder axis the upper corner TRP experiences an increased supplement of momentum and, in return, pushes the intake jet back down towards the cylinder axis. Now, the main TRP experiences an increase in momentum and, therefore, pushes the intake jet back up to increase the supply of momentum to the upper corner TRP. The possibilities of fluid dynamical interaction between the upper corner TRP and the intake jet comprise then both options of flow field conduct delineated in section V.5.1.1, namely impinging of high momentum flow onto the jet and recirculation of low momentum flow. This is merely a hypothesis. But an intuitively appealing one. The time scale that is associated with the increasing supplement of momentum to the upper corner TRP with subsequent inclination of the induction angle towards the cylinder axis is of smaller order than the one associated with the corresponding mechanism enforced by the main TRP.

V.5.2 Analysis of individual engine cycles

There are issues, such as momentum exchange of intake jet as well as magnitudes and correlations of small scale motion, that cannot be discussed in the EA domain since the procedure of averaging destroys instantaneous information about the flow field. Averaging melts the diversity of information available from individual engine cycles about, for instance, a flow structure at a particular location in the flow field -- information such as size and the different states of development of that flow structure -- into one *average* flow structure -- which never, of course, actually exists. This virtual flow structure summarizes the behaviour of the instantaneous flow structures. Furthermore, the averaging process levels out extreme values. The discussion of issues like the momentum exchange of the intake jet requires cycle resolved maps of instantaneous velocity vectors that reveal instantaneous in-cycle flow field information.

Unfortunately, as demonstrated in section V.5.1, the spatial spacing of the applied investigation grid for the study of the intake jet is much too coarse in this work to achieve a thorough picture of fluid dynamical mechanisms that involve a free annulus jet flow interacting with toroidal recirculation patterns on either side of the jet. Hence, it is impossible to infer a comprehensive, coherent fluid dynamics model of the flow within and around the annulus intake jet. Furthermore, it turns out that intersection areas encountered in conjunction with the LIPA grid from Figure II.2.3b are not small enough to resolve the small scale motion inherent in the flow. But, they do resolve the large scale energy containing motion. Thus, a few interesting features of the intake flow field, beyond those found in the preceding section, can be deduced from the analysis of individual engine cycles where results stem from the application of the 'close-up' grid of laser lines.

In the following, some details from the maps of velocity vectors from individual engine cycles (EC) will be discussed. For the 20 RPM engine speed and 3 mm valve lift case,

engine cycle #49 is a good example of an individual realization of the intake stroke. Results for this EC are displayed in Figure V.5.4. For 30 RPM and 3 mm VL, EC #24 is analyzed (Figure V.5.5); for 20 RPM and 9 mm VL it is EC #14 (Figure V.5.6).

V.5.2.1 20 and 30 RPM engine speed, 3 mm valve lift

For 20 RPM engine speed and 3 mm VL it can be observed in Figure V.5.4 that the intake jet is displayed by the velocity vectors in the maps at particular moments (crank-angles) when the axis of the intake jet lies very close to one laser line that is part of the laser grid (e.g. at 132° CA, Figure V.5.4q). At crank-angle 128° the axis of the incoming jet coincides with the laser line as well, indicating that for two consecutive maps of velocity information (crank-angle resolution for 20 RPM engine speed is 4°) the induction angle possesses the same value. On the other hand, at 152° CA (not shown in figure) the intake jet is depicted by velocity vectors #2, 4, 6, 8, and 11 also, however, four degrees before as well as after 152° CA, the axis of the jet is away from this laser line (for the velocity field at 156° CA see Figure V.5.4r). The succession of these three maps serves as an illustration for the fluctuation of the induction angle after midstroke. The sequence of velocity maps in Figure V.5.4 shows that the intake jet is highest back up (local maximum for induction angle) for 84° crank-angle (Figure V.5.4j). It also shows that at 132° CA the induction angle has about the same value as for 84°. The results on the induction angle inferred from EA velocity maps in section V.1.2 indicate that the induction angle does not reach the value of the local maximum before the very end of the induction stroke. This is another incidence where instantaneous data is not properly represented by results deduced in the EA domain.

The flow visualization results in section IV.2.2 suggest a repetition time scale for the toroidal vortex structures in the intake jet of about 33 ms (or 4° CA) between 25° and 40° crank-angle. If one assumes that there is a correlation between the repetition rate of

vortex rings and the fluctuation of the induction angle after midstroke, the time scale associated with the fluctuations of the induction angle after midstroke should be of the order of 33 ms as well. The range of 25° to 40° CA corresponds to 140° and 155° CA if one assumes symmetry of fluid dynamical behaviour for the intake jet about midstroke due to the symmetrical acceleration characteristic attained by the forcing movement of the piston head. As observed in the preceding paragraph, at 128° and 132° CA the intake jet assumes about the same induction angle indicating a time scale in association with the fluctuation of the induction angle of 33 ms. This corresponds closely with what has been found from the flow visualization results as a time scale for the development of azimuthal vortex rings in the intake jet. However, the time scale associated with the fluctuation of the induction angle has large error bounds since the temporal resolution of 4° crank-angle for an engine speed of 20 RPM transforms into a sampling rate lower than the Nyquist frequency for this problem. A closer comparison of time scales will stem from an investigation employing a higher sampling rate.

The observed congruity of vortex structures at 28° and 32° CA in the flow visualization results in section IV.2.2 cannot be observed unambiguously in the respective maps of velocity vectors inferred from LIPA - data provided by the close-up laser grid. Again higher resolution quantitative data is needed. It would be interesting to see whether LIPA results based on a field of velocity vectors derived from a LIPA grid with denser spatial spacing of the laser lines would show the basic similarity seen in the flow visualization, but still quantify the effects of the environment on the formation of these vortices.

Even with the higher resolution grid, Figure II.2.3b, it is not possible to study the vortex structures that are generated by the intake jet. However, it was indicated in section V.5.1.1 that there is evidence of some sort in the velocity maps for flow of vortex structures in the vicinity of the core of the intake jet. More specifically, as could be observed in section V.5.1.1, velocity vector #12 which is located in the interface zone was

found to exhibit at times, in EA, an orientation that cannot be expected to stem from a flow that is parallel to the axis of the incoming jet. From the maps containing instantaneous velocity vectors now (Figure V.5.4), it can be seen that the velocity vectors representing the fluid dynamics in the interface zone -- basically #9 and 12 -- have intermittently an orientation away from the jet axis; for vector #12 more often than for #9. This fluctuation of orientation of these two vectors might denote the motion of a fluid particle which is turned away from the jet axis by either the motion of a toroidal vortex ring, that of a fluid particle being entrained into the vortex ring, or that of a fluid particle within an eddy in the turbulent flow phase of the intake jet -- for the latter case velocity vector #14 can be included in the study. This assumption that velocity vectors #9 and 12 depict the motion of a vortex structure obtains support from the images generated by superposition of a map of velocity vectors with the corresponding picture from the flow visualization results where velocity vectors #9 and 12 are located at the edge of the intake jet. An attempt to quantify the flow structures as represented by velocity vectors #9 and 12 is not being performed because of the uncertainty about the location of the vectors within the flow structure at any particular moment due to the fluctuation of the induction angle.

In this context, similar results can be obtained from a study of the velocity maps stemming from an engine parameter setting of 30 RPM engine speed and 3 mm valve lift (Figure V.5.5).

There are two options to quantify flow structures using maps that contain velocity vectors: Either the LIPA results obtained with the coarse investigation grid has to be accompanied with a visual picture of the flow field that is recorded at the very same instant as the distorted LIPA grid, or much closer spacing of the intersection areas in a LIPA grid has to be accomplished yielding distances between knots in the laser grid far smaller than the length scale of the flow structures that are being studied.

In an analysis of the velocity vectors in the periphery of the main TRP (#7, 10, 13, and 15) in engine cycle #49 as exhibited in Figure V.5.4 it can be established from visual analysis of the vector maps that after midstroke these velocity vectors seem to be correlated at times (96° and 100° CA, Figure V.5.4l&m) and uncorrelated at others (120° CA, Figure V.5.4o). For 30 RPM and 3 mm VL (Figure V.5.5) correlation is encountered at 108° and 132° CA (Figure V.5.5c&d); at 144° CA (not shown in Figure V.5.5) the vectors appear to be uncorrelated.

As an example for an individual velocity vector that is located within the main recirculation pattern, vector #13 describes the strong fluctuating motion characteristic of the eddies in the main TRP, especially after midstroke when a consistent flow field is established for the engine cylinder as a whole. This is the case for 20 as well as for 30 RPM engine speed and 3 mm VL.

V.5.2.2 20 RPM engine speed, 9 mm valve lift

For 20 RPM engine speed and 9 mm valve lift, engine cycle #14 is displayed in Figure V.5.6. At midstroke (88° CA, Figure V.5.6b) the axis of the intake jet overlaps with one laser line from the LIPA grid. The velocity vectors depicted in the map in Figure V.5.6b to either side of the jet exhibit identical low magnitude characteristics, in fact, they suggest the width of the intake jet for this setting of engine parameters; even the orientation of these velocity vectors match roughly on a vector-to-vector basis when the axis of the intake jet is taken as symmetry line. This suggests that the velocity vectors generated by the laser line that overlaps with the intake jet depicts the jet at its centerline. A very symmetric flow situation about the axis of the intake jet is encountered at this particular moment. It is conceivable that the velocity vectors to either side of the intake jet describe the interactions between the flow structures at the edge of the jet with the recirculation patterns to either side. However, no unequivocal statement can be made

about the fluid dynamics that are described by the vectors to either side of the jet since these velocity vectors cannot be assigned indisputably to regions in the flow field around the intake jet due to the lack of simultaneous flow visualization results at this engine parameter setting.

V.5.2.3 Momentum of the free annular intake jet

At around midstroke of induction, at least for one map of instantaneous velocity vectors for each of the three data sets examined in this section, the axis of the intake jet coincides more or less with a laser line. This enables a rough quantification of momentum in the intake jet by using the magnitudes of the velocity vectors that depict the incoming jet as velocities encountered at the jet axis U_c. The result is exhibited in Table V.5.3 where the momentum flux J is calculated according to equation V.2.d in section V.2.2 and normalized by density. The trend of the change of angular momentum with engine parameter setting is as expected: The normalized momentum increases with decreasing valve lift and increasing engine speed.

In Table V.5.4 two ratios are evaluated for the increase of momentum flux when engine parameters are varied. The first ratio II/I denotes the increase of momentum when the valve lift is lowered to 3 mm at constant engine speed; the second ratio III/II tells the increase when engine speed is increased to 30 RPM at constant valve lift. The very same ratios were calculated using the data available on the content of kinetic energy in the area of scrutiny from section V.2.2. It can be stated that for momentum flux as well as for kinetic energy in the area of scrutiny the first ratio II/I is smaller than the second ratio III/II. These tendencies assert that the increase of momentum with increasing engine speed from 20 to 30 RPM is stronger than the increase of momentum when the valve is being closed from 9 mm to 3 mm. The fact that the momentum flux and the kinetic energy content in the area of scrutiny both exhibit similar tendencies as speed is increased and valve lift decreased,

underline the notion of an existence of a proportional link between the level of momentum carried by the intake jet and the level of kinetic energy in the area of scrutiny.

Table V.5.3: Normalized momentum as a function of engine parameter setting.

	Engine Parameter Setting		
	20RPM9mmVL	20RPM3mmVL	30RPM3mmVL
	I	II	III
Maximum velocity at center of jet [in m/s]	1.09	2.1	3.55
Momentum J / ρ [in m^3/s^2]	7.56E-03	9.39E-03	2.67E-02

Table V.5.4: Comparison of ratios as encountered for momentum and for kinetic energy.

	Ratio	
	II/I	III/II
Momentum	1.24	2.85
Kinetic Energy	1.91	3.07

V.5.3 Velocity fluctuation within the intake jet

Miller and Comings (1957) found a distribution of the streamwise velocity fluctuation for a two-dimensional jet flow that can be described as 'M'-shaped about the jet-axis with round edges of the 'M'. The local maxima of this distribution to either side of the jet can be found, according to their study, at about $\eta^*=1$ where the jet width b is at about $\eta^*=4$

(η^* is the normalized parameter of the distance ζ perpendicular to the jet axis divided by the jet width where the origin of ζ is at the axis of the jet). Their velocity fluctuation profile for the velocity component in ζ - direction exhibits an axisymmetric Gaussian-like distribution about the jet axis.

To compare Miller and Comings' results to a velocity fluctuation distribution evaluated from LIPA - data the velocity fluctuation in z - direction is displayed in Figure V.5.7 where the singular evaluations of the fluctuations within the examined x, z - plane are exhibited in a three-dimensional needle plot for the RMS value of the velocity fluctuation w_{RMS} as well as for its normalized counterpart w_{RMS}/W_{EA}. As mentioned elsewhere the velocity fluctuation in z - direction has been chosen because of the higher accuracy in connection with the data acquisition and reduction process for the z - component of the velocity vector. Note that the velocity fluctuation in z - direction does not represent the one in streamwise direction as was examined by Miller and Comings, thus, the results of this study will not strictly match the curves by Miller and Comings. However, in investigating the velocity fluctuation results in Figure V.5.7, especially the normalized fluctuation intensity distributions, one can discern a distinct valley (low values of the fluctuation) with the sole of the valley being at the axis of the jet. This valley is most distinct for the case of 30 RPM engine speed and 3 mm VL. Note that the error due to the movement of the highest intensity spot within an intersection area has been taken out of the data in Figure V.5.7 (see section III.3.3).

It would be tempting to determine the edge of the annular jet from the fluctuation intensity distributions taking into account Miller and Comings' scaling measure that the maximum of the distribution has to be at $\eta^*=1$. But from the results of the superposition of a velocity map onto the corresponding flow visualization image for 20 RPM and 3 mm valve lift (Figure IV.2.2g, j, and k) it is known that for this set of engine parameters velocity vectors #9 and 12 represent the edge of the intake jet. This knowledge makes it possible to locate the edge of the jet in Figure V.5.7β. From these diagrams it can be seen

that with a further increase in ζ beyond the edge of the jet the velocity fluctuation increases. In this region of increased ζ, the locations of velocity vectors (#10, 13, and 15) must be assigned to the periphery of the main toroidal recirculation pattern. It can be speculated then that between velocity vectors #12 and 15, and between #9 and 13 there ought to be a maximum in the fluctuations representing the interactions between the intake jet and the periphery of the main TRP.

For 30 RPM engine speed, thus higher Reynolds number than for 20 RPM, and equal valve lift the spread of the intake jet is slower meaning that the width of the jet is smaller at any given ξ. This is reflected in the plots of Figure V.5.7γ. Based on the argument for 20 RPM and 3 mm VL that the maximum velocity fluctuation ought to be found between vectors #9 and 13 this very same maximum has to move to a smaller ζ due to the higher Re and can thus be found now at a location close to velocity vector #9. This is exactly the situation encountered in Figure V.5.7bγ.

When comparing the three plots in Figure V.5.7 containing the distributions of the normalized velocity fluctuation intensity for the three engine parameter settings (Figure V.5.7b) the expectation that the intensity increases with decreasing valve lift and increasing engine speed is confirmed. The expected reciprocal behaviour for the width of the intake jet -- namely the decrease of the width with decreasing VL and increasing RPM -- is verified as well.

Contradictory to what had been conjectured in section V.5.1.1 on the basis of the velocity maps in the EA domain for velocity fluctuations encountered in the two recirculation patterns, the velocity fluctuations within the periphery of the main TRP and within the upper corner TRP can be found to be, in the plots of Figure V.5.7, of the same order of magnitude.

Due to the coarse spatial spacing of intersection areas and the mediocre accuracy (section III.3.3) in connection with the LIPA grid from Figure II.2.3b the main goal set forth for section V.5, namely the description and quantification of flow structures in the vicinity of the axis of the annular intake jet fell significantly short. Predominantly, qualitative observations stemming from maps of velocity vectors were delineated where at some points the study did not go beyond an achievement of fluid dynamical justifications of specific velocity vectors. With a few exceptions no quantifications of fluid motion was accomplished. However, this study is useful for a follow-up investigation where the know-how acquired in this work can be used to design LIPA experiments.

Chapter VI
CONCLUSION AND OUTLOOK

The prime objective of this investigation was to apply the velocimetry technique LIPA (Laser Induced Photochemical Anemometry) to study the induction stroke of a model four-stroke engine in order to quantify the fluid dynamics of the encountered flow fields. A secondary objective was to develop algorithms to enable accurate automation of the data reduction technique for LIPA. Also, as a consequence of the research, new flow visualization has uncovered detail here-to-fore unexplored in very low RPM engines. The research has paved the way to using whole field data by creating diagnostics that give information about vortical structures -- their scales and intensities and number -- needed to study engine modifications that lead to enhanced mixing in engines.

LIPA was successfully implemented for the examination of the induction stroke of the water analog model. Data acquisition as well as reduction procedures were established that assured the generation of LIPA - data (laser grids exhibiting distorted grid lines) and ultimately velocity and vorticity information on induction. Similarities between flow visualization images obtained for the induction stroke of the water analog model and fields of velocity vectors corroborated the LIPA results. Flow visualization results also helped to formulate new fluid dynamical conclusions about the flow field during induction.

In order to determine the accuracy of the LIPA - data, several tests were performed to achieve estimations of errors. The main source of error in the LIPA technique as employed in this work occurs because of the fact that intersections formed by crossings of laser lines of the LIPA grids possess considerable extent. Within these intersection areas, regions of highest pixel intensity were able to move driven by, for instance, mechanical vibration in the apparatus. Thinness of laser lines and spatial resolution obtained by the lines of the

LIPA laser grid were found to be the essential issues in conjunction with the optical implementation of the LIPA grid employed for flow field investigation.

Based on the planar information of two-dimensional velocity vectors at assigned and consistent locations within a flow field, the fluid dynamics encountered during induction of the water analog model were examined. Two engine parameters (engine speed and valve lift) were varied to establish a dependency between the flow field and fluid dynamical quantities encountered during the intake stroke of an engine, and boundary conditions. Engine speeds of 10, 20, and 30 RPM were investigated as well as 3, 6, and 9 mm valve lifts employing two LIPA grids with different spatial spacing of the laser lines: One grid with which it was possible to obtain a field of velocity vectors whose region of study covered most of a plane containing the axis of the engine cylinder; and another grid of higher spatial resolution with which the incoming jet flow was analyzed.

In general, the information density in terms of spatial and temporal resolution in connection with the LIPA images acquired was found to be adequate to examine the large scale structures, but too low to examine the dissipative structure and the induction jet. However, as mentioned elsewhere, it was beyond the scope of this study to achieve a thorough, comprehensive understanding of the physics of the flow field. Shortcomings in regard to resolution together with suggestions for their improvement are outlined.

On the basis of fields of velocity vectors (section V.1) and supported by flow visualization results the flow field has been dissected into fluid dynamical elements; namely a free annulus jet emanating from the tip of the valve, two toroidal recirculation patterns -- one occupying most of the volume of the engine cylinder, and the other one in the corner between cylinder wall and the intake jet --, a boundary layer flow along the cylinder wall, and a buffer zone above the piston head. Some bilateral interactions between these elements as well as effects of one element on another have been investigated.

Considering the intake jet first, the angle under which the intake jet enters the engine cylinder (induction angle) as a function of crank-angle is dependent on the setting of the engine parameters. For a constant engine speed it can be observed that the intake jet soon after it is established, inclines fastest towards the cylinder axis, and then back up towards the chamber head to assume a constant 'plateau' value for small valve lifts. The larger valve lifts have the smaller plateau value. It can be observed, furthermore, that the higher the engine speed is the smaller is the difference between the highest and smallest plateau value for a particular engine speed. It was argued in the text that the rates of change of jet inclination are faster for small valve lifts because the built-up of the main recirculation pattern is quicker in connection with smaller valve lifts, thus forcing the incoming annular jet back up faster. A reason for the plateau value towards which the induction angle converges being smaller for larger valve lifts is that the main recirculation pattern is less strong in this case, and is not able to push the intake jet back up as far.

The 'strength' of the main recirculation pattern has been established through an evaluation of kinetic energy in a particular region of the main TRP, the so-called 'area of scrutiny' which is a sub-region of the main recirculation pattern. Clear linear characteristics were obtained in a single-logarithmic plot indicating the dependency of the kinetic energy with engine speed and valve lift. According to these curves kinetic energy decreases with decreasing engine speed and increasing valve lift. This same characteristic is experienced for the momentum flux contained in the intake jet. Quantitative evaluation of momentum flux could be achieved for three settings of the engine parameters when inferring velocity information from maps of velocity vectors. The change of momentum flux -- exhibited by the jet -- with setting of the engine parameters turned out to be very similar to the change of kinetic energy when varying the same engine parameters. This was seen to be evidence for a correlation between the momentum flux carried by the intake jet and the kinetic energy content of the main recirculation pattern.

Evaluations of recirculativity (see sections V.2.1 and V.2.2 for definition and results) and vortical energy in the area of scrutiny for the nine data sets witness inconsistencies in the results at an engine speed of 20 RPM (corresponding to 340 RPM in air) when results achieved at 10 and 30 RPM engine speed are used as comparison. For 10 and 30 RPM engine speed curves for recirculativity exhibit fairly linear characteristics -- recirculativity increases with valve lift. For 20 RPM engine speed the three data points do not fall on a straight line. For 10 and 30 RPM engine speed it was more or less possible to overlap curves depicting vortical energy with the corresponding ones depicting the kinetic energy by scaling. This was not possible in connection with the curves for 20 RPM engine speed. The character of the flow field encountered during the induction stroke of an axisymmetrical engine appears to exhibit a transition when at 20 RPM engine speed the valve lift is being decreased. It was argued in section V.4 that this transition might be attributed to the fact that at 20 RPM engine speed toroidal vortex rings created by the intake jet get destroyed for 3 mm valve lift, however survive until the jet reaches the cylinder wall in the case for 9 mm valve lift, enabling for 9 mm VL ingestion mechanisms between vortex rings and the main toroidal recirculation pattern to supply the main TRP with angular momentum on convective time scales.

One major finding from this study is that there have been strong indications that the ratio of ξ/ℓ_J describing the location where the intake jet turns turbulent has considerable significance in connection with the fluid dynamics of the flow field in an engine. If ξ/ℓ_J is small the intake jet turns turbulent shortly after it enters the engine cylinder. In this case the intake jet exhibits strong turbulent motion when it supplies momentum to the main recirculation pattern. For large ξ/ℓ_J the turbulent motion of the jet is weaker resulting in more structured motion of the main TRP.

A feeling for the complexity of the flow field has been conveyed in section V.3.1 by means of fields of instantaneous velocity vectors. The manifold structure of the flow field

makes it very difficult to grasp the flow field computationally or even analytically. It was concluded that each fluid dynamical element of the flow field as identified in section V.1, e.g. the intake jet, should be considered separately with initial and boundary conditions supplied by the surrounding fluid dynamical elements. The property of complexity is stripped from the flow field when ensemble averaging of velocity vectors is performed over individual engine cycles. In the EA domain very stable and structured flow fields are encountered in an axisymmetrical engine after midstroke. Hence, EA techniques have to be applied with the awareness that after ensemble averaging fluid dynamical quantities, these quantities do not reflect properly fluid dynamics of the flow field during individual events, but that these quantities point out general tendencies inherent in the fluid flow during induction. Ensemble averaging will be the technique needed to quantify differences in flow structure that can be attributed to engineering design changes.

Velocity fluctuations were evaluated in this work in the area of scrutiny (see Figure V.2.2). These fluctuations incorporate those due to cycle-to-cycle variability and due to turbulent motion exhibited by the flow field. Evaluations of these velocity fluctuations for nine variations of engine speed and valve lift showed strong velocity fluctuations in connection with high engine speed and small valve lift and low fluctuation for large VL and low engine speed. Since the velocity fluctuations contain those due to CtC-variations and due to turbulence no conclusive statement can be drawn from these correlations. Information on instantaneous velocity magnitudes at one location in the flow field in form of velocity profiles was used for 10 RPM engine speed and 3 mm valve lift to attempt the separation of velocity fluctuations due to cycle-to-cycle variability and turbulent motion within the flow field in this study. Velocity fluctuation in connection with turbulence was found to be higher than those in connection with cyclic variations by a factor of between 1.2 and 1.5, in the area governed by the intake jet as well as in the area of scrutiny. In their cycle resolved study of engine data Catania and Mittica (1989) evaluated the velocity fluctuations due to turbulence to be, in the vicinity of the jet axis,

one quarter of those due to cyclic variations. Their experiments were conducted in a commercial engine at 1600 RPM. This demonstrates the profound influence of engine speed and engine geometry on velocity fluctuations. In this study it was found furthermore that turbulence intensities increase towards the end of the induction stroke in the region close to the axis of the intake jet as well as in the area of scrutiny. This is a very welcome fact since it has been shown by previous studies that an increased level of turbulence intensity enhances combustion performance in an IC engine.

Parametric quantities were evaluated from vorticity distributions in the area of scrutiny for the nine sets of data representing magnitude and frequency of hill/valley fluctuations encountered in the distributions. These quantities were evaluated to provide measures of the number of rotating scales, their energy and size. -- The calculation of these quantities replaces an evaluation scheme where Fourier transforms vorticity information into the frequency domain since the amount of vorticity data available for the area of scrutiny was not sufficient for the application of the Fourier transform. -- The measure representing the frequency of hill-valley variation in the vorticity distribution shows that neither engine speed nor valve lift has an influence on the hill/valley fluctuation indicating that the overall spatial structure of the flow field is similar -- for the length scale investigated -- for all nine flow fields stemming from the nine settings of the engine parameters. The magnitude of the hill/valley fluctuations, on the other hand, is highest for 30 RPM engine speed and 3 mm VL and decreases with decreasing engine speed and increasing valve lift. The statement delivered in the two preceding sentences bear an indication that size-wise comparable flow structures possess increasingly higher rotational flow as valve lift decreases and engine speed increases.

The spatial spacing of laser lines in the investigation grid for the examination of the intake jet was very coarse with respect to the vortices created by the intake jet, so that only a few fruitful results could be obtained from its application to the flow field in the

vicinity of the axis of the annular intake jet. One of the results of this quantification was, that the toroidal recirculation pattern in the upper corner between the cylinder wall and the intake jet, observed by several investigators, and detailed further in this investigation, does not for an axisymmetrical engine come into significant strength until midstroke. This was also supported by observations from flow visualization results performed in this study. It was furthermore argued for after midstroke that the upper corner flow pattern recirculates only intermittently.

Another discovery stemming from the closer examination of the intake jet is that for the crank-angle range of about 130° to 155° typical time scales of about 33 ms exist for the fluctuation of the induction angle for 20 RPM engine speed and 3 mm valve lift. Similar time scales can be found for convection mechanisms of azimuthal vortex rings shed by the intake jet in flow visualization results for a crank-angle range of about 25° to 40° for the same setting of engine parameters. This suggests a correlation between the generation and convection of toroidal vortex rings created by the intake jet and the fluctuation of the induction angle.

Following is an itemized account of the most important fluid dynamical results stemming from this investigation.

- The flow field encountered in an axisymmetrical engine configuration can be dissected into an annulus free jet, a boundary layer flow along the engine cylinder wall, two toroidal recirculation patterns, and a buffer zone on top of the piston head.

- The characteristic of the induction angle comprises a decrease towards a minimum, followed by an increase towards a local maximum, with a final approach towards a plateau value; the characteristic is independent of the setting of engine parameters between 10 and 30 RPM engine speed.

- Results from the EA domain and from analyses of instantaneous data have both importance in scientific research of fluid flow. From EA data it is possible to determine,

e.g., induction angle, centers of rotational flow, structure of flow field; from instantaneous data one evaluates in-cycle mixing, velocity and vorticity magnitudes, etc.

- The amount of kinetic, vortical, and fluctuation energy contained in the main TRP increases with increasing engine speed and decreasing valve lift.

- A new parameter, 'recirculativity', was defined. It gives information on fluid flow, about its structure and its tendency to recirculate. It was found that the recirculativity basically increases with increasing engine speed and decreasing valve lift.

- The length of transitional flow of the intake jet, ξ/ℓ_J, is an important parameter in the evaluation of the degree of structure of the main recirculation pattern.

Throughout the entire text improvements have been suggested for an application of LIPA to a fluid dynamics problem in general, and to the induction stroke of an engine in particular. Space for improvement is certainly encountered with the optical implementation of the investigation grid. By setting up the optical system on an optical bench and using micron-adjustable enclosures for optical elements one can achieve, for instance, thinner laser grid lines, higher spatial resolution of the grid, and equality of line thickness throughout the area of investigation.

A suggestion for further research in the study of the intake stroke of the water analog model employing LIPA includes the investigation of horizontal planes at different locations of z to quantify swirl and the tornado visualized in chapter IV, quantification of flow motion on smaller length scales by using a LIPA grid of laser lines with higher spatial resolution, extension of engine speed to more practical speeds, and attempts to accomplish an ultimate hybrid technology where LIPA results are obtained from images that also depict flow visualization information on the flow field to attain immediate quantification of visualized flow structures. The basis for the latter project was laid in this investigation where LIPA images were retrieved on film showing superimposed both a distorted laser grid and visualized flow structures of the intake jet in one picture (Figure II.2.6b-e).

The author pointed out at various locations within this text that the length of the transitional flow experienced for the annulus intake jet is an important parameter for the development of the flow field during induction of an engine. Experiments including LIPA and flow visualization incorporating higher temporal -- as well as spatial -- resolution should be conducted on the intake stroke of a reciprocating quartz model. Then, it will be possible to determine the extent to which the location of vortex ring break-up demonstrates significance for the development of the intake flow field. It will also be possible then to generate a model for the interactions between the annulus intake jet and the two toroidal recirculation patterns.

It is important to understand to what extent there are interactions between the azimuthal vortex structures of the intake jet and the main toroidal recirculation pattern in the interface zone, and of what nature they are. We have seen that for 1.5 RPM engine speed and 9 mm VL the vortex structures get suppressed, they cannot really develop; on the other hand, we have seen for the same engine speed and 6 mm VL, that there seems to be a mechanism that resembles vortex coalescing between vortex rings and the main TRP. A laser grid with denser spatial spacing of intersection areas has to be spanned around the valve in order to obtain fields with velocity vectors that would yield coherent information about the flow structure in the interface zone in terms of magnitude and orientation of the flow field at multiple locations. One can use the knowledge about these fluid dynamical processes to generate new engineering modifications, as well as to describe a model of, as was suggested, an iterating control system of bilateral influence between the intake jet and the main TRP and try to, thus, ultimately predict the internal fluid dynamics of the main recirculation pattern. The apprehension about the fluid dynamics of the main TRP during induction is the key to evaluate mixing performance and level of turbulence intensity during the induction stroke of an engine for most of the volume of the engine cylinder under investigation.

APPENDICES

APPENDIX A

Generation of Piston Motion

Since water is the basis for the working fluid, the engine setup has to account for the consequences of using an incompressible medium. Therefore, the compression and expansion strokes had to be avoided during engine performance. This was accomplished by a specially designed cam-shaft. For a depiction of the cam's physical shape see Figure A.1b. The engine-speed vs. crank-angle characteristic of the cam-shaft can be seen in Figure A.1a.

Since one engine cycle comprises for the particular cam-shaft used for this research project one revolution of the cam (360° CA incorporating two moving and two quiescent strokes) and one engine cycle of a regular engine comprises two revolutions of its shaft (four moving strokes, Figure A.1a) the effective engine speed used for the presentation of results in this study must be doubled when transforming fluid dynamical results gained with the utilized engine model to real engine applications. For example, if the model engine is run at an engine speed of 10 RPM, the equivalent, real engine speed as encountered in four-stroke IC engines is 20 RPM. In a phase-space diagram (Figure A.1a) the difference between the engine-speed-vs-crank-angle diagrams as induced by the cam-shaft and by the shaft of a regular engine is being pointed out. For one turn of the 'circle' in connection with the cam-shaft used in this study (I, II, III, IV; at II and IV the piston is at rest) one has to make two turns in conjunction with a regular engine (1, 2, 3, 4).

Because the optical encoder that is electronically timing the data acquisition process (section II.2.2.2 & Appendix C) puts out 360 pulses per cycle and thus achieving a crank-angle resolution of 1° in the used data acquisition setup, one can concede on the grounds

179

of the above discussion on engine speed that the temporal resolution in this study cannot be better than 2° CA when results are to be converted to the real engine domain.

During engine performance one encounters fluctuation of the engine speed of the order of about ±0.5 Hz for 10 RPM engine speed at which the crank-angle frequency is 60 Hz, thus an uncertainty in engine speed of 0.8%. This instability can be ascribed to causes such as uneven friction between the O-ring and the cylinder wall, to an unstable providing of the driving torque, to friction in the mechanical elements transferring the torque, etc.

Sealing and Lubrication between Piston Head and Cylinder Wall

An attempt had to be made to achieve two goals concerning the O-ring that served as interface between the piston head and the cylinder wall which are both made of quartz: On the one hand the O-ring had to establish an impenetrable connection with the quartz of the cylinder wall in order to inhibit the working fluid from leaking, on the other hand the connection was not to be too tight in order to allow the piston head to move harmoniously. The use of a plastic named 'Rulon' accomplished cardinal sealing of the working fluid yet allowed the piston head to move smoothly within the cylinder. The actual O-ring constellation consists of two Rulon rings of equal width. Tightness of the O-ring was enhanced by placing a regular rubber band between the quartz of the piston head and the Rulon rings. The Rulon rings were cut on the side facing the piston head in such a way as to allow the rubber band to rest in a groove, a configuration which according to the O-ring text-book allows for increased sealing. Lubrication between O-ring and cylinder wall was assured by the fact that a thin layer of liquid builds up between the two materials during engine performance.

One unpleasant side-effect of the Decahydronaphthalene used for the flow visualization experiments in connection with the phosphorescent dye (section IV.1) is its property to expand regular rubber dramatically (which I experienced on a daily basis when DHN came

into contact with my rubber gloves). Hence, when the flow visualization experiments were performed using Kodak's photochromic chemical where DHN was the working fluid the regular rubber band in the 'Rulon O-ring' configuration had to be replaced by DHN resistant Viton V14 O-rings. These O-rings needed machining to substitute the rubber band properly.

APPENDIX B

Issues on refractive Index Matching

Since the point in 2D space for a refractive index matched compound is dependent on temperature, the temperature in the measurement site has to be kept constant which was assured roughly by a constant temperature of the ambient air in the laboratory.

Also, Hexane as index matching agent for Decahydronaphthalene exhibits a considerable evaporation rate when the DHN/Hexane solution is exposed to air so that the outer tank in which the DHN/Hexane solution constitutes the index matched fluid had to be sealed from ambient air [still about 50 ml Hexane evaporated during a day of experiments which, however, is just a fraction of the 6000 ml DHN/Hexane solution in the outer tank]. From empirical observation it can be maintained that no fast diffusion (mixing) mechanism between Hexane and the DHN/Hexane solution is encountered when Hexane is added to the top of the fluid reservoir. This means in inverting terms, that after evaporation of Hexane from the free surface the DHN/Hexane solution stays index matched at the site where the laser grid enters the outer tank.

As could be observed, a slight mismatch of the index of refraction is not that crucial in the investigation performed for this work. Furthermore, the relevant time in conjunction with data acquisition with respect to index matching issues is the time between taking the reference grids and the recording of the actual data (distorted grids) during engine performance. This time is generally less than 5 minutes since only the first engine cycles recorded were used for data reduction. During this time neither a significant change in temperature nor significant evaporation of the alcohol component in the LIPA - chemical in the engine cylinder and of Hexane in the DHN/Hexane solution in the outer tank can be experienced.

A considerable mismatch of the index of refraction for the test facility as a whole was noticed when a white paper square was recorded with the imager system for calibration purposes (Appendix D). In order to record the square the imager was turned away from the test facility with the focus length of the camera lens remaining unchanged. In air, the square (and also a ruler) was then moved along the optical axis of the camera lens until the object was in focus. As turned out after the object was in focus, the distance between the camera lens and the object (8.125 in) was significantly smaller than the distance between the camera lens and the cylinder axis (8.875 in) of the test facility (grid of laser lines) during the LIPA experiments. It is assumed that this is essentially due to the fact that that portion of the outer tank that is situated between engine and camera is made of Plexiglas where the optical system of indices of refraction quartz - Plexiglas - air has the effect of a concave lens. It is assumed furthermore that the effect of hypothetically index mismatched fluids in the apparatus and the outer tank is negligible.

Optical Issues

Background noise of the grid of laser lines: The edges of the glass bodies on the basis of the beam divider introduce diffraction lines between the generated parallel laser lines. Not only are these diffraction lines responsible for enhanced background noise (decrease in quality factor; equation II.2.d), they also tie up energy in higher order lines, thus taking energy away from the lines of 'zero' order which are used to perform LIPA. There exists a certain distance between near and far field where diffraction is not experienced. It is desired to move the grating that distance away from the site of investigation. However, for the experiments where the imposed grid of laser lines was to cover most of a two-dimensional plane of the engine cylinder the distance between the beam divider and the region of interest was determined by issues concerning (1) the achievement of highest spread between the laser lines, (2) the implementation of the paths of the laser lines in

185

APPENDIX C

Synchronization Aspects, its Difficulties, and related Uncertainties

Because LIPA - data was to be taken at particular fixed crank-angles within engine
cycles -- in order to perform ensemble averaging over a number of ECs at these selected
CAs -- the facility providing the measure for data acquisition is the running engine
(motor). Fluctuations encountered in engine speed during engine performance
(Appendix A) made it impossible to use the 30 Hz timing scheme provided by a CCD
camera to time the data acquisition process; with this approach pictures cannot be taken at
consistent piston positions for the examined engine cycles. The width of a window around
a crank-angle position -- at which fluid dynamics ought to be examined -- into which
samples of LIPA information fall during data acquisition denotes the accuracy of the
application of an ensemble averaging technique.

The electronic timing procedure is initiated by an optical encoder that rotates in sync
with the cam-shaft (Figure II.2.4) and which puts out an electronic signal with every
degree rotation of the cam-shaft (360 signals per cycle) as well as a single signal once
every cycle (index). In general, the former signal is transferred to the Excimer Laser and
forces it to pulse. The signal is also piped to a frequency generator. This device provides
TTL signals of selectable length which can be delayed relative to the triggering input
signal from the optical encoder where length and delay of the TTL signal constitute
exposure and delay time, respectively, of the data acquisition procedure (section II.2.3).
The conditioned signal from the frequency generator is applied to the external trigger
facility of the image intensifier lens (Figure II.2.4; more on the imager system in
Appendix D).

In the experimental setup employed in this study, an 'electronic signal valve' is inserted into the electronic circuit right behind the optical encoder (Figure II.2.4). This valve enables the investigator to select from the signals provided by the encoder those signals which are necessary for electronic synchronization in the data acquisition process at a particular engine speed. A technical drawing of the electronic realization of the electronic device is shown in Figure C.1. The device was designed and implemented by John Brandon at the National Cyclotron Laboratory at Michigan State University upon the author's specifications. The two main features of this electronic valve are that (1) it allows the experimentalist to transfer only every 2nd, 3rd, 4th, ..., or 10th crank-angle pulse output by the optical encoder to the electronic network behind the 'valve' and that (2) there is an option to assign a window with a length to cover 100 degree crank-angle during which only pulses are admitted through the electronic valve and provided at its output. -- Using the index pulse provided by the optical encoder this window can be set; e.g. for the experiments conducted for this work the window was moved such that LIPA images could be recorded during the intake stroke. -- The remaining 260 pulses in one cycle are blocked in order to save on the lifetime of the elements comprising the experimental system, especially to save on laser energy. The option to choose every 2nd, 3rd, and so forth signal has been added to ensure timing between the gating of the image intensifier lens (IIL) and the Video camera at particular engine speeds upon which will be deliberated next.

Electronic signal conditioning, i.e. timing to acquire data with the imager, is implemented as follows: The Video camera is running continuously to record what is provided at the exiting plane of the image intensifier lens (refer to Figures II.2.4 and C.2 for graphical support for the following presentation of the timing procedure). The IIL is gated and admits information at its exit to be recorded by the camera only during assigned periods of time which are initiated by signals from the optical encoder mentioned above

(or ultimately by the investigator). The time slots during which the shutter of the IIL opens and data is recorded by the camera commence after the chosen 'delay time' between the firing of the laser grid and the intentional documentation of the distorted grids. Their lengths, i.e. exposure time, are determined by the intensity of the laser light of the investigation grid and the f-stop of the camera lens (for optimization of exposure time see section II.2.3.2). The conditioning of the gating signal for the IIL is, as outlined above, performed by the frequency generator. Upon reception of a signal from the 'electronic valve' the frequency generator outputs a TTL signal after the assigned time delay with a width of the TTL signal corresponding to the chosen exposure time which is transferred to the IIL.

Since the Canon camcorder could not be triggered externally synchronization problems must occur. With the camcorder running continuously and the IIL being gated, opening of the shutter of the IIL occurs one time during the camera's 33.33 ms sampling intervals (for appr. 0.1 ms in the average; exposure time) to reveal information from the investigated area. Since during these 33.33 ms sampling intervals two sets of lines of the camcorder's CCD array have to be filled (RS170), the IIL however opening the gate only once for a fraction of the sampling rate, only one set of lines in an image obtains information from the scene of interest. That means that spatial resolution of images is literally cut in half in vertical direction. The loss of spatial resolution could, however, be compensated for partially (section III.1.4). Another problem evolves from this method of data acquisition in that the setting of the engine speed and thus the implementation of the measure for data acquisition cannot be achieved precise enough to match the robust 30 Hz sampling rate of the camcorder. Also, as mentioned in Appendix A, the engine speed fluctuates. Therefore, it can be stated that due to the uncertainty in engine speed it can happen that either two LIPA images can be interlaced in one picture acquired by the camcorder or that a frame can be empty. To avoid this uncertainty it was attempted to run the engine at an engine

speed that transforms into a crank-angle repetition rate which is slightly lower than the 30 Hz sampling rate of the camcorder. The consequence is that empty frames are encountered. With the data acquisition system at hand only *virtual* synchronization is achieved.

Improvement of the temporal resolution by a factor of 2 can be achieved by designing a 'crank-angle clock' that assigns the appropriate CA to an image (field) containing a distorted laser grid. A set of horizontal lines carrying distortion information of one investigation grid can then be interlaced in one LIPA picture with information of the distorted grid from the succeeding crank-angle position.

Another uncertainty enters through a bi-directional ambiguity (shifting) of the temporal position of the start of piston motion in the electronic domain (index pulse from encoder) in a sequence of LIPA images for one engine cycle. This fluctuation accounts for a vacillation of less than $\pm 1^{\circ}$ CA. Its effect is minimized by conditionally sampling those engine cycles where the crank-angle position representing the beginning of piston motion in the sequence of LIPA images for one EC can be assigned to a marginally small crank-angle window that defines the commencement of the induction stroke.

Due to the aboveoutlined problems (empty or double-filled frames, shifting of initial crank-angle position in sequences of LIPA pictures) the single LIPA images had to be assigned to crank-angle positions by hand.

An engine speed of 10 RPM for the investigated water analog model (which transforms into 20 RPM if one considers the cam-shaft factor of 2; Appendix A) corresponds to a time interval between two degrees of crank-angle of 16.67 ms. Having a prescribed data acquisition rate of 33.33 ms by the Video camcorder, images are thus acquired at every other degree CA. Since 10 RPM for this water analog model relates to 20 RPM for a 'real' engine (in this application a whole cycle consists of all four strokes whereas in real engine

applications one cycle consists of two strokes) the crank-angle resolution is cut in half again. Hence, for 10 RPM (20 RPM) there is a crank-angle resolution of 4°. In this text statements of engine speeds always refer to the engine speed in conjunction with a 'real' four-stroke engine.

The imager system is turned by 90° for the experiments in the investigation of the whole cylinder -- so that the quartz valve is located in the LIPA images on the right side (Figure II.2.7), oriented vertically -- in order to make most use of the 500 x 820 lines offered by the CCD array of the camcorder. Thus, it is in the x - direction of the engine reference frame that LIPA information suffers from the dividing in half of spatial resolution due to the acquisition of only one set of horizontal lines by the Video Camcorder as was outlined earlier in this section. As it turns out this loss of resolution is minor in the aspect of accuracy.

APPENDIX D

Specifications of Hardware

IMAGER SYSTEM

For the recording of LIPA images an assembly consisting of two electro-optical components was used; Figure II.2.4b and c. The first component is a commercial color Video Camera & Recorder from Canon Inc., L1A Hi8 (high resolution, 8 mm). This camcorder works on the basis of the interlacing (TV) standard RS170, thus, sampling 'complete' images at a rate of 30 Hz. The RS170 standard defines that for a complete image two sets (fields) of horizontal lines are filled with information from the scene of interest at a frequency of 60 Hz (see Figure C.2), one after the other, and that these two sets of lines are then interlaced, yielding a complete image (frame) at a frequency of 30 Hz. The camcorder's array of photodiodes consists of 500 horizontal and 820 vertical lines. Since the facility that digitizes LIPA images (MegaVision) can only digitize frames of up to 512 by 512, data reduction could not take fully advantage of the potential of the horizontal resolution. The Canon camcorder L1A offers many features such as variation of exposure time and control of aperture which can be inferred from the Service Manual for the L1A. However, it is unfortunately *not* possible to externally trigger the camera, thus, no locking of the camera into the electronic measure provided by the running engine, i.e. the optical encoder, could be established.

Mounted in front of the camcorder is the second electro-optical element, a lens/image intensifier component that was custom-made for the 'Turbulence Structure Laboratory' by Electro-Optical Services, Inc. (EOSI). This image intensifier lens (IIL) -- basically two tandem image intensifiers which are equipped with P-46 high speed phosphors -- yields a photon magnification of 50,000 while offering a resolution of 30 line pairs per millimeter.

The IIL can be gated where electronic shutter input ranges from 100 ns exposure to continuous operation. Its receptive S-20 photocathodes exhibit a peak of 'sensitivity' for electro-magnetic waves at a wavelength of 480 nm. The image intensifier system requires a 12 Volt DC power supply.

IMAGE DIGITIZING FACILITY

The facility to digitize the data that is stored on Video Hi8 tape is the '1024xm' designed by MegaVision. The MegaVision (as the digitizer is referred to from now on) offers a resolution of 1024 x 1024, however, only 525- or 875-line images can be read in. This means that when acquiring 500 x 820 format (x, y) images as is the capacity of the employed data recording facility (L1A camcorder by Canon), MegaVision truncates as well as compresses information in the horizontal plane. MegaVision discriminates information into 256 grey scale levels. There are 12 frames of memory in which each four 512 x 512 images can be stored. It has been apperceived that images can move -- essentially in y - direction -- within a quadrant of a frame during the digitization procedure. This movement might be due to synchronization problems of the used VCR. Using a calibration procedure for LIPA images where a fixed spot of high pixel intensity (reference point) is added into the images it is possible to adjust for this movement of the image within the memory frame. This fixed spot assures that the coordinates of the origin of the engine assembly (Figure II.2.3a, x, z - reference frame depicted at the valve) are at (0,0) in all LIPA images which contain the undistorted and the distorted grids. The reference point is implemented by a continuously emitting LED whose light is projected onto the photodiode of the imager by a mirror. The combination of LED and mirror can be seen in the picture of the setup of the data acquisition system contained in Figure II.2.4b between the imager and the outer tank of the engine apparatus. The

reference point can be seen as a circle in Figure II.2.3a and as a white point in the upper left corner in the pictures of Figure II.2.7.

A software package provided by MegaVision comprises many image processing algorithms. However, only data management routines were employed within the data reduction process for this work since it was more convenient to incorporate image processing software in the programs which were discussed in chapter III. The MegaVision system works within the frame of this investigation in conjunction with a Sun 3/260 Workstation.

In order to scale the distances -- that fluid particles convect -- as they are found in the digitized images to the distances convected in real physical space one has to find out how MegaVision maps the 500 x 820 images provided by the Video camera into its own memory. It was found, as mentioned above, that during the digitization procedure MegaVision truncates part of the image in the horizontal plane -- the left side -- and then compresses the rest to 512 pixel. A test object -- a ruler was recorded with the Video camera and its mapping into memory by MegaVision was then assessed -- showed that 25 x 25 mm is represented by 400 x 438 pixel after digitization yielding a compression factor of 1.095 in the horizontal direction.

To determine in LIPA images the correct number of pixel that represents a distance in the physical space, to thus find conversion factors for the two different investigation grids applied in chapter V (grids for the investigation of the engine cylinder as a whole and for the more scrutinizing examination of the intake jet), illuminated square sheets of paper were recorded by the Canon camcorder onto tape and the images holding these squares digitized. Now, the number of pixel for each side of the square was evaluated in the digitized domain to determine the necessary conversion factors.

APPENDIX E

FORTRAN Program

Following is the listing of the FORTRAN program that implements the HIS approach as delineated in section III.1.2.

```fortran
      program WindowIADet

c   Description:
c      The algorithm seeks Intersection Areas using
c      a Window based approach. A window is moved over the
c      input image and the pixel values lying inside this
c      window are added yielding an increasing number
c      when the window approaches an intersection area.
c
c   Author: Bernd Stier, Jan-19-93 {(b&s)}
c          Modified versions:      Aug-15-93 {(b&s)}
c                                  Sep-15-93 {(b&s)}
c
c   Input : -parList.datI
c           -assign.datI
c           -imgXXX.pic
c           -imgXXX.REF
c
c   Output : -imgXXX.LOC (into /vision/LIPA/Engine/RPMmm/Location)
c            -test
c
c   Comment: This program is called by "Frame" and
c            should be run only by that shell.
c
c------------------------------------------------------
c
c Section 0 -- Define fields, variables, and parameters
c
      parameter (jma=1024,kma=1024)
      common / array / L(jma,kma),LA(jma,kma)
      common / IntAreaAver / AintA(100,100)
      dimension jIP(100),kIP(100)
      character fname*70,fname2*70,fname3*70,fname4*8,number*6
      character DN(512,512)
      logical   exist
      character header(512)
      character Runs(300)*6
      character answer*3
      integer   flag1
```

```
      write (*,'(///A/A/A)')
    & ' DETECTION OF INTERSECTION AREAS USING A WINDOW',
    & '      INTEGRATION APPROACH',
    & ' _____'
      write (*,'(/A/A/A)')
    &          'Algorithm moves a 10x10 pixel window over',
    &          'the intensity array of an image, determines',
    &          'the weight of the window at coordinate'
      write (*,'(A/A/A)')
    &          'points by integration and assigns local',
    &          'maximum weights to Intersection Areas.',
    &          'Evaluate parameters for intensity slopes!!'


      write (*,1000)




c
c——————————————————————————————————————
c
c Section I — Recall the coordinates of the undistorted
c             laser grid and scrutinize area around them
c
      open (45,file='test')
      open (46,file='assign.datI')
      open (47,file='parList.datI')

c    — This section assigns the data directory —
      read (46,*) mAnz
      do 20 inz=1,mAnz
          read (46,*) Runs(inz)
c         write (*,*) Runs(inz)
20    continue
      close (46)
      if (mAnz.EQ.1) goto 27
      open (46,file='assign.datI')
      write (46,*) mAnz-1
      do 25 inz=2,mAnz
          write (46,*) Runs(inz)
25    continue
c    ——————————————————————————


c    — TAUFE (assigns filenames) ——————
27    flag1=0
      read (47,'(I10/A)') kAnz,number
      read (47,'(A/A)') fname4,answer

c—————————— BIG LOOP 30 ——————————————
      do 30 krunch=1,kAnz
      fname='/usr3/stier/'//Runs(1)//'/'//number//'.pic'
      fname3='/vision/LIPA/Engine/'//fname4//'/'//
```

```fortran
     &Runs(1)//'/Location/'//number//'.LOC'
c     — Find appropriate reference grid for 5 RPM —
      if (fname4(1:2).EQ.'05') then
           jindex=krunch/2+1
           if (jindex.LT.10)
     &        fname2='/usr3/stier/img00'//CHAR(jindex+48)//'.REF'
           if (jindex.GE.10 .AND. jindex.LT.20) then
              jindex=jindex-10
              fname2='/usr3/stier/img01'//CHAR(jindex+48)//'.REF'
           endif
           if (jindex.GE.20 .AND. jindex.LT.28) then
              jindex=jindex-20
              fname2='/usr3/stier/img02'//CHAR(jindex+48)//'.REF'
           endif
           if (jindex.GE.28) fname2='/usr3/stier/img2845.REF'
           goto 35
      endif
c     — Find appropriate reference grid for 15 RPM —
      if (fname4(1:2).EQ.'15') then
         if (fname4(8:8).EQ.'T') goto 33
             if (ICHAR(number(6:6)).GT.55 .AND. flag1.EQ.0 .AND.
     &                   ICHAR(number(5:5)).GT.48) flag1=1
             if (flag1.EQ.1) then
                fname2='/usr3/stier/img1830.REF'
         else
                fname2='/usr3/stier/'//number//'.REF'
         endif
             goto 35
      endif
c     — Find appropriate reference grid for 10 RPM —
33    if (fname4(8:8).EQ.'T') then
             if (ICHAR(number(6:6)).GT.50 .AND. flag1.EQ.0 .AND.
     &                   ICHAR(number(5:5)).GT.48) flag1=1
             if (flag1.EQ.1) then
                fname2='/usr3/stier/img1345.REF'
         else
                fname2='/usr3/stier/'//number//'.REF'
         endif
             goto 35
      endif
      if (ICHAR(number(6:6)).GT.55 .AND. flag1.EQ.0 .AND.
     &                   ICHAR(number(5:5)).GT.49) flag1=1
      if (flag1.EQ.1) then
             fname2='/usr3/stier/img2845.REF'
      else
         fname2='/usr3/stier/'//number//'.REF'
      endif
c     --------------------------------------------
35    write (45,*) fname,fname2,fname3,ICHAR(number(5:5))
      write (*,'(/A/A,A,A,A,A/A/)')
     &'--------------------------------',
     &'—— WORKING ON  ',Runs(1),'/',number,'.pic ——',
     &'--------------------------------'
      i=ICHAR(number(6:6))
```

```fortran
      if (i.EQ.57) then
        number(6:6)='0'
        number(5:5)=CHAR(ICHAR(number(5:5))+1)
      else
        number(6:6)=CHAR(ICHAR(number(6:6))+1)
      endif
      INQUIRE (file=fname,exist=exist)
      if (exist) goto 40
      write (*,*) ' — FILE DOES NOT EXIST !! —'
      goto 30
c     ------------------------------------------------


40    continue
      open (2,file=fname2)
      open (3,ACCESS='DIRECT',FILE=fname,FORM='UNFORMATTED',
     &                   RECL=512)
      open (4,file='higSpot.datO')
      open (8,file=fname3)


c     — Determine which line is missing —
      Lsum1=0
      Lsum2=0
      mode=1
      read (3,rec=1) (header(lok),lok=1,512)
      read (3,rec=250+1) (DN(i,250),i=1,512)
      read (3,rec=251+1) (DN(i,251),i=1,512)
      do 333 i=300,500
           L(i,250)=ICHAR(DN(i,250))
           if (L(i,250).LT.0) L(i,250)=L(i,250)+256
           L(i,251)=ICHAR(DN(i,251))
           if (L(i,251).LT.0) L(i,251)=L(i,251)+256
        Lsum1=Lsum1+L(i,250)
        Lsum2=Lsum2+L(i,251)
333   continue
      if (Lsum1.GT.Lsum2) mode=2


      write (*,*) ' — READ IN PIXEL INTENSITIES —'
      do 80 k=1,256
           if (mode.EQ.1) then
        read (3,rec=2*k-1+1) (DN(j,2*k-1),j=1,512)
           elseif (mode.EQ.2) then
             read (3,rec=2*k+1) (DN(j,2*k),j=1,512)
           endif
80    continue
```

```
c-------------------------------------------------
c  Preparing Image for Analysis              |
c-------------------------------------------------
     write (*,*) ' — FILLING LINES —'
     do 90 k=1,256
       do 90 j=1,512
           if (mode.EQ.1) then
           L(j,2*k-1)=ICHAR(DN(j,2*k-1))
           if (L(j,2*k-1).LT.0) L(j,2*k-1)=L(j,2*k-1)+256
             L(j,2*k)=L(j,2*k-1)
         elseif (mode.EQ.2) then
             L(j,2*k)=ICHAR(DN(j,2*k))
             if (L(j,2*k).LT.0) L(j,2*k)=L(j,2*k)+256
             L(j,2*k-1)=L(j,2*k)
           endif
90   continue


     write (*,*) ' — PERFORMING AVERAGING —'
     do 350 j=2,511
       do 350 i=2,511
         LA(i,j)=(L(i-1,j-1)+L(i,j-1)+L(i+1,j-1)+
   &            L(i-1,j)+L(i,j)+L(i+1,j)+
   &            L(i-1,j+1)+L(i,j+1)+L(i+1,j+1))/9
         DN(i,j)=CHAR(LA(i,j))
350  continue


     write (*,*) ' — WRITING —'
     OPEN (unit=11, file='caXXXma.pic', form='UNFORMATTED',
   +     access='DIRECT', recl=512)
     write (11,rec=1) (header(lok),lok=1,512)
     do 400 j=1,512
       write (11,rec=j+1) (DN(i,j),i=1,512)
400  continue
c-------------------------------------------------
c  Preparation finished                      |
c-------------------------------------------------


     read (2,*) IAanz
     write (*,'(A,I2,A)')
   &  ' — FINDING HIGHEST INTENSITY SPOTS (**',IAanz,'**) —'
     if (answer.EQ.'yes' .OR. answer.EQ.'y')
   &      write (*,*) ' —      by DOUBLING RESOLUTION —'

     do 500 i=1,IAanz
c     — jIP and kIP are the coordinates for IPs in reference grids —
           read (2,*) jIP(i),kIP(i)
           if (jIP(i).EQ.0) then
             PIntj=0
             PIntk=0
             jIntP=0
```

```
            kIntP=0
            goto 580
            endif
c-------- DOUBLE RESOLUTION (DYNAMIC RANGE) OF IA --------
      if (answer.NE.'yes' .AND. answer.NE.'y') goto 530
      write (*,'(A$)') 'X'
      krux=0
      do 520 kIntP=kIP(i)-15,kIP(i)+15
      jrux=0
      krux=krux+1
      do 520 jIntP=jIP(i)-15,jIP(i)+15
      jrux=jrux+1
      AintA(2*jrux-1,2*krux-1)=(4*LA(jIntP,kIntP)+2*LA(jIntP-1,kIntP)
     &           +2*LA(jIntP,kIntP-1)+LA(jIntP-1,kIntP-1))/9.0
      AintA(2*jrux,2*krux-1)=(4*LA(jIntP,kIntP)+2*LA(jIntP+1,kIntP)+
     &           2*LA(jIntP,kIntP-1)+LA(jIntP+1,kIntP-1))/9.0
      AintA(2*jrux-1,2*krux)=(4*LA(jIntP,kIntP)+2*LA(jIntP-1,kIntP)+
     &           2*LA(jIntP,kIntP+1)+LA(jIntP-1,kIntP+1))/9.0
      AintA(2*jrux,2*krux)=(4*LA(jIntP,kIntP)+2*LA(jIntP+1,kIntP)+
     &           2*LA(jIntP,kIntP+1)+LA(jIntP+1,kIntP+1))/9.0
520   continue
c---------------------------------------------------
530      Wmax=0
      if (answer.NE.'yes' .AND. answer.NE.'y') then
         jmi=jIP(i)-13
         jmx=jIP(i)+7
         kmi=kIP(i)-13
         kmx=kIP(i)+7
      else
         jmi=8
         jmx=48
         kmi=8
         kmx=48
      endif
         do 550 k=kmi,kmx
            do 550 j=jmi,jmx
               CALL Integrate(j,k,W,answer)
               if (W.GT.Wmax) then
                    Wmax=W
                    jhelp=j
                    khelp=k
               endif
550      continue
         if (jhelp.EQ.jmi .OR. jhelp.EQ.jmx .OR.
     &               khelp.EQ.kmi .OR. khelp.EQ.kmx) then
           write (45,*)
     &      i,' Out of range! Intensity: ',LA(jhelp+3,khelp+3)
         PIntj=0
         PIntk=0
         jIntP=0
         kIntP=0
            goto 580
         endif
      W=Wmax
```

```
c       — TRANSFORM BACK TO ORIGINAL COORDINATE SYSTEM —
        if (answer.EQ.'yes' .OR. answer.EQ.'y') then
          PIntj=jIP(i)-15+INT(((jhelp+3)-1)/2)
          if (MOD(jhelp+3,2).GT.0) PIntj=PIntj-0.25
          if (MOD(jhelp+3,2).EQ.0) PIntj=PIntj+0.25
          PIntk=kIP(i)-15+INT(((khelp+3)-1)/2)
          if (MOD(khelp+3,2).GT.0) PIntk=PIntk-0.25
          if (MOD(khelp+3,2).EQ.0) PIntk=PIntk+0.25
          goto 580
        endif
c         write (*,'(A,I2,A,I6,I10/8X,A,I5,I10)') 'IA# ',i,': initial',
c     &              jIP(i),kIP(i),'accurate',jhelp+3,khelp+3
        jIntP=jhelp+3
        kIntP=khelp+3
        write (4,'(/A)') 'Area of highest intensity'
      do 560 k=khelp,khelp+6
        write (4,'(12I4)') (L(j,k),j=jhelp,jhelp+6)
560     continue
580     continue
        if (answer.EQ.'yes' .OR. answer.EQ.'y') then
          write (8,'(2(F10.3))') PIntj,PIntk
        else
          write (8,'(2(I5))') jIntP,kIntP
        endif
500   continue


      do 700 klax=480,500
        if (LA(450,klax).LE.60) then
          write (8,'(A,I10,I12)') ' 450',klax,LA(450,klax)
          write (45,'(A,I10,I12)') ' 450',klax,LA(450,klax)
          goto 710
        endif
700   continue
710   continue
      close (2)
      close (8)


30    continue
c—————————— BIG LOOP 30 —————————————————————


1000  format (//,
     & '————————————————————————————————————————————————')


      end
```

```
c
c-----------------------------------------------------------------
c
c  Appendix AI: Integration
c

      subroutine Integrate(jmi,kmi,W,answer)

c   Description:
c       Subroutine to sum intensities within window
c
c   Author: Bernd Stier, Jan-18-93 {(b&s)}
c
c-----------------------------------------------------------------
c
      parameter (jma=1024,kma=1024)
      common / array / L(jma,kma),LA(jma,kma)
      common / IntAreaAver / AintA(100,100)
      character answer*3

      W=0
      n=-4
      m=-4
c    ----
      do 540 k=kmi,kmi+6
          n=n+1
          m=-4
        do 540 j=jmi,jmi+6
            m=m+1
            if (n.EQ.-3 .OR. n.EQ.3 .OR. m.EQ.-3 .OR. m.EQ.3) then
              alpha=1
            elseif (n.EQ.-2 .OR. n.EQ.2 .OR. m.EQ.-2 .OR. m.EQ.2) then
              alpha=4
            elseif (n.EQ.-1 .OR. n.EQ.1 .OR. m.EQ.-1 .OR. m.EQ.1) then
              alpha=14
            else
              alpha=17
            endif
          if (answer.NE.'yes' .AND. answer.NE.'y') then
            W=W+alpha*LA(j,k)
          else
            W=W+alpha*AintA(j,k)
          endif
540   continue
c    ----

      return
      end
```

BIBLIOGRAPHY

BIBLIOGRAPHY

Aïta, S., Tabbal, A., Munck, G., Fujiwara, K., Hongoh, H., Tamura, E., and Obana, S. 1990 Numerical simulation of port-valve-cylinder flow in reciprocating engines," *SAE* Paper No. 900820.

Aïta, S., Tabbal, A., Munck, G., Montmayeur, N., Takenaka, Y., Aoyagi, Y., and Obana, S. 1991 Numerical simulation of swirling port-valve-cylinder flow in Diesel engines, *SAE* Paper No. 910263.

Arcoumanis, C., Bicen, A.F., Vlachos, N.S., and Whitelaw, J.H. 1982a Effects of flow and geometry boundary conditions on fluid motion in a motored IC model engine, *Proc. Instn Mech. Engrs*, **196**, pp 1-10.

Arcoumanis, C., Bicen, A.F., and Whitelaw, J.H. 1982b Measurements in a motored four-stroke reciprocating model engine, *J. Fluids Engng*, **104**, pp 235-241.

Arcoumanis, C., Green, H.G., and Wong, K.Y. 1987 Flow structure visualisation in reciprocating engines, Flow Visualization IV, Proceedings of the Fourth (International) Symposium on Flow Visualization, Paris, France, August 26-29, 1986, 705-711, Hemisphere Publ. Co., Washington, D.C..

Arcoumanis, C. and Whitelaw, J.H. 1987 Fluid mechanics of internal combustion engines -- a review, *Proc. Instn Mech. Engrs*, **201**, pp 57-74.

Ballard, D.H. and Brown, C.M. 1982 Computer Vision, Prentice - Hall, Englewood Cliffs, NJ.

Bicen, A.F., Vafidis, C., and Whitelaw, J.H. 1985 Steady and unsteady airflow through the intake valve of a reciprocating engine, *J. Fluids Engng*, **107**, pp 413-420.

Buchner, S. 1992 Flow field and mixture separation measurements in a dense solid-liquid two-phase vertical pipe flow, Diplomarbeit, Dept. Mech. Engrg, Michigan State University.

Catania, A.E. and Mittica, A. 1985 Cycle-by-cycle, correlation, and spectral analysis of I.C. engine turbulence, Flows in Internal Combustion Engines - III, FED-Vol. **28**, T. Uzkan, W.G. Tiederman, and J.M. Novak, eds., ASME, New York.

Catania, A.E. and Mittica, A. 1989 Extraction techniques and analysis of turbulence quantities from in-cylinder velocity data, *Basic Processes in Internal Combustion Engines*, ASME, Proceedings of the Twelfth Annual Energy-Sources Technology Conference, Houston, Texas, ICE-Vol. 6.

Champagne, F.H. and Wygnanski, I.J. 1971 An experimental investigation of coaxial turbulent jets, *Int. J. Heat Mass Transfer*, **14**, pp 1445-1464.

Chan, W.T. and Ko N.W.M. 1978 Coherent structures in the outer mixing region of annular jets, *J. Fluid Mech.*, **89**, pp 515-533.

Chu, C.C. 1987 A study of turbulence production and modification in boundary layers using a new photochromic visualization technique, PhD Thesis, Dept. Mech. Engrg, Michigan State University.

Chu, C.C., Hsieh, C.S., Shi, S.T., and Wang, C.T. 1991 A quantitative study of the flow near surfaces induced by vortex motion, *AIAA* 91-1816.

Dahm, W.J.A., Frieler, C.E., and Tryggvason, G. 1992 Vortex structure and dynamics in the near field of a coaxial jet, *J. Fluid Mech.*, **241**, pp 371-402.

Daneshyar, H. and Fuller, D.E. 1986 Definition and measurement of turbulence parameters in reciprocating I.C. engines, *SAE* Paper No. 861529.

Eaton, A.R. and Reynolds, W.C. 1989 Flow structure and mixing in a motored axisymmetric engine, *SAE* Paper No. 890321.

Ekchian, A. and Hoult, D.P. 1979 Flow visualization study of the intake process of an internal combustion engine, *SAE* Paper No. 790095.

Falco, R.E and Chu, C.C. 1987 Measurements of two-dimensional fluid dynamic quantities using a photochromic grid tracing technique, *Proceedings of SPIE*, **814**, pp 706-710, San Diego.

Falco, R.E. and Chu, C.C. 1988 Experimental determination of skin friction modifications due to elastic compliant surfaces using quantitative visual techniques, *Report TSL-88-3*, Dept. Mech. Engrg., Michigan State University.

Falco, R.E., Chu, C.C., Hetherington, M.H., and Gendrich, C.P. 1988 The circulation of an airfoil starting vortex obtained from instantaneous vorticity measurements over an area, *AIAA* 88-3620.

Falco, R.E., Gendrich, C.P., and Chu, C.C. 1989 Vorticity field measurements using Laser Induced Photochemical Anemometry (LIPA), *Seventh Symposium on Turbulent Shear Flows*, Stanford University, August 21-23.

Falco, R.E. and Nocera, D.G. 1991 A study of flow properties of wet solids using Laser Induced Photochemical Anemometry (LIPA), Liquid-Solid-Flows-1991, M.C. Roco and T. Masuyama, ASME Fed-Vol. **118**, pp 143-145.

Falco, R.E. and Nocera, D.G. 1993 Quantitative multipoint measurements and visualization of dense solid-liquid flows using Laser Induced Photochemical Anemometry (LIPA), Particulate Two-Phase Flow, Chapter 3, M.C. Roco, Butterworth-Heinemann.

Foster, D.E. and Witze, P.O. 1988 Two-component laser velocimetry measurements in a spark ignition engine, *Combust. Sci. and Tech.*, **59**, pp 85-105.

Fox, R.W. and McDonald, A.T. 1973 Introduction to Fluid Mechanics, John Wiley & Sons, New York, Santa Barbara, Chichester, Brisbane, Toronto.

Gieselmann, M. 1991 Implementation of and measurement with the LIPA - technique in a subsonic jet, Diplomarbeit, Dept. Mech. Engrg, Michigan State University.

Gosman, A.D., Tsui, Y.Y., and Watkins, A.P. 1984 Calculation of three dimensional air motion in model engines, *SAE* Paper No. 840229.

Hadded, O. and Denbratt, I. 1991 Turbulence characteristics of tumbling air motion in four-valve SI engines and their correlation with combustion parameters, *SAE* Paper No. 910478.

Henriot, S., Le Coz, J.F., and Pinchon, P. 1989 Three dimensional modelling of flow and turbulence in a four-valve spark ingnition engine - comparison with LDV measurements, *SAE* Paper No. 890843.

Hilbert, H.S. 1991 Measurements of flows during scavenging in a two-stroke engine, M.S. Thesis, Dept. Mech. Engrg, Michigan State University.

Hilbert, H.S. and Falco, R.E. 1991 Measurements of flows during scavenging in a two-stroke engine, *SAE* Paper No. 910671.

Hilton, A.D.M., Roberts, J.B., and Hadded, O. 1991 Autocorrelation based analysis of ensemble averaged LDA engine data for bias-free turbulence estimates: a unified approach, *SAE* Paper No. 910479.

Jain, A.K. and Dubes, R.C. 1988 Algorithms for Clustering Data, Prentice - Hall, Englewood Cliffs, NJ.

Kent, J.C., Mikulec, A., Rimai, L., Adamczyk, A.A., Mueller, S.R., Stein, R.A., and Warren, C.C. 1989 Observations on the effects of intake-generated swirl and tumble on combustion duration, *SAE* Paper No. 892096.

Ko, N.W.M. and Chan, W.T. 1978 Similarity in the initial region of annular jets: three configurations, *J. Fluid Mech.*, **84**, pp 641-656.

Lancaster, D.R. 1976 Effects of engine variables on turbulence in a spark-ignition engine, *SAE* Paper No. 760159.

Lee, K., Yoo, S.C., Stuecken, T., McCarrick, D., Schock, H., Hamady, F., LaPointe, L.A., Keller, P., and Hartman, P. 1993 An experimental study of in-cylinder air flow in a 3.5L four-valve SI engine by high speed flow visualization and two-component LDV measurement, *SAE* Paper No. 930478.

Lempert, W.R., Magee, K., Ronney, P., Nosenchuck, D.M., Miles, R.B., Gee, K., and Haugland, R.P. 1993 Flow tagging in water by Photo-Activated Nonintrusive Tracking Of Molecular Motion (PHANTOMM), *AIAA* 93-0517.

Liou, T.-M. and Santavicca, D.A. 1985 Cylce resolved LDV measurements in a motored IC engine, *J. Fluids Engng*, **107**, pp 232-240.

Miller, D.R. and Comings, E.W. 1957 Static pressure distribution in the free turbulent jet, *J. Fluids Mech.*, **3**, pp 1-16.

Mohr, B. and Ertel, H. 1986 Brechungsindexanpassung für Geschwindigkeitsmessungen mittels Laser-Doppler-Anemometrie, *Internal Study* by the 'Lehrstuhl für Strömungsmechanik', Universität Erlangen-Nürnberg, Erlangen.

Moriyoshi, Y., Kamimoto, T., Ohtani, H., and Yagita, M. 1991 Stratification of swirl intensity in the axial direction for control of turbulence generation during the compression stroke, *SAE* Paper No. 910261.

Namazian, M., Hansen, S., Lyford-Pike, E., Sanchez-Barsse, J., Heywood, J., and Rife, J. 1980 Schlieren visualization of the flow and density fields in the cylinder of a spark-ignition engine, *SAE* Paper No. 800044.

Omori, S., Iwachido, K., Motomochi, M., and Hirako, O. 1991 Effect of intake port flow pattern on the in-cylinder tumbling air flow in multi-valve SI engines, *SAE* Paper No. 910477.

Ponce, A., Wong, P.A., Way, J.J., and Nocera, D.G. 1993 Intense phosphorescence triggered by alcohols upon formation of a cyclodextrin ternary complex, *J. of Physical Chemistry*, **97**, pp 11137-11142.

Popovich, A.T. and Hummel, R.L. 1967 Light-induced disturbances in photochromic flow visualization, *Chem. Engrg Sci.* **29**, pp 308-312.

Potter, M.C. and Foss, J.F. 1982 Fluid Mechanics, Great Lakes Press, Inc., Okemos.

Rask, R.B. 1979 Laser Doppler anemometer measurements in an internal combustion engine, *SAE* Paper No. 790094.

Rask, R.B. 1981 Comparison of window, smoothed-ensemble, and cycle-by-cycle data reduction techniques for laser Doppler anemometer measurements of in-cylinder velocity, Fluid Mechanics of Combustion Systems, T. Morel, R.P. Lohmann, and J.M. Rackley, eds., ASME, New York.

Regan, C.A., Chun, K.S., and Schock, H.J. 1987 New developments and applications in gas lasers, *Proceedings of SPIE*, 737, pp 17-27, Los Angeles.

Rockwell, D.O. and Niccolls W.O. 1972 Natural breakdown of planar jets, *J. of Basic Engng*, 72-FE-5, pp 720-730.

Semenov, E.S. 1963 Studies of turbulent gas flow in piston engines, Tech. Transl. F-97 NASA, pp 122-147.

Shack, D.H. and Reynolds, W.C. 1991 Application of particle tracking velocimetry to the cyclic variability of the pre-combustion flow field in a motored axisymmetric engine, *SAE* Paper No. 910475.

Stier, B. and Falco, R.E. 1993 New developments in LIPA (Laser Induced Photochemical Anemometry), *Proceedings of SPIE*, San Diego, July.

Stier, B. and Falco, R.E. 1994 Application of LIPA (Laser Induced Photochemical Anemometry) to a water analog model of a four-stroke IC engine, *SAE* Paper No. 940282.

Tennekes, H. and Lumley J.L. 1972 A First Course in Turbulence, The MIT Press, Cambridge, Massachusetts, and London, England.

Trigui, N., Affes, H., and Kent, J.C. 1994a Use of experimental data as initial conditions for in-cylinder CFD simulations, *SAE* Paper No. 940280.

Trigui, N., Kent, J.C., Guezennec, Y., and Choi, W.C. 1994b Characterization of intake generated fluid flow fields in IC engines using 3-D Particle Tracking Velocimetry, *SAE* Paper No. 940279.

Vafidis, C. and Whitelaw, J.H. 1986 Intake valve and in-cylinder flow development in a reciprocating model engine, *Proc. Instn Mech. Engrs*, 200, pp 143-152.

White, F.M. 1991 Viscous Fluid Flow, McGraw-Hill, New York.

Winsor, R.E. and Patterson, D.J. 1973 Mixture turbulence -- a key to cyclic combustion variation, *SAE* Paper No. 730086.

Witze, P.O. 1977 Measurements of the spatial distribution and engine speed dependence of turbulent air motion in an IC engine, *SAE* Paper No. 770220.

Witze, P.O., Martin, J.K., and Borgnakke, C. 1984 Conditionally-sampled velocity and turbulence measurements in a spark ignition engine, *Combustion Science and Technology*, **36**, pp 301-317.

Yoo, S.C. 1994 An in-cylinder air flow study in a four-valve SI engine by three-dimensional LDV measurements and high speed flow visualization, PhD Thesis, Dept. Mech. Engrg, Michigan State University.

Yule, A.J. 1978 Large-scale structure in the mixing layer of a round jet, *J. Fluid Mech.*, **89**, pp 413-432.

Yurechko, V.N. and Ryazantsev, Y.S. 1991 Fluid motion investigation by the photochromic flow visualization technique, *Expt'l. Thermal and Fluid Sci.*, pp 273-288.

FIGURES
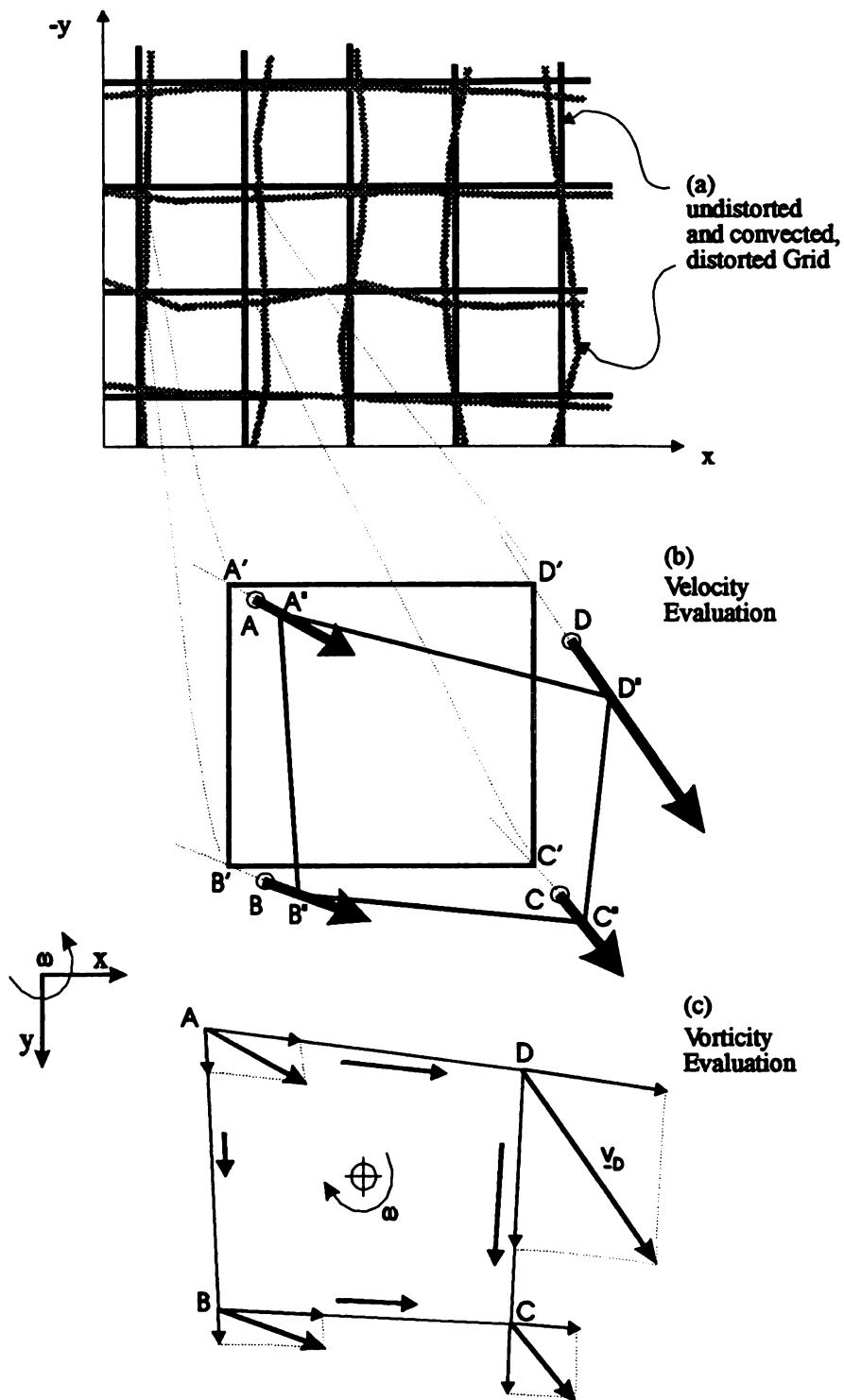
Figure II.1.1: Evaluation of velocity and vorticity vectors from convection of investigation grid with the fluid flow.
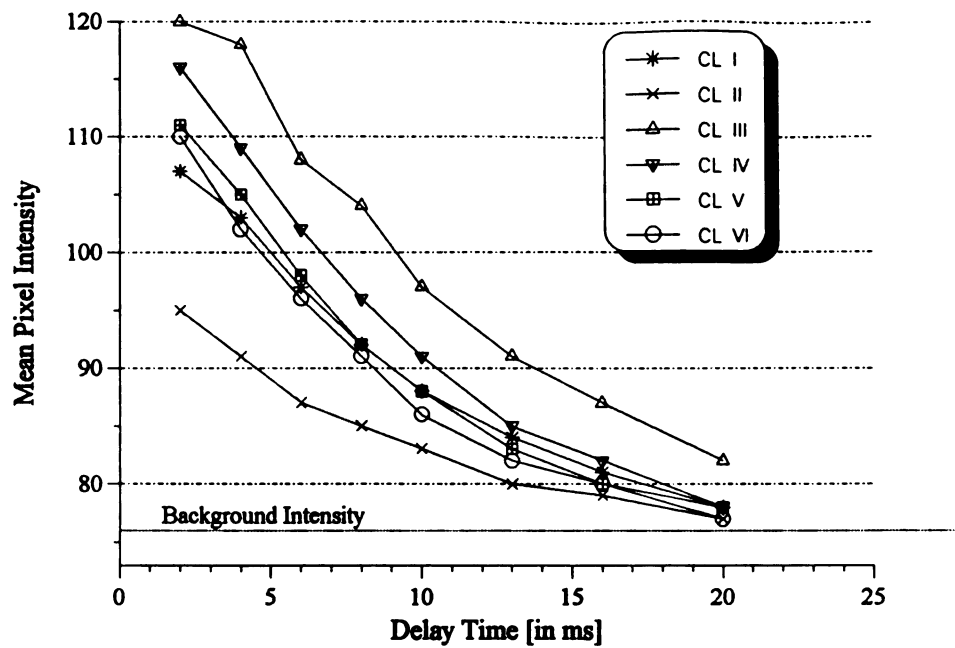
Figure II.1.2: Degradation of intensity of radiation emitted from investigation grid with time; influence of bleaching and shelf-life.
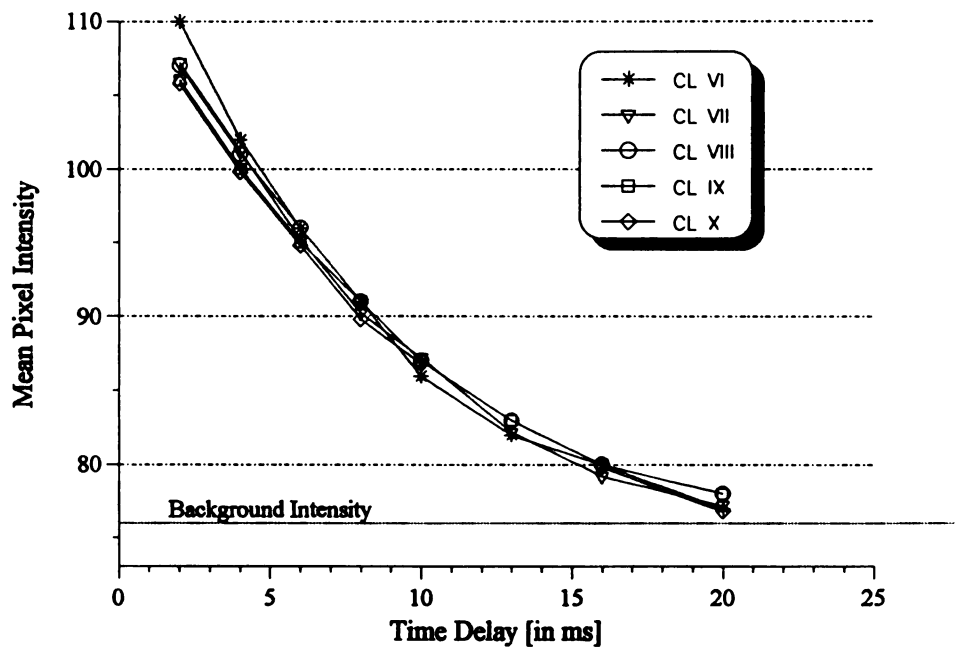
Figure II.1.3: Results of attempt for refinement of used LIPA - chemical by adding supplements of the alcohol component t-BuOH.

(a)

Coordinate System for Cylinder

Table II.2.1: Engine geometry

Engine Parameter	Dimension
Bore	82 mm
Stroke	82.4mm
Clearance	18 mm
Valve-Ø	32 mm
Valve-Ø/Bore	0.39
Bore/Stroke	0.995

(b)
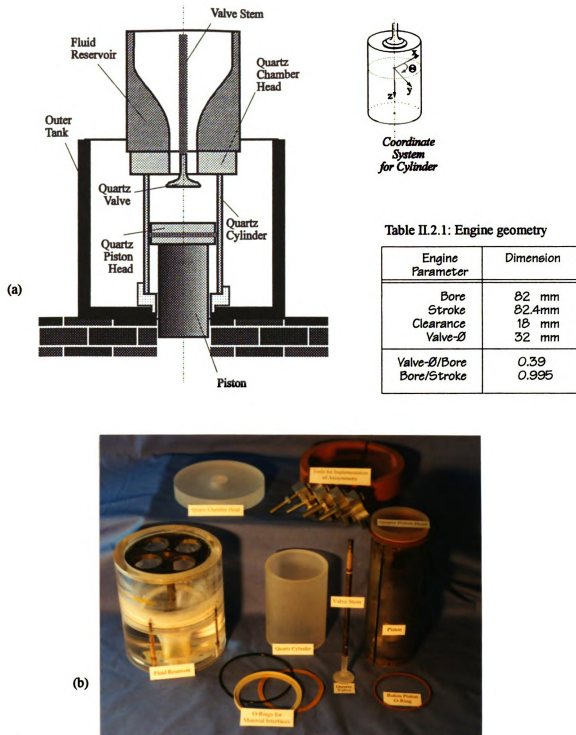
Figure II.2.1: (a) Schematic of the water analog model showing the essential quartz pieces [included in (a) are the measures of the engine geometry].
(b) The quartz cylinder, head, piston, and valve along with diverse other components of the engine configuration. Also shown are the four metal 'riders' for the four sides of the outer tank -- used for the calibration of axisymmetry --, that hold the fluid reservoir at the right distances from the outer tank after the collar established axisymmetry.

(a)

(b)
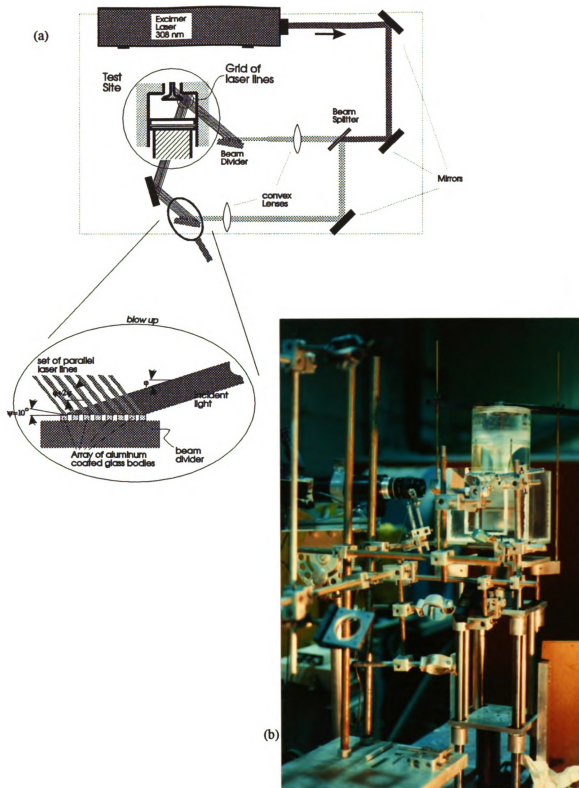
Figure II.2.2: Apparatus used to create the grid of laser lines in the quartz engine.
(a) Schematic showing the paths of light and grid location.
(b) Photograph of the setup, with the image acquisition system in the background.

Investigation of Fluid Dynamics ...
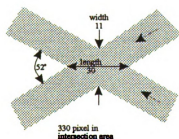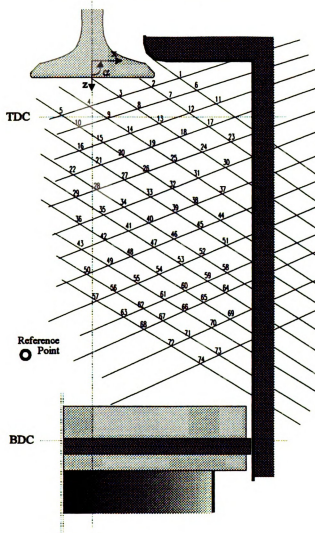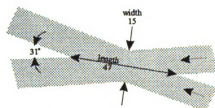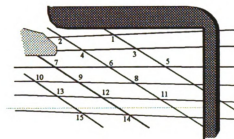
Figure II.2.3: Grids of laser lines for investigation of (a) most of the cylinder volume
and (b) intake jet. For both grids a typical intersection area is shown
magnified and scrutinized.
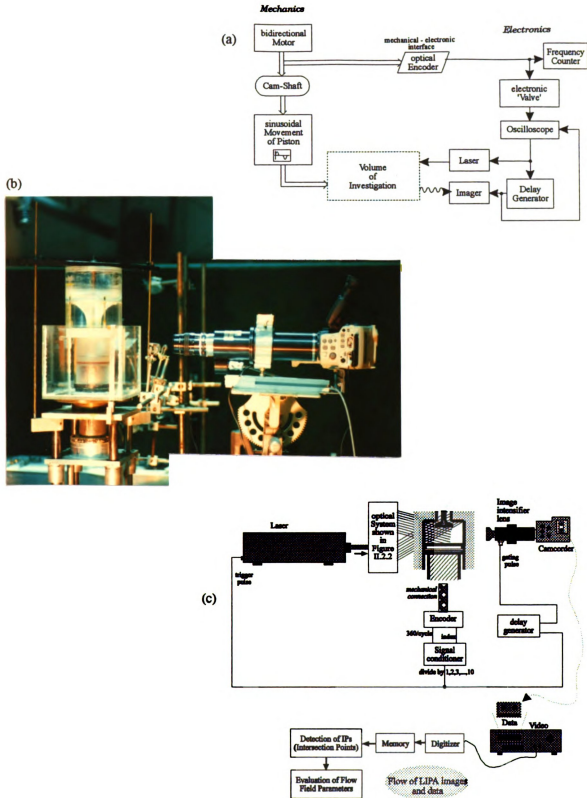
Figure II.2.4: (a) Schematic of the timing system; (b) Photo of the image intensified CCD
camera in data taking position; (c) Schematic of the overall data acquisition
system.
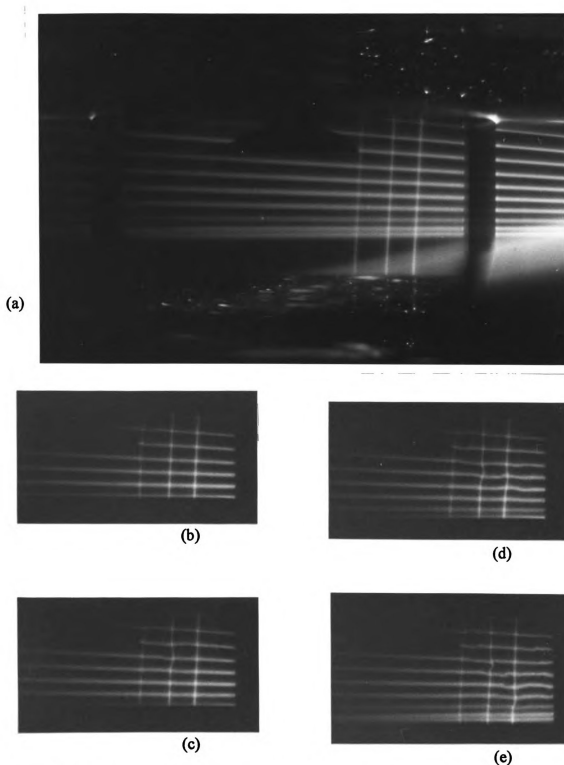
Figure II.2.5: Black and white images holding LIPA grids generated by the optical system.
(a) The reference grid (light enters the cylinder wall on the right, and can be seen coming out of the other side of the quartz valve -- near the center of the picture).
(b - e) Four independent photos showing distortions in the laser grid larger than useful for data acquisition (long delay time). Engine speed is 20 RPM.
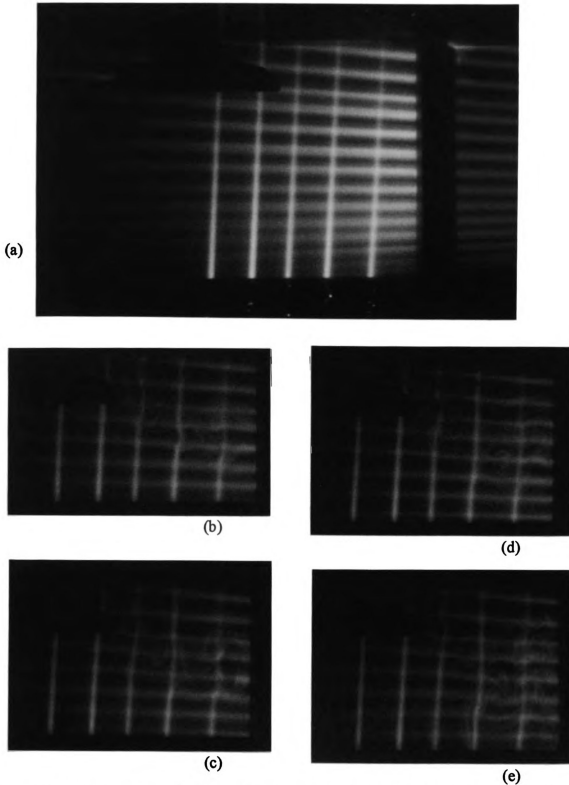
Figure II.2.6: Color images of LIPA grids showing a sequence of four data photos and the calibration grid used with them from preliminary tests. (a) Calibration grid. (b - e) Four successive data frames; these frames also reveal the flow pattern of intake vortices because the LIPA - chemical irradiated in the previous laser pulses is still glowing after it has been warped around the vortices (20 RPM).
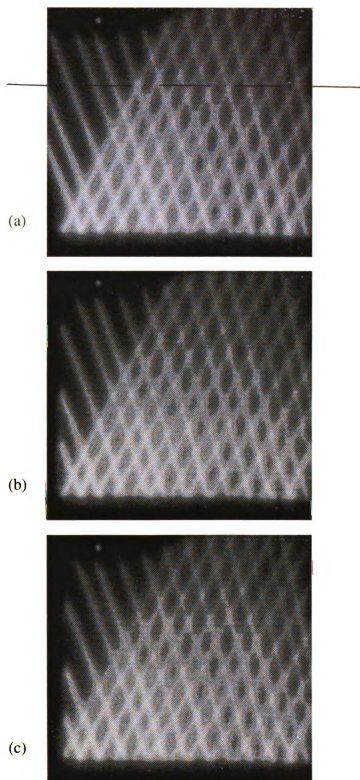
Figure II.2.7: Examples of the undistorted (a) and distorted (b, c) LIPA grids acquired with the IIL/camcorder combination. To optimize the CCD format, the camcorder was turned 90° so that the valve is on the right side of the image, and the cylinder wall on the bottom.
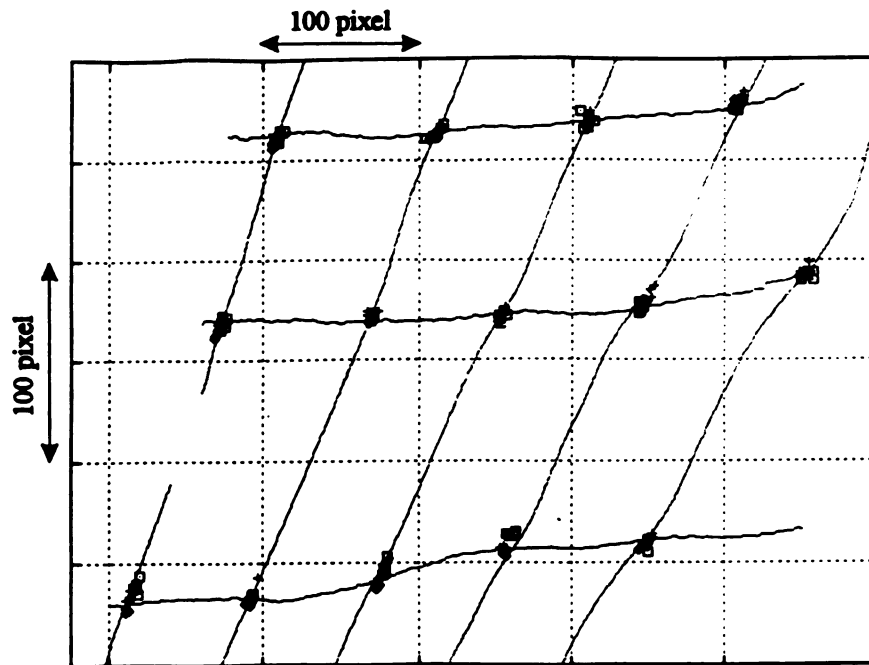
Figure III.1: Comparison between results of inference of coordinates of illuminated
'particles' from LIPA images as deduced by hand (cross, square,
and diamond) and by machine (dotted lines).
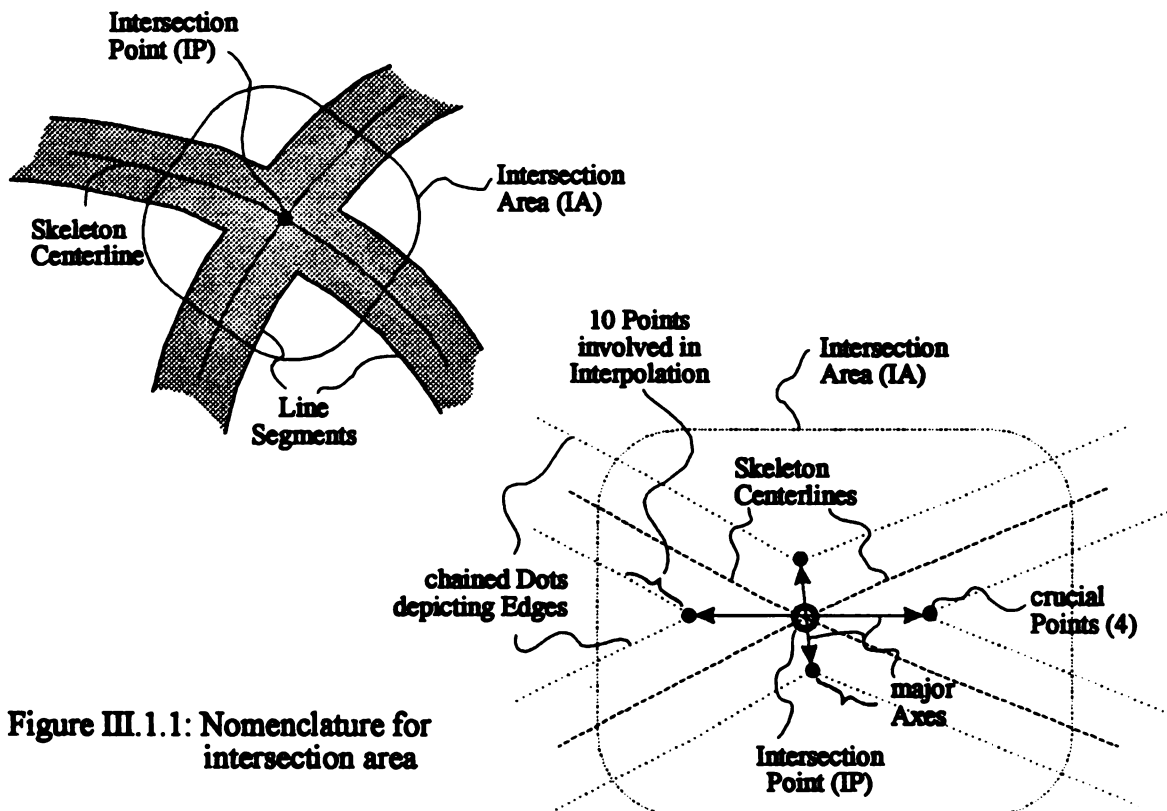
Figure III.1.1: Nomenclature for
intersection area
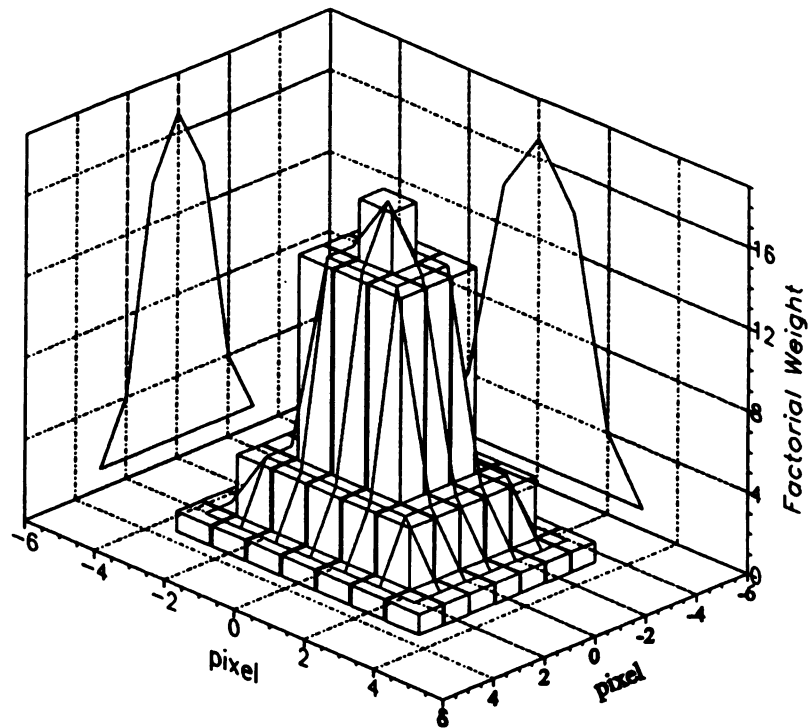
Figure III.1.2: Weight distribution used for the evaluation of intensity distribution in an IA according to which 'HIS' chooses the highest intensity spot.

IP determined by IAR

IP evaluated by HIS
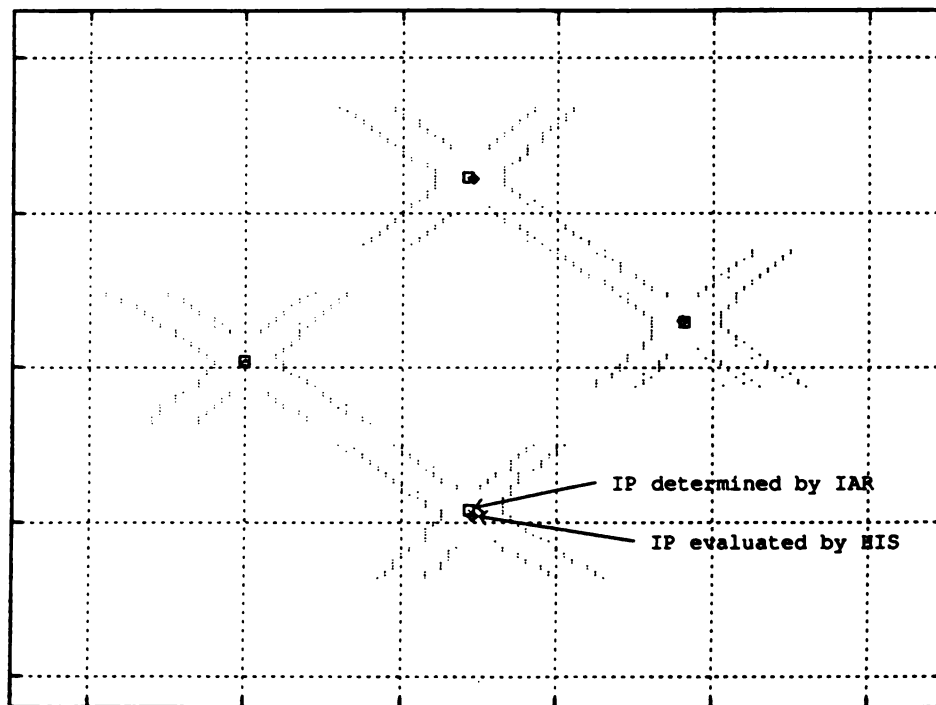
Figure III.1.3: Comparison between the results of applications of 'IAR' and 'HIS' to four intersection areas.
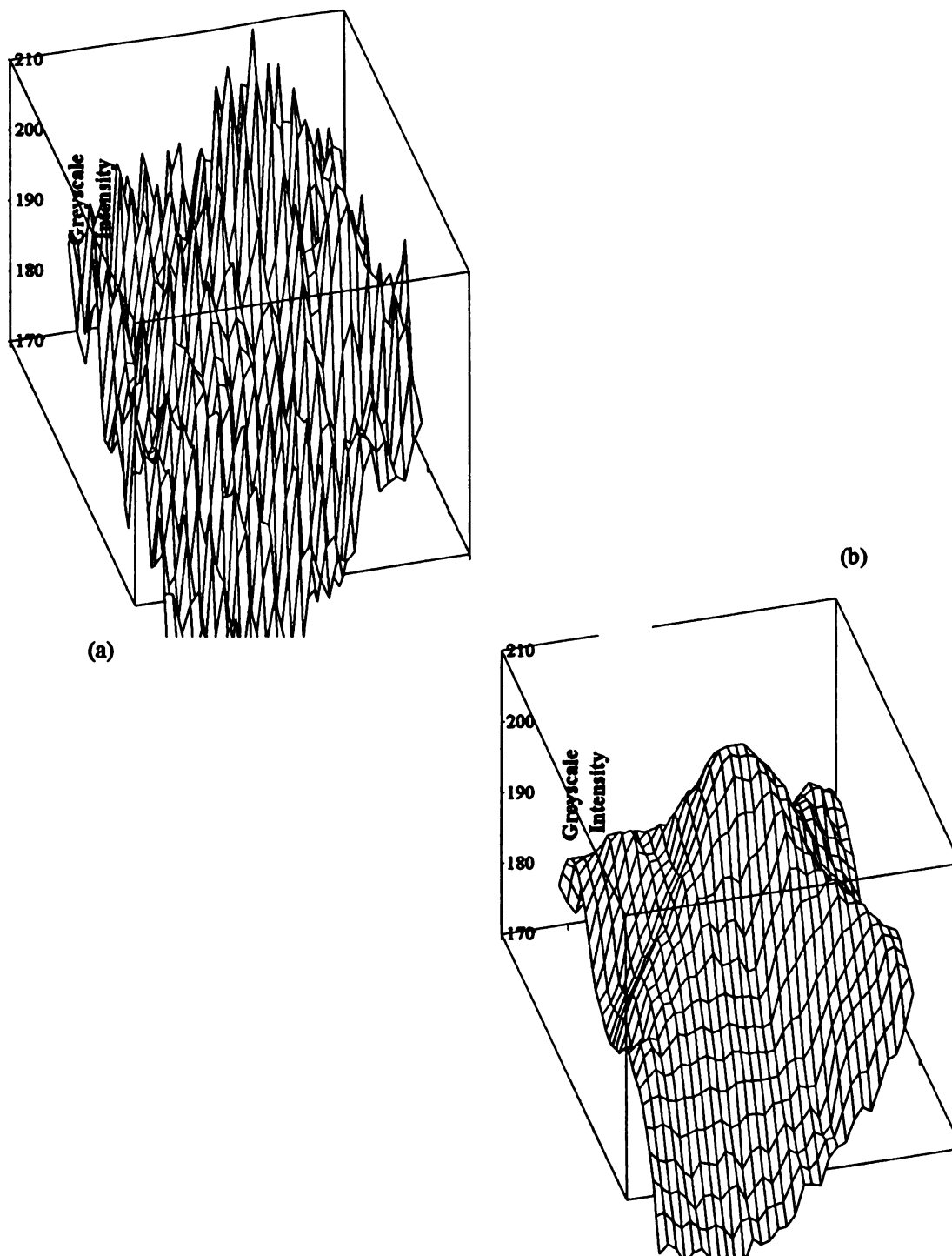
Figure III.1.4: Depiction of an intersection area in
terms of pixel intensity; (a) shows the pixel
intensity distribution for an IA as it is delivered
at the output of the CCD camera, (b) exhibits the
same distribution after the image was conditioned.
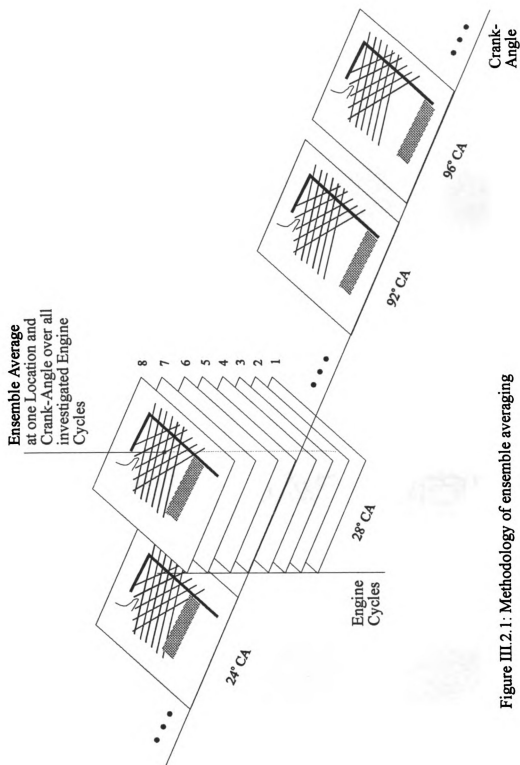
Figure III.2.1: Methodology of ensemble averaging
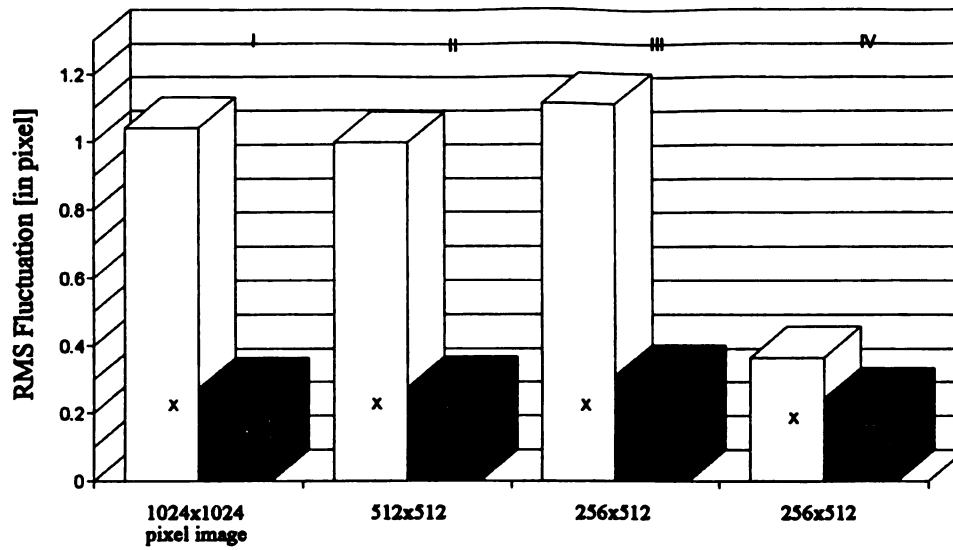
Figure III.3.1: Effect of change in number of pixel per image and extent of object in image in x - and z - direction.
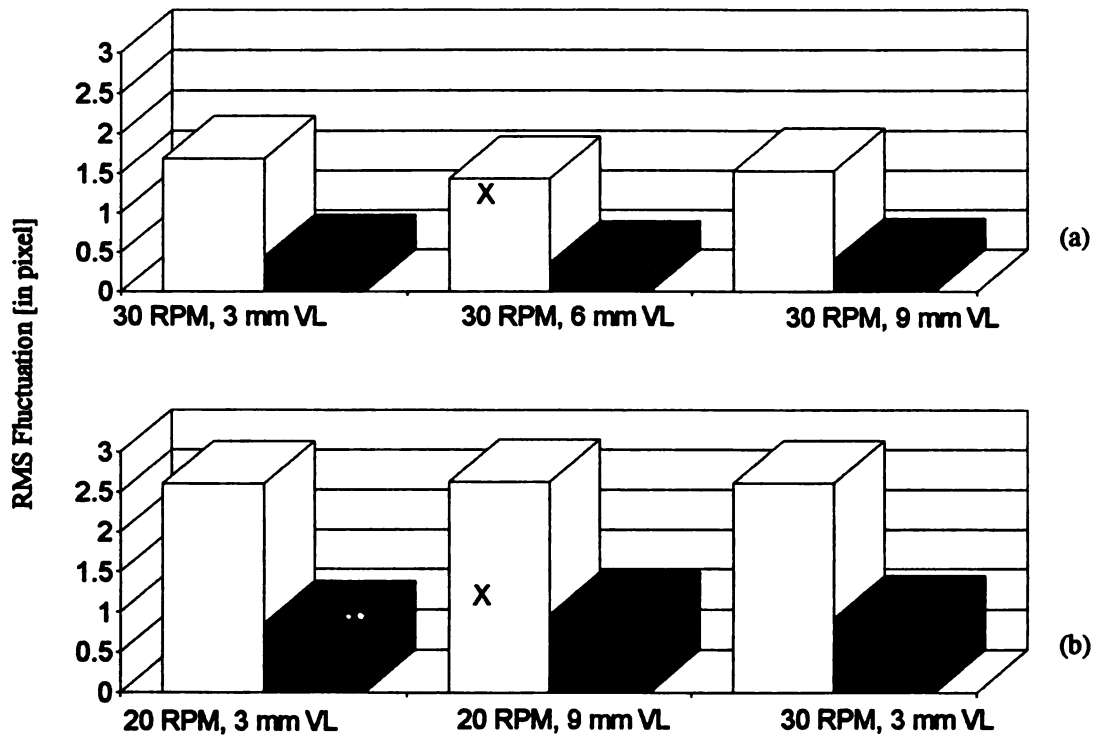
Figure III.3.2: Velocity fluctuations exhibited by reference laser grids employed in investigation of (a) whole engine cylinder and (b) the intake jet as close up.
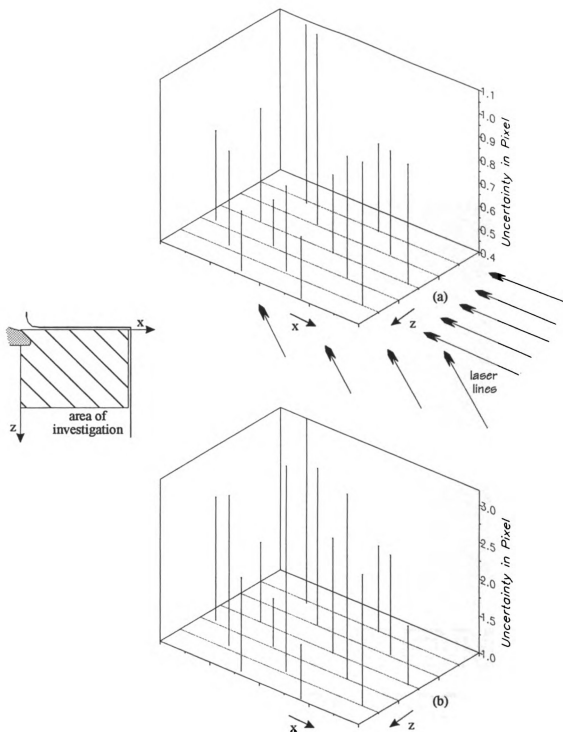
Figure III.3.3: Uncertainty about determination of initial positions in reference grids for 20 RPM engine speed and 3 mm valve lift as encountered for the close-up investigation grid;
(a) in z - direction, (b) in x - direction.
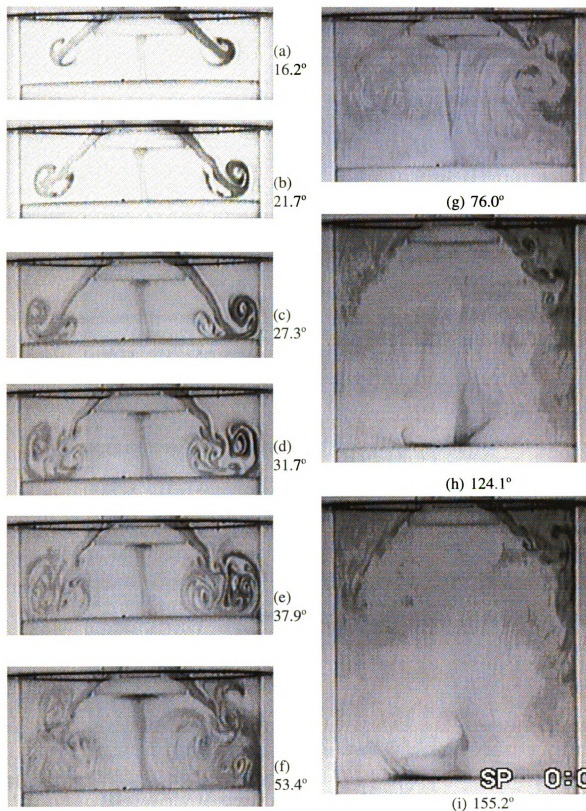
Figure IV.1.1: Flow visualization of the intake stroke using photochromic dye (color change upon irradiation). The piston head is visible near the bottom of each photo, and the cylinder head and intake valve are visible near the top. It is interesting to note a spiral up-flow of fluid that has reached the piston head exists throughout the sequence.
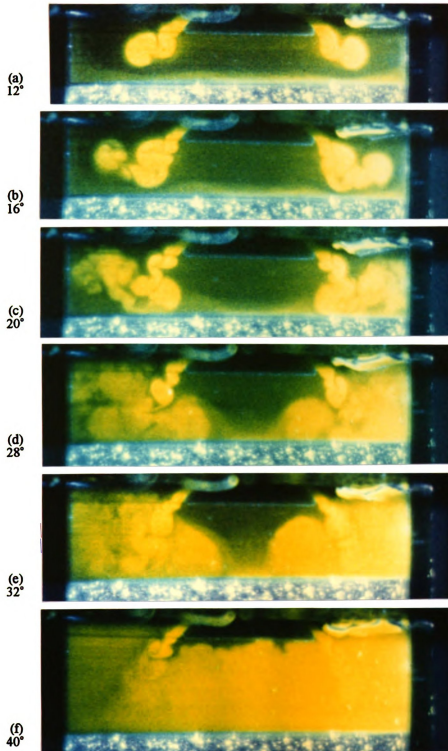
Figure IV.2.1: Flow visualization of the intake stroke using a fluorescent dye in the
reservoir above the valve (MODE I). A laser sheet of 308 nm light is slicing
the cylinder both above and below the valve (the impurities in the quartz of
the piston head make it clearly visible). Results are at 20 RPM and 3 mm
valve lift. The numbers are in degrees crank-angle. By 40° CA the cylinder
is filled with dye and the experiment is stopped. Some air bubbles have
formed from air in the water and partly obscure the view.

(a)
8°
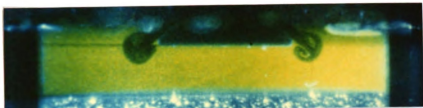
(b)
12°
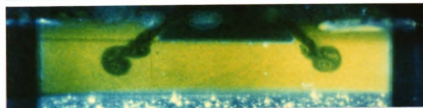
(c)
16°
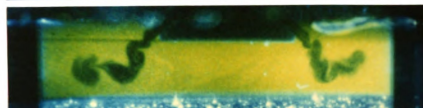
(d)
20°
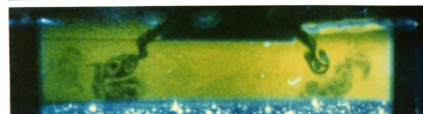
(e)
24°
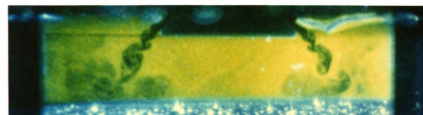
(f)
28°
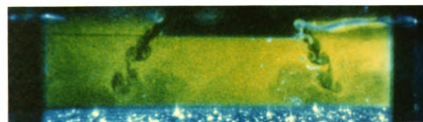
(g)
32°

(Caption is on next page.)

(h)
36°

(i)
44°

(j)
52°

(k)
92°
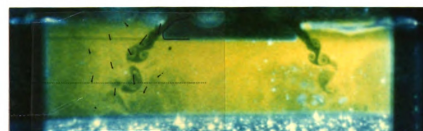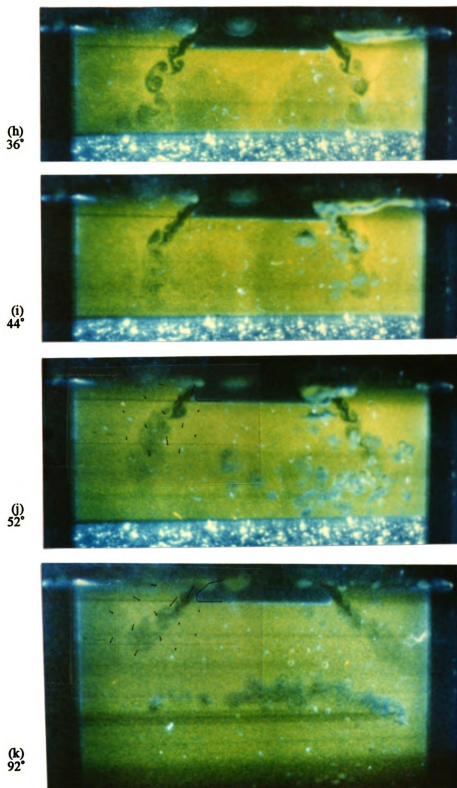
Figure IV.2.2: Flow visualization of the induction stroke, where the inducted fluid is dye-free and the fluid in the cylinder has been dyed (MODE II). Engine speed is 20 RPM and valve lift is 3 mm. The LIPA results for CAs 32°, 52°, and 92° (see section V.5.1) are superimposed on the visualizations.

4° CA (a)

16° CA (b)

20° CA (c)

32° CA (d)

36° CA (e)

44° CA (f)

48° CA (g)

TDC

56° CA (h)

64° CA (i)

72° CA (j)

84° CA (k)

92° CA (l)

→
1m/s
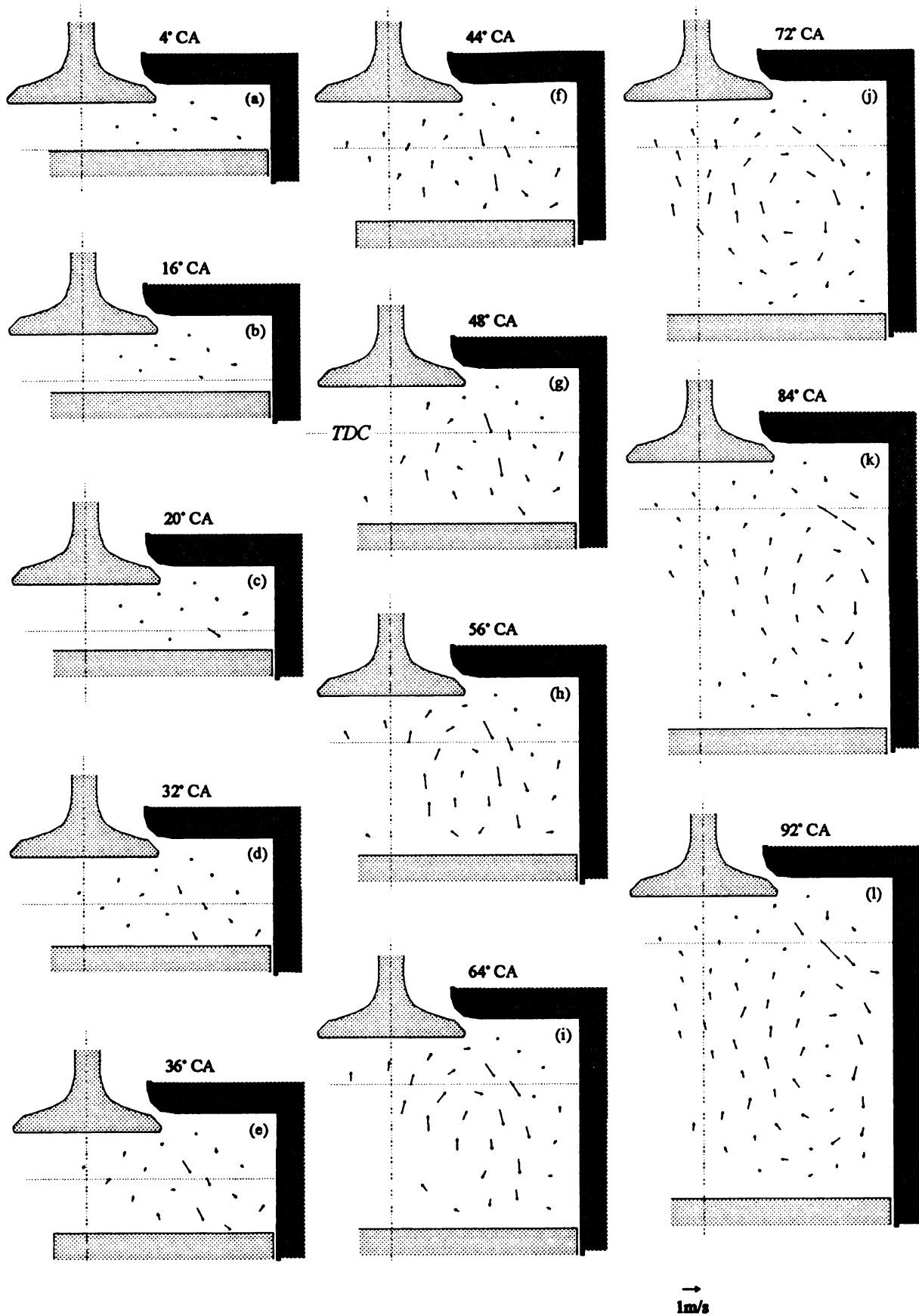
Velocity Vector

(Caption and reference frame are on next page.)
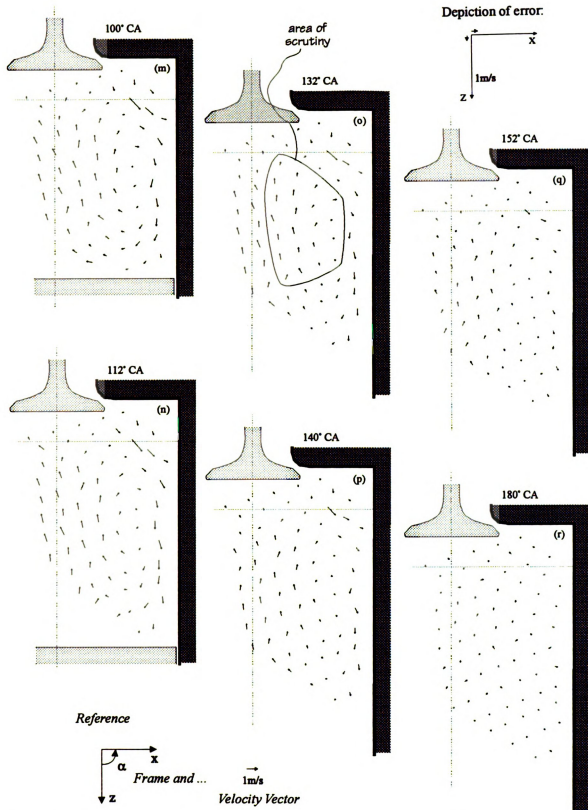
Figure V.1.1: Maps of ensemble averaged velocity vectors (over 42 ECs) at selected crank-angle positions for 20 RPM engine speed and 3 mm valve lift illustrating the development of intake flow.
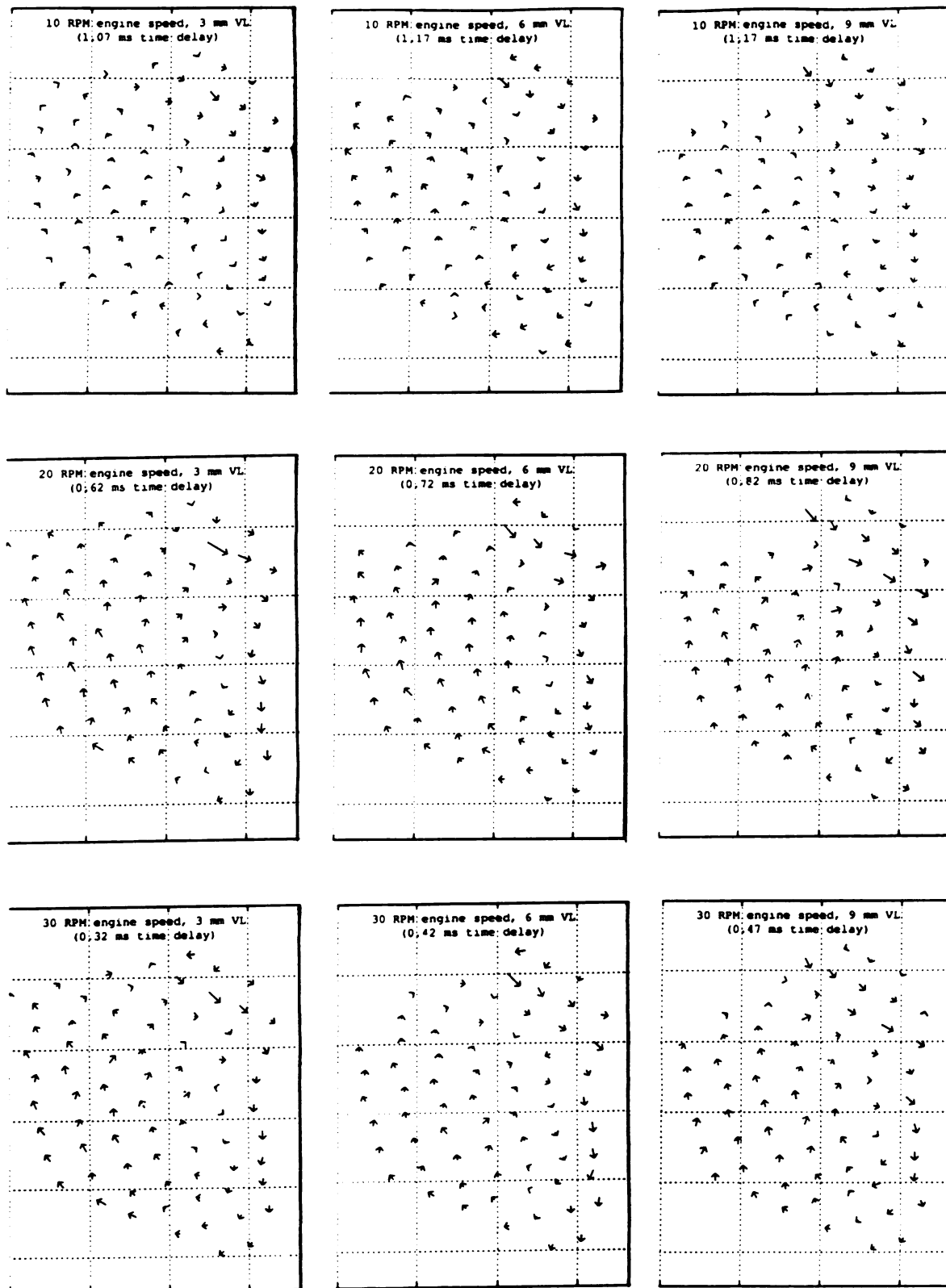
Figure V.1.2: Ensemble averaged velocity vectors at 132° crank-angle
for all nine settings of the engine parameters.
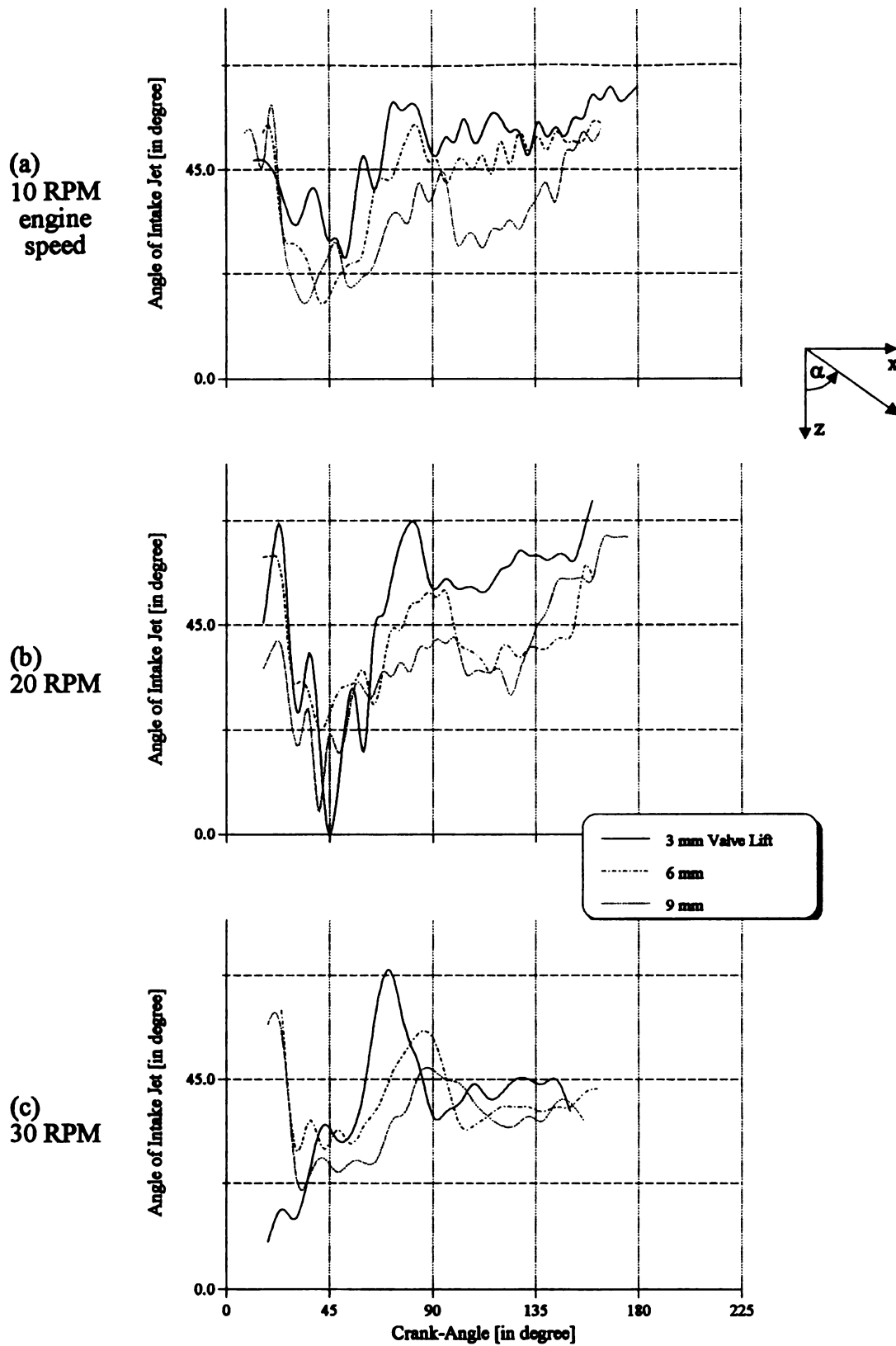
Figure V.1.3: Profiles of induction angle in dependence of engine speed and valve lift.

(a)

(b)
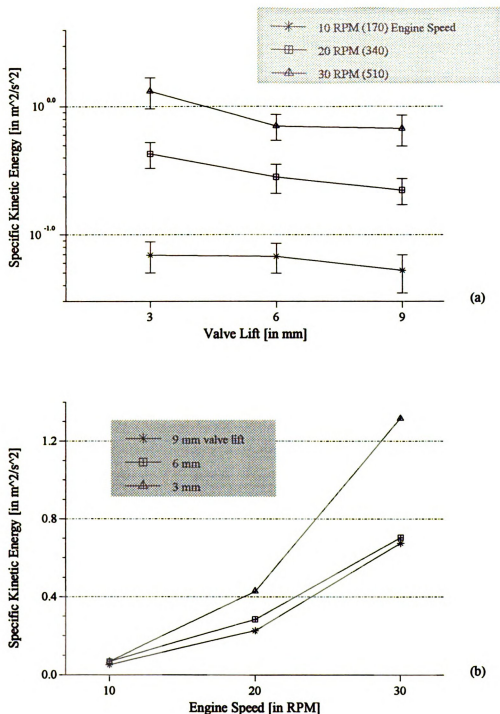
Figure V.2.1: Specific kinetic energy inherent in area of scrutiny at
132° crank-angle as a function of valve lift and engine speed;
(a) KE versus valve lift, (b) KE versus engine speed.
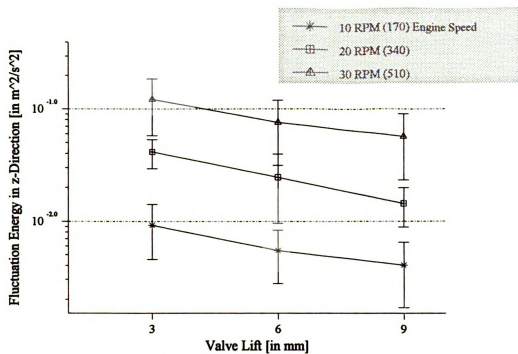
Figure V.2.2: Energy content in velocity fluctuations for z - direction
inherent in area of scrutiny at 132° crank-angle in
dependence of valve lift and engine speed.
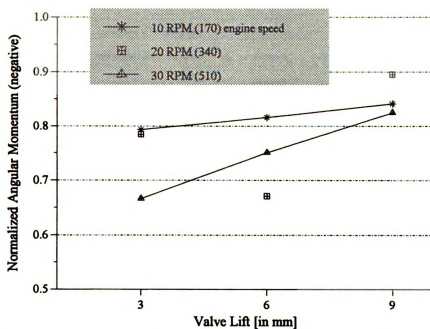
Figure V.2.3: Comparison of angular momentum in area of scrutiny for different
settings of valve lift and engine speed at 132° crank-angle.
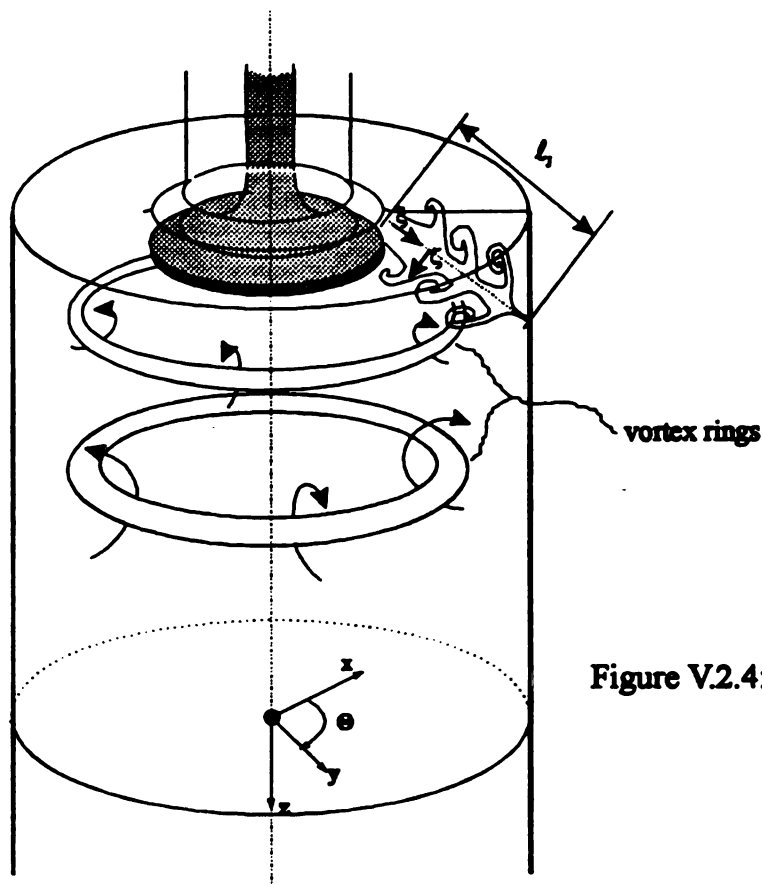
Figure V.2.4: Mechanism of vortex ring
ingestion
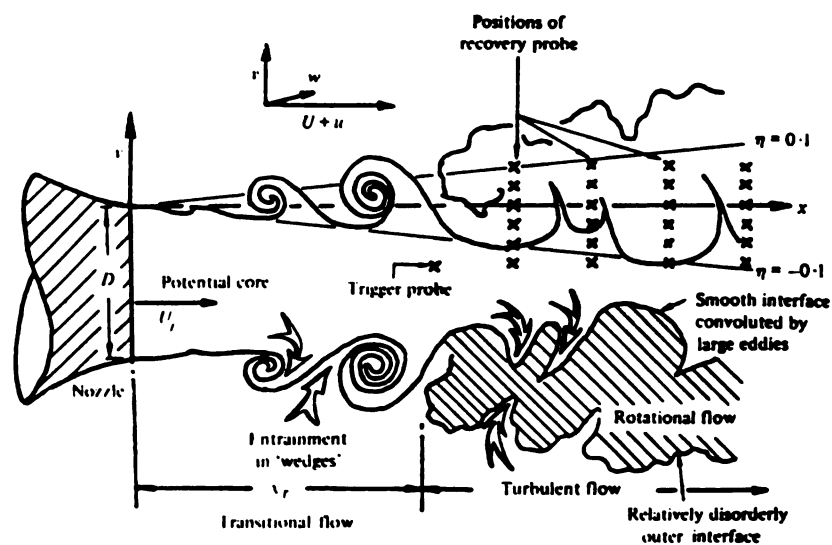
Figure V.2.5: Schematic decomposition of an axisymmetric jet flow field
into two characteristic regions of flow. [Source: Yule 1978]

(a) 4° CA
(b) 16° CA
(c) 20° CA
(d) 32° CA
(e) 36° CA
(f) 44° CA
(g) 48° CA — TDC
(h) 56° CA
(i) 64° CA
(j) 72° CA
(k) 84° CA
(l) 92° CA
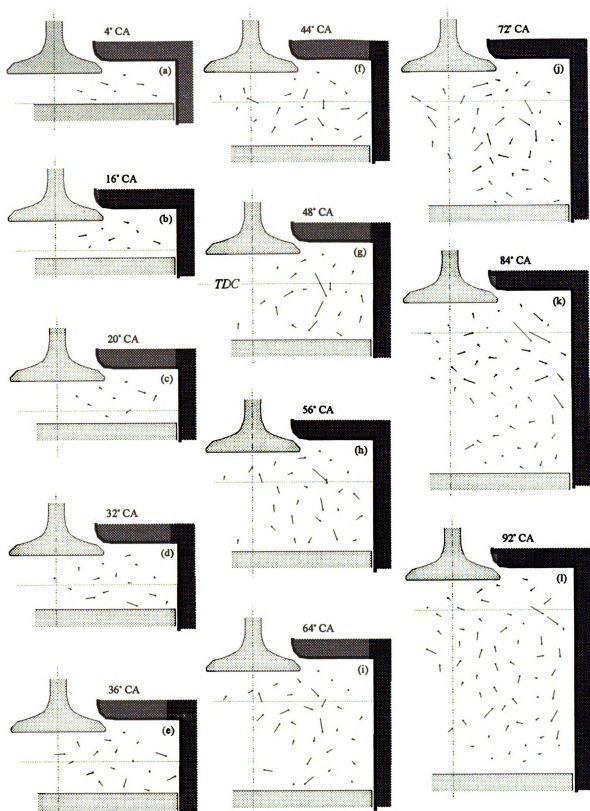
(Caption and reference frame are on page 235; error considerations are given on next page.)

→ 1m/s
Velocity Vector

Depiction of error:

100° CA (m)

116° CA (o)

132° CA (q)

112° CA (n)

128° CA (p)

140° CA (r)

Reference

Frame and ...

1m/s
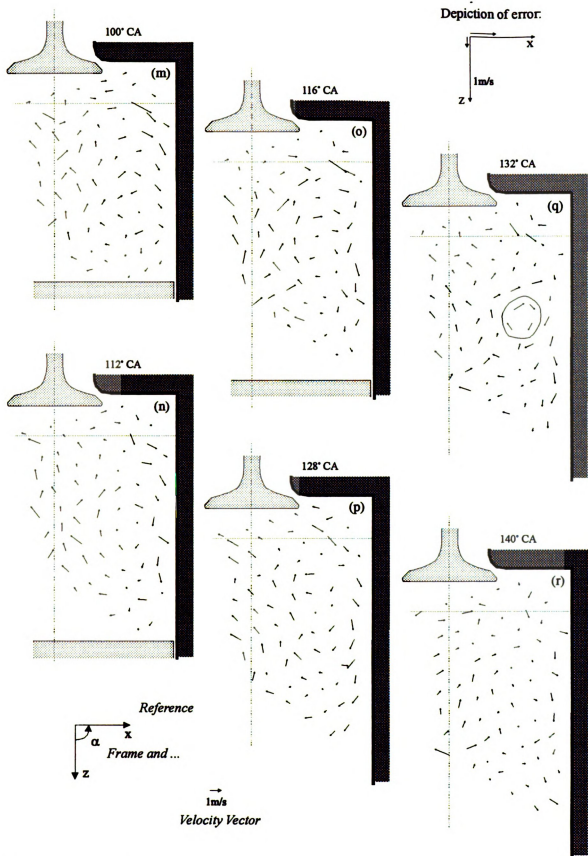
Velocity Vector

Figure V.3.1: Maps of instantaneous velocity vectors for one engine cycle
at selected crank-angle positions for 20 RPM engine speed
and 3 mm valve lift illustrating the development of intake flow.
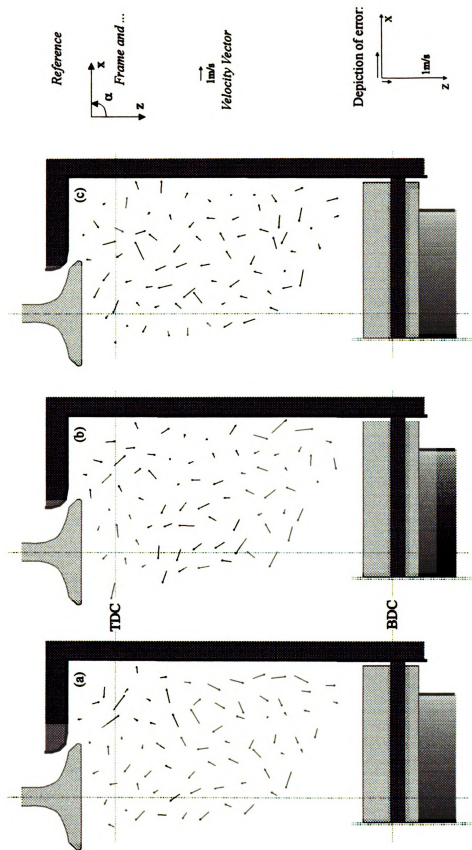
Figure V.3.2: Maps of instantaneous velocity vectors for three consecutive engine cycles at 20 RPM and 3 mm VL. Crank-angle 132°, engine cycles #27, 28, and 29. (Time delay: 0.64 ms)
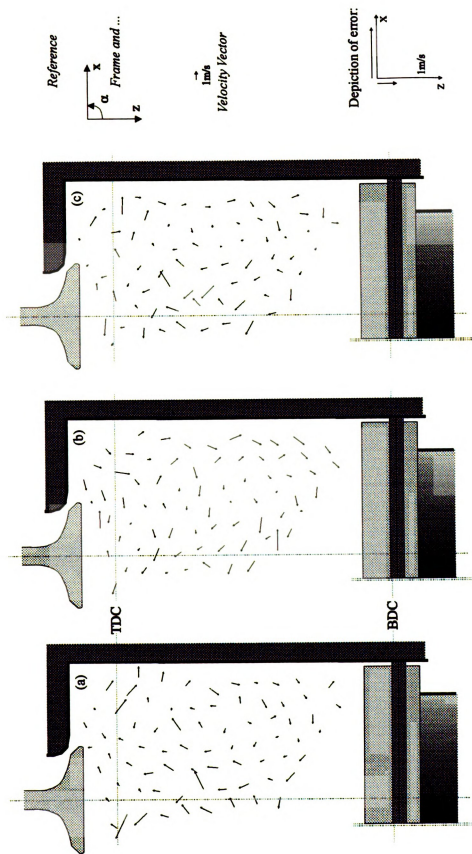
Figure V.3.3 : Maps of instantaneous velocity vectors for three consecutive engine cycles at 30 RPM and 3 mm VL. Crank-angle 132°, engine cycles #38, 39, and 40. (Time delay: 0.32 ms)

238
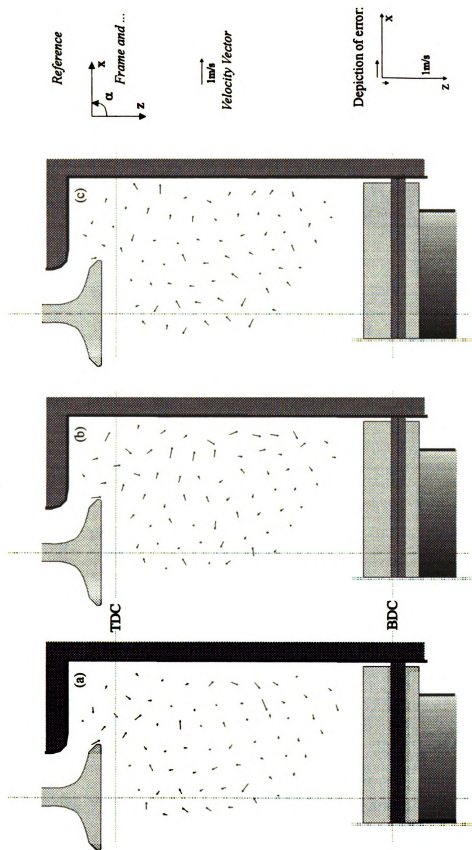
Figure V.3.4: Maps of instantaneous velocity vectors for three consecutive engine cycles at 10 RPM and 9 mm VL. Crank-angle 132°; engine cycles #15, 16, and 17. (Time delay: 0.96 ms)
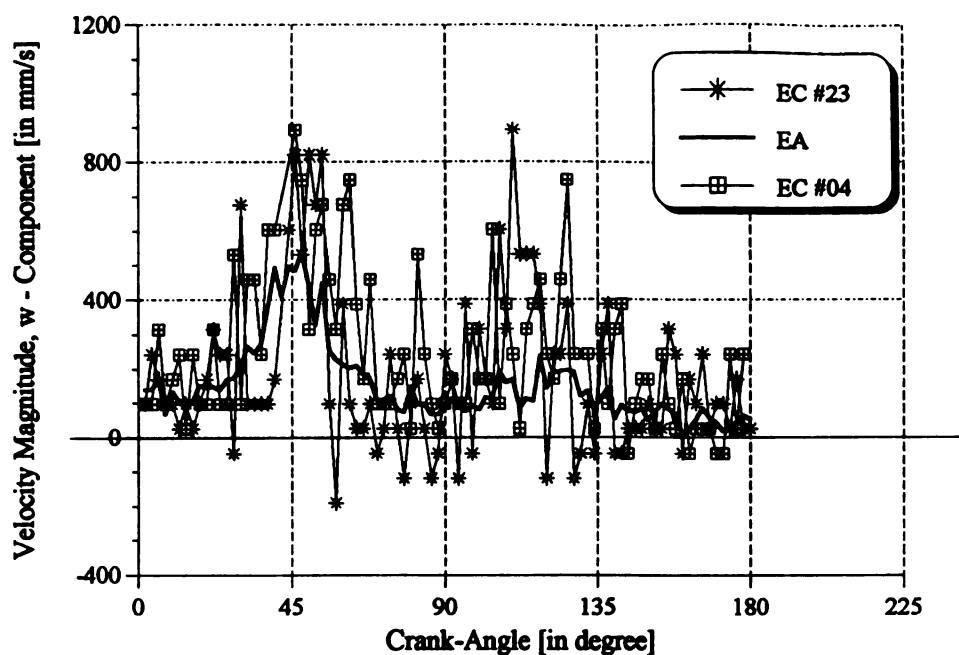
Fig. V.3.5: Velocity profile for 10 RPM engine speed and 3 mm valve lift; location is in the vicinity of the axis of the intake jet.
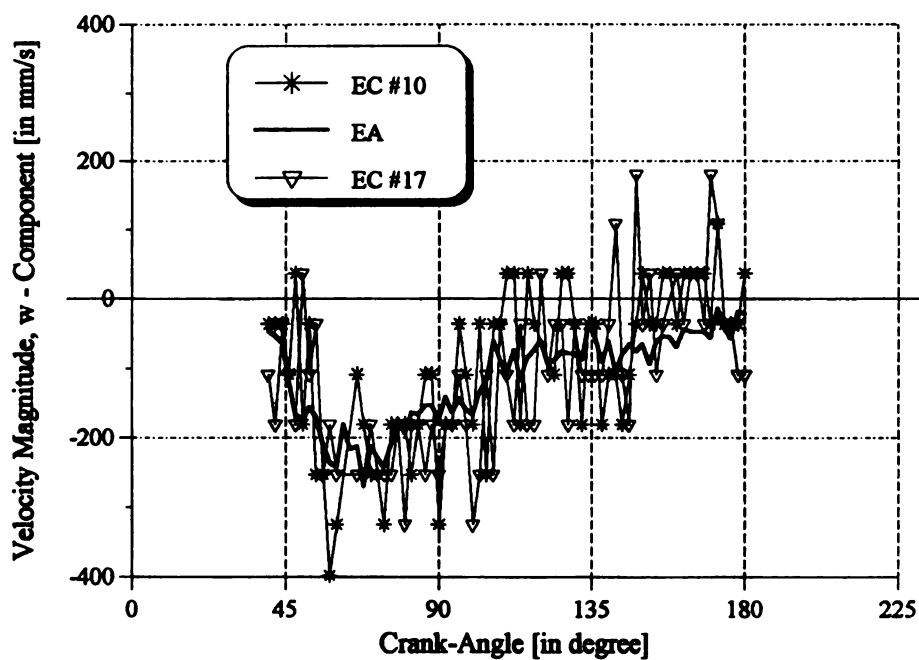
Fig. V.3.6: Velocity profile for 10 RPM engine speed and 3 mm valve lift; location is in the area of scrutiny.
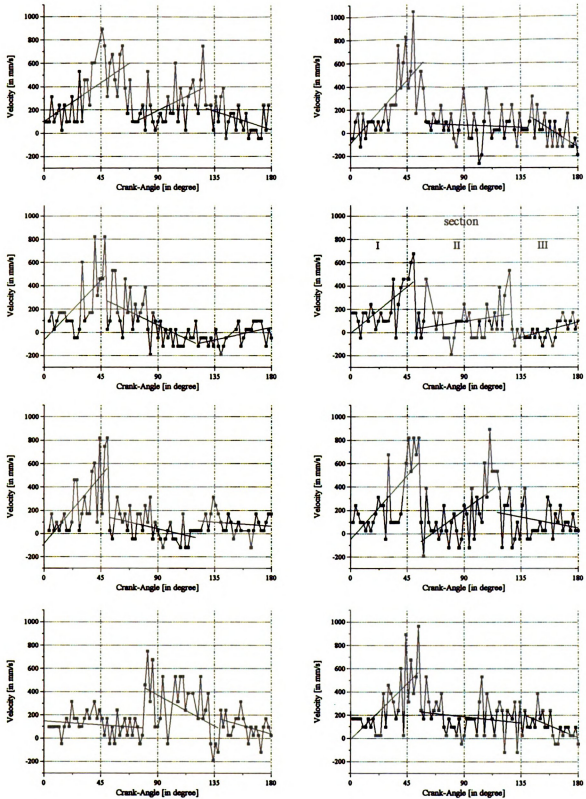
Figure V.3.7: Profiles of the z - component of the instantaneous velocity vector located in the region governed by the intake jet for eight different engine cycles; the plots also contain linear curve fits for the profiles.
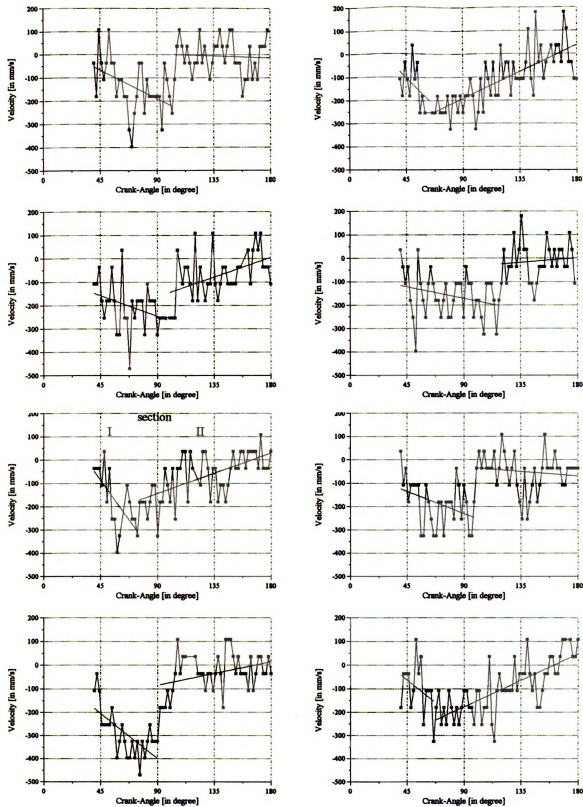
Figure V.3.8: Profiles of the z - component of the instantaneous velocity vector located in the area of scrutiny for eight different engine cycles; the plots also contain linear curve fits for the profiles.
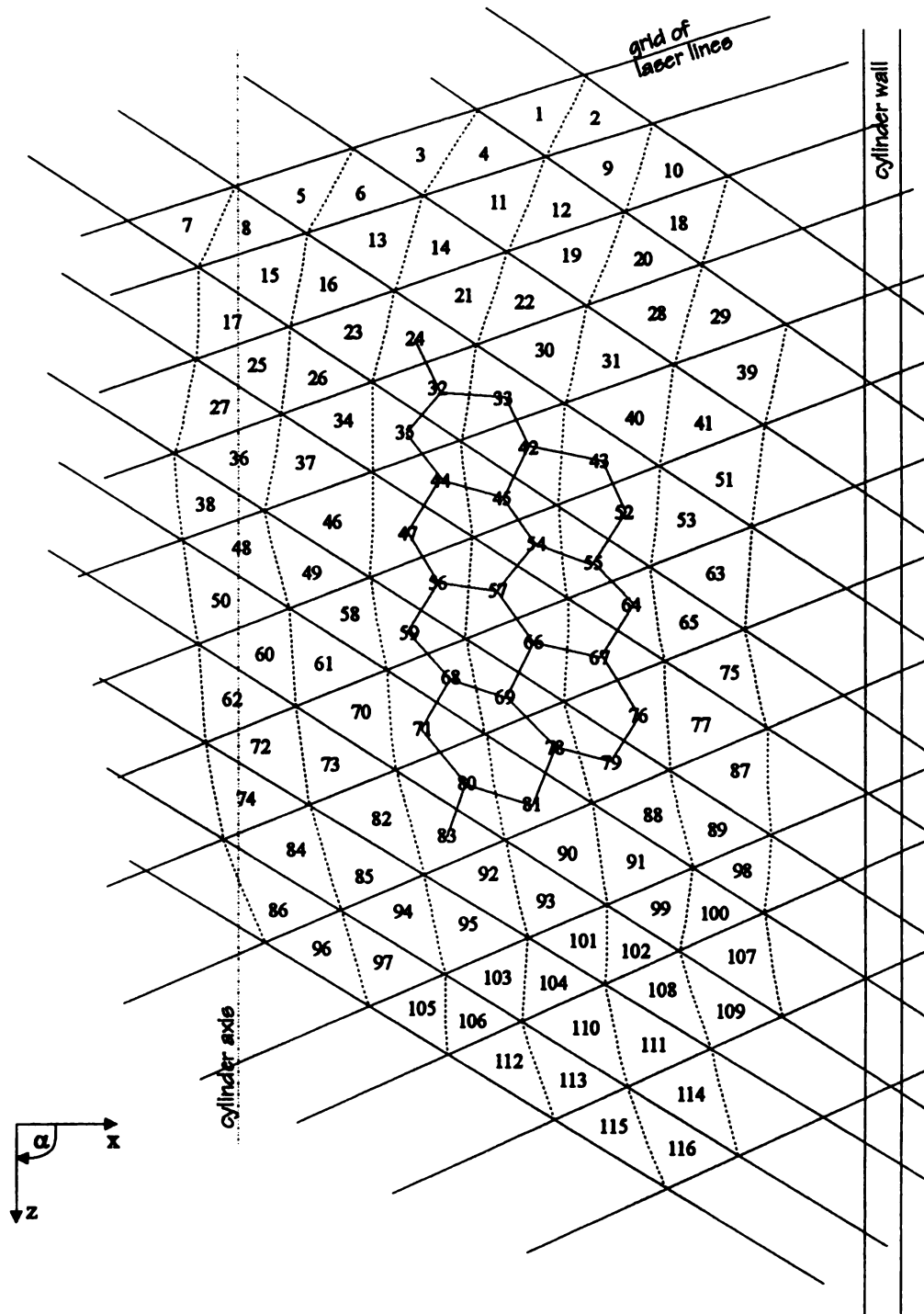
Figure V.4.1: Investigation scheme for vorticity distributions.
   Scheme includes hexagonal pattern formed by vorticity vectors
   from area of scrutiny. The 116 vorticity vectors are derived
   from the 74 intersections in the grid of laser lines exhibited in
   Figure II.2.3a.

2D contour plot

3D contour plots

TDC

BDC

azimuth -20°

vorticity [in 1/s]

x

z

elevation 30
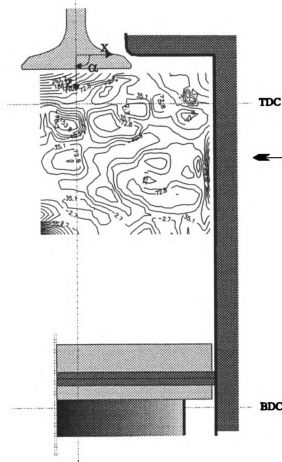
10 RPM, 3 mm;
EC #23, 132° CA

view for
azimuth = 0°

Vorticity [in 1/s]

x

z
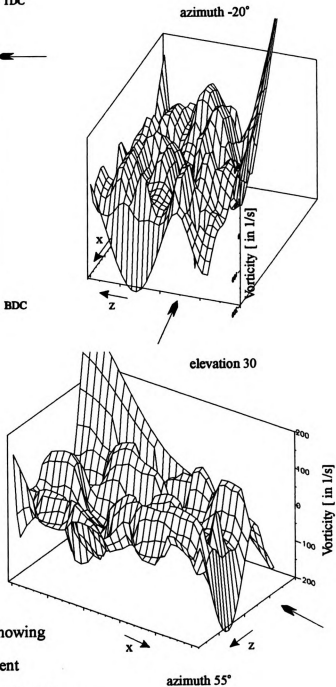
azimuth 55°

Figure V.4.2: Different perspectives showing
the distribution of the
circumferential component
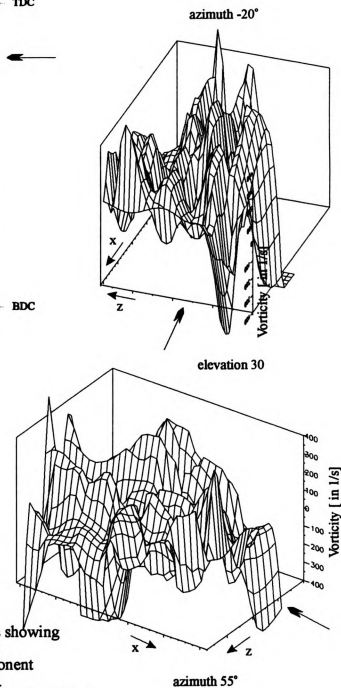of the vorticity vector.
The area covered is about 50x50 mm.

2D contour plot

3D contour plots

TDC

BDC

azimuth -20°

x

z

Vorticity [in 1/s]

elevation 30

10 RPM, 6 mm;
EC #13, 132° CA

view for
azimuth = 0°

azimuth 55°

x

z

Vorticity [in 1/s]

200
400
100
200

Figure V.4.3: Different perspectives showing
the distribution of the
circumferential component
of the vorticity vector.
The area covered is about 50x50 mm.

2D contour plot

TDC

BDC

3D contour plots

azimuth -20°

x

z

Vorticity [in 1/s]

elevation 30

200
400
0
100
200

Vorticity [in 1/s]

x

z
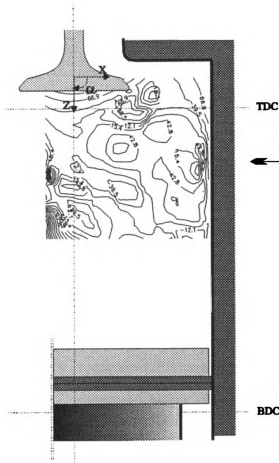
azimuth 55°

10 RPM, 9 mm;
EC #28, 132° CA

view for
azimuth = 0°
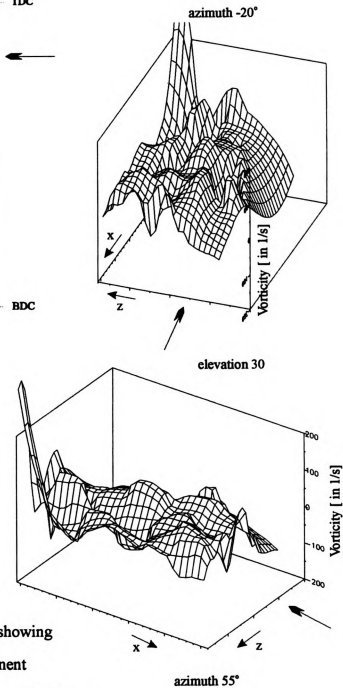
Figure V.4.4: Different perspectives showing
the distribution of the
circumferential component
of the vorticity vector.
The area covered is about 50x50 mm.

2D contour plot

TDC

BDC

3D contour plots

azimuth -20°

Vorticity [in 1/s]

elevation 30

20 RPM, 3 mm;
EC #27, 132° CA

view for
azimuth = 0°

Vorticity [in 1/s]

azimuth 55°

Figure V.4.5: Different perspectives showing
the distribution of the
circumferential component
of the vorticity vector.
The area covered is about 50x50 mm.

2D contour plot

TDC

3D contour plots

azimuth -20°

BDC

Vorticity [in 1/s]

x

z
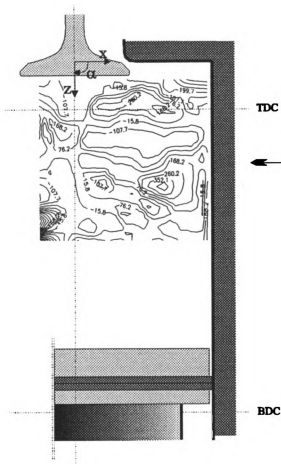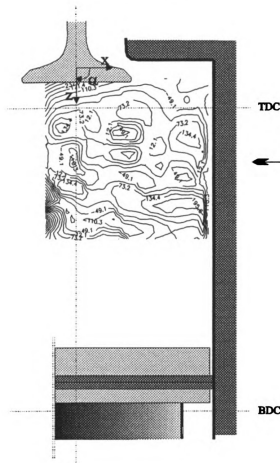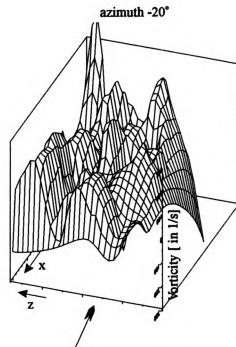
elevation 30
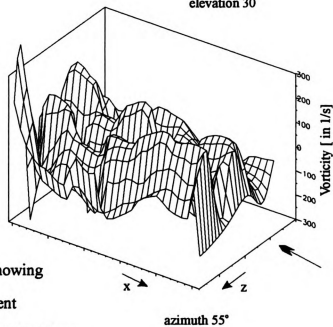
20 RPM, 6 mm;
EC #28, 132° CA

view for
azimuth = 0°

Figure V.4.6: Different perspectives showing
the distribution of the
circumferential component
of the vorticity vector.
The area covered is about 50x50 mm.

x

z

azimuth 55°

Vorticity [in 1/s]

300
200
100
0
100
200
300

2D contour plot

3D contour plots

TDC

azimuth -20°

BDC

elevation 30
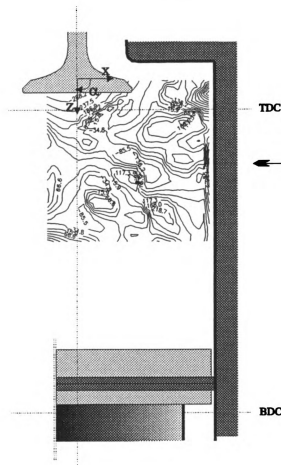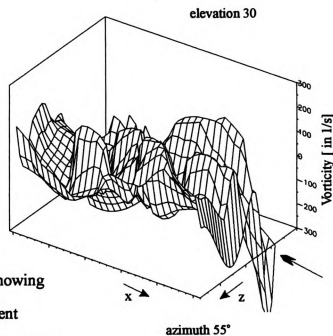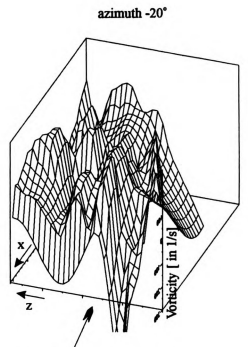
20 RPM, 9 mm;
EC #28, 132° CA

view for
azimuth = 0°

azimuth 55°

Figure V.4.7: Different perspectives showing
the distribution of the
circumferential component
of the vorticity vector.
The area covered is about 50x50 mm.

2D contour plot

3D contour plots

azimuth -20°

TDC

BDC

elevation 30

30 RPM, 3 mm;
EC #27, 132° CA

view for
azimuth = 0°

Vorticity [in 1/s]

azimuth 55°

Figure V.4.8: Different perspectives showing
the distribution of the
circumferential component
of the vorticity vector.
The area covered is about 50x50 mm.

2D contour plot

TDC

BDC

3D contour plots

azimuth -20°

Vorticity [in 1/s]

elevation 30

30 RPM, 6 mm;
EC #28, 132° CA

view for
azimuth = 0°

Vorticity [in 1/s]

azimuth 55°

Figure V.4.9: Different perspectives showing
the distribution of the
circumferential component
of the vorticity vector.
The area covered is about 50x50 mm.

251

2D contour plot

3D contour plots

TDC

BDC

azimuth -20°

elevation 30

*30 RPM, 9 mm;
EC #27, 132° CA*

view for
azimuth = 0°

Figure V.4.10: Different perspectives showing
the distribution of the
circumferential component
of the vorticity vector.
The area covered is about 50x50 mm.

azimuth 55°
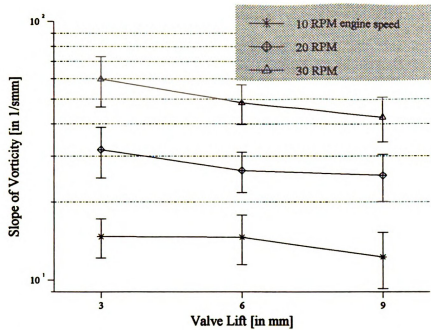
Vorticity [in 1/s]

Figure V.4.11: Evaluation of slope in circumferential vorticity distribution
in area of scrutiny as a function of valve lift and engine speed
at 132° crank-angle. Error bars are evaluated in the same manner
as for Figures V.2.1a and V.2.2.
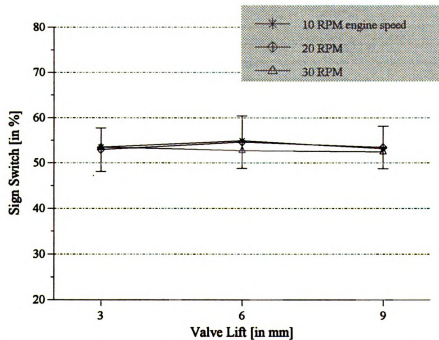
Figure V.4.12: Sign switches of slope in vorticity distribution in area of
scrutiny as a function of valve lift and engine speed
at 132° crank-angle. Error bars are evaluated in the same manner
as for Figures V.2.1a and V.2.2. Error bars for 20 RPM are
representative for other two speeds.
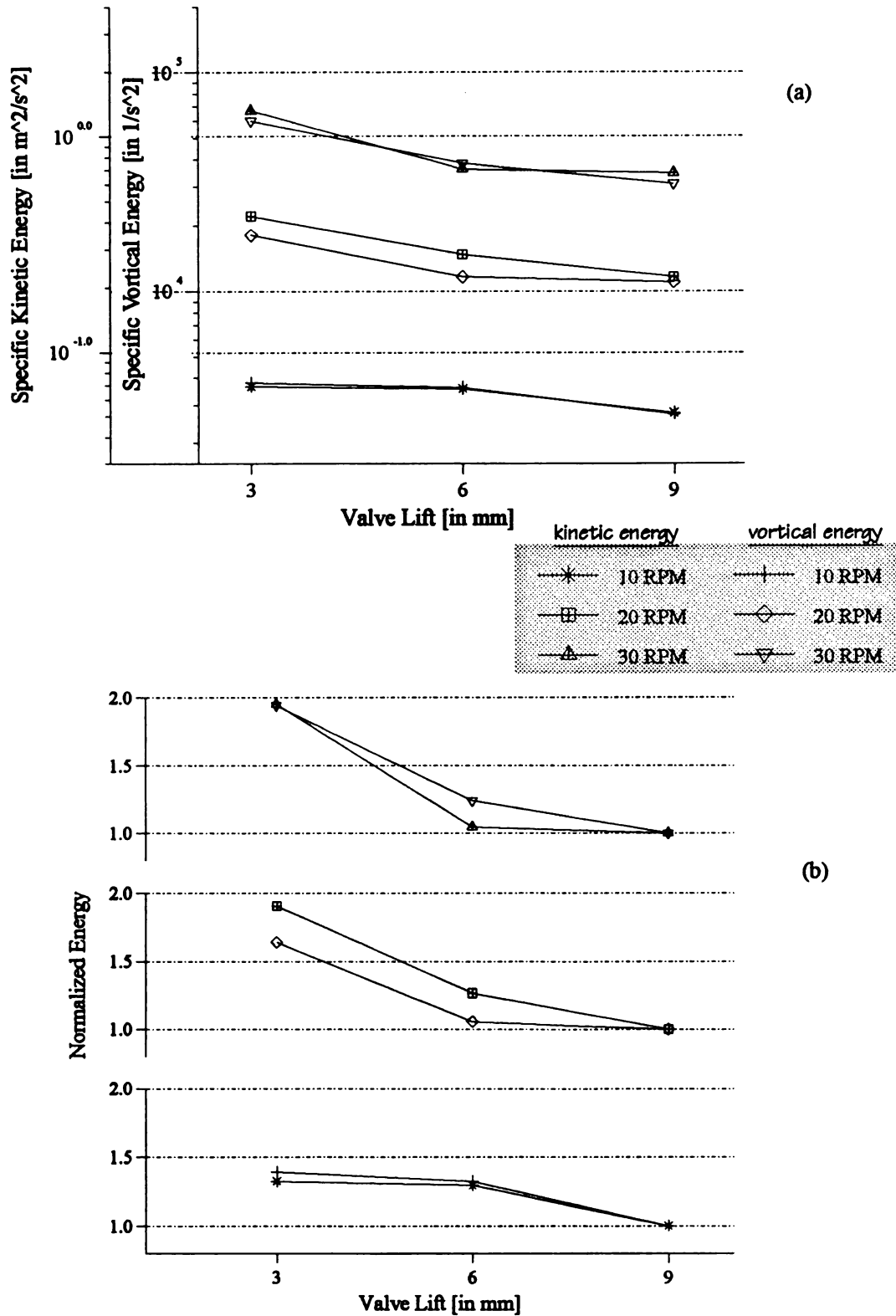
Figure V.4.13: Comparison of kinetic and vortical energy stored in area of scrutiny as a function of valve lift and engine speed at 132° CA; (a) denoting magnitudes, (b) after normalization by values for 9 mm VL.

around 50° crank-angle

around midstroke

highest piston speed

curvature is
determined by
piston position

streamlines

after midstroke
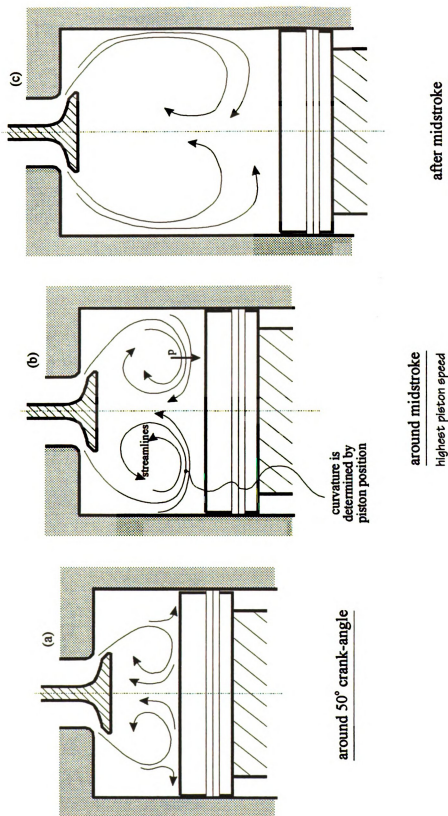
Figure V.4.14: Illustration of boundary effect on the fluid dynamics of
the main toroidal recirculation pattern.
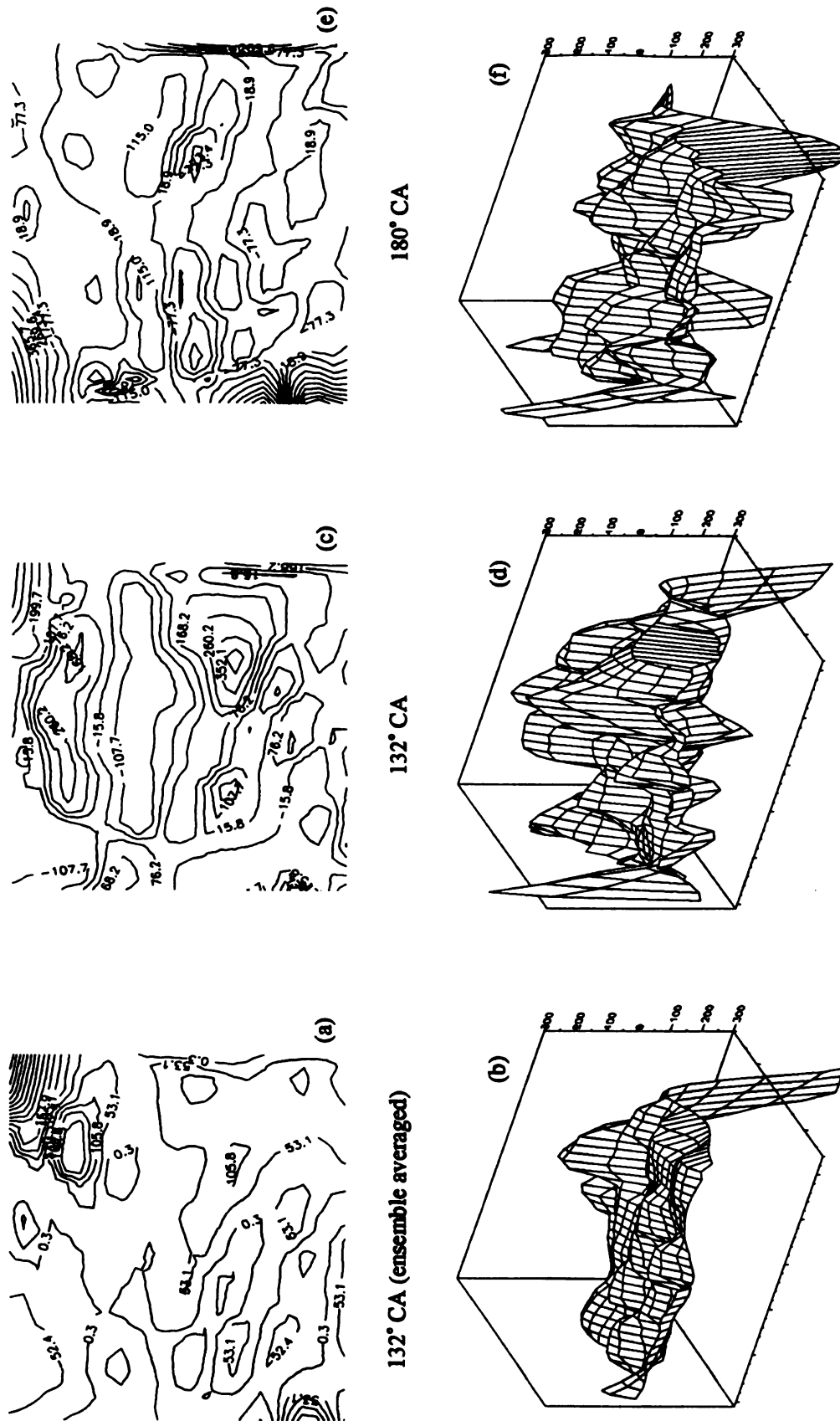
Figure V.4.15: Comparison of vorticity distributions for 20 RPM engine speed and 3 mm VL between vorticity results from ensemble averaged and from instantaneous velocity field, and also comparison between vorticity distributions from CAs 132° and 180° (end of induction stroke) within one engine cycle (EC #27). Investigated area is about 50x50 mm.
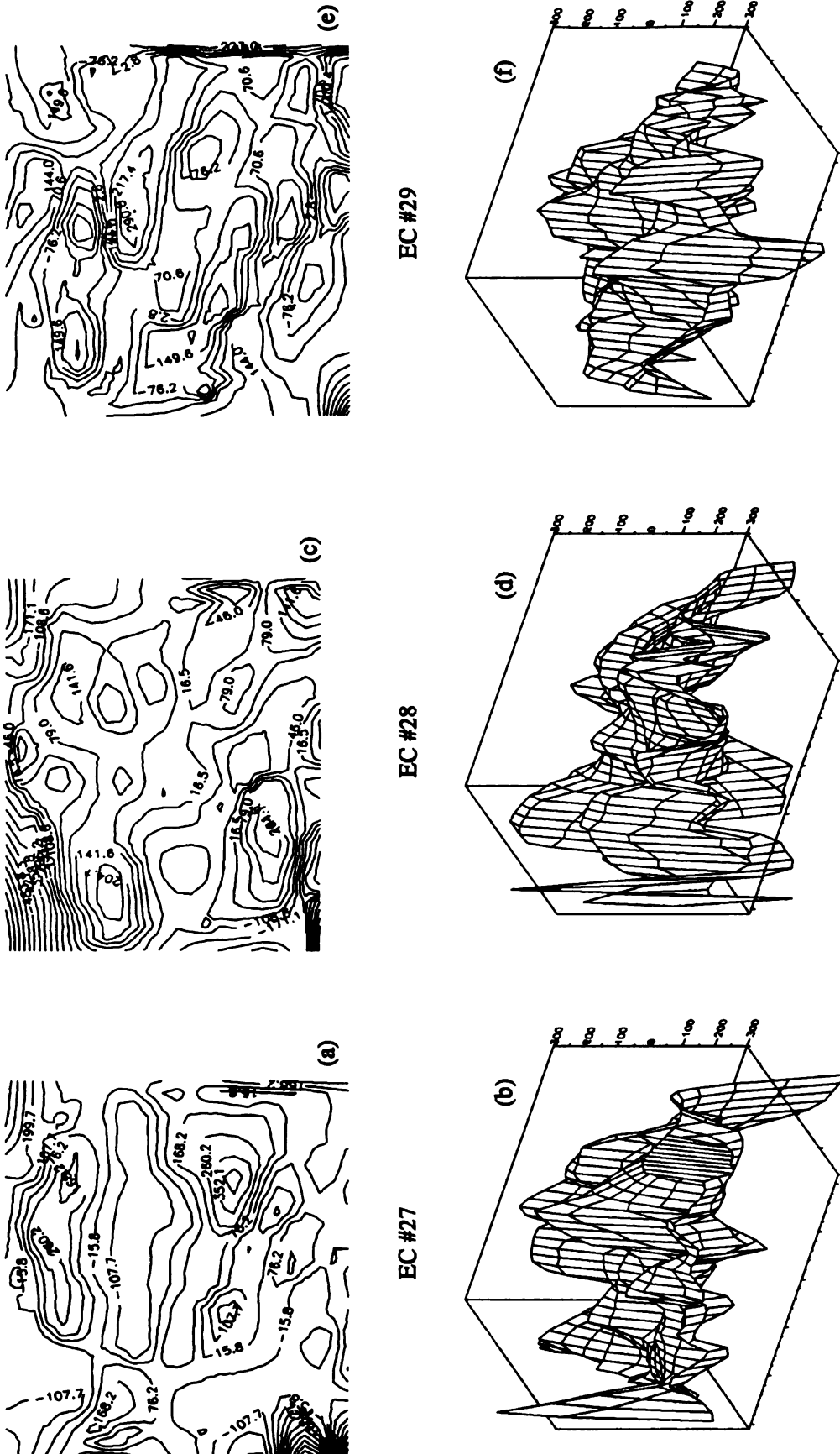
Figure V.4.16: Sequence of vorticity data for three consecutive engine cycles for 20 RPM engine speed and 3 mm valve lift at 132° crank-angle. Investigated area is about 50x50 mm.
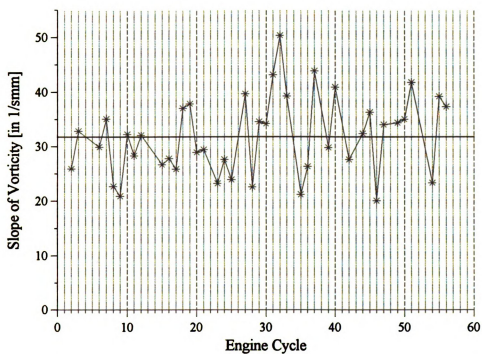
Figure V.4.17: Slope determined from the distribution of vorticity in the area of scrutiny at crank-angle 132° for individual engine cycles for 20 RPM engine speed & 3 mm VL.
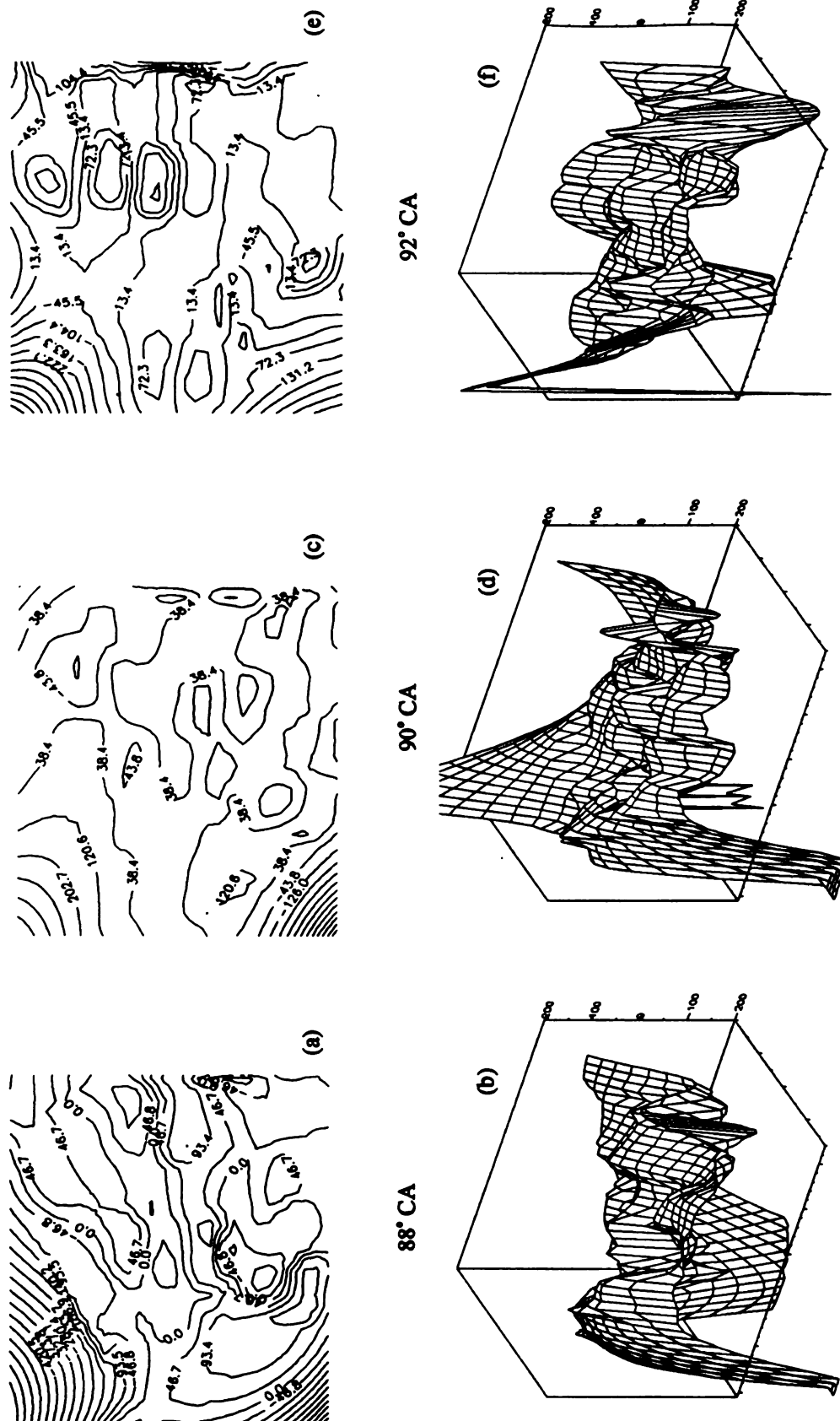
Figure V.4.18: Sequence of vorticity distributions for one engine cycle (EC #17) for 10 RPM and 9 mm VL around midstroke at crank-angles 88°, 90°, and 92°. Investigated area is about 50x50 mm.

(e)

(c)

(a)

154° CA

152° CA

150° CA

(f)

(d)

(b)
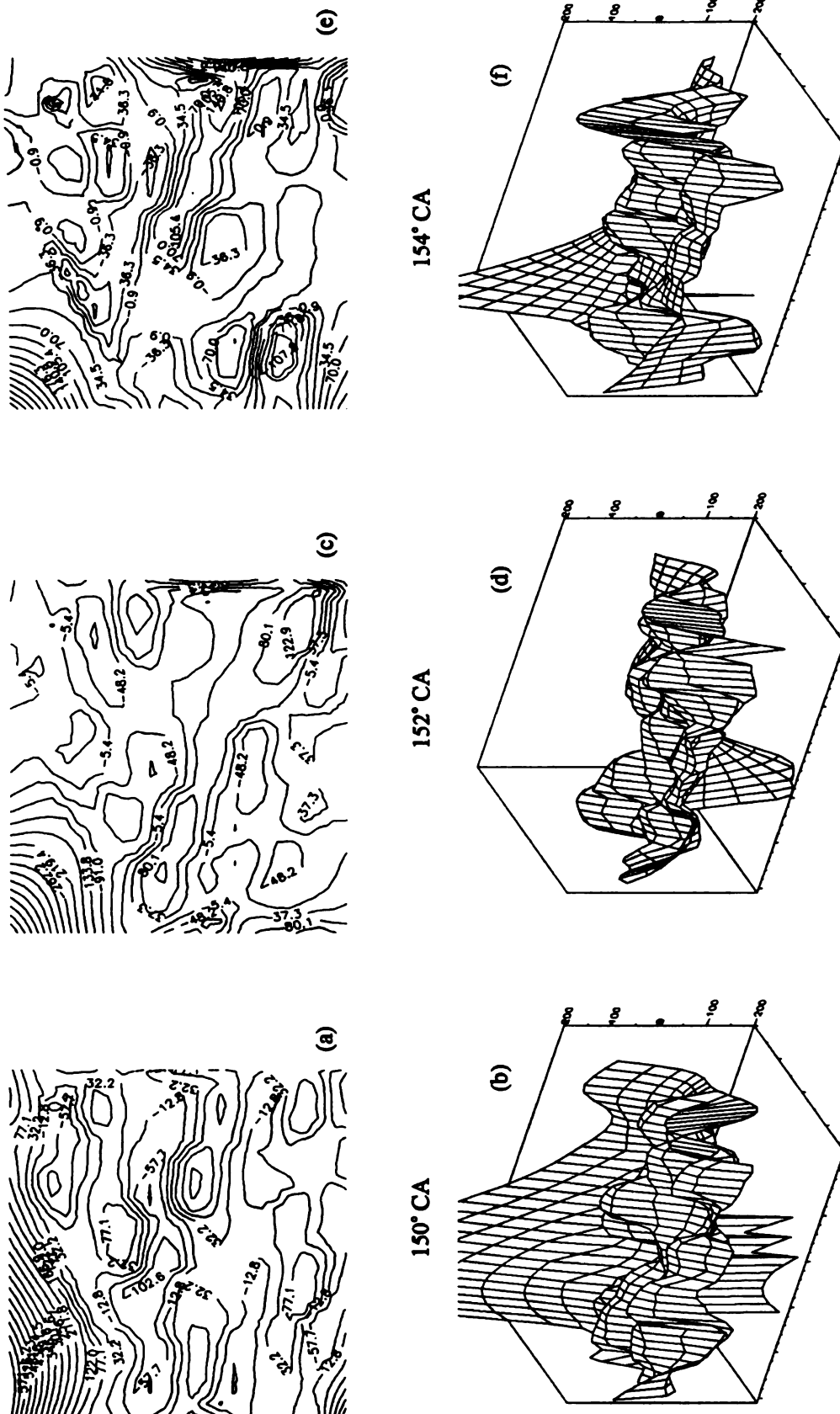
Figure V.4.19: Sequence of vorticity distributions for one engine cycle (EC #17) for 10 RPM and 9 mm VL at crank-angles 150°, 152°, and 154°. Investigated area is about 50x50 mm.
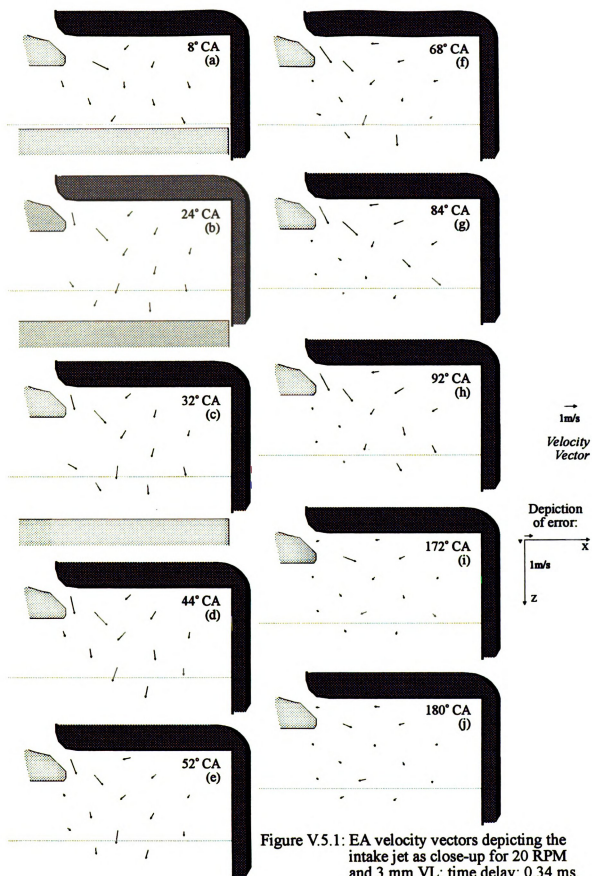
Figure V.5.1: EA velocity vectors depicting the
intake jet as close-up for 20 RPM
and 3 mm VL; time delay: 0.34 ms.
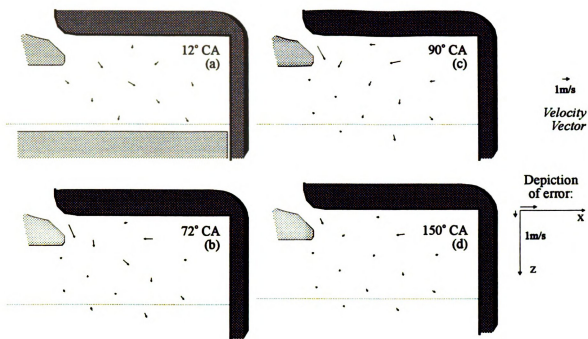
Figure V.5.2: Fields of ensemble averaged velocity vectors depicting the intake jet as close-up for 30 RPM engine speed and 3 mm valve lift at selected crank-angle positions; time delay: 0.17 ms.
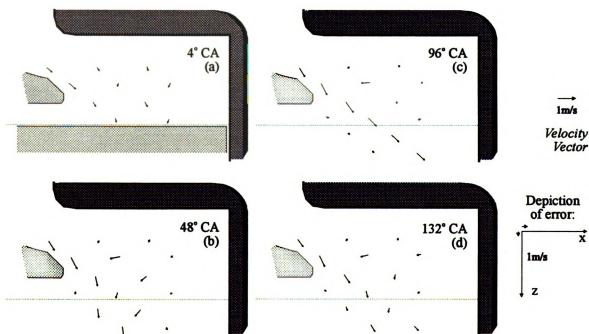
Figure V.5.3: Fields of ensemble averaged velocity vectors depicting the intake jet as close-up for 20 RPM engine speed and 9 mm valve lift at selected crank-angle positions; time delay: 0.51 ms.

1m/s
Velocity Vector

Depiction of error:

1m/s

x

z
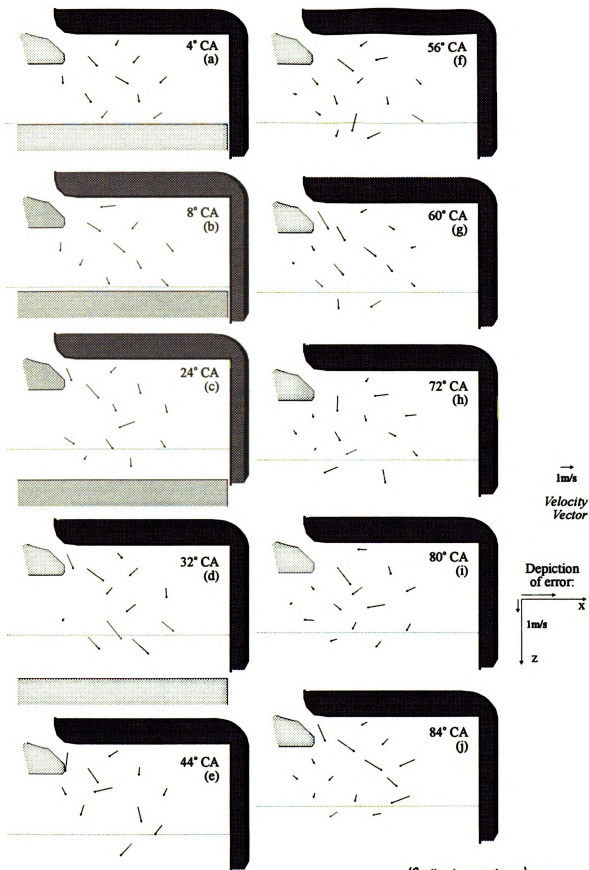
(Caption is on next page.)
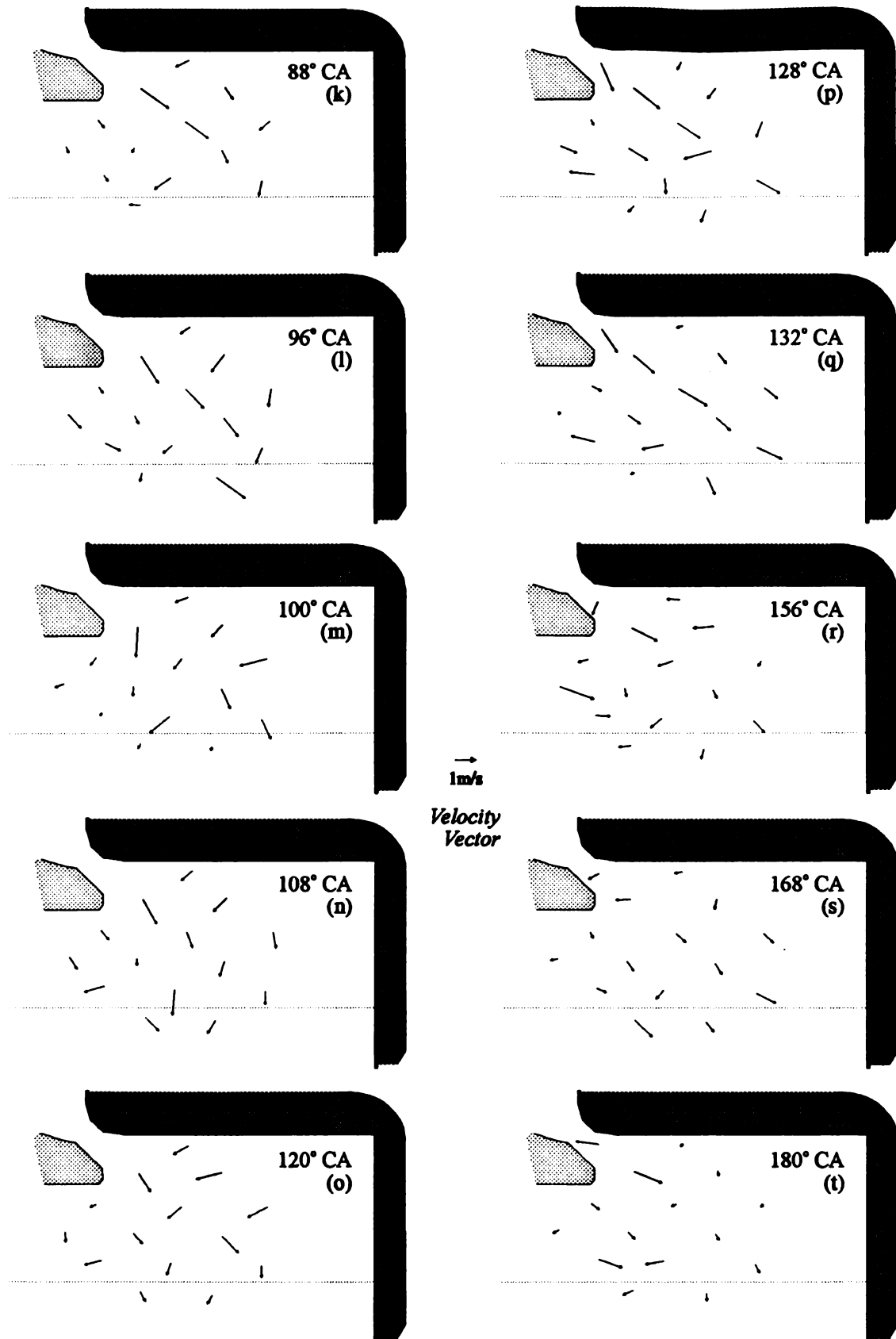
Figure V.5.4: Maps of instantaneous velocity vectors from one individual engine cycle illustrating the dynamics of the intake jet at selected CAs for 20 RPM engine speed and 3 mm valve lift; time delay: 0.34 ms.

264
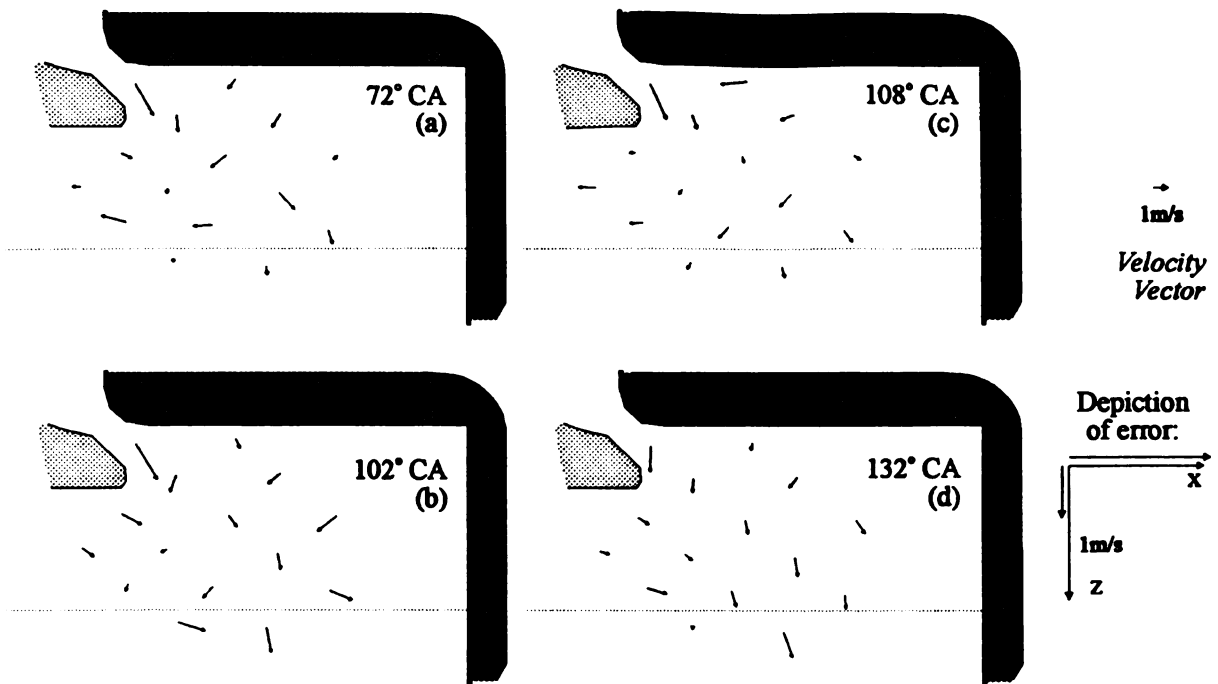
Figure V.5.5: Maps of instantaneous velocity vectors from one individual engine cycle illustrating the dynamics of the intake jet at selected CAs for 30 RPM engine speed and 3 mm valve lift; time delay: 0.17 ms.
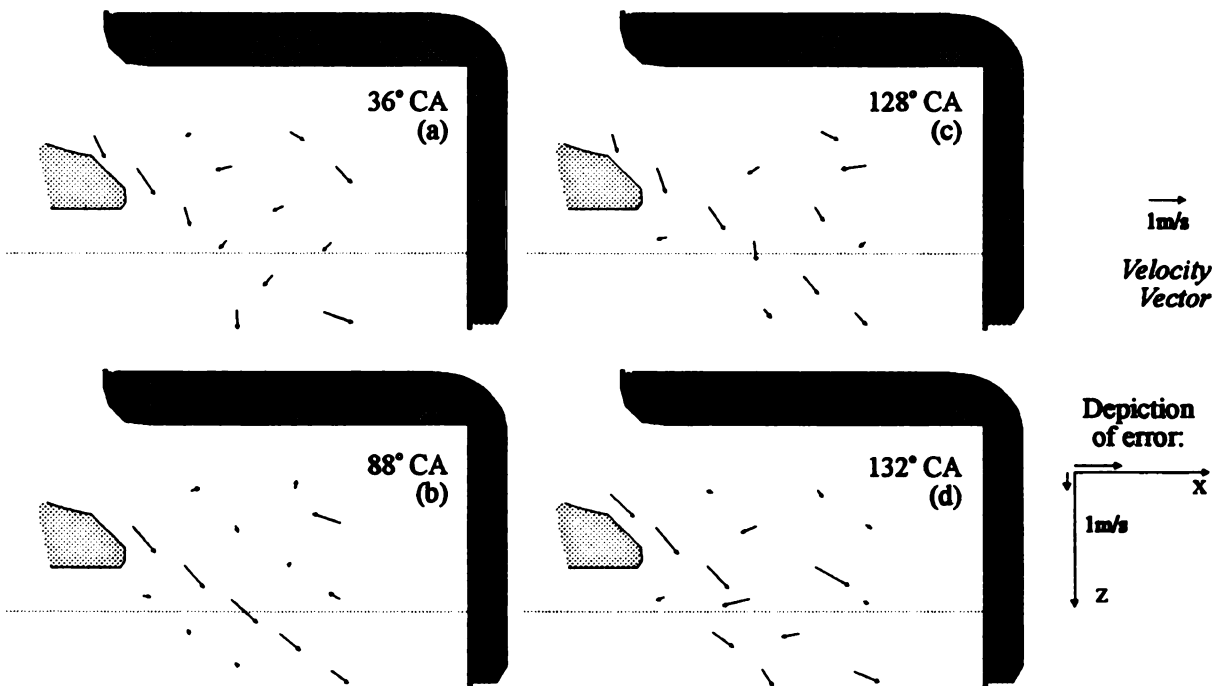
Figure V.5.6: Maps of instantaneous velocity vectors from one individual engine cycle illustrating the dynamics of the intake jet at selected CAs for 20 RPM engine speed and 9 mm valve lift; time delay: 0.51 ms.

(a) RMS Fluctuation w_{RMS} (b) Fluctuation Intensity w_{RMS}/W_{EA}
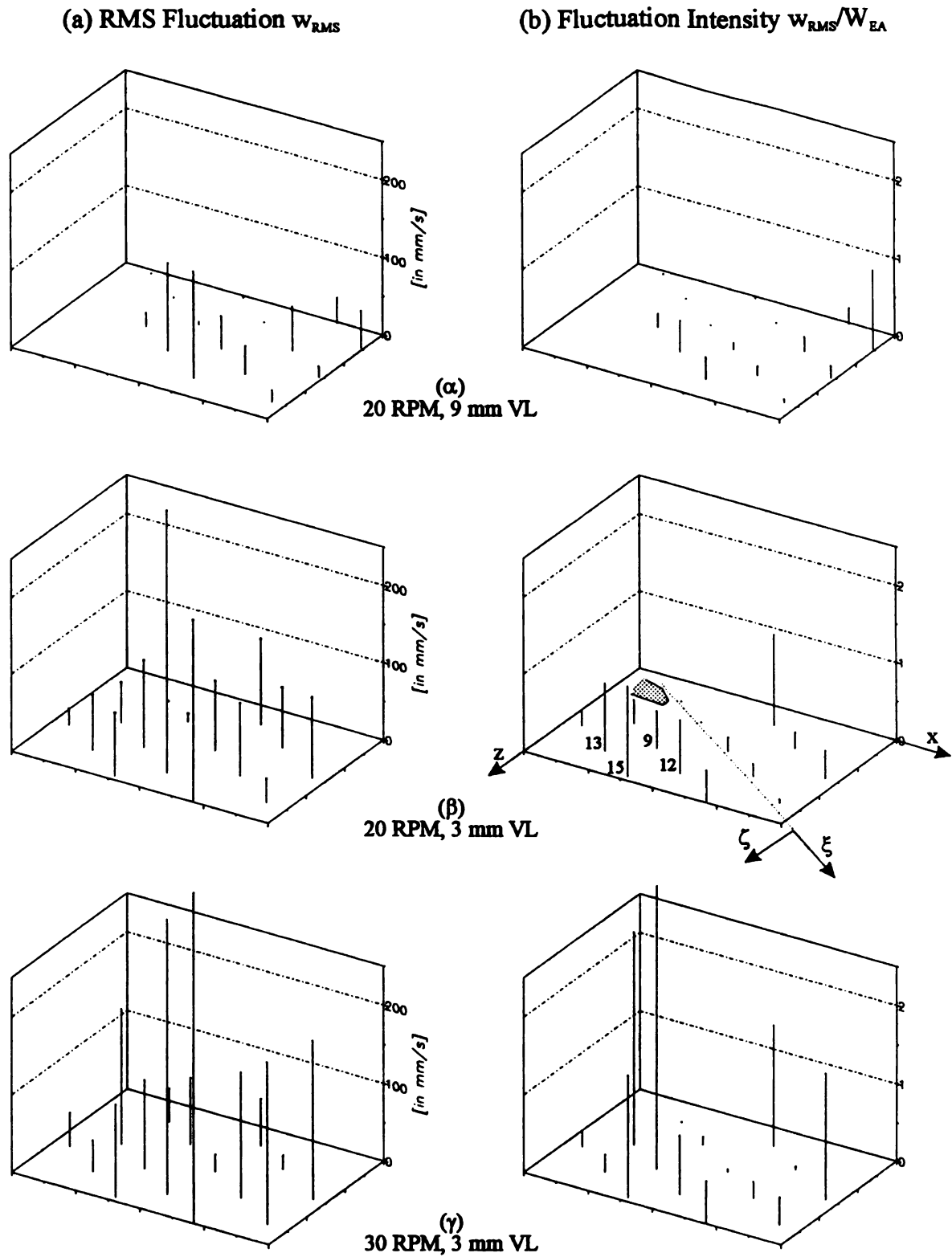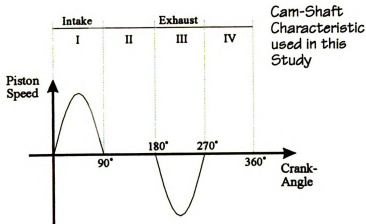

Figure V.5.7: Velocity fluctuations for (a) RMS fluctuations and (b) fluctuation intensities at 132° CA for 20 and 30 RPM engine speed and 3 and 9 mm valve lift.
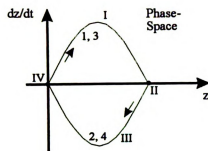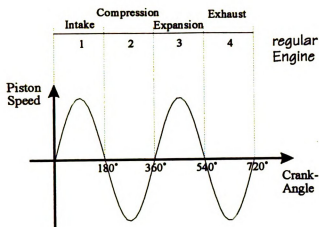
Figure A.1: (a) The differences between the piston motion of a normal four-stroke engine and the water analog model used in this work. The differences, required because of incompressibility of water, are also shown in phase space.
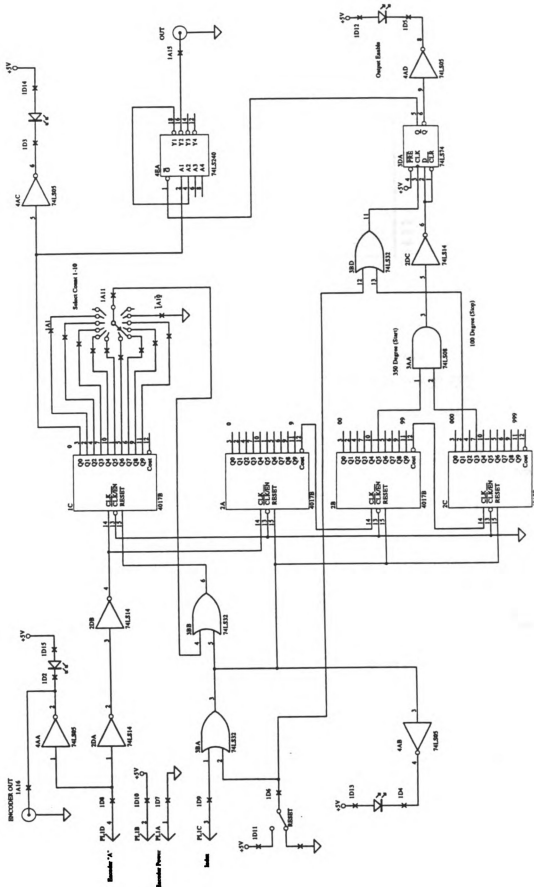(b) A picture of the cam-shaft used to create the piston motion.

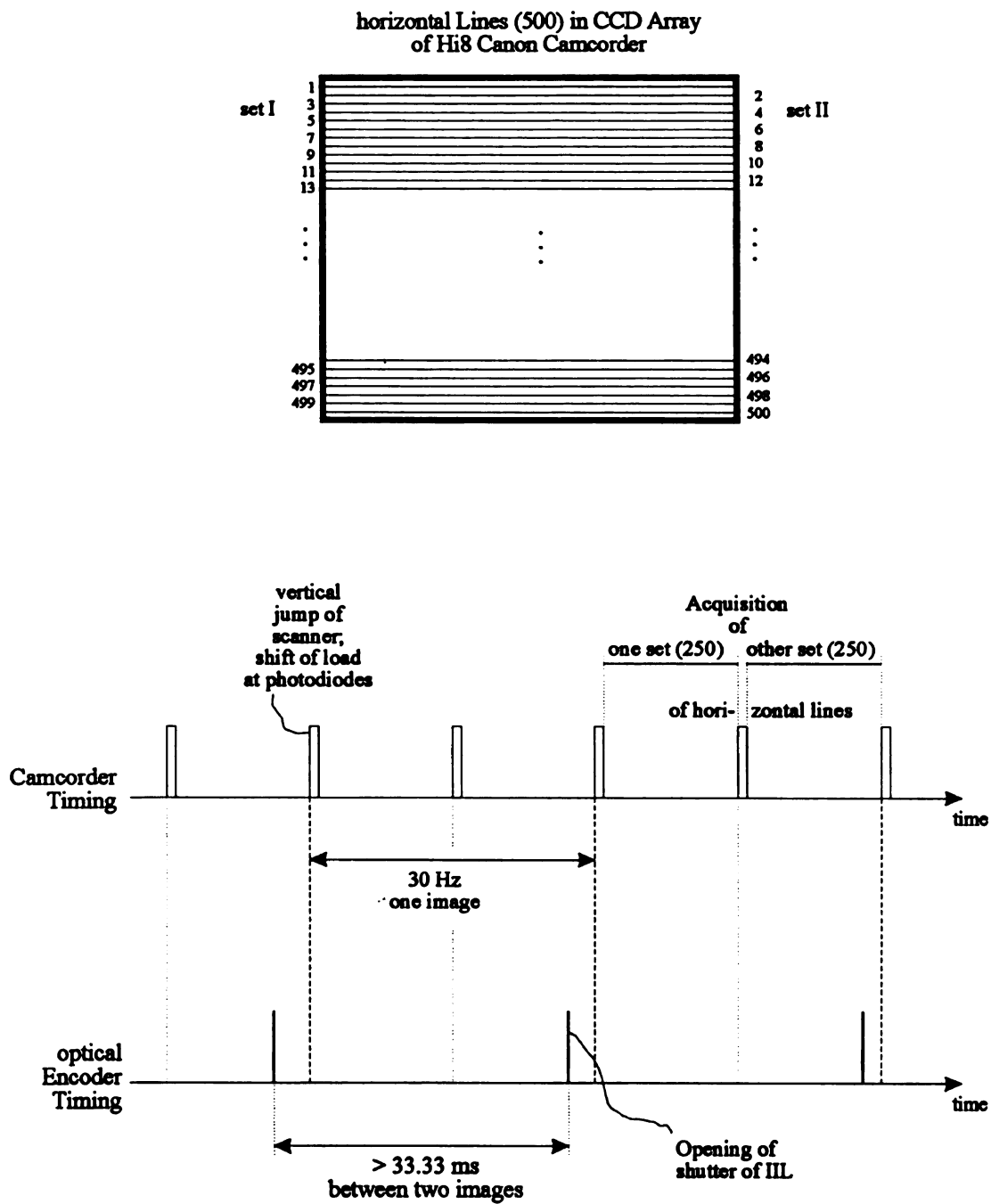Figure C.1: Drawing of circuit 'electronic signal valve'

268

Figure C.2: Virtual synchronization between timing on engine side (optical encoder) and continuously running camcorder on camera side.